Imperial College London

Spectroelectrochemical studies of multi-redox catalysts for water splitting

Carlota Bozal-Ginesta

Supervised by

James R. Durrant

Department of Chemistry

Thesis submitted in partial fulfilment of the requirements for the degree of Doctor of Philosophy

October 2017 - April 2021

The work presented in this thesis was carried out under the supervision of Prof. James R. Durrant from October 2017 to April 2021 in the Department of Chemistry of Imperial College London. A specific reference is made when the work is the result of a collaborative project or was done by someone else. This manuscript does not exceed 100 000 words in length.

Carlota Bozal Ginesta

London, April 2021

Abstract

Time-resolved absorption spectroscopy and electrochemistry have been applied to the investigation of catalyst materials that facilitate water splitting for the conversion of water and renewable energy into hydrogen and oxygen. The goal of this thesis has been to better understand structure-property relationships in different water splitting catalysts by identifying multi-redox states and establishing their role in the catalytic mechanism and the catalytic activity.

Chapters 1-2 investigate photocatalytic electrodes based on molecular organometallic catalysts for water reduction and carbon dioxide reduction immobilised on mesoporous TiO_2. This research seeks to parametrise the interplay between charge accumulation, recombination, and catalytic reaction pathways, and their impact on the catalytic efficiency of photocatalytic systems. Chapter 1 focuses on investigating the charge transfer and accumulation processes from the TiO_2 to the catalyst in acetonitrile. Chapter 2 studies the activity of H_2-production systems in the presence of water to monitor protonated multi-reduced catalytic intermediates. It has been possible to minimise recombination and to optimise the catalytic production by regulating the applied potential, the excitation light intensity, and the photoelectrode surface coverage.

Chapters 4-5 focus on iridium-based water oxidation electrocatalysts and aim at measuring their activity per iridium atom or state. In Chapter 4, a mathematical method is developed to deconvolve the absorption coefficient, the potential-dependent concentration and the water-oxidation kinetics of different redox states in electrodeposited hydrous iridium oxide IrO_x under different conditions. Chapter 5 compares the results of IrO_x with different iridium content to those of a molecular dimeric iridium complex immobilised on mesoporous ITO. Active redox states are identified under different applied potentials, and their kinetics are measured. Their mechanism and the role of the coordination sphere and chemical surrounding is discussed. Finally, Chapter 7 explores the photoreducing properties of an iridium-based molecular photocatalyst by measuring the reaction kinetics of the photoexcited reduced state.

Lay summary Resum *Resumen*

English

Hydrogen is a fuel that could be produced to store intermittent renewable energy and could potentially replace fossil fuels in high-energy demanding industries, heavy-duty transport and residential heating. This PhD thesis investigates various materials that produce hydrogen and oxygen from water and renewable energy. To better understand the reactivity of these materials, their interaction with light and their capacity to transport and accumulate charges was measured. The studied materials included highly active scarce iridium materials, and less-active earth-abundant cobalt materials. Different charged states were identified and were related to the hydrogen and oxygen production activity of the different materials. This insight could be useful for the optimisation of the hydrogen production conditions and the design of better materials.

Català

L'hidrogen és una substància combustible que pot produir-se per emmagatzemar energia renovable intermitent i podria substituir els combustibles fòssils en indústries que requereixen molta energia, transport pesat i calefacció residencial. Aquesta tesis doctoral investiga diversos materials que produeixen hidrogen i oxigen a partir d'aigua i energia renovable. Per entendre millor la reactivitat d'aquests materials, s'ha estudiat la seva interacció amb la llum i la seva capacitat de transportar i acumular càrregues. Els materials estudiats inclouen materials d'iridi que són escassos però molt actius, i materials de cobalt que són més abundants però poc actius. S'han identificat diferents estats carregats que s'han relacionat amb l'activitat d'hidrogen i oxigen dels diferents materials. Aquest coneixement podria servir per optimitzar les condicions de producció d'hidrogen i per dissenyar millors materials.

Español

El hidrógeno es una sustancia combustible que puede producirse para almacenar energía renovable intermitente y podría reemplazar a los combustibles fósiles en industrias de alta demanda de energía, transporte pesado y calefacción residencial. Esta tesis doctoral investiga varios materiales que producen hidrógeno y oxígeno a partir de agua y energía renovable. Para entender mejor la reactividad de estos materiales, se ha estudiado su interacción con la luz y su capacidad para transportar y acumular cargas has sido medida. Los materiales estudiados fueron materiales de iridio que son altamente activos pero escasos, y materiales de cobalto menos activos pero abundantes. Se identificaron diferentes estados cargados que se han relacionado con la actividad de producción de hidrógeno y oxígeno de los diferentes materiales. Este conocimiento podría ser útil para optimizar las condiciones para la producción de hidrógeno y para diseñar mejores materiales.

Acknowledgements

Thank you to my supervisor Prof. James R. Durrant for all the opportunities and guidance throughout my PhD. Thank you to Dr. Laia Francàs, Dr. Camilo Mesa and Dr. Reshma R. Rao for the help and the stimulating discussions. Thank you to all the collaborators who have made the research described here possible, with special thanks to Dr. Annika Eisenschmidt, Prof. Erwin Reisner, Dr. Yuanxing Wang, Dr. Yanyan Zhao, Prof. Dunwei Wang, Dr. Gongfang Hu, Prof. Gary Brudwig, Dr. Ravi Shankar, Prof. Ifan Stephens and their groups. Thank you to Xinyi Liu and Dr. Zhuo Li for doing some of the measurements. Thank you to all the members of the Durrant group for their kindness, especially to Dr. Ludmilla Steier for her adventurousness in trying new ideas, and to Dr. Xiaoe Li and Pabitra Shakya Tuladhar for making everything much easier both inside and outside the lab. Finally, thank you to the Engineering and Physical Sciences Research Council (EPSRC) for funding and to the European and British taxpayers for backing my education and research.

This PhD thesis is dedicated to my mother Inés and to my grandmother Teresina

Aquesta tesis doctoral està dedicada a la meva mare Inés i a la meva àvia Teresina

Contents

List of publications

Charge Accumulation Kinetics in multi-redox molecular catalysts immobilised on TiO_2, Bozal-Ginesta, C., Mesa, C.A., Eisenschmidt, A., Francàs, L., Shankar, R., Antón-García, D., Warnan, J., Willkomm, J., Reynal, A., Petit, C., Reisner, E., Durrant, J.R., *Chemical Science*, 2021, 12, 946-959

Insights from transient absorption spectroscopy into electrondynamics along the Ga-gradient in Cu(In,Ga)Se_2 solar cells, Chan, Y-H., Carron, R., Ochoa, M., Bozal-Ginesta, C., Tiwari, A.N., Durrant, J.R., Steier, L., *Advanced Energy Materials*, 2021, 11, 2003446

Covalent grafting of molecular catalysts on $C_3N_xH_y$ as robust, efficient and well-defined photocatalysts for solar fuel synthesis, Windle, C., Wieczorek, A., Sachs, M., Bozal-Ginesta, C., Cha, H., Cockcroft, J., Durrant, J., Tang, J., *Chemical Science*, 2020, 11, 8425-8432

Artificial photosynthesis – concluding remarks, Bozal-Ginesta, C., Durrant, J.R., 2019, *Faraday Discussions*, 2019, 215, 439-451

Operando spectroelectrochemical analysis of active state kinetics in water-oxidation IrO_x electrocatalysts, Bozal-Ginesta, C., Rao, R.R., Mesa, C.A., Liu, X., Hillman, S., Stephens, I., Durrant, J.R., *in preparation*

Comparative study of active states in a molecular iridium dimer and IrO_x water-oxidation electrocatalysts, Bozal-Ginesta, C., Rao, R.R., Mesa, C.A., Wang, Y., Zhao, Y., Hu, G., Antón-García, D., Reisner, E., Brudvig, G., Wang, D., Durrant, J.R., *in preparation*

Revisiting the $[Ir(ppy)_2bpy]^+$ Reductive Quenching Photochemistry, Kandoth, N., Pascual, D., Bozal-Ginesta, C., Mesa, C.A., Béjar-González, M., Pérez, J., Pérez-Prieto, J., Durrant, J.R., Lloret-Fillol, J., *in preparation*

Solar-driven enzymatic CO_2, Eisenschmidt, A., A., Miller, M., Oliviera, Bozal-Ginesta, C., Durrant, J.R., A.R., Pereira, I., Reisner, E., *in preparation*

List of figures, schemes & tables

List of abbreviations

A	Absorbance
abs.	Absorption
ACN	Acetonitrile
BET	Brunauer-Emmett-Teller
bpy	2,2'-bipyridine
C	Concentration
CB	Conduction band
CE	Counter electrode
COF	Covalent-organic framework
CoP[1]	[Co^{III}Cl(dimethylglyoximato)$_2$ (pyridyl-4-hydrophosphonate)]
CoP[2]	[$Co^{III}Br_2$(N^2,$N^{2'}$-2,2-($CH_2(C_6H_4)PO_3H$)propanediyl-bis(2,3-butanedione-2-imine-3-oxime))]
CotpyP	([Co^{II}-bis(2,2':6',2''-terpyridine-4'-phosphonate)]
CV	Cyclic voltammetry
DAQ	Data acquisition system
DFT	Density functional theory
DMF	Dimethylformamide
dmgH	dimethylglyoximato
DSSC	Dye-sensitised solar cell
E	Redox potential
e^-	Electron
em.	Emission
Et_3N	Triethylamine
Fc	Ferrocene
FTO	Fluorine doped tin oxide
h^+	Hole
i.e.	*Id est* (that is)
ILCT	Inter-ligand charge transfer
IrPS	Ir^{III}(phenylpyridine)$_2$(2,2'-bipyridine)]PF_6
ISC	Intersystem crossing
ITO	Indium tin oxide
LED	Light emitting diode
max.	Maximum
MeOH	Methanol
min.	Minimum
MLCT	Metal-to-ligand charge transfer
MOF	Metal-organic framework
Nd:YAG	Neodymium-doped yttrium aluminium garnet
NHE	Normal hydrogen electrode
OCP	Open circuit potential
OEC	Oxygen evolution complex
OER	Oxygen evolution reaction
ox.	Oxidised
PC	Photocatalyst
PEM	Polymer exchange membrane
PGM	Platinum group metal
PIAS	Photoinduced absorption spectroscopy
POM	Polyoxometalate
ppy	phenylpyridine
PSII	Photosystem II
PV	Photovoltaics
RE	Reference electrode
RHE	Reversible hydrogen electrode
SEC	Spectroelectrochemistry
SEM	Scanning electron microscopy
SP-SEC	Step potential spectroelectrochemistry
STH	Solar-to-hydrogen
t	Time
TA	Transient absorption
TAS	Transient absorption spectroscopy
TBA	Tetrabutylammonium
TD-DFT	Time-dependent density functional theory
TEOA	Triethanolamine
TOF	Turnover frequency
TON	Turnover number
TPC	Transient photocurrent
UV-Vis	Ultraviolet visible
VB	Valence band
vs.	*Versus*

Chapter 1

Water splitting – the key to artificial photosynthesis

Sections 1.1-3 in this Chapter are published in Faraday Discuss., 2019, 215, 439-451. (DOI: 10.1039/c9fd00076c)*, with the contribution of Prof. James R. Durrant.*

This chapter aims to discuss the context for the research in artificial photosynthesis, which is the framework underlying this thesis (Section 1.1). First, the motivation for this research in the context of renewable energy conversion and storage is overviewed (Section 1.2). The composition and trends in the field of artificial photosynthesis are then analysed and its scale is assessed relative to other related research areas (Section 1.3). The conclusions are primarily drawn from the results of searches in publication data bases (Sections 1.3 and 1.7). Finally, the current research challenges in the field are discussed (Section 1.4) and the aims of the thesis are presented (Section 1.5).

1.0. Contents

1.1. Introduction

Artificial Photosynthesis is a term used to describe most widely any man-mediated process which stores sunlight energy in useful, high energy chemicals.[1-4] One of its most studied applications is the production of fuels (so-called Solar Fuels) and, in particular, the production of H_2 and O_2 from water (*i.e.*, water splitting) to replace fossil fuels and enable the carbon neutral exploitation of the energy subsequently freed to their combustion. Artificial Photosynthesis draws inspiration from natural photosynthesis, which selectively and reversibly produces multiple sorts of chemicals under mild conditions, being the main source of energy-rich organic compounds on the planet.[5-7] Taking natural photosynthesis as a reference, Artificial Photosynthesis is usually composed of three main steps (Scheme 1.1): (a) the absorption of light, (b) the generation and separation of charges through space, and, finally, (c) the chemical conversion of these charges and substrates into fuels or other chemicals, which is enabled by catalyst materials.[8, 9]

Since Fukushima and Honda first reported the splitting of water into hydrogen and oxygen with light in 1972,[10] many efforts have been devoted to this goal, but the most promising devices and materials still suffer from fast component degradation and/or large efficiency losses.[11-13] Progress in the field has been limited by scientific factors (*i.e.*, the fundamental understanding of the charge generation and separation processes,[14-16] the available techniques,[17-21] the development of better photoabsorbers and catalysts, etc.[22-26]) but also by other variables such as the severity of energy and climate crisis,[27, 28] differing funding priorities and changing innovation strategies.[29, 30] The main motivations to continue working on Artificial Photosynthesis, however, have remained intact.

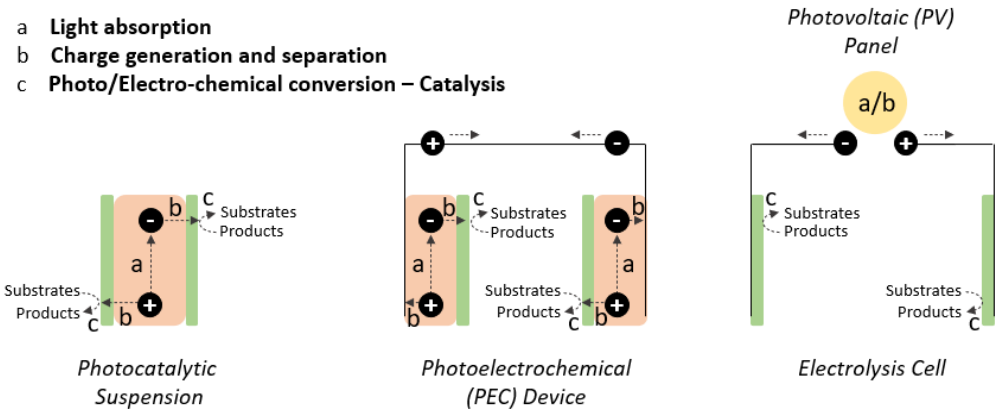

Scheme 1.1. Representation of the Artificial Photosynthesis steps in different device architectures.

Different possible approaches to develop a functional and commercially viable solar-to-chemical energy conversion device have been proposed, as illustrated in Scheme 1.1. These approaches in Artificial Photosynthesis research can be broadly classified into three main groups, depending on (1) the nature of the catalyst materials used,[31-44] (2) the degree of system integration,[45-48] and (3) the substrates and products involved.[49-52] This thesis mostly belongs to the first group. The work described in the following Chapters focuses on investigating the physicochemical properties of different catalyst materials, and understanding the effect of these properties on the electro- and photo-chemical reactivity of the catalysts. To contextualise this research, in the following Sections, the trends in the field are analysed based on publication data, and the key challenges in the field are discussed.

1.2. Motivation: the energy problem

Artificial Photosynthesis is one strategy to address growing energy demand worldwide and the dependence of our current energy system on fossil fuels,[53, 54] complimentary to the development of renewable sources of electrical power, sustainable bio-derived energy and increases in energy efficiency. It offers a potentially low-carbon or carbon-neutral pathway for the synthesis of sustainable fuels (for example, 'green' hydrogen from water). It also offers scalable pathways for carbon dioxide reduction and utilisation, as well as the potential for carbon-neutral nitrogen reduction for fertiliser manufacture.

A key motivation for artificial photosynthesis concerns the geographical location of energy resources. Fossil fuels reserves are unequally spread geographically.[53, 54] The wealthiest countries in the world are the largest energy consumers, and they are typically dependent on the large scale transportation of energy to them, primarily in the form of fossil fuels transported in marine tankers or gas pipes.[53, 55, 56] On the other hand, sunlight is the largest available renewable energy resource (Figure 1.1)[57] and renewable sources are geographically relatively dispersed compared to fossil fuels. Given the limitations of long distance electrical power distribution, the storage of solar and renewable in chemical fuels, and their transportation in tankers or gas pipes presents a scalable pathway to transport and distribute renewable energy globally.[58]

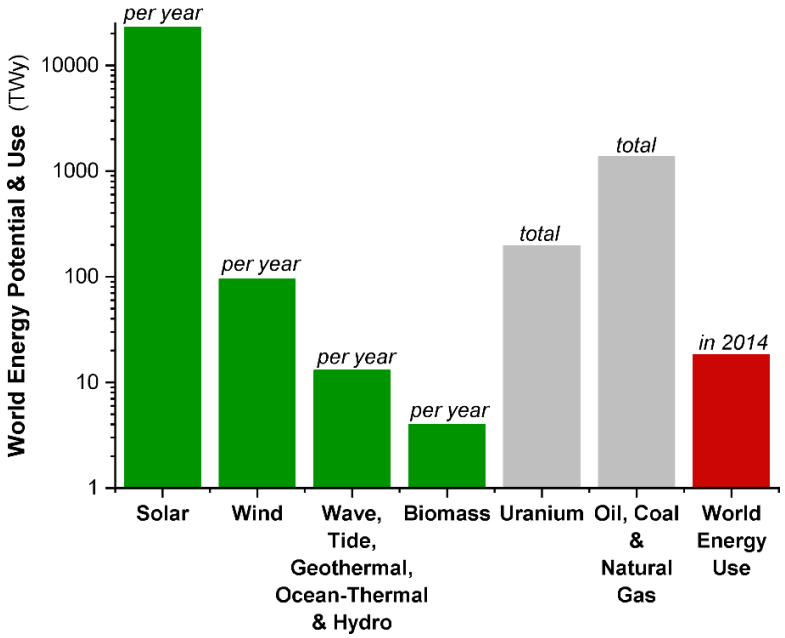

Figure 1.1. World energy use and world energy potential of renewable sources yearly (in TW) and non-renewable sources (total recoverable reserves of uranium, oil, coal and natural gas in TWy).[53, 56, 57]

A further motivation for artificial photosynthesis results from the intermittency of most renewable energy sources. The availability of most renewable energies is variable, depending on the weather conditions, the time of the day, the month and the season. Since peak energy demands occur during the evening and in winter, and because energy-intensive industries and heavy-duty transport cannot rely on fluctuating and unpredictable energy sources, the large scale deployment of renewable energy systems increasingly requires that the energy generated can be stored efficiently and cheaply.[59, 60] Electrical power can be stored in batteries and related technologies to address short term (up to days/weeks) fluctuations in renewable electricity generation, but they lack scalability and their relatively high cost make them unsuitable for long term and, in particular, interseasonal storage.[61, 62] Moreover, batteries have a limited volumetric and gravimetric energy density compared to chemical fuels (Figure 1.2).[63, 64] This means that whilst batteries are rapidly becoming the energy storage medium of choice for cars, they are likely to remain too heavy to power effectively long-distance marine and aviation sectors. For both of these storage challenges, the efficient storage of renewable energy as chemical fuels (*i.e.*, Artificial Photosynthesis) provides a potentially attractive low carbon solution.

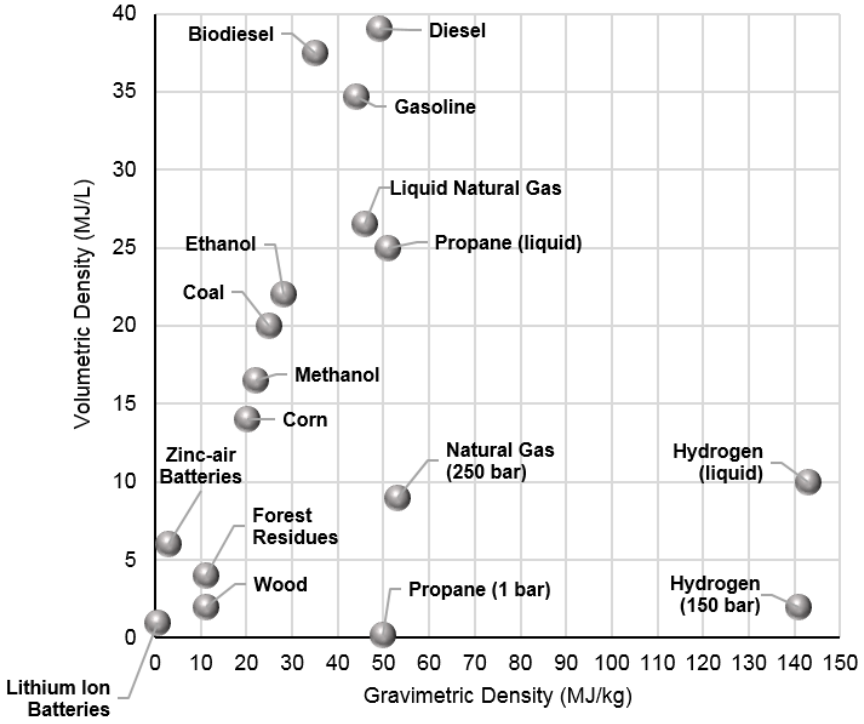

Figure 1.2. Volumetric and gravimetric energy density of different fuels and batteries. Adapted from references [63, 64].

A particular concern with many developing artificial photosynthesis strategies is that the best catalysts converting electrical potential into chemicals, both in electrolysers and in many direct artificial photosynthesis systems such as photo(electro)chemical devices, are based on metals belonging to the platinum group (*i.e.*, ruthenium, rhodium, palladium, osmium, iridium and platinum). These metals are classified as critical raw materials by the European Union because of their high supply risk and economic importance, and are therefore of limited suitability for large scale mass production.[65-67] This is a potentially limiting constrain for Artificial Photosynthesis and motivates fundamental research towards developing more sustainable components based on earth-abundant materials.[23, 25, 26, 68, 69]

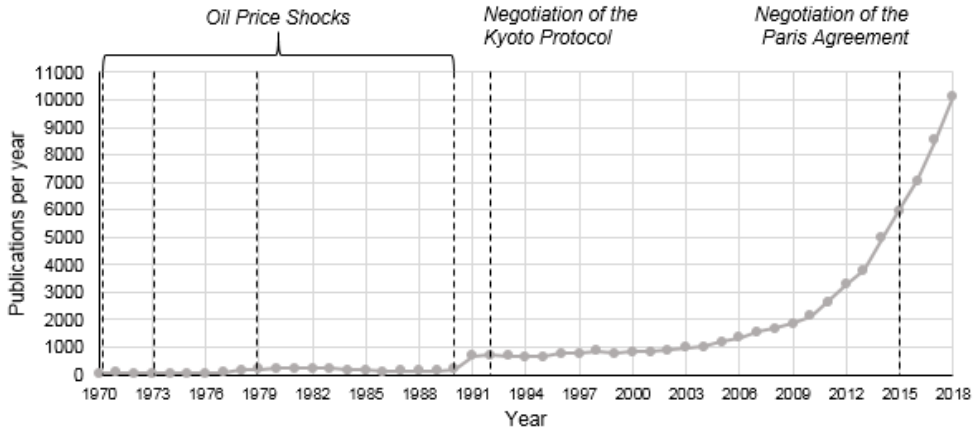

Figure 1.3. Historical evolution of publications per year in Artificial Photosynthesis. Reference: https://login.webofknowledge.com/, *Web of Science*, consulted on April 2019.

1.3. The Artificial Photosynthesis research field

An analysis of the artificial photosynthesis research field has been carried out by considering the amount of publications related to different sets of search terms. The results of any such search depends critically on the choice of search terms, and is therefore only partially objective. Many terms and expressions can be used to refer to processes inherent to Artificial Photosynthesis, with light-driven catalysis at their heart. Herein, publications are considered to address artificial photosynthesis if the title, abstract or keywords include words with the prefix *photo* followed by *reduction* or *oxidation,* or include the word *electrochemical* or words with the prefix *photo* combined with terms referring to water splitting and CO_2 reduction (see sections 1.7.1. and 1.7.2. in the Annex for the exact search criteria). Different ways to express the same concept have been considered in each one of the searches, including singular and plural terminologies, chemical formulas and the most common synonyms, and broadly yielding similar trends. This search is not perfectly complete, because publications do not always explicitly mention the technical definition of the materials and devices studied, and because less common expressions and word combinations have been omitted. The aim has been to make the selected groups of publications reasonably representative and indicative of trends in the artificial photosynthesis field.

Figure 1.3 illustrates the growth in publications in the field of Artificial Photosynthesis. Whilst the field was initiated in the 1970's with the pioneering work of Fukushima and Honda, it has only grown significantly since the early 1990's, motivated by increased concerns over oil prices and the environmental impact of fossil fuels, as well as by scientific advances in our understanding of electron transfer in natural photosynthesis and liquid-semiconductor junctions.[55, 70-73] Since then, it has grown rapidly, exhibiting an exponential increase in the number of publications.[74] However, compared to other energy conversion technologies, Artificial Photosynthesis is still at an early development stage, with relatively few patents and companies compared to the related fields of batteries, electrolysers and solar cells (Figure 1.4). This perhaps reflects the particularly complex scientific challenge associated with the development of artificial photosynthesis technologies.

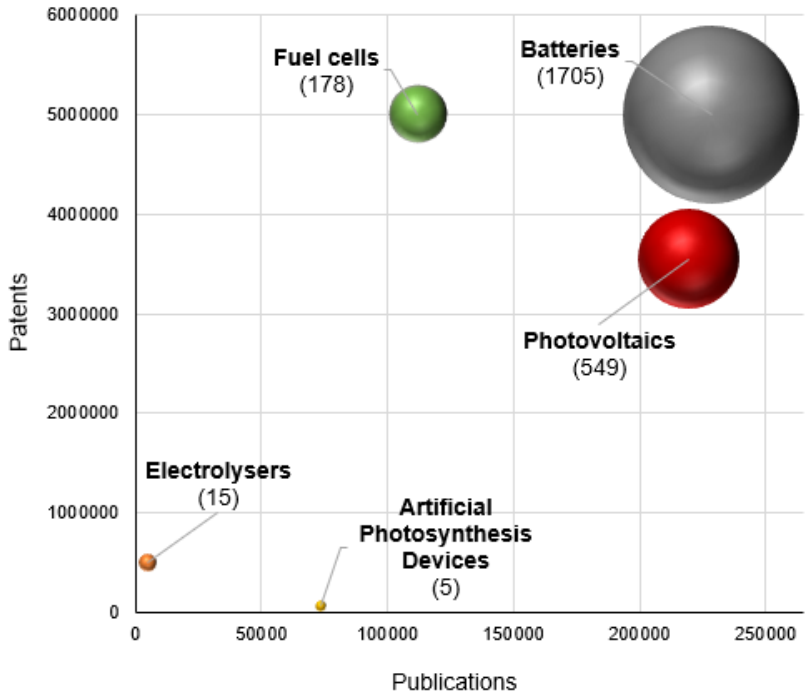

Figure 1.4. Comparison between battery, photovoltaic, fuel cell, electrolyser and artificial photosynthesis technologies based on the number of patents (y-axis), publications (x-axis) and companies (bubble size in parenthesis). Search details are given below – the uncertainty on the most appropriate search terms for each technology means this figure has a higher degree of subjectivity than other search results reported in this Chapter.

The classification by research area of publications to date in the field of artificial photosynthesis is considered in Figure 1.5.[74] Perhaps unsurprisingly, Chemistry is the largest discipline, followed by Materials Science, Engineering, Physics and Biochemistry and Molecular Biology. On the other hand, Electrochemistry stands out as the key area of expertise followed by Energy Fuels.[75] From the geopolitical perspective, China, United States, the European Union and Japan are at the forefront in Artificial Photosynthesis research output, with most of these countries having implemented focused programs on this topic in the last 25 years (Figure 1.6).[76-78]

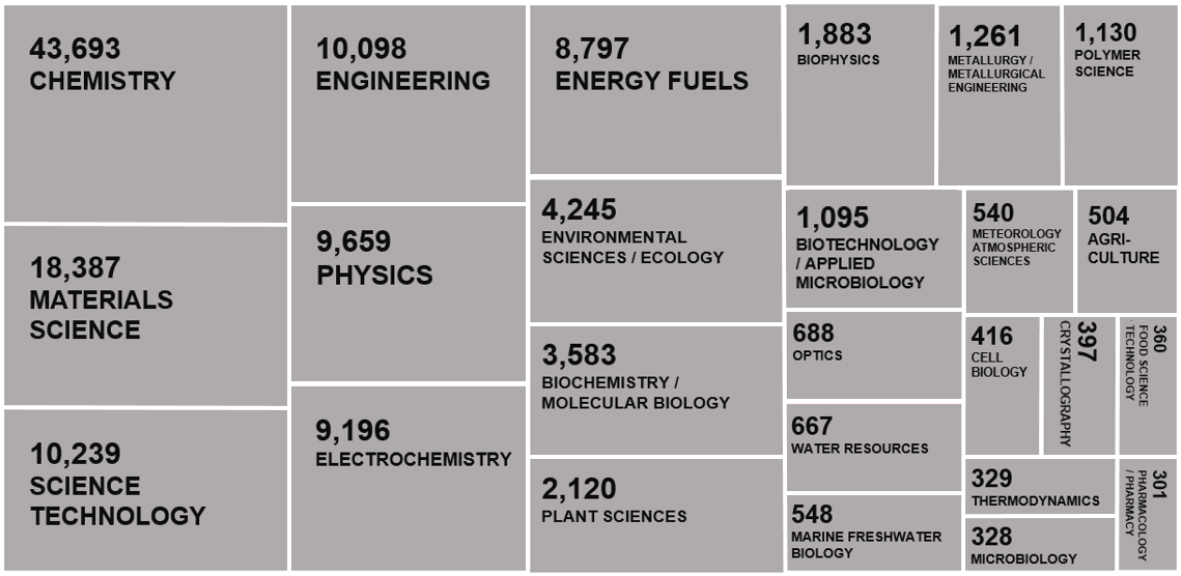

Figure 1.5. Publications to date in Artificial Photosynthesis classified by Research Area (see the Annex in section 1.7 for classification criteria).[74]

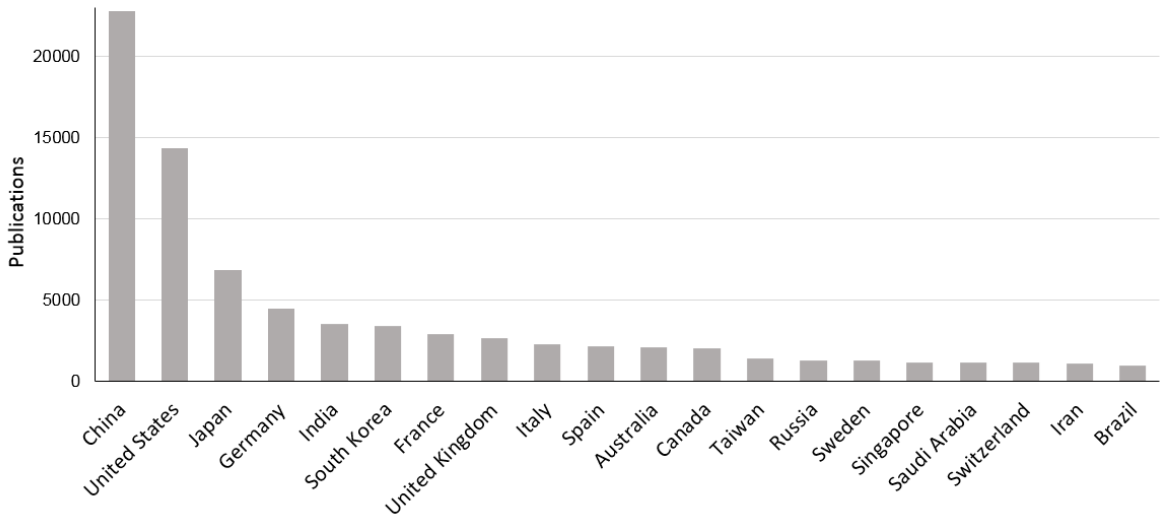

Figure 1.6. Publications to date in Artificial Photosynthesis per country. Reference: *https://login.webofknowledge.com/*, *Web of Science*, consulted on April 2019.

1.3.1. Classification according to Device Type

The degree of integration of components performing one or more steps (*i.e.*, light absorption, charge separation or catalysis) can be a criterion to distinguish different research categories. Most simply, three architectures have been proposed for artificial photosynthetic devices, as illustrated in Scheme 1.1.[8, 79] The first comprises coupling photovoltaic panels with electrolysers, which both are relatively mature technologies. The second architecture is based on photo(electro)chemistry, where light absorbing materials are integrated with catalytically active materials into electrodes that could be used in unbiased light driven electrolysers. The third architecture is based on photocatalysis, where light absorbing and catalytic materials are suspended in solution as homogeneous suspensions, most typically as particles. Other device architectures, such as photocatalyst sheets or photovoltaic buried junctions, are attracting increasing interest, but have resulted in relatively few publications to date.

Among the total of 74000 articles published to date related to Artificial Photosynthesis, 6300 can be readily identified as focusing on devices, junctions and photoelectrodes, and 11300 on catalysis (including photocatalysis) (see Section 1.7 for search criteria). A much lower proportion can be identified as targeting photoabsorbers, probably because such publications are rather oriented towards solar cell research and photovoltaics. Figure 1.7 represents the historical trends in the proportion of publications related to photocatalytic homogeneous suspensions and photoelectrodes; it is apparent that, since 2010, there has been increasing focus on photoelectrodes rather than photocatalytic suspensions. Relatively few publications can be identified as focusing on combined photovoltaics and electrolysers, which are most likely to be investigated together primarily at an industrial level, with ~3500 patents on combined photovoltaic and electrolyser systems, significantly more than the number of publications on this approach.

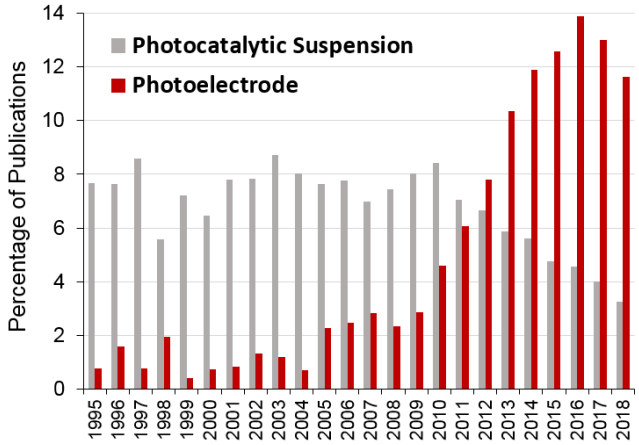

Figure 1.7. Percentage of the total amount of publications per year in Artificial Photosynthesis related to photoelectrodes or photocatalytic suspensions. Reference: *https://login.webofknowledge.com/, Web of Science*, consulted on April 2019.

1.3.2. Classification according to Catalyst Material

Leaving aside genetically modified photosynthetic organisms, the most widely investigated materials studied in the field of artificial photosynthesis as catalysts are earth-abundant metal oxides (e.g. TiO_2, CuO, $BiVO_4$), platinum group metals and metal oxides (for example, platinum, RuO_2, IrO_2), enzymes, carbon nitrides, metal- and covalent-organic frameworks (MOFs and COFs), molecular catalysts, polyoxometalates (POMs), dichalcogenides, perovskites, gallium nitrides and light-absorbing, conjugated polymers (Figure 1.8). The first are often regarded as robust and, together with dichalcogenides, MOFs, COFs, semiconducting polymers and carbon nitrides, are used as photocatalysts. POMs have been used both as electrocatalysts and photocatalysts. It is striking from Figure 1.8 that carbon nitrides and, to a smaller extent, POMs and dichalcogenides have experienced a particular growth in research activity recently. Carbon nitrides have also been used as dyes, while semiconducting polymers and oxides have been used as charge separation layers. On the other hand, enzymes, which have been investigated in both natural and artificial photosynthesis systems, and molecular catalyst need to be coupled to an electron source. Despite being faster, more selective and working at lower overpotentials, the latter are harder to obtain, typically less stable and more sensitive to the working conditions, which may account for the smaller representation in the field.

Silicon has been excluded because of its wide use as dopant. Furthermore, we have omitted platinum group metals (PGMs) and perovskites from the metal oxide search, PGMs and metal oxides from the perovskite search and carbon nitrides from the polymer one to guarantee that catalytic materials are not repeated twice. As a consequence, papers including mutually excluded materials have been filtered out (papers with polymers+carbon nitrides or metal oxides+perovskites). Publications including dyes based on PGM and either perovskites or metal oxides, are represented by the PGM category in Figure 1.8.

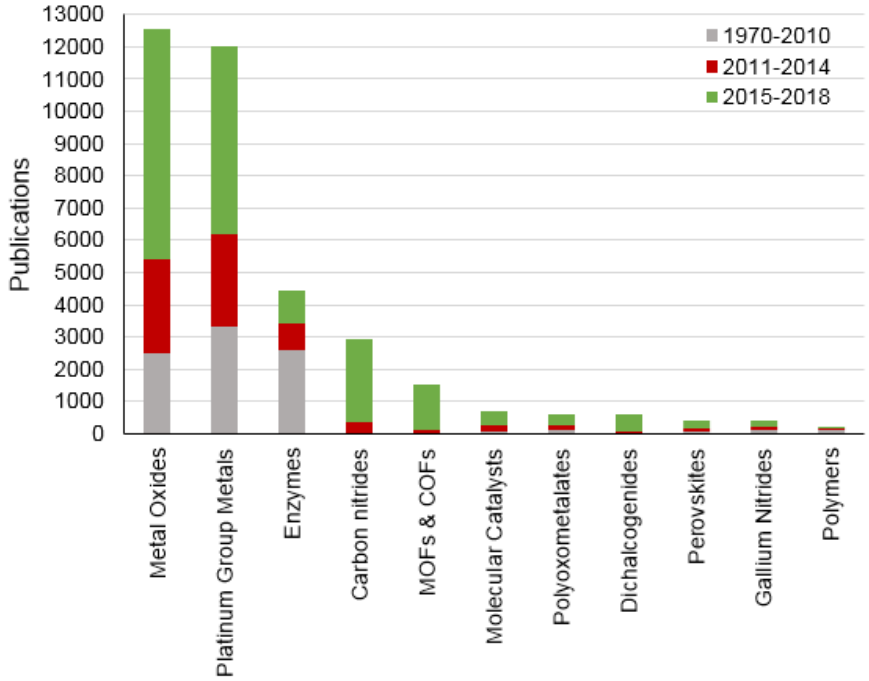

Figure 1.8. Publications in Artificial Photosynthesis related to different materials.[74] Publications employing semiconducting silicon were not categorised separately due to overlap with its use as a dopant in metal oxides.

1.3.3. Classification according to Substrates or Products

Finally, Artificial Photosynthesis research can also be sorted according to the type of substrate converted or the final product. Two categories represent ~90% of the publications in the field. The dominant one is water splitting, involving the reduction of water into hydrogen and its oxidation into oxygen.[23, 80, 81] The second is CO_2 reduction to form carbon monoxide, formate, formaldehyde, methanol or methane.[82-84] Alternative chemical targets of interest for photo-electrochemical conversion include N_2 fixation into ammonia,[85-87] photo-degradation of organic pollutants[88] or the utilization of low-value industrial side products such as glycerol.[89] Figure 1.9 shows the percentage of publications focused on water oxidation, water reduction or CO_2 reduction.

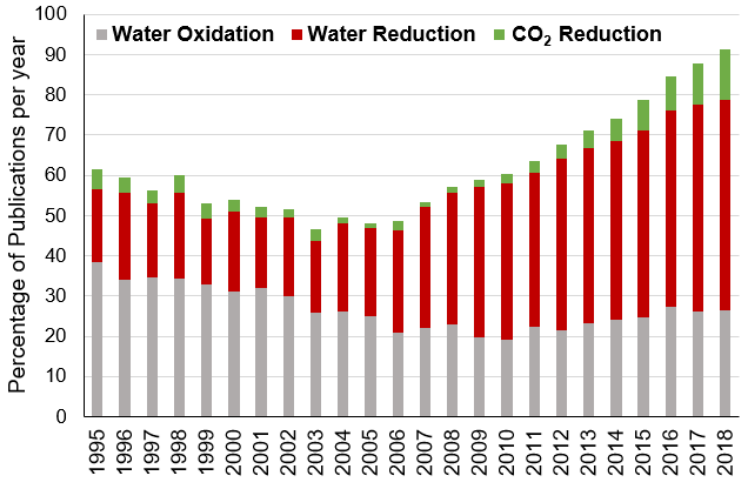

Figure 1.9. Percentage of the total amount of publications per year in Artificial Photosynthesis and Photocatalysis exclusively related to CO_2 reduction, water oxidation or water reduction.[74]

While 20 years ago a larger diversity of photocatalysed reactions was studied (including for example a range of organic oxidations), currently most published research in the field of artificial photosynthesis focuses on either CO_2 reduction, water reduction or water oxidation. The proportion of research dedicated to water reduction (or H_2 production) and CO_2 reduction has increased, while water oxidation (or O_2 evolution) has slightly decreased and plateaued at around 25%, although the total amount of publications have increased exponentially in all the sub-areas parallel to the general trend in the field. The evolution of water oxidation research may have been influenced by the progress in understanding Photosystem II in natural photosynthesis,[17, 90, 91] while attention on hydrogen evolution has been favoured by the huge potential of hydrogen as a fuel.[92-95] Last, CO_2 reduction, which can be catalytically more challenging and usually less selective, has gained more attention recently, although still significantly less than that on proton reduction (note thermochemical CO_2 reduction was not included in this analysis).[96-98]

1.4. Current challenges

The analysis above on publication data provides some overview of the field of artificial photosynthesis to date, even if it is limited by the scope and the selection of suitable search words. Some results of the analysis are particularly striking, such as the rapid growth of interest in carbon nitride photocatalysts, and the continued dominance of publications on water splitting and proton reduction rather than carbon dioxide reduction, despite major new initiatives on the latter. In parallel, there is increasing focus on photoelectrodes rather than photocatalyst suspensions, despite some cost projections indicating photocatalyst architectures (either as suspensions or sheets) having the greatest potential to be cost competitive with photovoltaics (PV) plus electrolysis.[99] Publications on artificial photosynthesis address many aspects of photo(electro)chemical conversion of renewable energy into high-energy chemicals, but they all aim at developing better components and devices that can be used in commercially viable renewable energy conversion and storage schemes.

The commercial viability of photo(electro)chemical renewable energy conversion and their chemical products depends on its *cost competitiveness* relative to that of other energy sources and methods.[100, 101] For example, hydrogen is deemed the most competitive low-carbon fuel for industrial and heavy-duty long-range transportation applications, with a price estimated to drop by up to 50% in the next 10 years.[102, 103] However, most of the production of hydrogen currently relies on fossil fuels rather than on the electrochemical conversion of renewable sources, which is around 2-3 times more expensive.[53, 103, 104] In turn, the cost of photo(electro)chemical devices depends on multiple factors including the cost of the device manufacture, the cost of the components, their durability, and their *energy conversion efficiency*.[99, 105, 106] The energy conversion efficiency in the production of H_2 from water and solar energy is called *solar-to-hydrogen efficiency* (η_{STH}), and is calculated as the proportion between the useable chemical energy in the generated hydrogen gas and the total amount of energy in the incident light.[80, 107, 108]

The energy conversion efficiency has been identified as one of the main parameters limiting the cost of photo(electro)chemical devices for H_2 production with potential for improvement.[106, 109, 110] In the case of direct photoelectrochemical conversion for water splitting (including photoelectrodes and photocatalytic suspensions, as defined in Section 1.3.1), the η_{STH} necessary to produce H_2 at a competitive cost (~2 $/kg) has been estimated by the Department of Energy of the United States to be 10% and 25% for photocatalytic suspensions and photoelectrodes respectively.[106, 109, 110] In contrast, solar-to-hydrogen efficiencies of 1% have been achieved with photocatalytic suspensions, and up to 18% and 8% for multi-layered photoelectrodes based on III-V group metals and transition oxide metals respectively.[11, 22, 111, 112] On the other hand, the case of electrolysers coupled to photovoltaic devices or renewable energy sources has become especially attractive because, in the last 10 years, the cost of photovoltaic technology has dropped by 82%, its installed capacity has increased 14 times and the device efficiencies have approached the thermodynamic Shockley-Queisser limit (up to 47% in tandem

devices).[113-115] Among electrolyser technologies, alkaline and polymer exchange membrane (PEM) electrolysers are already commercial with energy conversion efficiencies between 50 and 80%. Nevertheless, improvements in their cost and lifetime by optimising the activity of their components are considered to be cornerstones in driving their competitiveness further.[113]

Rather than the conversion of radiative to electrical energy, the *conversion of electrical energy into chemical energy* is typically the main limitation in the efficiency and cost of photo(electro)chemical water splitting, which is likely to extend to other less mature photo(electro)chemical processes. The electrical-to-chemical energy conversion efficiency critically depends on (a) the efficiency of the ion and charge transport across the electrolyte and between the electrodes, dependent on the device architecture and the structure of the electrodes, and (b) on the efficiency of the chemical reaction at the electrode-electrolyte surface.[116-118] The latter, specially the O_2 evolution reaction, accounts for more than half of the extra cell voltage needed in PEM electrolysers to drive water splitting,[107, 119-121] the minimum voltage E_{H2} being related to η_{STH} as follows:

Equation 1.1 $$\eta_{STH} = \frac{j \cdot E_{H2} \cdot f}{I}$$

Where j is the current density, f is the faradaic efficiency (*i.e.*, the charge transfer efficiency of the electrochemical reaction, which is <1 in the presence of side reactions), I is the incident light power density, and $E_{H2}=1.23\ V$ is the theoretical thermodynamic potential to drive the reaction.[107, 119-121] The key reactions in the electro- and photo-chemical production of fuels and chemicals are *multi-redox reactions*, reactions involving more than one charge for each produced molecule. For instance, water splitting into H_2 and O_2, and the reduction of CO_2 into CO or formate, some of the most commonly investigated reactions as discussed above (Figure 1.9), involve four and two charges respectively.[1, 122-124] These reactions are enabled by high temperatures and pressures, and by *catalyst materials* that can accumulate charges and facilitate their interaction with the substrates without degrading.[125-127] In particular, state-of-the-art polymer exchange membrane electrolysers rely on platinum and iridium oxide as proton reduction and water oxidation catalysts respectively, while alkaline electrolysers are based on nickel.[105, 128-131] The performance of electrocatalyst materials is typically evaluated as a function of three parameters (Scheme 1.2):[75, 80, 132-135]

- *Current density per geometric area or mass of catalyst – j*: current measured between the cathode and the anode normalised by area or mass, and representing the reaction rate. The higher the current density, the larger the amount of charges exchanged per unit of time and, therefore, the fastest and more efficient the reaction (in agreement with Equation 1.1). When the active site is well defined and quantifiable, the reaction rate is also expressed as *turnover*

frequency (TOF), calculated as the amount of generated product or charge per unit of time and active site.

- *Potential – E*: redox potential that the catalyst requires to drive the reaction, measured with respect to a reference electrode. The cell potential E_{cell} is the potential difference between the electrodes where the reduction and oxidation half-reactions take place (*i.e.*, the cathode and the anode respectively). This parameter is related to the energy needed to drive the reaction at the catalyst, as the Gibbs free energy difference of the reaction ΔG equals nFE_{cell}, where n is the number of electrons involved and F is the Faraday constant. In inorganic electrocatalysts, the *onset potential* is considered instead. Alternatively, the *overpotential* η is also used, which is the difference between the redox potential E and the thermodynamic theoretical potential of the half-reaction (E_{H2}, in the case of H_2 production). The larger the overpotential, the lower the energy conversion efficiency.

- *Stability*: lifetime of the material, sometimes expressed as *turnover number* (*TON*), the total amount of product or charge per total amount of active sites involved.

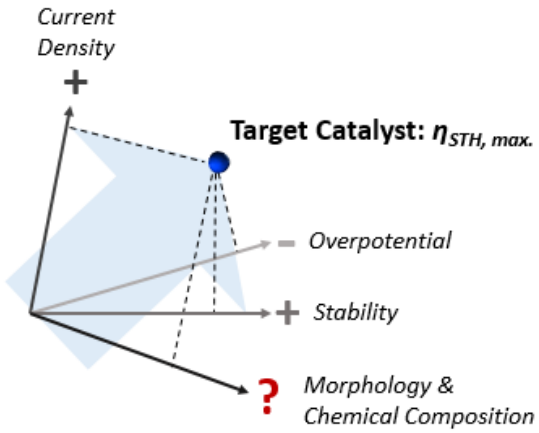

Scheme 1.2. Dependence of the energy conversion efficiency of a multi-redox catalyst on different performance parameters.

Given the scarcity and scalability issues of noble metals, and the low energy conversion efficiencies described above,[65, 66] research efforts to improve catalyst performance are currently heading in two main directions: (a) developing alternative earth-abundant catalysts with performances and stabilities as good as those of platinum and iridium oxides; (b) improving the utilisation of state-of-the-art catalysts like platinum, iridium oxide or nickel by increasing the activity per mass or atom.[136-138] To that end, it is necessary to understand how the photo- and electro-catalytic

performance of the catalysts (*i.e.*, *j*, *E* and *stability*) relates to their morphology and chemical composition at the atomic level, and, more specifically, to the nature of the catalyst surface, its electronic configuration and its bonding properties. This process depends on discerning the catalytic reaction step by step and all the atoms / species involved (*i.e.*, the reaction mechanism). Key questions include:

- **Question 1**: which atoms or parts of the catalysts (*i.e.*, the active sites) are involved in the catalytic reactions.
- **Question 2**: which intermediate species are formed from the active sites and in which order. In other words, how many reaction pathways can take place and how many steps they have.
- **Question 3**: how fast each reaction step is and which step limits the reaction rate (*i.e.*, rate-limiting step).

The mechanism of catalysts in artificial photosynthetic and photo(electro)chemical devices is usually not well understood, in particular because of the difficulty in characterising the reactive intermediates involved and the kinetics of the individual steps of the catalytic mechanism.[132, 133, 139-141] The multi-redox photocatalytic system in which charge accumulation steps have been most thoroughly studied to date is the oxygen evolution complex of photosystem II, where the sequential oxidative steps in the catalytic centre has received extensive attention.[5, 142-147] In either biological enzymes or inorganic and organic multi-redox catalysts, density functional theory (DFT) techniques and microkinetic models have been very useful to identify possible reaction mechanisms and intermediates compatible with experimental performances.[21, 148, 149] In parallel, several steady-state spectroscopies and microscopies have been used to identify catalyst states as a function of the applied electrochemical potential, particularly with the advent of techniques measuring under *operando / in situ* conditions (*i.e.*, working electrolyte-catalyst conditions) instead of vacuum.[150, 151] Furthermore, electrochemical studies on single atom catalyst and selected crystalline facets and microstructures have helped measuring the activity of individual atoms and surfaces.[152-158] Information on the reaction kinetics can be obtained from electrochemical methods, based on for example impedance or Tafel analyses.[75] The kinetics as a function of the catalysts species can mostly be investigated by combining time-resolved spectroscopy and electrochemical techniques. In the following subsections, key challenges in the elucidation of the reaction mechanisms of catalysts and, in particular, their kinetics, are identified based on the device type (Section 1.4.1), the catalyst material (Section 1.4.2) and the catalytic reaction (Section 1.4.3). In these subsections, the knowledge gaps and technical challenges are discussed.

1.4.1. Photo- *vs.* electro-catalysis – The problem of charge accumulation

Essential to high catalytic performances is the efficient transfer and accumulation of charges at the catalyst, forming multi-redox states. In electrochemical devices, the right electrochemical potential needs to be applied to the catalyst (*i.e.*, an *electrocatalyst*) through a suitable conductive substrate in order to form the catalytically necessary multi-redox states. In photochemical systems, the redox potential of the different components needs to be correctly aligned to favour charge transfer to the catalyst, unless the catalyst itself absorbs the light (*i.e.*, a *photocatalyst*). In photochemical reactions, in contrast to electrochemically driven reactions, accumulated charges can easily recombine with photo-generated charges of opposite sign in subsequent excitations. Therefore, recombination is a particular challenge in multi-redox photochemistry because the latter relies on the absorption of sufficient photons and the accumulation of enough charge equivalents to turn over the redox catalyst, as illustrated in the following Scheme:

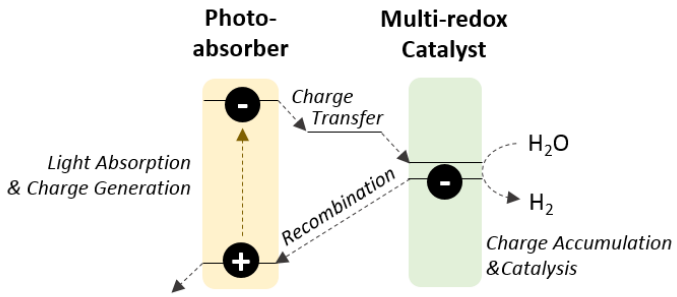

Scheme 1.3. Charge transfer and recombination pathways in multi-redox photochemical system for water reduction into hydrogen.

In natural photosynthesis, recombination is minimised by enabling fast charge transfer through an arrangement of adjacent redox co-factors with finely tuned redox potentials (*i.e.*, a *redox cascade*), resulting in an efficient separation of charges through space. Charge accumulation in photosynthetic microorganisms is facilitated by multi-redox sites such as the active sites of hydrogenase enzymes and the oxygen evolving complex of photosystem II, which are based on a few metal atoms and are protected by a protein scaffold. These active sites stabilise accumulated charges and catalyse the subsequent redox reactions.[6, 8] Alternatively, photocatalysts based on semiconductor metal oxides, which have been widely studied because of their robustness and material availability, facilitate charge accumulation through an in-built voltage difference at the surface (the *space charge layer*), but their energy conversion efficiency is limited by their bandgap and their capacity to absorb light in all the solar spectrum.[25, 112] Therefore, using natural photosynthesis as a blueprint,

in photochemical devices for solar energy conversion and storage, there is an interest in coupling the optimal light absorbing materials with the best multi-redox electrocatalysts. Placing them too closely is likely to cause too much recombination, while placing them too far apart is likely to slow down charge transfer and increase energy losses. In these systems, much progress has been made in understanding and optimising light absorption and charge separation,[159-163] but rather little is known about the catalytic mechanism and, in particular, the capacity of catalyst active sites to accumulate charge under different irradiation conditions.[11, 22, 24-26, 164]

There are few literature studies directly characterising the kinetics of photogenerated charge accumulation steps and individual catalyst intermediates in photochemical systems. Charge accumulation states for photocatalytic water oxidation or reduction (*i.e.*, the formation of multi-reduced or multi-oxidised catalyst species) have mostly been directly observed under constant irradiation or applied potential,[165-168] while the kinetics of different accumulation steps have been mainly resolved in donor-sensitiser-acceptor molecular compounds without catalytic activity.[9, 169-171] Therefore, charge accumulation to catalysts in light driven multi-component systems and the relationship of this charge accumulation with charge recombination losses, which can limit device efficiency, remain poorly described. Technically, the challenge in photochemical systems is to generate enough multi-redox species for their detection, compared to an easier detection of charge accumulation or multi-redox states under constant applied potential in electrochemical systems. A second challenge in both cases is to distinguish the several different reactions occurring in parallel and measure their individual kinetics.

1.4.2. Molecular *vs.* inorganic catalysts – Finding the sweet spot between activity and stability

Most catalysts used in artificial photosynthesis are based on transition metals with empty *d* orbitals (see Figure 1.8). This electronic configuration determines their electrophilicity and tendency to form relatively stable oxidisation states.[172-175] The reactivity of catalysts in photo(electro)chemical systems is activated generating multi-redox states either electrochemically or by photoexcitation, so that the resulting activated states can spontaneously react with the substrates with Gibbs free energies smaller than zero.[176, 177] These multi-redox states are most likely based on charges accumulated at the metal atoms. In multi-redox molecular catalysts based on organometallic complexes, the charges are known to localise primarily on the metal centres.[172-174] On the other hand, the electronic configuration of metal oxides has a more delocalised nature and, although catalysis has to take place at the interface of the material with the electrolyte, the role of the bulk atoms and the degree of activity of different surface atoms or facets is often unclear.[25, 178-180]

Different strategies exist to rationalise the relationship between catalytic activity and chemical composition, with the goal of understanding the difference between catalysts and designing better ones. The activity of electrocatalysts is usually compared based on the exponential dependence between the current density and the applied potential, described by the *Butler-Volmer equation* and represented as *Tafel plots*. In crystalline metal and semiconductor materials, this behaviour is typically assigned to the changing energy of free charges in the material, assuming a continuum distribution of states.[75, 181] However, non-crystalline disordered materials as water-oxidation hydrous iridium oxides and nickel iron hydroxides are likely to deviate from this picture. In such amorphous materials, the increasing current density with potential is more likely to be related to changes in the population of a discrete multi-redox active state instead, as has been shown for iron and nickel hydroxides.[182, 183] Following the *Sabatier principle* and the classic thermodynamic principles, the ideal catalyst should have low activation energy barriers and intermediates with the optimal energy, maximising the reaction rate and efficiency. Intermediates cannot be either too stable or too unstable and, therefore, the bond between the catalyst and the substrate at the surface cannot be either too strong or too weak. The relationship between the catalytic activity and the intermediate or bond formation energies has a triangular shape, the so-called *Volcano plots*.[21] This trend has been mostly investigated in metals and metal oxides. In these materials, the electronic configuration of inorganic catalysts can be modified to approach the top of the *Volcano* by introducing traces of other chemical elements (*doping*) or controlling the catalyst nanostructure. In contrast, molecular catalysts have a localised well-defined active sites that can be easily tuned by modifying the coordinated ligands.[184-187]

Broadly, more localised catalysts have been observed to have higher turnover frequencies at lower overpotentials, which reach values of $6\text{-}9\cdot10^3$ H_2/s in iron-iron hydrogenases, up to $4\cdot10^5$ and 10^4 H_2/s at η=1.2 V and $7.5\cdot10^4$ H_2/s at η=0.5V in iron, cobaltoxime and nickel DuBois molecular catalysts for H_2 production, while

larger Pt nanoparticles have TOFs of around 10^3 H_2/s at η=1.2 V.[21, 132, 188] In contrast, molecular catalysts and enzymes often have lifetimes of a few hours in the majority of cases, compared to the better robustness of noble metals and metal oxides. This also extends to disordered materials and oxidation reactions, with amorphous iridium oxides having larger current densities, lower onset potentials but worse stability than crystalline IrO_2.[189, 190] However, it is very possible that, in crystalline materials, the activity is underestimated by assuming that all surface atoms are active sites or by normalising the activity per unit of mass. Therefore, the challenge is to better characterise the chemical nature of multi-redox states of solid-state inorganic materials and quantify their respective catalytic activity.

1.4.3. Water splitting *vs.* carbon-bond formation – The challenge of catalysing more complex reactions

Beyond water splitting, reactions involving carbon bond formation or breakage such as CO_2 reduction into formate, methane or methanol tend to involve larger molecules, more steps and a larger amount of possible products.[124, 191, 192] As a consequence, catalysts have lower selectivities and higher overpotentials.[24, 124] Research to improve their selectivity have been focusing on breaking linear scaling relations, the linearly related binding adsorption of intermediates on one catalyst, which limits the catalyst choice and the control over the final product.[193, 194] In parallel, various approaches have been investigated to provide higher electrochemical potentials in photo(electro)chemical schemes: (a) choosing or designing materials with both the optimal bandgap and redox potentials; (b) photo-inducing single electron transfer to form reactive intermediates such as organic radicals; (c) multi-photon absorption; (d) photoionisation generating highly reductive solvated electrons.[191, 195-198] In all these cases, the challenge is to find alternative sustainable pathways to drive energy-demanding chemical reactions of interest in mild conditions.

1.5. Aims of this thesis

This thesis aims at contributing to a better understanding of structure-property relationships in catalyst materials. The catalysts investigated are multi-redox catalysts as the ones described in the previous Sections with a potential application in the conversion and storage of solar energy and renewable electricity. In particular, this thesis investigates catalysts for water splitting (water reduction in Chapters 3-4 and water oxidation in Chapters 5-6), for CO_2 reduction (Chapter 3) and for the generation of precursors for organic synthesis (Chapter 7). The studies herein focus on discerning the catalytic mechanism of these materials at the active sites and their reaction kinetics. The relationship between the mechanism and the catalytic activity per atom or intermediate species, which has been identified above as one of the challenges to understand and improve the performance of catalysts materials, is discussed accordingly. The light absorbance (A) in the ultraviolet-visible (UV-Vis) range, related to electronic transitions between orbitals involved in catalysis, is used to monitor the main active sites and multi-redox states. Steady-state spectroscopy measurements have been applied to identify different multi-redox species, and time-resolved measurements have served to directly measure under catalytic conditions the charge carrier dynamics and the reactivity and kinetics of intermediate states.

The kinetics of photo-induced charge accumulation is studied in multi-redox molecular catalysts immobilised at the surface of TiO_2, which works as a photoabsorber. Chapter 3 compares the formation kinetics of multi-redox states in two cobalt-based molecular catalysts: a cobalt diimine–dioxime catalyst for proton reduction and a cobalt bis(terpyridine) catalyst for CO_2 reduction, both containing phosphonate anchors for their immobilisation to the metal oxide surface. These studies are carried out in an aprotic solvent to prevent multi-redox states from reacting with water and to facilitate their detection. The efficiency of sequential charge transfers from TiO_2 to the catalyst is investigated as a function of the light intensity and the applied bias. To further analyse the impact on the reaction kinetics of the concentration of multi-redox species, Chapter 4 studies in aqueous solution two H_2-reduction molecular catalysts on TiO_2, including a diamine-dioxime catalyst and a cobaltoxime catalyst. The degree of charge accumulation and its reaction kinetics at the microsecond to second timescale are contrasted with the catalyst activity and the different possible DFT-calculated reaction pathways.

The reactivity of active sites in metal oxide catalysts is likely to be underestimated from current density measurements alone because of the presence of inactive bulk states and surface species to a larger extent than in molecular catalysts. To have a better insight into the activity per atom of water-oxidation electrocatalysts, amorphous iridium oxide (IrO_x) is investigated in Chapter 5 by combining electrochemical and spectroscopical techniques. Mathematical optimisation methods are applied to deconvolve the spectroelectrochemical signal (Chapter 5) and a molecular analogue is investigated (Chapter 6) to have a better understanding of the nature of individual multi-redox states in IrO_x catalysts. A unique perspective on the steady-state population and its intrinsic kinetics is provided by looking at the decay

of the characteristic optical signal after applying different electrochemical potentials. Finally, alternative photo(electro)chemical pathways based on multi-photon and anion excitation of an iridium molecular photocatalyst are investigated in Chapter 7.

1.6. References

1. N. S. Lewis and D. G. Nocera, *Proc. Natl. Acad. Sci. U. S. A.*, 2006, **103**, 15729-15735.
2. W. Song, Z. Chen, M. K. Brennaman, J. J. Concepcion, A. O. T. Patrocinio, N. Y. Murakami Iha and T. J. Meyer, *Pure Appl. Chem.*, 2011, **83**, 749-768.
3. M. Grätzel, *Nature*, 2001, **414**, 338-344.
4. S. Styring, *Faraday Discuss.*, 2012, **155**, 357-376.
5. J. Barber, *Chem. Soc. Rev.*, 2009, **38**, 185–196.
6. I. McConnell, G. Li and G. W. Brudvig, *Chem. Biol.*, 2010, **17**, 434-447.
7. D. Gust and T. A. Moore, *Science*, 1989, **244**, 35-41.
8. A. J. Cowan and J. R. Durrant, *Chem. Soc. Rev.*, 2013, **42**, 2281-2293.
9. L. Hammarström, *Acc. Chem. Res.*, 2015, **48**, 840-850.
10. A. Fukushima and K. Honda, *Nature*, 1972, **238**, 37-38.
11. J. W. Ager, M. R. Shaner, K. A. Walczak, I. D. Sharp and S. Ardo, *Energy Environ. Sci.*, 2015, **8**, 2811-2824.
12. S. Tembhurne, F. Nandjou and S. Haussener, *Nat. Energy*, 2019, **4**, 399-407.
13. O. Khaselev, A. Bansal and J. A. Turner *Int. J. Hydrog. Energy*, 2001, **26**, 127–132.
14. M. R. Wasielewski, *Acc. Chem. Res.*, 2009, **42**, 1911-1921.
15. Hirakawa and P. V. Kamat, *J. Am. Chem. Soc.*, 2005, **125**, 3928-3934.
16. Y. Tachibana, J. E. Moser, M. Grätzel and J. R. Durrant, *J. Phys. Chem.*, 1996, **100**, 20056-20062.
17. M. Suga, F. Akita, K. Hirata, G. Ueno, H. Murakami, Y. Nakajima, T. Shimizu, K. Yamashita, M. Yamamoto, H. Ago and J. R. Shen, *Nature*, 2015, **517**, 99-103.
18. M. H. Zewail, *J. Phys. Chem. A.*, 2000, **104**, 5660-5694.
19. A. J. Bard, F. R. F. Fan, D. T. Pierce, P. R. Unwin, D. O. Wipf and F. Zhou, *Science*, 1991, **254**, 68-74.
20. F. F. Abdi, T. J. Savenije, M. M. May, B. Dam and R. van de Krol, *J. Phys. Chem. Lett.*, 2013, **4**, 2752-2757.
21. Z. W. Seh, J. Kibsgaard, C. F. Dickens, I. Chorkendorff, J. K. Nørskov and T. F. Jaramillo, *Science*, 2017, **355**.
22. T. Hisatomi, J. Kubota and K. Domen, *Chem. Soc. Rev.*, 2014, **43**, 7520-7535.
23. I. Roger, M. A. Shipman and M. D. Symes, *Nat. Rev. Chem.*, 2017, **1**, 0003.
24. D. L. DuBois, *Inorg. Chem.*, 2014, **53**, 3935-3960.
25. K. Sivula and R. van de Krol, *Nat. Rev. Mater.*, 2016, **1**, 15010.
26. L. Steier and S. Holliday, *J. Mater. Chem. A*, 2018, **6**.
27. J. Goldemberg, T. B. Johansson, A. K. N. Reddy and R. H. Williams, *World Resources Institute*, 1987.
28. Climate Change 2014. Synthesis Report, *The Intergovernmental Panel on Climate Change*, 2015.
29. Horizon 2020 - Executive Summary of the Impact Assessment, *European Comission*, 2011.
30. Executive Summary. Quadrennial Technology Review. An Assessment of Energy Technologies and Research Opportunities, *U.S.A. D.O.E.*, 2015.
31. M. Grattieri, K. Beaver, E. M. Gaffney and S. D. Minteer, *Faraday Discuss.*, 2019, **215**, 15-25.
32. A. Stikane, E. T. Hwang, E. V. Ainsworth, S. E. H. Piper, K. Critchley, J. N. Butt, E. Reisner and L. J. C. Jeuken, *Faraday Discuss.*, 2019, **215**, 26-38.
33. D. Buesen, T. Hoefer, H. Zhang and N. Plumere, *Faraday Discuss.*, 2019, **215**, 39-53.
34. A. Vogel, M. Forster, L. Wilbraham, C. L. Smith, A. J. Cowan, M. A. Zwijnenburg, R. S. Sprick and A. I. Cooper, *Faraday Discuss.*, 2019, **215**, 84-97.
35. I. Heath-Apostolopoulos, L. Wilbraham and M. A. Zwijnenburg, *Faraday Discuss.*, 2019, **215**, 98-110.
36. Z. Kap and F. Karadas, *Faraday Discuss.*, 2019,**215**, 111-122.
37. A. P. Walsh, J. A. Laureanti, S. Katipamula, G. M. Chambers, N. Priyadarshani, S. Lense, J. T. Bays, J. C. Linehan and W. J. Shaw, *Faraday Discuss.*, 2019, **215**, 123-140.

38. W. Viertl, J. Pann, R. Pehn, H. Roithmeyer, M. Bendig, A. Rodriguez-Villalon, R. Bereiter, M. Heiderscheid, T. Muller, X. Zhao, T. S. Hofer, M. E. Thompson, S. Shi and P. Brueggeller, *Faraday Discuss.*, 2019, **215**, 141-161.
39. S. I. Shylin, M. V. Pavliuk, L. D'Amario, I. O. Fritsky and G. Berggren, *Faraday Discuss.*, 2019, **215**, 162-174.
40. A. Venugopal and W. A. Smith, *Faraday Discuss.*, 2019, **215**, 175-191.
41. M. Hojamberdiev, K. Kawashima, T. Hisatomi, M. Katayama, M. Hasegawa, K. Domen and K. Teshima, *Faraday Discuss.*, 2019, **215**, 227-241.
42. W. H. Huang and C. Y. Lin, *Faraday Discuss.*, 2019, **215**, 205-215.
43. A. R. Paris and A. B. Bocarsly, *Faraday Discuss.*, 2019, **215**, 192-204.
44. D. Tetzlaff, C. Simon, D. S. Achilleos, M. Smialkowski, K. Junge Puring, A. Bloesser, S. Piontek, H. Kasap, D. Siegmund, E. Reisner, R. Marschall and U. P. Apfel, *Faraday Discuss.*, 2019, **215**, 216-226.
45. J. Gao, D. Ren, X. Guo, S. M. Zakeeruddin and M. Grätzel, *Faraday Discuss.*, 2019, **215**, 282-296.
46. Y. H. Lai, K. C. Lin, C. Y. Yen and B. J. Jiang, *Faraday Discuss.*, 2019, **215**, 297-312.
47. A. Kudo, S. Yoshino, T. Tsuchiya, Y. Udagawa, Y. Takahashi, M. Yamaguchi, I. Ogasawara, H. Matsumoto and A. Iwase, *Faraday Discuss.*, 2019, **215**, 313-328.
48. E. Kalamaras, M. Belekoukia, J. Z. Y. Tan, J. Xuan, M. M. Maroto-Valer and J. M. Andresen, *Faraday Discuss.*, 2019, **215**, 329-344.
49. M. Schmalzbauer, I. Ghosh and B. Konig, *Faraday Discuss.*, 2019, **215**, 364-378.
50. Y.-H. Liu, M.-H. Vu, J. Lim, T.-O. Do and M. C. Hatzell, *Faraday Discuss.*, 2019, **215**, 379-392.
51. T. Bouwens, S. Mathew and J. N. H. Reek, *Faraday Discuss.*, 2019, **215**, 393-406.
52. S. Gavrielides, J. Z. Y. Tan, E. S. Fernandez and M. M. Maroto-Valer, *Faraday Discuss.*, 2019, **215**, 407-421.
53. http://energyatlas.iea.org, April 2019.
54. Key world energy statistics, *Intenational Energy Agency*, 2017.
55. J. D. Colgan and J. B. Stockbruegger, *The Oxford Handbook of Energy Politics*, 2018.
56. gapminder.org, April 2019.
57. R. Perez and M. Perez, *Newsletter of the International Energy Agency Solar Heating and Cooling*, 2015, **62**, 4-6.
58. Chemical Energy Storage, R. Schlögl, *De Gruyter*, 2013.
59. Net Zero Technical report, *Committee on Climate Change, UK*, 2019.
60. Erneuerbare Energien in Zahlen, *Bundesministerium für Wirtschaft und Energie, Germany*, 2017.
61. T. Napp, H. Hills, M. S. Soltani, J. Bosch and C. Mazur, *Grantham Institute*.
62. B. V. Mathiesen and H. Lund, *IET Renewable Power Generation*, 2009, **3**, 190.
63. T. Mays and D. Book, *H2FC Supergen Annual Conference*, 2019.
64. Engineering ToolBox, (2008). Fossil and Alternative Fuels - Energy Content. Available at: https://www.engineeringtoolbox.com/fossil-fuels-energy-content-d_1298.html, April 2010.
65. Study on the review of the list of Critical Raw Materials. Criticality Assessments, *European Comission*, 2017.
66. Study on the review of the list of Critical Raw Materials. Non-critical Raw Materials Factsheets, *European Comission*, 2017.
67. Energy Critical Elements: Securing Materials for Emerging Technologies, *American Physical Society and Materials Research Society*.
68. R. S. Sprick, B. Bonillo, R. Clowes, P. Guiglion, N. J. Brownbill, B. J. Slater, F. Blanc, M. A. Zwijnenburg, D. J. Adams and A. I. Cooper, *Angew. Chem. Int.*, 2016, **55**, 1792-1796.
69. T. E. Rosser, M. A. Gross, Y.-H. Lai and E. Reisner, *Chem. Sci.*, 2016, **7**, 4024-4035.
70. R. A. Marcus and N. Norman Sutin, *Biochim. Biophys. Acta*, 1985, **811**, 265-322.
71. G. McLendon, *Acc. Chem. Res.*, 1988, **21**, 160-167.
72. A. J. Bard, A. B. Bocarsly, F. R. F. Fan, E. G. Walton and M. S. Wrighton, *J. Am. Chem. Soc.*, 1980, **102**, 3671-3677.
73. H. Gerischer and W. Ekardt, *Appl. Phys. Lett.*, 1983, **43**, 393-395.
74. https://login.webofknowledge.com/, *Web of Science*, April 2019.

75. A. J. Bard and L. R. Faulkner, *John Wiley & Sons, Inc.*, 2001, 2nd edition.
76. https://solarfuelshub.org/.
77. https://www.solarfuelsnetwork.com/.
78. http://www.solarfuel.se/.
79. J. R. McKone, N. S. Lewis and H. B. Gray, *Chem. Mater.*, 2013, **26**, 407-414.
80. C. C. McCrory, S. Jung, I. M. Ferrer, S. M. Chatman, J. C. Peters and T. F. Jaramillo, *J. Am. Chem. Soc.*, 2015, **137**, 4347-4357.
81. M. G. Walter, E. L. Warren, J. R. McKone, S. W. Boettcher, Q. Mi, E. A. Santori and N. S. Lewis, *Chem. Rev.*, 2010, **110**, 6446–6473.
82. T. Inoue, A. Fujishima, S. Konishi and K. Honda, *Nature*, 1979, **277**, 637-638.
83. F. Studt, I. Sharafutdinov, F. Abild-Pedersen, C. F. Elkjaer, J. S. Hummelshoj, S. Dahl, I. Chorkendorff and J. K. Nørskov, *Nat. Chem.*, 2014, **6**, 320-324.
84. G. O. Larrazabal, A. J. Martin and J. Perez-Ramirez, *J. Phys. Chem. Lett.*, 2017, **8**, 3933-3944.
85. J. Yu, Y. Zhang and A. Kudo, *J. Solid State Chem.*, 2009, **182**, 223-228.
86. X. Chen, N. Li, Z. Kong, W.-J. Ong and X. Zhao, *Mater. Horiz.*, 2018, **5**, 9-27.
87. H. Wang, Y. Su, H. Zhao, H. Yu, S. Chen, Y. Zhang and X. Quan, *Environ. Sci. Technol.*, 2014, **48**, 11984-11990.
88. D. Bahnemann, *Solar Energy*, 2004, **77**, 445-459.
89. V. M. Daskalaki and D. I. Kondarides, *Catalysis Today*, 2009, **144**, 75-80.
90. I. D. Young, M. Ibrahim, R. Chatterjee, S. Gul, F. Fuller, S. Koroidov, A. S. Brewster, R. Tran, R. Alonso-Mori, T. Kroll, T. Michels-Clark, H. Laksmono, R. G. Sierra, C. A. Stan, R. Hussein, M. Zhang, L. Douthit, M. Kubin, C. de Lichtenberg, P. Long Vo, H. Nilsson, M. H. Cheah, D. Shevela, C. Saracini, M. A. Bean, I. Seuffert, D. Sokaras, T. C. Weng, E. Pastor, C. Weninger, T. Fransson, L. Lassalle, P. Brauer, P. Aller, P. T. Docker, B. Andi, A. M. Orville, J. M. Glownia, S. Nelson, M. Sikorski, D. Zhu, M. S. Hunter, T. J. Lane, A. Aquila, J. E. Koglin, J. Robinson, M. Liang, S. Boutet, A. Y. Lyubimov, M. Uervirojnangkoorn, N. W. Moriarty, D. Liebschner, P. V. Afonine, D. G. Waterman, G. Evans, P. Wernet, H. Dobbek, W. I. Weis, A. T. Brunger, P. H. Zwart, P. D. Adams, A. Zouni, J. Messinger, U. Bergmann, N. K. Sauter, J. Kern, V. K. Yachandra and J. Yano, *Nature*, 2016, **540**, 453-457.
91. L. Vogt, D. J. Vinyard, S. Khan and G. W. Brudvig, *Curr. Opin. Chem. Biol.*, 2015, **25**, 152-158.
92. Mission-oriented R&I policies: In-depth case studies, *European Comission,* 2018, DOI: 10.2777/516513.
93. R. M. Pratt, E. Wilcox Freeburg and F. Luzi, *U.S.A. D.O.E.*, 2017.
94. B. D. James, D. A. DeSantis and G. Saur, *U.S.A. D.O.E. Strategy Analysis*, 2016.
95. I. Staffell, P. Dodds, D. Scamman, A. Velazquez Abad, N. K. Ward, P. Agnolucci, L. Papageorgiou, N. Shah and P. Ekins, *H2FC Supergen*, 2017.
96. Y. Hori, H. Wakebe, T. Tsukamoto and O. Koga, *Electrochim. Acta*, 1994, **39**, 1833-1839.
97. C. D. Windle and R. N. Perutz, *Coord. Chem. Rev.*, 2012, **256**, 2562-2570.
98. W. Tu, Y. Zhou and Z. Zou, *Adv. Mater.*, 2014, **26**, 4607-4626.
99. B. D. James, G. N. Baum, J. Perez and K. N. Baum, *Directed Technologies, U.S.A. D.O.E.*, 2009.
100. K. Ardani, E. O'Shaughnessy, R. Fu, C. McClurg, J. Huneycutt and R. Margolis, *U.S.A. N.R.E.L.*, 2017, NREL/TP-7A40-67474.
101. D. Timmons, K. Elahee and M. Lin, *Sol. Energy*, 2020, **206**, 171-180.
102. Path to Hydrogen Competitiveness. A Cost Perspective, *Hydrogen Council*, 2020.
103. The Future of Hydrogen, *International Energy Agency*, 2019, https://www.iea.org/reports/the-future-of-hydrogen.
104. Key world energy statistics, *International Energy Agency*, 2017.
105. B. D. James and A. B. Spisak, *Strategic Analysis*, 2012.
106. B. A. Pinaud, J. D. Benck, L. C. Seitz, A. J. Forman, Z. Chen, T. G. Deutsch, B. D. James, K. N. Baum, G. N. Baum, S. Ardo, H. Wang, E. Millere and T. F. Jaramillo, *Energy Environ. Sci.*, 2013, **6**, 1983-2002.
107. Photoelectrochemical Hydrogen Production, R. van de Krol and M. Grätzel, *Springer, Electronic Materials: Science & Technology*, 2012.

108. Integrated Solar Fuel Generators, I. D. Sharp, *Royal Society of Chemistry, Energy & Environment Series*, 2019, DOI: 10.1039/9781788010313-fp001, pp. P001-P006.
109. L. C. Seitz, Z. Chen, A. J. Forman, B. A. Pinaud, J. D. Benck and T. F. Jaramillo, *ChemSusChem*, 2014, **7**, 1372-1385.
110. Multi-Year Research, Development, and Demonstration Plan. Planned program activities for 2011-2020, *U.S.A. D.O.E., Fuel Cell Technologies Office*, 2011, *https://www.energy.gov/eere/fuelcells/doe-technical-targets-hydrogen-production-photoelectrochemical-water-splitting*.
111. Q. Wang, T. Hisatomi, Q. Jia, H. Tokudome, M. Zhong, C. Wang, Z. Pan, T. Takata, M. Nakabayashi, N. Shibata, Y. Li, I. D. Sharp, A. Kudo, T. Yamada and K. Domen, *Nat. Mater.*, 2016, **15**, 611-615.
112. B. Moss, O. Babacan, A. Kafizas and A. Hankin, *Adv. Energy Mater.*, 2021, **11**, 2003286.
113. Green Hydrogen Cost Reduction: Scaling up Electrolysers to Meet the 1.5^{0}C Climate Goal, *International Renewable Energy Agency*, 2020.
114. Best Research-Cell Efficiency Chart, *U.S.A. N.R.E.L*, 2020, *https://www.nrel.gov/pv/cell-efficiency.html*.
115. B. Ehrler, E. Alarcón-Lladó, S. W. Tabernig, T. Veeken, E. C. Garnett and A. Polman, *ACS Energy Lett.*, 2020, **5**, 3029-3033.
116. M. Dumortier, S. Tembhurne and S. Haussener, *Energy Environ. Sci.*, 2015, **8**, 3614-3628.
117. S. Haussener, C. Xiang, J. M. Spurgeon, S. Ardo, N. S. Lewis and A. Z. Weber, *Energy Environ. Sci.*, 2012, **5**, 9922.
118. K. T. Fountaine, H. J. Lewerenz and H. A. Atwater, *Nat. Commun.*, 2016, **7**, 13706.
119. M. Bernt and H. A. Gasteiger, *J. Electrochem. Soc.*, 2016, **163**, F3179-F3189.
120. M. Bernt, A. Siebel and H. A. Gasteiger, *J. Electrochem. Soc.*, 2018, **165**, F305-F314.
121. C. Wei, R. R. Rao, J. Peng, B. Huang, I. E. L. Stephens, M. Risch, Z. J. Xu and Y. Shao-Horn, *Adv. Mater.*, 2019, **31**, e1806296.
122. T. J. Meyer, *Nat. Chem.*, 2011, **3**, 757-758.
123. E. E. Benson, C. P. Kubiak, A. J. Sathrum and J. M. Smieja, *Chem. Soc. Rev.*, 2009, **38**, 89-99.
124. C. Costentin, M. Robert and J. M. Savéant, *Chem. Soc. Rev.*, 2013, **42**, 2423-2436.
125. Z. Chen, T. F. Jaramillo, T. G. Deutsch, A. Kleiman-Shwarsctein, A. J. Forman, N. Gaillard, R. Garland, K. Takanabe, C. Heske, M. Sunkara, E. W. McFarland, K. Domen, E. L. Miller, J. A. Turner and H. N. Dinh, *J. Mater. Res.*, 2011, **25**, 3-16.
126. S. Wang, A. Lu and C. J. Zhong, *Nano Converg.*, 2021, **8**, 4.
127. M. Grätzel, *Philos. Trans. A Math. Phys. Eng. Sci.*, 2007, **365**, 993-1005.
128. M. Carmo, D. L. Fritz, J. Mergel and D. Stolten, *Int. J. Hydrog. Energy*, 2013, **38**, 4901-4934.
129. A. Marshall, B. Børresen, G. Hagen, M. Tsypkin and R. Tunold, *Energy*, 2007, **32**, 431-436.
130. P. Millet, R. Ngameni, S. A. Grigoriev and V. N. Fateev, *Int. J. Hydrog. Energy*, 2011, **36**, 4156-4163.
131. PEM Fuel Cell Electrocatalysts and Catalyst Layers Fundamentals and Applications, X.-Z. Yuan, H. Wang and J. Zhang, *Springer*, 2008.
132. V. Artero and J. M. Savéant, *Energy. Environ. Sci.*, 2014, **7**, 3808-3814.
133. C. Costentin and J.-M. Savéant, *ChemElectroChem*, 2014, **1**, 1226-1236.
134. M. Inaba, A. W. Jensen, G. W. Sievers, M. Escudero-Escribano, A. Zana and M. Arenz, *Energy Environ. Sci.*, 2018, **11**, 988-994.
135. C. M. Pedersen, M. Escudero-Escribano, A. Velázquez-Palenzuela, L. H. Christensen, I. Chorkendorff and I. E. L. Stephens, *Electrochim. Acta*, 2015, **179**, 647-657.
136. Technological Roadmap, *Sunergy*, 2020.
137. Basic Research Needs: Catalysis for Energy, *U.S.A. D.O.E.*, 2007.
138. Research needs towards sustainable production of fuels and chemicals, J. K. Nørskov, A. Latimer and C. F. Dickens, 2019.
139. S. Wang, A. Aster, M. Mirmohades, R. Lomoth and L. Hammarström, *Inorg. Chem.*, 2018, **57**, 768-776.
140. M. Mirmohades, S. Pullen, M. Stein, S. Maji, S. Ott, L. Hammarström and R. Lomoth, *J. Am. Chem. Soc.*, 2014, **136**, 17366-17369.
141. L. Duan, F. Bozoglian, S. Mandal, B. Stewart, T. Privalov, A. Llobet and L. Sun, *Nat. Chem.*, 2012, **4**, 418-423.

142. F. A. Armstrong, *Philos. Trans. R. Soc. Lond. B Biol. Sci.*, 2008, **363**, 1263-1270; discussion 1270.
143. F. A. Armstrong and J. Hirst, *Proc. Natl. Acad. Sci. U. S. A.*, 2011, **108**, 14049-14054.
144. N. Cox and J. Messinger, *Biochim. Biophys. Acta*, 2013, **1827**, 1020-1030.
145. M. Karge, K.-D. Irrgang and G. Renger, *Biochemistry*, 1997, **36**, 8904-8913.
146. G. Renger, *Photosynth. Res.*, 2007, **92**, 407-425.
147. G. Renger, *J. Photochem. Photobiol. B*, 2011, **104**, 35-43.
148. B. Hammer and J. K. Nørskov, *Adv. Catal.*, 2000, **45**.
149. B. A. Rohr, A. R. Singh, J. A. Gauthier, M. J. Statt and J. K. Nørskov, *Phys. Chem. Chem. Phys.*, 2020, **22**, 9040-9045.
150. V. M. V and G. Nageswaran, *Front. Chem.*, 2020, **8**, 23.
151. C. H. Chen, L. Jacobse, K. McKelvey, S. C. Lai, M. T. Koper and P. R. Unwin, *Anal Chem*, 2015, **87**, 5782-5789.
152. X.-F. Yang, A. Wang, B. Qiao, J. Li, J. Liu and T. Zhang, *Acc. Chem. Res.*, 2013, **46**, 1740–1748.
153. M. T. Koper, *Nanoscale*, 2011, **3**, 2054-2073.
154. J. Liu, *ACS Catal.*, 2016, **7**, 34-59.
155. R. R. Rao, M. J. Kolb, L. Giordano, A. F. Pedersen, Y. Katayama, J. Hwang, A. Mehta, H. You, J. R. Lunger, H. Zhou, N. B. Halck, T. Vegge, I. Chorkendorff, I. E. L. Stephens and Y. Shao-Horn, *Nat. Catal.*, 2020, **3**, 516-525.
156. R. R. Rao, M. J. Kolb, N. B. Halck, A. F. Pedersen, A. Mehta, H. You, K. A. Stoerzinger, Z. Feng, H. A. Hansen, H. Zhou, L. Giordano, J. Rossmeisl, T. Vegge, I. Chorkendorff, I. E. L. Stephens and Y. Shao-Horn, *Energy Environ. Sci.*, 2017, **10**, 2626-2637.
157. K. A. Stoerzinger, O. Diaz-Morales, M. Kolb, R. R. Rao, R. Frydendal, L. Qiao, X. R. Wang, N. B. Halck, J. Rossmeisl, H. A. Hansen, T. Vegge, I. E. L. Stephens, M. T. M. Koper and Y. Shao-Horn, *ACS Energy Lett.*, 2017, **2**, 876-881.
158. K. A. Stoerzinger, L. Qiao, M. D. Biegalski and Y. Shao-Horn, *J. Phys. Chem. Lett.*, 2014, **5**, 1636-1641.
159. Best Research-Cell Efficiency Chart, NREL, *https://www.nrel.gov/pv/cell-efficiency.html*, June 2019.
160. S. Gunes, H. Neugebauer and N. S. Sariciftci, *Chem. Rev.*, 2007, **107**, 1324-1338.
161. P. V. Kamat, *J. Phys. Chem. C*, 2008, **112**, 18737-18753.
162. A. Hagfeldt, G. Boschloo, L. Sun, L. Kloo and H. Pettersson, *Chem. Rev.*, 2010, **110**, 6595-6663.
163. M. A. Green, A. Ho-Baillie and H. J. Snaith, *Nat. Photonics*, 2014, **8**, 506-514.
164. M. D. Symes, Y. Surendranath, D. A. Lutterman and D. G. Nocera, *J. Am. Chem. Soc.*, 2011, **133**, 5174-5177.
165. H. Y. Chen and S. Ardo, *Nat. Chem.*, 2018, **10**, 17-23.
166. S. Ardo, D. Achey, A. J. Morris, M. Abrahamsson and G. J. Meyer, *J. Am. Chem. Soc.*, 2011, **133**, 16572-16580.
167. V. Saavedra Becerril, E. Sundin and M. Abrahamsson, *J. Phys. Chem. C*, 2018, **122**, 25822-25828.
168. W. Song, A. Ito, R. A. Binstead, K. Hanson, H. Luo, M. K. Brennaman, J. J. Concepcion and T. J. Meyer, *J. Am. Chem. Soc.*, 2013, **135**, 11587-11594.
169. S. Karlsson, J. Boixel, Y. Pellegrin, E. Blart, H.-C. Becker, F. Odobel and L. Hammarström, *J. Am. Chem. Soc.*, 2010, **132**, 17977–17979.
170. K. J. Elliott, A. Harriman, L. Le Pleux, Y. Pellegrin, E. Blart, C. R. Mayer and F. Odobel, *Phys. Chem. Chem. Phys.*, 2009, **11**, 8767-8773.
171. M. P. O'Neil, M. P. Niemczyk, W. A. Svec, D. Gosztola, G. L. Gaines III and M. R. Wasielewski, *Science*, 1992, **257**, 63-65.
172. Photochemistry and Photophysics of Coordination Compounds I, V. Balzani, S. Campagna, A. Barbieri, F. Barigelletti, E. C.-C. Cheng, L. Flamigni, T. Gunnlaugsson, R. A. Kirgan, D. Kumaresan, J. P. Leonard, C. B. Nolan, D. P. Rillema, C. Sabatini, R. H. Schmehl, K. Shankar, F. Stomeo, B. P. Sullivan, S. Vaidya, B. Ventura, J. A. G. Williams and V. W.-W. Yam, *Springer, Topics in Current Chemistry*, 2007.

173. Photochemistry and Photophysics of Coordination Compounds II, V. Balzani, S. Campagna, A. de Meijere, K. N. Houk, H. Kessler, J.-M. Lehn, S. V. Ley, S. L. Schreiber, J. Thiem, B. M. Trost, F. Vögtle and H. Yamamoto, *Springer, Topics in Current Chemistry*, 2007.
174. Photochemistry and photophysics: concepts, research, applications, V. Balzani, P. Ceroni and A. Juris, *Wiley-VCH*, 2014.
175. Inorganic Chemistry, M. Weller, T. Overton, J. Rourke and F. A. Armstrong, *Oxford University Press*, 2014, 6th edition.
176. Energy Resources Through Photochemistry and Catalysis, M. Grätzel, *Academic Press Inc.*, 1983.
177. J. M. Savéant, *Chem. Rev.*, 2008, **108**, 2348-2378.
178. J. Rossmeisl, Z. W. Qu, H. Zhu, G. J. Kroes and J. K. Nørskov, *J. Electroanal. Chem.*, 2007, **607**, 83-89.
179. K. T. Butler, J. M. Frost, J. M. Skelton, K. L. Svane and A. Walsh, *Chem. Soc. Rev.*, 2016, **45**, 6138-6146.
180. D. W. Davies, C. N. Savory, J. M. Frost, D. O. Scanlon, B. J. Morgan and A. Walsh, *J. Phys. Chem. Lett.*, 2020, **11**, 438-444.
181. Scanning Electrochemical Microscopy, A. J. Bard and M. V. Mirkin, *CRC Press, Taylor & Francis group*, 2012, 2nd edition.
182. C. A. Mesa, L. Francàs, K. R. Yang, P. Garrido-Barros, E. Pastor, Y. Ma, A. Kafizas, T. E. Rosser, M. T. Mayer, E. Reisner, M. Grätzel, V. S. Batista and J. R. Durrant, *Nat. Chem.*, 2020, **12**, 82-89.
183. L. Francàs, S. Corby, S. Selim, D. Lee, C. A. Mesa, R. Godin, E. Pastor, I. E. L. Stephens, K. S. Choi and J. R. Durrant, *Nat. Commun.*, 2019, **10**, 5208.
184. N. Weder, B. Probst, L. Sévery, R. J. Fernández-Terán, J. Beckord, O. Blacque, S. D. Tilley, P. Hamm, J. Osterwalder and R. Alberto, *Catal. Sci. Technol.*, 2020, **10**, 2549-2560.
185. J. J. Leung, J. Warnan, D. H. Nam, J. Z. Zhang, J. Willkomm and E. Reisner, *Chem. Sci.*, 2017, **8**, 5172-5180.
186. J. S. Lee, D. I. Won, W. J. Jung, H. J. Son, C. Pac and S. O. Kang, *Angew. Chem. Int.*, 2017, **56**, 976-980.
187. B. Zhang and L. Sun, *Chem. Soc. Rev.*, 2019, **48**, 2216-2264.
188. M. Frey, *ChemBioChem*, 2002, **3**, 153-160.
189. S. Geiger, O. Kasian, M. Ledendecker, E. Pizzutilo, A. M. Mingers, W. T. Fu, O. Diaz-Morales, Z. Li, T. Oellers, L. Fruchter, A. Ludwig, K. J. J. Mayrhofer, M. T. M. Koper and S. Cherevko, *Nat. Catal.*, 2018, **1**, 508-515.
190. S. Cherevko, S. Geiger, O. Kasian, A. Mingers and K. J. J. Mayrhofer, *J. of Electroanal. Chem.*, 2016, **774**, 102-110.
191. N. A. Romero and D. A. Nicewicz, *Chem. Rev.*, 2016, **116**, 10075-10166.
192. T. Uekert, M. F. Kuehnel, D. W. Wakerley and E. Reisner, *Energy Environ. Sci.*, 2018, **11**, 2853-2857.
193. M. B. Ross, P. De Luna, Y. Li, C.-T. Dinh, D. Kim, P. Yang and E. H. Sargent, *Nat. Catal.*, 2019, **2**, 648-658.
194. A. K. Buckley, M. Lee, T. Cheng, R. V. Kazantsev, D. M. Larson, W. A. Goddard III, F. D. Toste and F. M. Toma, *J. Am. Chem. Soc.*, 2019, **141**, 7355-7364.
195. T. P. Yoon, *Acc. Chem. Res.*, 2016, **49**, 2307-2315.
196. D. M. Arias-Rotondo and J. K. McCusker, *Chem. Soc. Rev.*, 2016, **45**, 5803-5820.
197. M. H. Shaw, J. Twilton and D. W. MacMillan, *J. Org. Chem.*, 2016, **81**, 6898-6926.
198. K. L. Skubi, T. R. Blum and T. P. Yoon, *Chem. Rev.*, 2016, **116**, 10035-10074.
199. *patents.google.com*, April 2019.
200. *crunchbase.com*, April 2019.
201. *http://mjl.clarivate.com/scope/scope_scie/*, April 2019.
202. *https://images.webofknowledge.com /images/help/WOS/hp_subject_category_terms_tasca.html*, April 2019.

1.7. Annex

1.7.1. Data on the different technologies

To assess the commercial maturity of artificial photosynthesis, it has been compared to similar technologies, including batteries, photovoltaics, fuel cells and electrolysers (Section 1.3, Figure 1.4). Three different parameters have been considered in this comparison: the number of patents,[199] the number of companies,[200] and the number of publications based on these technologies.[74] The terms used in the database search are the following:

a) ***Batteries****: "Battery" or "Batteries"*

b) ***Photovoltaics****: "Photovoltaic" or "Photovoltaics" or "Solar cell" or "Solar cells"*

c) ***Fuel Cells****: "Fuel cells" or "Fuel cell"*

d) ***Electrolysers****: "Electrolyzer" or "Electrolyzers" or "Electrolyser" or "Electrolysers"*

e) ***Photosynthesis****: "Artificial Photosynthesis" or "Solar fuels" or "Solar fuel" for the number of patents and companies; terms defined in section 1.3.2. to determine the number of publications.*

The number of patents is obtained from the addition of results associated to each one of the terms defined above. The number of companies has been taken from the search that yielded the maximum amount of results. The number of publications is described in the next section 1.7.2.

1.7.2. Search in the Web of Knowledge

The number of publications over time related to different topics were extracted from the database *Web of Science*,[74] including the classification of publications according to research area and geography (Section 1.3, Figures 1.5-6).[201, 202] The groups of keywords used in the different searches are the following:

a) **Artificial Photosynthesis**: TS=("solar fuel*") OR TS=("artificial photosynthesis") OR TS=("photo* reduction") OR TS=("photo* oxidation") OR TS=("electrochemical photolysis") OR TS=(photo* AND "water splitting") OR TS=(photo* AND "water-splitting") OR TS=(photo* AND "CO2 reduction") OR TS=(photo* AND "carbon dioxide reduction") OR TS=(photo* AND "water oxidation") OR TS=(photo* AND "oxygen evolution") OR TS=(photo* AND "oxygen production") OR TS=(photo* AND "O2 evolution") OR TS=(photo* AND "O2 production") OR TS=(photo* AND "water reduction") OR TS=(photo* AND "proton reduction") OR TS=(photo* AND "hydrogen evolution") OR TS=(photo* AND "H2 evolution") OR TS=(photo* AND "hydrogen production") OR TS=(photo* AND "H2 production") OR TS=(electrochemical AND "water splitting") OR TS=(electrochemical AND "water-splitting") OR TS=(electrochemical AND "CO2 reduction") OR TS=(electrochemical AND "carbon dioxide reduction") OR TS=(electrochemical AND "water oxidation") OR TS=(electrochemical AND "oxygen evolution") OR TS=(electrochemical AND "oxygen production") OR TS=(electrochemical AND "O2 evolution") OR TS=(electrochemical AND "O2 production") OR TS=(electrochemical AND "water reduction") OR TS=(electrochemical AND "proton reduction") OR TS=(electrochemical AND "hydrogen evolution") OR TS=(electrochemical AND "H2 evolution") OR TS=(electrochemical AND "hydrogen production") OR TS=(electrochemical AND "H2 production")

b) **Molecular Catalysts** (search within *a*): TS=("molecular catalyst*") OR TS=("organometallic complex*") OR TS=("organometallic molecule*")

c) **Platinum Group Metals** (search within *a*): TS=(PGM) OR TS=("Platinum Group Metal*") OR TS=(Platinum) OR TS=(Pt) OR TS=(Ruthenium) OR TS=(Ru) OR TS=(Iridium) OR TS=(Ir) OR TS=(Rhodium) OR TS=(Rh) OR TS=(Palladium) OR TS=(Pd) OR TS=(Osmium) OR TS=(Os) OR TS=("IrO2") OR TS=("RuO2")

d) **Metal Oxides** (search within *a*, excluding *c* and *h*): TS=("metal oxide*") OR TS=("oxide*") OR TS=("inorganic semiconductor*")

e) **Enzymes** (search within *a*): TS=(enzyme*) OR TS=(protein*)

f) **Carbon Nitrides** (search within *a*): TS=("carbon nitride*")

g) **Polymers** (search within *a*, excluding *f*): TS=(polymer*)

h) **Perovskites** (search within *a*, excluding *c* and *d*): TS=("perovskite*) OR TS=("PVK")

i) **Gallium Nitrides** (search within *a*): TS=("gallium nitride*) OR TS="(GaN")

j) **Dichalcogenide** (search within *a*): TS=("dichalcogenide*")

k) **Polyoxometalates** (search within *a*): TS=("polyoxometalate*") OR TS=("POM")

l) **Metal and Covalent Organic Frameworks** (search within *a*): TS=(*organic framework*) OR TS=("MOF") OR TS=("COF")

m) **Photocatalytic Suspension** (search within *a*): TS=(homogeneous OR suspension*)

n) **Photoelectrodes** (search within *a*): TS=(photoelectrode*) OR TS=(photoanode*) OR TS=(photocathode*)

o) **Catalyst** (search within *a*): TS=(*catalyst*)

p) **CO_2 Reduction** (search within *a*): TS=("CO2 reduction") OR TS=("carbon dioxide reduction")

q) **Water Oxidation** (search within *a*): TS=("water oxidation") OR TS=("oxygen evolution") OR TS=("oxygen production") OR TS=("O2 evolution") OR TS=("O2 production")

r) **Water Reduction** (search within *a*): TS=("water reduction") OR TS=("proton reduction") OR TS=("hydrogen evolution") OR TS=("H2 evolution") OR TS=("hydrogen production") OR TS=("H2 production")

Where *TS* limits the search to the title, abstract and keywords of publications; *" "* searches for the exact expression inside the quotation marks; * searches for any possible prefix or suffix; *OR* searches papers containing either of the search terms; *NOT* searches for papers that do not contain the search terms that follow; *AND* searches only for papers containing all the search terms. All searches have been done within the publications in Artificial Photosynthesis (search *a* above). The abbreviation "Ir" for the iridium atom has been omitted from the search on platinum group metals to avoid filtering papers involving infrared light (commonly abbreviated as "IR").

Chapter 2

Methods

Different steady-state and time-resolved spectroscopic and electrochemistry techniques have been used to identify catalyst intermediate states and to investigate their reactivity. These studies have been mostly carried out in the microsecond to second timescale, but also in the femtosecond to nanosecond timescale. This Chapter starts by describing the general procedures followed to prepare the different samples (Section 2.1) and by establishing the basis of steady-state techniques, including electrochemistry (Section 2.2) and spectroelectrochemistry (Section 2.3). It then moves on to explain the various time-resolved techniques which have been used here (Sections 2.4-6). Finally, the different approaches to treat the data are introduced (Section 2.7).

2.0. Contents

2.1. Samples and Preparation

Five multi-redox electrocatalysts and one photocatalyst were investigated in this work. Their structures are shown in Figure 2.1. Five catalysts are organometallic complexes, also called molecular catalysts (Figure 2.1A-E). Among the molecular catalysts, three are mono-metallic electrocatalysts based on a cobalt atom: the CO_2-reduction catalyst **CotpyP**, and the proton-reduction catalysts **CoP^1** and **CoP^2**.[1-7] The two other molecular catalysts studied are based on iridium: the reductive photocatalyst **IrPS** and the water-oxidation electrocatalyst **Ir$_{molecular}$**[8, 9]. Finally, the water-oxidation electrocatalyst **IrO$_x$**,[10] which is a mesoporous hydrous oxide, was investigated and compared with its iridium-based molecular analogue.

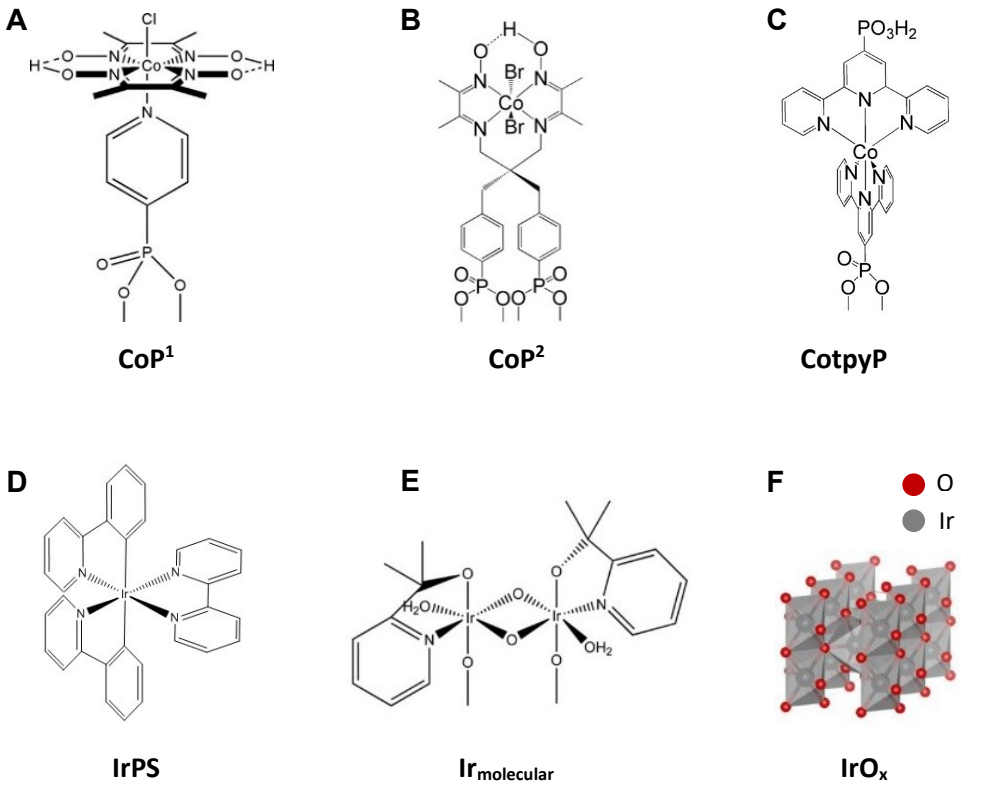

Figure 2.1. Structure of all the molecules and the inorganic compound studied herein. **(A)** H_2-production catalyst CoP^1 (*[Co^{III}Cl(dimethylglyoximato)$_2$(pyridyl-4-hydrophosphonate)]*).[1, 2] **(B)** H_2-production catalyst CoP^2 (*[$Co^{III}Br_2$(N^2,$N^{2'}$-2,2-(CH_2(C_6H_4)PO_3H)propanediyl-bis(2,3-butanedione-2-imine-3-oxime))]*).[3-5] **(C)** CO_2-reduction electrocatalyst CoterpyP (*[Co^{II}-bis(2,2':6',2''-terpyridine-4'-phosphonate)]*).[6, 7] **(D)** Iridium photosensitizer IrPS (*[Ir^{III}(phenylpyridine)$_2$bipyridine]$^+$*).[11] **(E)** O_2-evolution electrocatalyst $Ir_{molecular}$ (*[Ir^{IV}(2-(2'-pyridyl)-2-propanolate)(H_2O)$_2$(μ-O)]$_2^{2+}$*).[8] **(F)** Hydrous oxide films electrodeposited from organometallic complexes (*IrO_x*).[10]

The H_2-reduction molecular catalysts **CoP^1** and **CoP^2** were prepared by Dr. Daniel Antón-García (Prof. Erwin Reisner's Group, University of Cambridge), and are investigated in Chapters 3 and 4 in acetronitrile and acetronitrile:water respectively. The CO_2-reduction molecular catalyst **CotpyP** was synthesised by Dr. Julien Warnan (Prof. Erwin Reisner's Group, University of Cambridge), and its charge accumulation properties are compared in Chapter 3 to those of **CoP^2**. The **IrO_x** water oxidation electrocatalyst is analysed in Chapter 5 and it was prepared with the help of Dr. Reshma R. Rao (Prof. James R. Durrant's Group, Imperial College London). In Chapter 6, the water oxidation electrocatalysts **$Ir_{Molecular}$** on mesoporous indium tin oxide (ITO) and some of the **IrO_x** samples are compared. The catalyst samples were prepared by Dr. Yuanxing Wang, Dr. Yanyan Zhao and Dr. Gongfang Hu (Prof. Dunwei Wang's group at the Boston College, and Prof. Gary Brudvig's group at Yale University), while the mesoporpous ITO substrates were made by Dr. Daniel Antón-García. Finally, the photocatalysts **IrPS** was synthesised by Dr. Noufal Kandoth (Prof. Julio Lloret-Fillol's group, Institute of Chemical Research of Catalonia *ICIQ*) and its excited state dynamics are studied in Chapter 7.

All the molecular catalysts except for **IrPS** (Figure 2.1A-C and E) were immobilised onto electrode substrates in order to enhance electron transfer from the electrode to the catalyst and to facilitate the study of the catalyst electrocatalytic properties, as detailed in the following Chapters. These molecular catalysts were immobilised on conductor or semiconductor metal oxide films, which were mesoporous to maximize the amount of catalyst loaded per unit area. Regarding the attachment point, the molecular catalysts were covalently anchored through phosphate or oxygen groups to the metal oxide films, as illustrated in Figure 2.1.[12-15] In the case of the CO_2- and proton-reduction catalysts **CotpyP**, **CoP^1** and **CoP^2**, the electrode substrate was mesoporous TiO_2 on fluorine doped tin oxide (FTO) working as photoabsorber and, in the case of **$Ir_{Molecular}$**, the substrate was mesoporous ITO on FTO, which served as high-surface area conductive contact. The loading of the molecular catalysts to the films was enabled by soaking the films in a solution of dissolved catalyst. Prior to the catalyst loading, the films were prepared by doctor-blading a suspension of nanoparticles on an FTO-glass substrate and the resulting films had a thickness of around 4 μm in all the cases. In parallel, the **IrO_x** was prepared on FTO by electrodeposition of an iridium salt aqueous solution. Finally, **IrPS** was investigated dissolved in acetonitrile solution. All the samples were studied in liquid electrolyte that was freshly prepared before each experiment. Further details are provided in the following Chapters.

2.2. Electrochemistry

Electrochemical techniques were key to characterise the oxidation states of the different materials and compounds.[16, 17] With these techniques, it is possible to detect **electrochemical or redox reactions**, where one or more charges are exchanged during the chemical process and an electrical current is generated. All the measurements were done in an electrochemical cell schematically illustrated in Scheme 2.1A, where the electrical current is transported as ions through an ionic conductor (*i.e.*, the electrolyte), and as free electrons between two electrodes soaked in the electrolyte and connected by an external conductor (*i.e.*, the working and the counter electrodes, WE and CE). Equation 2.1 represents a **redox reaction** taking place at the working and counter electrodes, where ν is the stoichiometric coefficient of a species in the redox reaction, x is the amount of transferred electrons e^-, and R and O are the reduced and oxidised species respectively:

Equation 2.1 $\upsilon_R R \rightleftharpoons xe^- + \upsilon_O O$

The processes occurring at the electrodes of an electrochemical cell (Scheme 2.1B) are influenced by multiple factors including the nature of the electrodes and species in the electrolyte, and their surface area or concentration. The intrinsic electrochemical properties of a material or compound are represented by the **electrochemical potential** $\bar{\mu}$ (also called **Fermi level** when referring to the electrochemical potential of electrons**)**, shown in Equation 2.2. The electrochemical potential represents the energy cost associated with moving or generating a charged species i at a specific location under constant pressure and temperature. Under equilibrium or open-circuit conditions, when no current flows, the electrochemical potential is related to the experimentally available **redox potential** E through the Nernst equation, which is calculated for the working electrode relative to the reference electrode in Equation 2.3:

Equation 2.2 $\bar{\mu}_i = \left(\frac{\delta G}{\delta n_i}\right)_{T,P,n(j\neq i)} + z_i F\phi = \mu_i^0 + RTln(a_i) + z_i F\phi$

Equation 2.3 $E_{WE} = E_{cell} - E_{RE} = \frac{-\Delta G}{xF} - E_{RE} = E^0 + \frac{RT}{xF}\ln\left(\frac{a_R^{\nu_R}}{a_O^{\nu_O}}\right) - E_{RE}$

Where G is the Gibbs free, n_i is the number of moles of i, μ_i is the chemical potential of the species i, z_i is the charge of species i, F is the Faraday constant, Φ is the electrostatic potential, the subscript ^{0} denotes standard conditions, R is the ideal gas constant, T is the temperature, P is the pressure, and a is the activity.

The redox potential is an indicator of the tendency of the solution and the electrode to exchange electrons and it depends on the activity and concentration of the redox species present, following Equation 2.3. Herein, the catalyst samples were investigated as working electrodes. To measure the redox potential on the working electrode (E_{WE}) during an electrochemical reaction, a third non-polarizable electrode was added to the electrochemical cell and connected to the working electrode *via* a voltammeter containing a virtually infinite resistor. The potential of the reference electrode remains constant throughout the experiment and allows the measurement of E_{WE} *versus* E_{RE} under equilibrium conditions, independently of the counter electrode. In all the experiments presented here, a platinum mesh was used as counter electrode and a Ag/AgCl electrode saturated with KCl was the reference electrode. The counter and reference electrodes can potentially contaminate the electrolyte and eventually the working electrode (e.g. platinum at the counter electrode can be oxidized, dissolved and electrodeposited on the working electrode),[18,19,20] but its effect is expected to be minimal in the time-frame of the experiments herein.

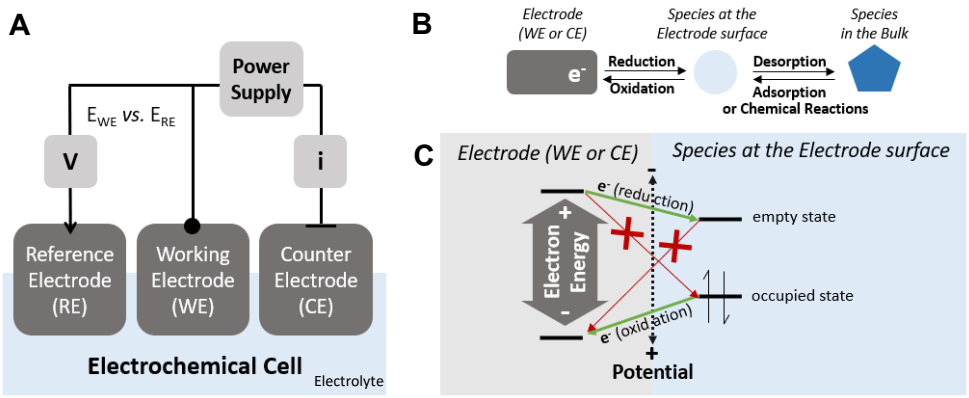

Scheme 2.1. **(A)** Three-electrode electrochemical cell, where *V* is a voltmeter measuring the electric potential difference between the reference and working electrodes, and *i* is an ammeter measuring the current between the working and the counter electrodes. **(B)** The different processes occurring at the electrode/electrolyte interface between the electrode and electroactive species in solution. **(C)** Representation of the electronic configuration required for species to undergo reduction and oxidative reactions.

In this work, most of the measurements were done in a **three-electrode spectroelectrochemical cell** similar to the one illustrated in Scheme 2.1A. Compared to a typical electrochemical cell, this spectroelectrochemical cell had a quartz window so that the absorbance changes (ΔA) of the samples could be measured in parallel to the redox potential and electric currents. Cyclic voltammetries (*i.e.*, applied potential scans) were done to identify the redox potentials of different redox states of the catalysts. As shown in Scheme 2.1B,

positive currents were an indication of oxidative processes and were expected to happen at more positive relative potentials, while negative currents were the result of reductive reactions and occurred at more negative relative potentials.

In Chapters 3 and 4, all the redox potentials are expressed *versus* the Normal Hydrogen Electrode (NHE). To convert the redox potentials from Ag/AgCl saturated with KCl to NHE, the potential of ferrocene (Fc) was first measured *versus* the Ag/AgCl sat. KCl electrode. The redox potential $E_{1/2}(Fc^{+}/Fc)$ was 0.55 V in acetonitrile (ACN) 0.1 M $TBAPF_6$ (TBA=tetrabutylammonium), where the half-wave potential was calculated as the average between the potentials of the oxidative and the reductive peaks.[21, 22] Taking into account a difference of +0.63 V between Fc and NHE,[23] potentials *versus* NHE were calculated from the potentials *versus* Ag/AgCl sat. KCl by subtracting −0.08 V ($E_{NHE} = E_{Ag/AgCl(sat.KCl)} - 0.08$ V). In Chapters 5 and 6, all the potentials are reported *versus* the Reference Hydrogen Electrode (RHE) and are iR_u corrected. Using the Nernst equation (Equation 2.3), the potentials *versus* Ag/AgCl saturated with KCl ($E_{Ag/AgCl(sat.KCl)}$) were converted into potentials *versus* RHE (E_{RHE}) as follows:

Equation 2.4

$$\begin{aligned} E_{RHE} &= E_{Ag/AgCl(sat.KCl)} + E^{0}_{Ag/AgCl(sat.KCl)} + \frac{2.30RT}{xF}pH \\ &= E_{Ag/AgCl(sat.KCl)} + 0.197 + 0.059pH \\ &= E_{Ag/AgCl(sat.KCl)} + 0.2678 \end{aligned}$$

Where R is the ideal gas constant (8.314 $J \cdot mol^{-1} \cdot K^{-1}$), T is the temperature (298K), F is the Faraday constant (96485 C/mol electrons), x is the number of electrons transferred (1 mol of electrons), and $E_{Ag/AgCl(sat.KCl)}{}^{0}$ is the standard potential of the Ag/AgCl reference electrode saturated with KCl. The pH used was 1.2.

2.3. Spectroelectrochemistry – SEC

Spectroelectrochemistry enabled the optical characterisation of key catalytic intermediates. This technique consists in probing the absorbance (A) of a sample under constant applied potential (Scheme 2.2). Using the spectroelectrochemical cell described in Section 2.2, the potential was controlled by a potentiostat and applied between a platinum mesh counter electrode (CE) and the sample, which was the working electrode (WE). The potential at the working electrode was measured with respect to an Ag/AgCl reference electrode (RE) saturated with KCl. The absorbance was recorded after applying the corresponding potential for 5 minutes, when the current was stable (Scheme 2.2B-C). Every spectrum was measured at least three times to check its reproducibility. The instruments that were used in all spectroelectrochemistry measurements were a *Metrohm Autolab PGSTAT101* potentiostat and an *Agilent Technologies Cary 60* UV-Vis spectrometer. The same results were also obtained using an alternative home-built setup integrated by an *OceanOptics HL-2000-FHSA* halogen light source and an *OceanOptics Maya2000 Pro* spectrometer.

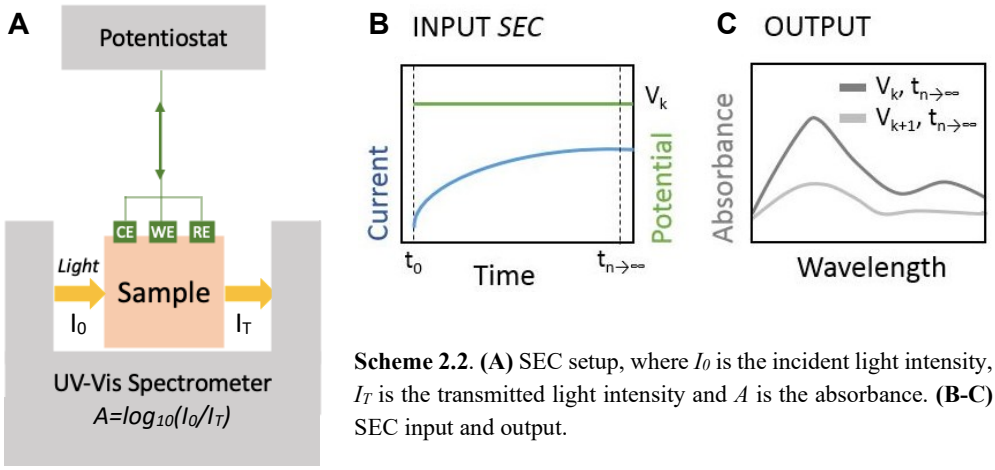

Scheme 2.2. **(A)** SEC setup, where I_0 is the incident light intensity, I_T is the transmitted light intensity and A is the absorbance. **(B-C)** SEC input and output.

This method has been used to find out the spectra of the different oxidation states of the catalysts. The absorbance of the different states was measured under an applied potential close to the oxidation potential of the species, the latter being deduced from the corresponding cyclic voltammetry (CV) (Section 2.2). The absorbance of the electrons in the semiconductor or conductor substrates has been subtracted to the final overall spectra in order to isolate the absorbance of the catalyst. In some cases, the catalysts have been anchored to ITO because this material has a high transmission of visible light and, at the same time, is conductive in the required potential range. The electric field generated at the surface may have an impact on the absorbance spectra of the catalyst, a phenomenon that is known as Stark effect, but this effect is likely to alter the spectra by a few nanometers and it has been neglected in the analysis.

2.4. Transient Absorption Spectroscopy & Photocurrent – TAS & TPC

The kinetics and reactivity of catalytic species with characteristic optical signals was investigated with time-resolved absorption spectroscopy. Time-resolved absorption spectroscopy (TAS) is based on two light beams. The first beam (*i.e.*, the pump) is a high-intensity pulsed laser that is used to excite the sample; the second beam (*i.e.*, the probe) is used to measure the sample absorbance changes at different time delays after the excitation. The time span of the pump pulses needs to be shorter than a given chemical reaction for the latter to be detected. The absorbance changes (ΔA) are calculated from the light intensity of the probe detected after passing through the sample as follows:

Equation 2.5 $$\Delta A_\lambda(t) = A_{\lambda,\ after\ pump}(t) - A_{\lambda,\ before\ pump} = \log_{10}\left(\frac{I_{without\ pump}}{I_{with\ pump}\ (t)}\right)$$

Where t is the time delay between the pump and the probe; $A_{\lambda,\ after\ pump}\ (t)$ is the absorbance of the sample at time t and $A_{\lambda,\ before\ pump}$ is the absorbance of the sample before the pump ($t<0$); $\Delta A_\lambda(t)$ is the absorbance change at time t and at the probe wavelength λ; $I_{without\ pump}$ is the intensity of the probe after the sample without pump, and $I_{without\ pump}(t)$ is the intensity of the probe after the sample t seconds after the pump has reached the sample.

Some of the time-resolved absorption spectroscopy measurements were done in a setup that probed timescales from microseconds to seconds (µs-s) after the pump excitation (Scheme 2.3). The pump was a 355-nm 7-ns laser pulsed beam produced with a neodymium-doped yttrium aluminium garnet (Nd:YAG) crystal coupled to an optical parametric oscillator (*Opotek Opolette 355*). The probe light was generated with a 100 W tungsten lamp (*Bentham*). The wavelength of the probe beam was selected with two monochromators (*Horiba Scientific OBB*) which were placed before and after the sample in the probe light path. A suitable long-pass filter regulated by a mechanical colour wheel (*FW101C Thorlabs*) and a 400-nm long-pass filter were additionally placed after the sample to minimize the interference in the probe light detection of other light sources (for example, the high-intensity pump pulses). The probe light was detected by a silicon PIN photodiode (*Hamamatsu S3071*) and processed by an optical transient amplifier (*Costronics 2004*), a digital phosphor oscilloscope (Scope, *Tektronix DPO 3012*) and a data acquisition system (DAQ) (*National Instruments X Series Multifunction*). The probe was always on and the time delay was processed electronically once a trigger signal indicated the emission of a pump pulse to the DAQ and the Scope. All the results shown here are the average of a few measurements, each of which is based on one 7-ns 355-nm pulse. The frequency of the pump pulse was 0.8 Hz (referred to as ‘repetition rate’).

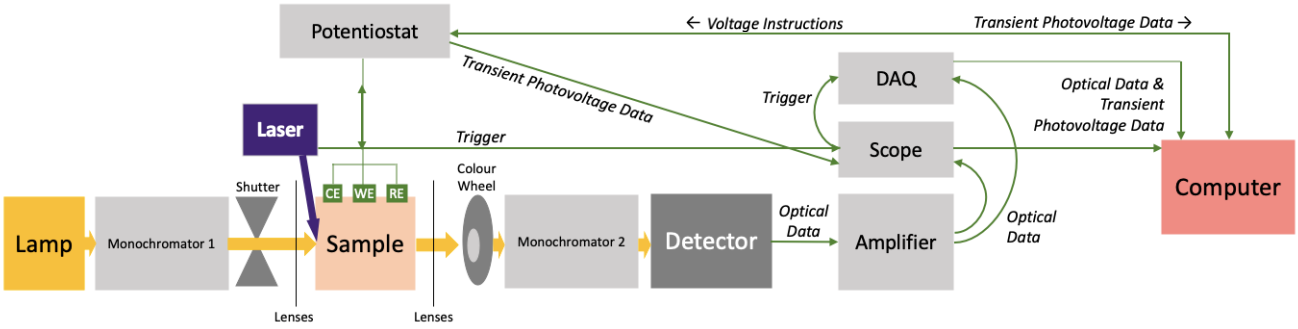

Scheme 2.3. Microsecond to second TAS and TPC setup.

A second time-resolved absorption setup in timescales of femtoseconds to nanoseconds (fs-ns) was used (*Helios, Ultrafast Systems*). In this case, both the pump and the probe beams originated from a seed beam produced by a regeneratively amplified Ti:sapphire laser (*Solstice, Spectra-Physics*). This seed beam consisted of 92-fs 800-nm laser pulses with a repetition rate of 1 kHz. The pulsed seed beam was split into the probe and the pump by a semi-transparent mirror. The wavelength of the pump beam was tuned with an optical parametric amplifier (*TOPAS Prime, Light Conversion*) and a frequency mixer (*NirUVis, Light Conversion*). The time difference between the pulse and pump pulses was automatically adjusted with a delay stage, in contrast to the slower µs-s setup above (Scheme 2.3). The power of the laser pulses was measured with an *Ophir Photonics PE9* energy meter in the fs-ns setup and with a *VEGA P/N 7Z01560* energy meter (*OPHIR Photonics*) in the µs-s setup.

In addition to the detection of the optical signal, the transient electric current induced upon light excitation (also called transient photocurrent or TPC) was also measured in microseconds to seconds. The measurement was done by connecting the sample to a potentiostat (see Scheme 2.3). The potentiostat monitored transient voltage differences between the sample (*i.e.*, the working electrode) and a platinum counter electrode across a 98.7 Ohm resistor. Finally, the current was calculated from the voltage by applying Ohm's law ($I=V/R$, where I is the electric current between the working and the counter electrode, R is the electrical resistance implemented by the external resistor, and V is the voltage difference across the resistance). Because the TPC signal is measured as a transient potential difference, TPC signals could only be obtained under an applied potential. The potential of the working electrode was monitored with a voltammeter with respect to the potential of the saturated Ag/AgCl reference electrode.

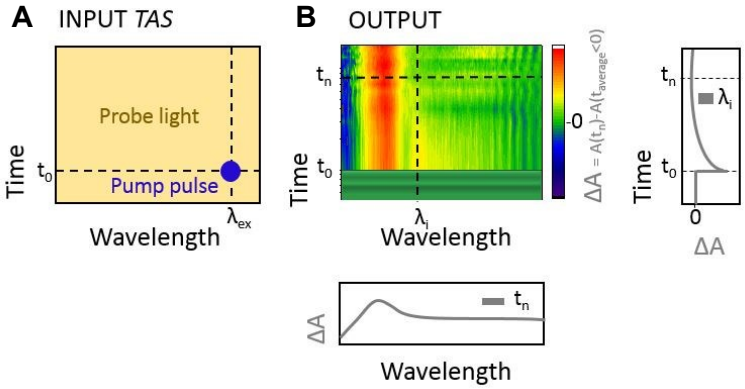

Scheme 2.4. Representation of TAS measurements (**A**, input) and results (**B**, output).

Scheme 2.4 shows the information than could be extracted from a TAS measurement: transient absorption spectra and kinetic traces throughout the microsecond to second timescale. In this work, this technique was used (1) to detect the depletion and formation of catalyst species, which react with electrons at the semiconductor electrode and species in solution, and (2) to deduce its catalytic mechanism from their kinetics. The diffusion limit of species in solution can be as fast as microseconds. On the other hand, thermodynamically favoured electron transfer between interlinked compounds is faster than microseconds, but it can be limited by the morphology of the material and the presence of low-energy trap or defect states.

2.5. Photoinduced Absorption Spectroscopy – PIAS

Photoinduced Absorption Spectroscopy (PIAS) is a technique which is very similar to TAS. The difference between the two is the timescale of light excitation and probe measurement. As shown in Scheme 2.5, the PIAS setup is the same as the TAS setup except for the pump. In PIAS, the pump is a light emitting diode (LED) turned on and off during intervals of several seconds, in contrast to the high-intensity 7-ns pulsed laser used in TAS. Consequently, the time resolution of PIAS is seconds while that of TAS is up to microseconds.

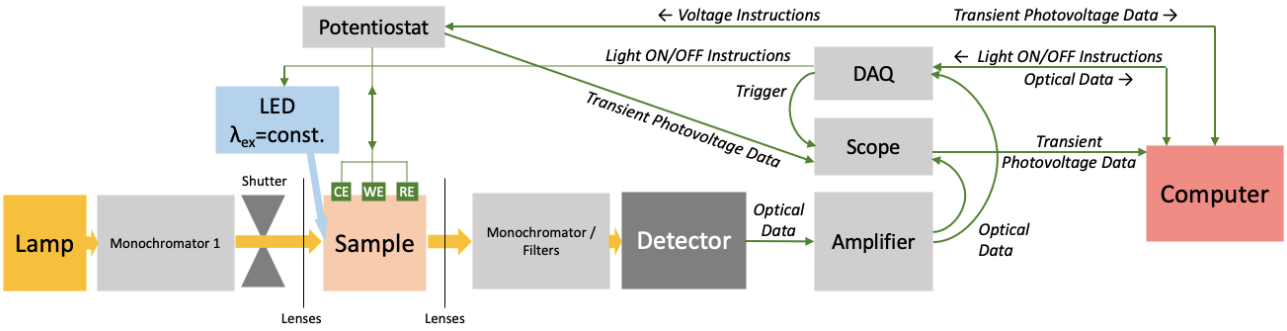

Scheme 2.5. The PIAS setup.

Both TAS and PIAS were mostly used to investigate photocatalytic electrodes consisting of catalysts immobilised on TiO_2, where catalysis was induced by exciting TiO_2 with 355-nm light. PIAS was used to detect slower processes than with TAS and to understand the catalytic mechanism under steady-state illumination conditions (Scheme 2.6). Compared to TAS, PIAS signals were usually larger in amplitude due to the lower power of the excitation source, which leads to less recombination.

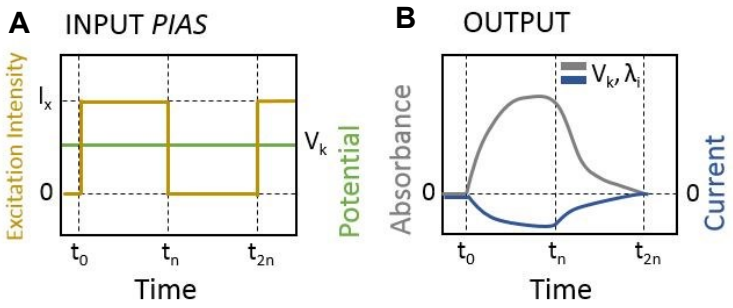

Scheme 2.6. PIAS input **(A)** and output **(B)**.

2.6. Step Potential Spectroelectrochemistry – SP-SEC

On the same timescales as PIAS (~s), Step Potential Spectroelectrochemistry (SP-SEC) measures absorbance changes induced by potential cycles. Therefore, there is no need for a pulsed laser or and LED pump to create a stimulus, but only for a potentiostat (Schemes 2.7-8). In this case, a *PalmSens3* potentiostat was used to cyclically apply two consecutive potential steps. This technique is similar to SEC but it provides with a better time resolution, allowing a more accurate measurement at shorter times of electrical currents and the redox state kinetics in electrocatalysts. As in TAS and PIAS, the electrical and optical signals resulting from the induced stimulus were processed with a digital phosphor oscilloscope / scope (*Tektronix DPO 3012*) and a data acquisition system DAQ (*National Instruments X Series Multifunction*). The pump light and resulting optical signal were generated, detected, filtered and amplified in the same way as in TAS and PIAS.

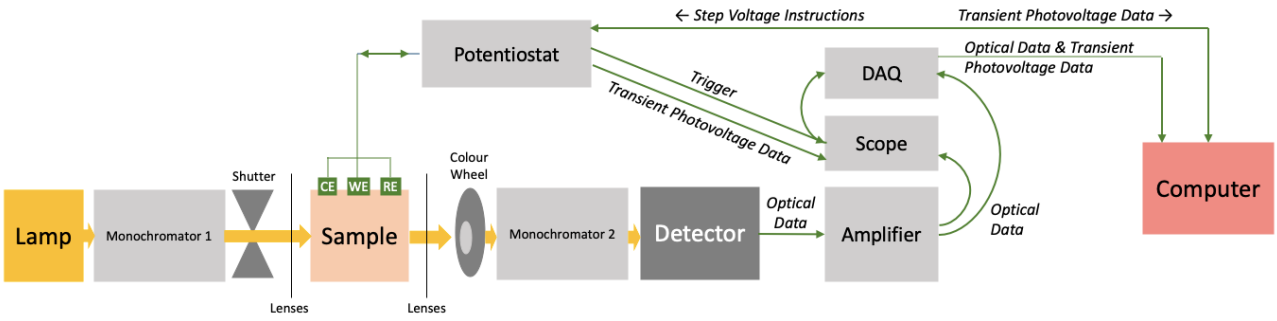

Scheme 2.7. The SP-SEC setup.

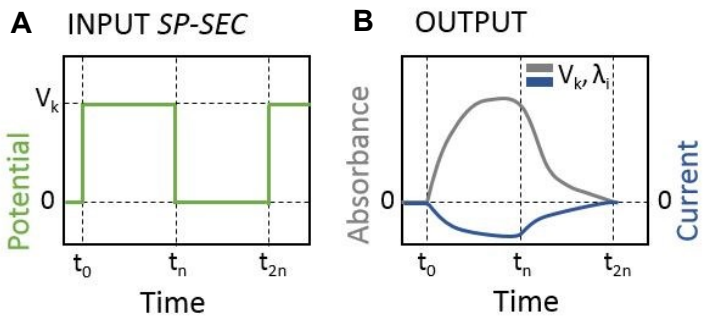

Scheme 2.8. **(A)** Input and **(B)** output in SP-SEC measurements.

2.7. Data Treatment

The kinetic data from TAS, SP-SEC and PIAS measurements was treated in two different ways using *Origin* and *Matlab*:

1. By **smoothing the noise** with a Savitzky-Golay filter, using 2-degree polynomials applied to every set of ~20 data points at early timescales (1 µs – 1 ms) and to every set of ~100 data points at later timescales (1 ms – 1 s).
2. By **adjusting the stitching between the signals** in the µs-ms timescale and the ms-s timescale, which are measured by two different instruments (the Scope and the DAQ respectively in Schemes 2.3, 2.5 and 2.7).

Furthermore, the kinetic and spectroelectrochemical data (Chapters 3-6) were fitted with different mathematical models in order to check the validity of its interpretation. A **global optimization** method was applied to minimize the difference between the experimental data and the data predicted by a mathematical model. The value which was minimized was the total residual (*i.e.*, *F* in Scheme 2.9), which was calculated as the sum of the differences at all data points between the model and the real data. The model data was generated in *Matlab* (versions *R2016* and *R2019a)*, and it was optimised in the same program with the global minimisation tool *GlobalSearch* and the constrained nonlinear multivariate solver *fmincon*.[24, 25] These tools were set to find the minimum total residual, starting with a set of 200 initial trial points and examining a total of 1000 trial points, each point consisting of a different combination of values for the optimisation variables (for example, the concentration *c*, the rate constant *k*, the redox potential *E* and absorption coefficient ε in Scheme 2.9) within pre-set constrains. The mathematical model used to predict the data in each specific case is described in the following Chapters.

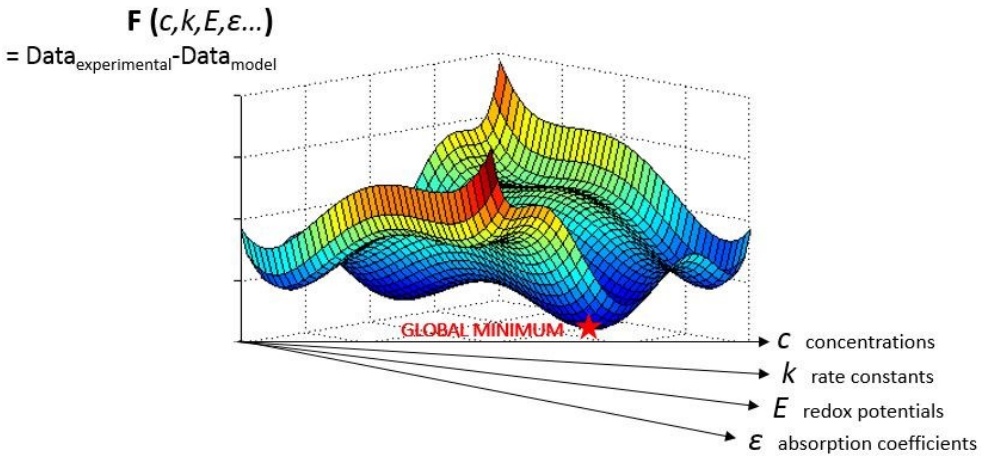

Scheme 2.9. Representation of the process of fitting the data with a mathematical model, which consists in finding the global minimum of the residual function (subtraction between the experimental and modelled data).

2.8. References

1. F. Lakadamyali and E. Reisner, *Chem. Commun.*, 2011, **47**, 1695-1697.
2. F. Lakadamyali, A. Reynal, M. Kato, J. R. Durrant and E. Reisner, *Chem. Eur. J.*, 2012, **18**, 15464-15475.
3. N. M. Muresan, J. Willkomm, D. Mersch, Y. Vaynzof and E. Reisner, *Angew. Chem. Int.*, 2012, **51**, 12749-12753.
4. M. R. Scherer, N. M. Muresan, U. Steiner and E. Reisner, *Chem. Commun.*, 2013, **49**, 10453-10455.
5. J. Willkomm, N. M. Muresan and E. Reisner, *Chem. Sci.*, 2015, **6**, 2727-2736.
6. J. J. Leung, J. Warnan, K. H. Ly, N. Heidary, D. H. Nam, M. F. Kuehnel and E. Reisner, *Nat. Catal.*, 2019, **2**, 354-365.
7. J. J. Leung, J. A. Vigil, J. Warnan, E. Edwardes Moore and E. Reisner, *Angew. Chem. Int.*, 2019, **58**, 7697-7701.
8. S. W. Sheehan, J. M. Thomsen, U. Hintermair, R. H. Crabtree, G. W. Brudvig and C. A. Schmuttenmaer, *Nat. Commun.*, 2015, **6**, 6469.
9. J. Li, P. I. Djurovich, B. D. Alleyne, M. Yousufuddin, N. N. Ho, J. C. Thomas, J. C. Peters, R. Bau and M. E. Thompson, *Inorg. Chem.*, 2005, **44**, 1713−1727.
10. J. D. Blakemore, N. D. Schley, G. W. Olack, C. D. Incarvito, G. W. Brudvig and R. H. Crabtree, *Chem. Sci.*, 2011, **2**, 94-98.
11. J. Li, P. I. Djurovich, B. D. Alleyne, M. Yousufuddin, N. N. Ho, J. C. Thomas, J. C. Peters, R. Bau and M. E. Thompson, *Inorg. Chem.*, 2005, **44**, 1713-1727.
12. J. Willkomm, K. L. Orchard, A. Reynal, E. Pastor, J. R. Durrant and E. Reisner, *Chem. Soc. Rev.*, 2016, **45**, 9-23.
13. T. E. Rosser and E. Reisner, *ACS Catal.*, 2017, **7**, 3131-3141.
14. B. J. Brennan, M. J. Llansola Portoles, P. A. Liddell, T. A. Moore, A. L. Moore and D. Gust, *Phys. Chem. Chem. Phys.*, 2013, **15**, 16605-16614.
15. R. M. Bullock, A. K. Das and A. M. Appel, *Chem. Eur. J.*, 2017, **23**, 7626-7641.
16. Electrochemical Methods. Fundamentals and Applications, A. J. Bard and L. R. Faulkner, *John Wiley & Sons, Inc.*, 2001, 2nd edition.
17. Electrochemical Systems, J. Newman and K. Thomas-Alyea, *Wiley Interscience, John Wiley & Sons*, 2004, 3rd edition.
18. X. Wang, R. Kumar, and D. J. Myers, *Electrochemical and Solid-State Letters*, 2006, **9**, 5, A225-A227
19. D. Voiry, M. Chhowalla, Y. Gogotsi, N. A. Kotov, Y. Li, R. M. Penner, R. E. Schaak, Paul S. Weiss, *ACS Nano*, 2018, **12**, 9635−9638
20. R. Chen, C. Yang, W. Cai, H.-Y. Wang, J. Miao, L. Zhang, S. Chen, B. Liu, *ACS Energy Lett.*, 2017, **2**, 1070−1075
21. E. S. Rountree, B. D. McCarthy, T. T. Eisenhart and J. L. Dempsey, *Inorg. Chem.*, 2014, **53**, 9983-10002.
22. E. M. Espinoza, J. A. Clark, J. Soliman, J. B. Derr, M. Morales and V. I. Vullev, *J. Electrochem. Soc.*, 2019, **166**, H3175-H3187.
23. V. V. Pavlishchuk and A. W. Addison, *Inorganica Chim. Acta* 2000, **298**, 97–102.
24. Introduction to nonlinear optimization: theory, algorithms and applications with MATLAB, A. Beck, *MOS-SIAM series on optimization, Philadelphia: Society for Industrial and Applied Mathematics*, 2014.
25. Optimization in practice with MATLAB for engineering students and professionals, A. Messac, *New York, NY: Cambridge University Press*, 2015.

Chapter 3

Charge accumulation kinetics in multi-redox molecular catalysts immobilised on TiO_2

The work in this Chapter is published as an Advance Article in the journal Chemical Science *(*DOI: 10.1039/d0sc04344c*). Dr. Annika Eisenschmidt did the TD-DFT calculations, Dr. Daniel Antón-García prepared the ITO films and synthesised the molecular catalysts* ***CoP[1]*** *and* ***CoP[2]****, and Julien Warnan synthesised the molecular catalyst* ***CotpyP****. Dr. Camilo A. Mesa, Dr. Laia Francàs, Dr. Janina Willkomm, Dr. Anna Reynal, Prof. Erwin Reisner and Prof. James R. Durrant contributed to the discussion of the results.*

Charge accumulation was investigated in two hybrid molecular / inorganic photocatalytic systems, consisting of two model multi-redox molecular catalysts for proton and CO_2 reduction attached onto mesoporous TiO_2 electrodes (Section 3.1-2). Steady-state (Section 3.3.1) and transient (Section 3.3.2) spectroelectrochemical techniques were employed to study the kinetics of photoinduced electron transfer from the TiO_2 to the H_2-production molecular catalyst **CoP[2]** in acetonitrile, with triethanolamine as the hole scavenger. The same techniques were applied to investigate the CO_2-reduction molecular catalyst **CotpyP** on TiO_2 in the same conditions (Section 3.3.3). At high light intensities, charge accumulation was detected in the millisecond timescale in the form of multi-reduced species. The redox potentials of the catalysts and the capacity of TiO_2 to accumulate electrons play an essential role in the charge accumulation process at the molecular catalyst. Recombination of reduced species with valence band holes in TiO_2 was observed to be faster than microseconds, while electron transfer from multi-reduced species to the conduction band or the electrolyte occurs in the millisecond timescale. Finally, under light irradiation, it was shown how charge accumulation on the catalyst could be regulated as a function of the applied bias and the excitation light intensity.

3.0. Contents

3.1. Introduction

Multi-redox catalysis requires the transfer of more than one charge carrier and is crucial for solar energy conversion into fuels and valuable chemicals. In photo(electro)chemical systems, however, the necessary accumulation of multiple, long-lived charges is challenged by recombination with their counterparts. In this work, the accumulation of photo-induced charges was studied in two multi-redox molecular catalysts attached to TiO_2: a cobalt diimine–dioxime catalyst for proton reduction and a cobalt bis(terpyridine) catalyst for CO_2 reduction, both containing phosphonate anchors for immobilisation to the metal oxide surface.[4] The efficiency and kinetics of sequential charge transfers from TiO_2 to the catalyst was investigated as a function of the starting oxidation state of the catalyst.

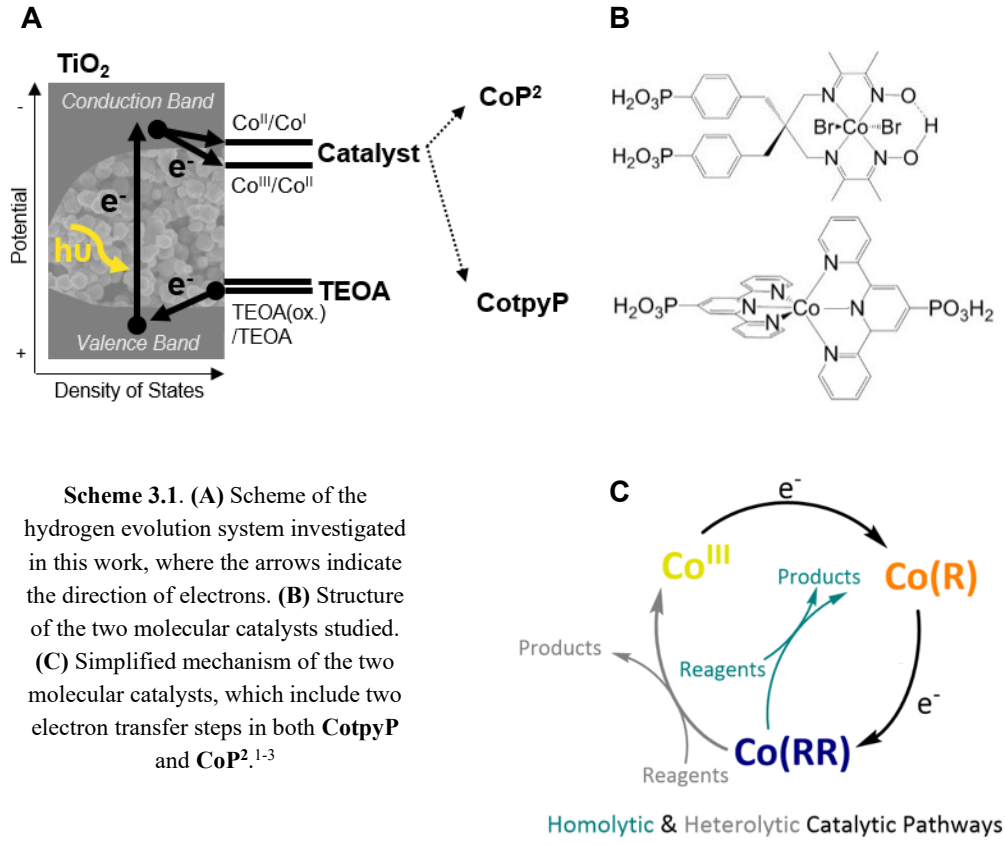

Scheme 3.1. **(A)** Scheme of the hydrogen evolution system investigated in this work, where the arrows indicate the direction of electrons. **(B)** Structure of the two molecular catalysts studied. **(C)** Simplified mechanism of the two molecular catalysts, which include two electron transfer steps in both **CotpyP** and **CoP²**.[1-3]

The structure-performance relationship of synthetic molecular catalysts in photocatalytic schemes is usually not well understood because of the difficulty in characterising the unstable intermediates involved and the kinetics of the individual steps of the catalytic mechanism.[5-9] The multi-redox photocatalytic system best defined to date is the antenna array and the oxygen evolution complex of photosystem II, where the accumulation of oxidising equivalents in the catalytic centre has received extensive attention.[10-16] In contrast, there are few literature studies directly characterising the kinetics of photogenerated charge accumulation steps in artificial photosynthetic systems; attention concerning these systems has mostly been focused on their photo- or electro-catalytic performance rather than on their capacity to accumulate charge. Charge accumulation states for photocatalytic water oxidation or reduction have only been directly observed under constant irradiation,[17-20] while the kinetics of different accumulation steps have been mainly resolved in donor-sensitiser-acceptor molecular constructs without catalytic activity.[21-24] As such, charge accumulation on such molecular catalysts in light driven systems, and the impact of this charge accumulation on charge recombination losses which can limit device efficiency, remain often poorly described.

This Chapter primarily focuses on the molecular hydrogen-evolution catalyst **CoP^2** attached onto TiO_2 as a model to study the kinetics of photo-induced charge accumulation in a multi-redox catalyst (Scheme 3.1A). Herein, the formation and accumulation of different oxidation states was modulated by two independent mechanisms: (i) by controlling the applied potential and (ii) the light intensity. TiO_2 was used as a UV-light photo-absorber to generate electrons in its conduction band (CB) and study consecutive electron transfers to the catalyst immobilised at its surface, while the whole photoelectrode is soaked in acetonitrile (ACN) with triethanolamine (TEOA) as valence-band hole scavenger.[25-27] Acetonitrile was used because it is an aprotic solvent and hence facilitated the study of catalyst reduced intermediates and charge accumulation, which are processes where protons are not involved. The TEOA enabled long electron lifetimes independent of applied bias by irreversibly scavenging holes from the valence band (VB) of TiO_2 through a two-electron oxidation involving an aminyl radical and the release of a proton.[28] The applied bias was then employed to modulate the initial TiO_2 Fermi level and therefore the initial redox state of the catalyst.

The molecular catalyst **CoP^2** used in this work belongs to the group of cobalt diamine-dioxime catalysts encompassing some of the best studied H_2-production molecular catalysts, which require two electrons and two protons to evolve one molecule of hydrogen.[1, 2, 29-33] Cobalt diimine–dioximes and related cobalt-based catalysts have relatively narrow absorbance bands in the UV-Vis range that vary with their electronic occupancy, as revealed by previous theoretical studies and steady-state absorbance measurements under photo- and electrocatalytic conditions.[1, 3, 34-37] Using these spectroscopic properties, **CoP^2** was used as a charge accumulation probe, in contrast to previous work where the electron and hole signals in TiO_2 (at 900 nm and 460 nm respectively) were employed to study charge transfer to the catalyst in water.[26, 38, 39] To corroborate the findings on CoP^2, a second molecular catalyst was tested in this study for comparison. This catalyst is the CO_2-reduction

cobalt-based **CotpyP**, which operates at exceptionally low overpotentials compared to other CO_2-reduction catalysts and hence can be coupled to TiO_2 photoelectrodes.[40-42] The **CotpyP** catalyst was chosen because it is a multi-redox catalyst based on a cobalt centre as for **CoP²** but also operates at more reductive potentials than **CoP²**. For both catalysts (see their structures in Scheme 3.1B), time-resolved absorption measurements with microsecond time resolution were undertaken under different applied potentials and excitation intensities to characterise the kinetics of charge accumulation and recombination.

3.2. Materials and Methods

3.2.1. Synthesis of molecular catalysts

The molecular catalysts used in this Chapter, **CoP[1]** (ref.[26, 27]) ([$Co^{III}Cl(dmgH)_2$(pyridyl-4-hydrophosphonate)], dmgH=dimethylglyoximato), **CoP[2]** (ref.[1, 31]) ([$Co^{III}Br_2(N^2,N^{2'}$-2,2-($CH_2(C_6H_4)PO_3H$)propanediyl-bis(2,3-butanedione-2-imine-3-oxime))]) and **CotpyP** (ref. [40, 41]) ([Co^{II}-bis(2,2':6',2''-terpyridine-4'-phosphonate)]), were synthesized and characterized as reported previously. All the chemicals, including acetonitrile anhydrous 99.8% (ACN), triethanolamine 99% (TEOA) and tetrabutylammonium hexafluorophosphate 98% ($TBAPF_6$), were purchased from Sigma Aldrich. Fluorine-doped tin oxide (FTO)-coated glass sheets (SnO_2/F, 7Ωsq^{-1} sheet resistance, 300 × 300 × 2 mm) and ITO nanopowder (diameter < 50 nm; Brunauer-Emmett-Teller (BET) area = 27 m^2 g^{-1} ; 90% In_2O_3, 10% SnO_2) were also purchased from Sigma Aldrich. The molecular catalysts were investigated on both mesoporous TiO_2 and ITO films on FTO-glass, which were prepared and loaded as described in the following sub-sections.

3.2.2. TiO_2 Film Preparation

A paste with 15 nm anatase TiO_2 nanoparticles was prepared from a sol-gel colloidal suspension containing 12.5 wt% TiO_2 particles and 6.2 wt% Carbowax 20000, which was prepared using the same reagents and procedure as in ref. [43, 44]. Films were then prepared by doctor-blading the paste on clean FTO on glass, drying for ~20 min. and sintering at 450 ˚C degrees for 30 min. The glass-FTO substrate was previously cleaned by washing with soap, distilled water and isopropanol and heating at 450 ˚C degrees for 30 min. The resulting films had a thickness of ~4 μm, 10-50 nm diameter pores, a porosity of 50±5%, a BET surface area per gram (S_g) of 106 m^2/g, and a roughness factor (surface area divided by projected area) around 450.[44-46]

3.2.3. ITO Film Preparation

FTO-coated glass was cleaned by immersing it in a solution of H_2O/37% NH_3/30% H_2O_2 (50:17:33 v/v) at 80 °C for 15 min. The electrodes were rinsed with water and successive sonication in ethanol and acetone for 15 minutes each, followed by drying at 70 °C in air before further use. A dispersion of 20% weight ITO nanoparticles was prepared in 5 M acetic acid in ethanol solution. After sonication for 30 minutes in an ice-cooled sonication bath, the ITO thin films were spin-coated onto the cleaned FTO-glass substrates. The electrodes were finally sintered at 450 °C for 30 minutes. The electrodes had a geometrical area of approximately 0.25 cm^2.

3.2.4. Film loading with catalyst

The TiO_2 films were prepared just before loading the catalyst; otherwise, they were heated to 450 ˚C for 30 min prior to the loading. The molecular catalysts **CoP[1]** and **CoP[2]** were loaded on TiO_2 by soaking ~1-cm^2 films on 1x2 cm^2 FTO-glass in 5 mL of methanol (MeOH) and water (H_2O) 1:1 with ~0.1 mM of catalyst for 12 h. **CotpyP** was loaded by soaking the TiO_2 films in 5 mL MeOH with 0.25 mM of catalyst for 12 h. Three films were soaked in each solution. Once loaded, all the films were rinsed first with methanol and then with acetonitrile and were left to dry in the air for at least 12h before they were used. The same procedure was followed to load the catalysts on ITO. The spectroscopic features of the catalyst were observed to remain constant in methanol for at least 48 h, more than 4 times the timespan of all the experiments. The amount of loaded catalyst was determined by measuring the absorbance differences in the soaking solution.

3.3. Results

3.3.1. Spectroelectrochemistry

Spectroelectrochemistry experiments were done to characterise the redox potentials and the spectroscopic features of the different catalyst oxidation states involved in the catalytic mechanism. First, the steady-state absorbance of the catalysts was measured in solution to determine the absorption coefficients of the initial state of the catalyst and the amount of catalyst loaded on the electrodes. Sections 3.3.1.1 and 3.3.1.2 describe the spectroelectrochemistry experimental results and theoretical predictions, which are used in Section 3.3.1.3 to assign the observed absorbance features to different multi-reduced intermediates of the catalyst. The experimental procedure is described in Chapter 2.3. These experiments were done with both **CoP²** and **CotpyP**, but the experimental results of **CotpyP** will not be shown and discussed until Section 3.3.3.

3.3.1.1. Experimental results

The absorption coefficients of the catalysts in MeOH and MeOH:ACN (1:1) were determined by measuring the absorbance of 4 solutions of MeOH with a known concentration of catalyst. Following the Lambert-Beer law, the amount of catalyst loaded on TiO_2 was calculated from the difference in the absorbance of the catalyst solution before and after the films had been immersed in it; the loading was calculated as an average between 10 samples. The absorption coefficients of reduced species of **CoP²** were deduced from the spectroelectrochemistry results of ITO-**CoP²**, where the concentration of catalyst was determined as on TiO_2, while those of **CotpyP** were determined from the spectroelectrochemistry results of the catalyst on TiO_2. The experimental errors were calculated by following conventional error propagation equations, and by considering standard deviations of the different identical measurements or regression errors.

In the case of the catalyst **CoP²**, the absorbance of its starting state $Co^{III}P^2$ in solution was determined to be 1600±100 M^{-1} cm^{-1} at 445 nm in accordance to literature[1] (measured in dimethylformamide, DMF, due to the catalysts insolubility in acetonitrile); similar data were obtained in MeOH and MeOH:ACN 1:1. The catalyst was then loaded on high-surface area mesoporous TiO_2 films (Sections 3.2.1. and 3.2.3). The average amount of loaded catalyst was 90±50 nmol cm^{-2} of projected area. Following previous reports[1, 38] on CoP^2 and in line with other literature[40, 47-49] of molecular catalyst on mesoporous TiO_2, the loading of this TiO_2-**CoP²** films corresponded approximately to a monolayer of anchored **CoP²**, the maximum amount of catalyst that can be covalently attached on the surface, which was optimal for the detection of strong and reproducible spectroscopic catalyst signals. Spectroscopic studies were undertaken in acetonitrile to enable the monitoring of charge accumulation on **CoP²** in the absence of subsequent proton reduction catalysis.

To characterise the redox potentials and the spectroscopic features of the different catalyst oxidation states involved in the catalytic reduction of hydrogen, **CoP²** was investigated on mesoporous indium tin oxide (ITO, particle size < 50 nm, film thickness ~3 µm), employing the same loading strategy as for TiO_2 (Sections 3.2.3-4).[1, 40, 50] The catalytic mechanism of cobalt diamine-dioximes and related cobalt catalysts is widely agreed to start by two consecutive reductions involving three redox states:[1, 3] Co^{III}, Co^{II} and Co^{I} (Scheme 3.1C), where Co^{III} is the initial state.[2, 29, 30] The redox potentials of these two reductions were determined by doing a cyclic voltammetry of ITO-**CoP²** (Figure 3.1A), which compared to ITO alone showed two characteristic reduction waves at ~ −0.4 and ~ −0.7 V vs. NHE, assigned to the Co^{III}/Co^{II} and Co^{II}/Co^{I} reductions respectively. Following this data, the absorbance of the three reduced ITO-**CoP²** species was determined at three different applied potentials, before and after the observed redox waves, where the catalyst was expected to be predominantly in one of the three oxidation states (Figure 3.1B). The experimental spectra were measured using ITO-**CoP²** films in ACN containing tetrabutylammonium hexafluorophosphate ($TBAPF_6$, 0.1 M) as supporting electrolyte. Mesoporous ITO was used instead of TiO_2 because of its conductivity in the potential range of interest and its lower absorbance in the visible range,[25, 51] therefore allowing a better identification of the absorbance features of the different redox species.

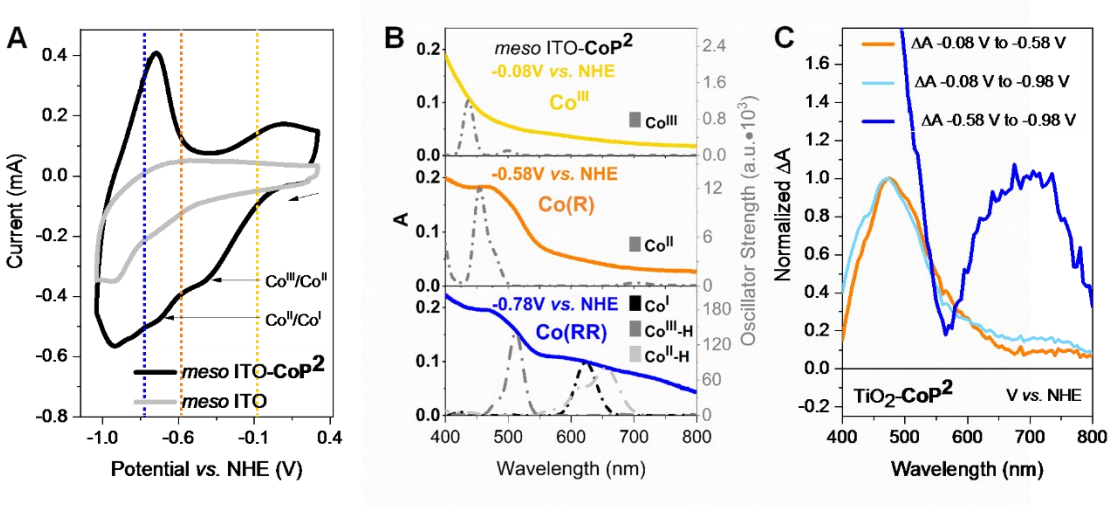

Figure 3.1. Electrochemical and spectroelectrochemical characterisation of the **CoP²** catalyst on ITO and TiO_2. **(A)** Cyclic voltammetry of **CoP²** attached to ITO in ACN 0.1 M $TBAPF_6$ *vs.* NHE. **(B)** Experimental (*coloured continuous*) and theoretical (*grey dotted*) steady-state absorption spectra of CoP^2 at different potentials. The baseline of the experimental spectra is ITO in ACN 0.1 M $TBAPF_6$. The predicted absorption spectra shown have been obtained from TD-DFT calculations using the hybrid functional B3LYP combined with the basis set 6-31G(d,p). **(C)** Experimental steady-state absorbance changes of TiO_2-**CoP²** in ACN 0.1 M $TBAPF_6$. *Co(R)* and *Co(RR)* stand for mono- and multi- reduced catalyst species respectively.

3.3.1.2. Theoretical results

Figure 3.1B also shows the theoretical spectra of different catalyst reduced species, which assume the replacement of the axial bromido ligands by acetonitrile molecules as previously observed in the literature[34, 52]. These were calculated by time-dependent density functional theory (TD-DFT) combining the hybrid functionals B3LYP and TPSSh and the basis sets 6-31G(d,p) and def2-TZVP, leading to absorbance bands with a deviation between the different calculation methods of ~30 nm (see Annex and Table 3.2 in Section 3.7.1).[53, 54] As seen in Figure 3.1B, the experimental and theoretical results are in good agreement.

3.3.1.3. Assignment

The absorbance features in the experimental UV-Vis range are assigned following the cyclic voltammetry in Figure 3.1A and the TD-DFT results, and in accordance with the literature[1, 3, 34-37, 55]: Co^{III} (−0.08 V *vs.* Normal Hydrogen Electrode, NHE) absorbs mostly below 400 nm (Figure 3.1B top), Co^{II} (−0.58 V *vs.* NHE) has an absorbance band at around 450-500 nm (Figure 3.1B middle) and Co^{I} (−0.78 V *vs.* NHE) has a characteristic absorbance between 600-700 nm (Figure 2B bottom). From these spectra, following the Lambert-Beer law, the absorption coefficients at 700 nm of Co^{III}, Co^{II} and Co^{I} were determined to be 350±30, 470±30 and 1130±70 $M^{-1}cm^{-1}$ respectively. At −0.78 V *vs.* NHE, the bands at 460 nm and at 600-700 nm are also consistent with the presence of electrochemically reduced hydride species due to traces of water, confirmed by TD-DFT calculations (Figures 3.1B and Table 3.2). Because of the likely presence of such hydride species at negative potentials, the reduced catalyst species are classified herein as mono-reduced species or *Co(R)* (*i.e.,* Co^{II}) and multi-reduced species or *Co(RR)* (*i.e.*, Co^{I}, Co^{II}-H, Co^{III}-H). The same spectroelectrochemical experiment was repeated with the catalyst on TiO_2. Similar absorption trends were observed on TiO_2 but at more negative potentials, probably because of the conductivity limitations of the conduction band of TiO_2 and / or differences in surface charge (Figures 3.1C and 3.2A). These spectra helped to determine differential spectra for the reduction of this catalyst on both ITO and TiO_2 (Figures 3.2A-D), which are used below to interpret transient absorption (TA) changes under photocatalytic conditions. Control spectroelectrochemical data on bare TiO_2 (Figure 3.2C and 3.3A) allowed tracking of electron accumulation in TiO_2 conduction band tail states, as is discusses further below, with this accumulation increasing approximately exponentially for applied potentials negative of −0.58 V *vs.* NHE, as reported previously.[56, 57]

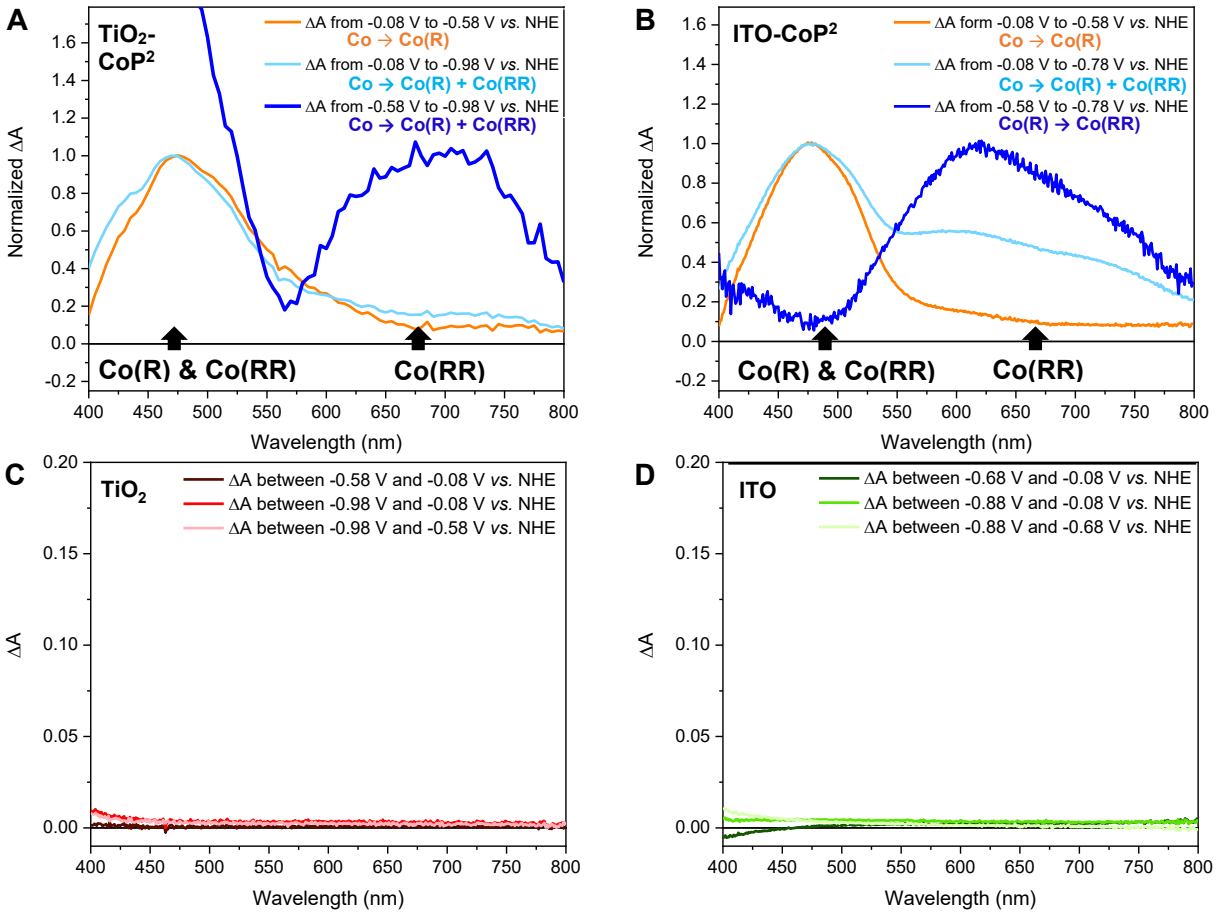

Figure 3.2. Steady-state absorbance changes of **(A)** TiO_2-**CoP^2** and **(B)** ITO-**CoP^2** in ACN 0.1 M $TBAPF_6$. Co(R) and Co(RR) stand for mono- and multi- reduced catalyst species respectively. Two main absorbance features were observed when reductive potentials were applied to a **CoP^2**-loaded electrode: at ~480 nm and at 650-700 nm. The first one (~450-500 nm) wes formed at higher potentials and it was assigned to the first one-electron reduction of **CoP^2** to yield Co(R). The second absorbance signal (600-700 nm) appeared at more negative (or reducing) potentials and it was assigned to the subsequent reduction of Co(R) to Co(RR). The approximate spectra of each of these reduced species was obtained by subtracting the absorption spectra at two different potentials: the potential where the less reducing species is formed and the more reducing potential where the species of interest is reduced. Following the TD-DFT calculations herein, the slight differences between the signals on ITO vs. TiO_2 at 600-700 nm were probably due to differences in the trace amount of water and the hydrophilicity of the samples, in addition to possible electrostatic effect, as described in the main text. **(C)** Steady-state absorbance changes of TiO_2 and **(D)** ITO in ACN 0.1 M $TBAPF_6$. The scale of the y-axis is similar to that of Figure 3.1B to facilitate the comparison.

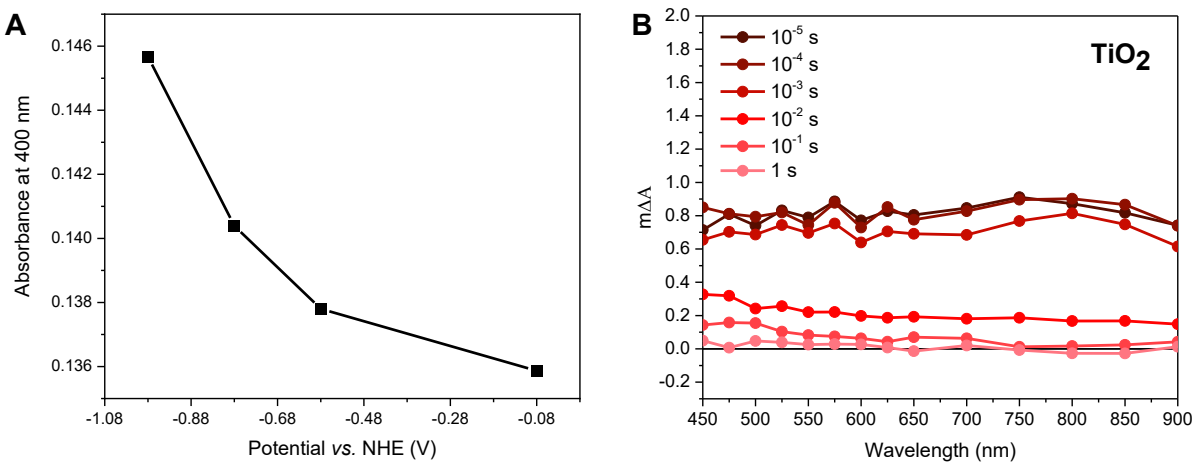

Figure 3.3. **(A)** Potential dependence of the steady-state absorbance at 400 nm in a 4-µm mesoporous TiO_2 film, prepared as detailed above. The absorbance of TiO_2 was calculated by subtracting the absorbance of the FTO substrate to the total absorbance of the FTO-TiO_2 sample. **(B)** Transient absorption spectra of TiO_2 in ACN 0.1 M TEOA 0.1 M $TBAPF_6$ at high 355-nm excitation intensities (1.29±0.04 J/cm^2, 0.8 Hz) under −0.08 V *vs.* NHE.

3.3.2. Time-resolved absorption

Time resolved absorption and current was measured in the microsecond to second timescales following the procedures described in Chapter 2.4. and 2.5. All measurements were done under argon after 15 minutes equilibration purging with argon and keeping the light pump on. These measurements were used to excite TiO_2 and monitor electron transfer to the catalyst (Section 3.3.2.1.), accumulation in the dark and recombination of reduced species (Sections 3.3.2.2.). The kinetics and the quantum yield of the electron transfer are investigated in more detail in Sections 3.3.2.3. and 3.3.2.4. respectively.

3.3.2.1. Transient spectra upon TiO_2 excitation

The spectra obtained spectroelectrochemically in the dark (Figures 3.1 and 3.2) were compared to photoinduced spectral changes obtained under two different light excitation regimes. Firstly, the transient absorption of **CoP²** on TiO_2 was recorded in the microsecond to second timescale under −0.08 V *vs.* NHE and strong (1.3 mJ / cm^2) 355 nm pulsed laser excitation intensity, allowing direct band gap excitation of TiO_2, measured in acetonitrile solution with the addition of 0.1 M TEOA as the hole scavenger. The resulting transient spectrum measured from 10 μs to 1 s after excitation shows an absorbance band peaking at 700 nm (Figure 3.4A), whereas the absorbance of bare TiO_2 under these conditions is relatively flat throughout the 450-900 nm range (Figure 3.3B), being characteristic of electrons in the conduction band of TiO_2.[58, 59] The photoinduced absorbance signal at 700 nm (Figure 3.4A) is long lived, only decaying by ~ 50% on the 1 s timescale of these transient measurements.

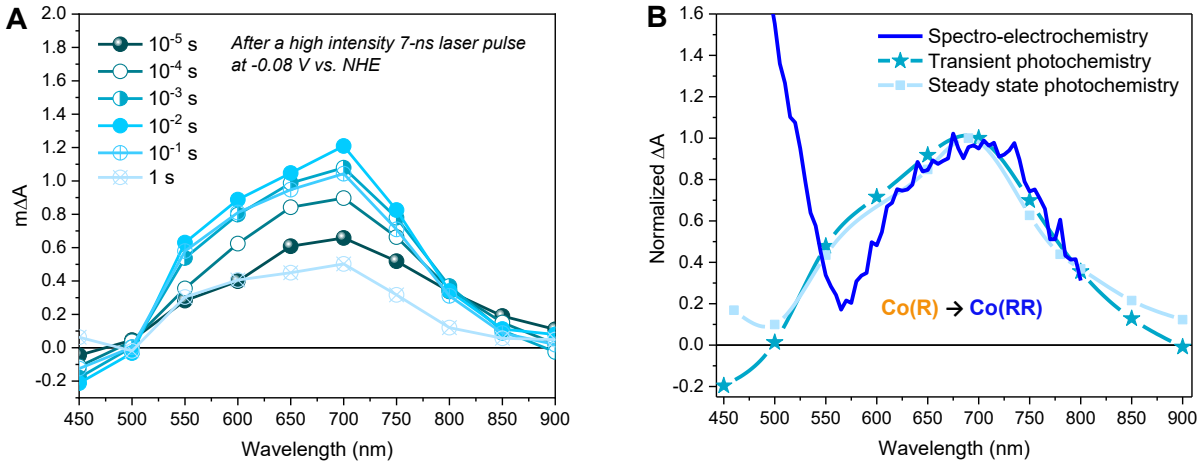

Figure 3.4. Transient photo-induced absorption spectra and comparison with steady-state spectra both electrochemically induced and under constant irradiation. **(A)** Transient absorption spectra of TiO_2-**CoP²** in ACN 0.1 M TEOA 0.1 M $TBAPF_6$ at 1.29±0.04 mJ/cm² 355-nm excitation intensity with 0.8 Hz laser repetition under −0.08 V *vs.* NHE. **(B)** Comparison of the difference spectra of TiO_2-**CoP²** in ACN 0.1 M $TBAPF_6$ 0.1 M TEOA after 355-nm excitation at −0.08 V *vs.* NHE (*Photochemistry* techniques) and between −0.78 V and −0.98 V *vs.* NHE in the dark (*Spectroelectrochemistry* technique). The transient photochemistry signal was measured 10 µs after a high-intensity 7-ns laser pulse, while the steady-state photochemistry signal was measured after 5 s under constant irradiation. *Co(R)* and *Co(RR)* stand for mono- and multi- reduced catalyst species respectively.

Secondly, under 5 s steady-state irradiation while applying the same bias (−0.08 V *vs.* NHE), the same absorbance band at 600-700 nm was observed in TiO_2-**CoP²**, as shown in Figure 3.4B. This photo-induced band at 700 nm is in excellent agreement with the Co(RR)-minus-Co(R) absorbance difference spectrum obtained electrochemically in the dark (*Δ(Co(RR)-(Co(R))*, Figure 3.2A-3.4B), and is clearly distinct from both the Co(R)-minus-Co^{III} and Co(RR)-minus-Co^{III} spectra (*Δ(Co(R)-Co^{III})* and *Δ(Co(RR)-Co^{III})* respectively). It is therefore assigned to the reduction of Co(R) (accumulated starting state of the catalyst under both of these irradiation conditions) leading to the formation of Co(RR). This assignment is supported by further results detailed in the following paragraph. Following this assignment, under these conditions, the absorbance of the possible remaining electrons on TiO_2 electrons is very likely to be masked by the formation of Co(RR), absorbing above 600 nm, and the depletion of Co(R), bleaching below 500 nm. The spectroelectrochemical signal below 500 nm measured in the dark (determined by subtracting spectra at −0.58 V and −0.98 V vs NHE) differs significantly from the photoinduced one probably due to contribution, in the dark spectroelectrochemical data, of the reduction of Co^{III} to Co(R), which can only be electrochemically reduced at more negative potentials than the conduction band simultaneously to the reduction of Co(R) to Co(RR) (Figures 3.2A-B). Evidence from these three different studies therefore suggests that, under photocatalytic conditions at −0.08 V *vs.* NHE, the first

reduced state (Co(R)) accumulates under the aprotic conditions used in this study, with subsequent light pulse further reducing this state transiently to Co(RR). These results also indicate that reduction of Co(R) to Co(RR) can be readily monitored by the appearance of a photoinduced absorbance at 700 nm; the latter is therefore taken as the reference wavelength to study Co(RR) formation kinetics on this timescale in the studies below.

3.3.2.2. Accumulation of species in the dark

To further investigate the assignments, and, in particular, the accumulation and reactivity of the mono-reduced state Co(R)-TiO_2 under high light intensities in acetonitrile, the 700 nm transient absorbance signal was monitored over consecutive measurements (an average of 16 laser pulses) with intervals of ~3 min between each measurement. If the photogenerated species are short-lived (less than the time lapse between experiments, ~3 min.), the experiment presents invariable kinetic traces. On the other hand, if the generated species are long lived (more than ~3 min.), they accumulate and correspond to the initial state for the subsequent measurement, thus changing the shape of the consecutive signals. Figure 3.5A illustrates the changing 700 nm TA dynamics of a fresh sample photoexcited at 355 nm under −0.08 V *vs.* NHE over time until signal stabilisation. Following the assignment above, the final (stabilised) TA signal (lightest blue in Figure 3.5A) corresponds to the laser pulse induced formation of Co(RR) from accumulated Co(R) species (Figure 3.5, step 5). On the other hand, the initial signal (darkest blue in Figure 3.5A) exhibits a relatively small photoinduced absorbance, with no microsecond growth phase but rather a circa 1 ms decay to zero. This signal, and its decay kinetics, is similar, but smaller in amplitude, than the 700 nm signal of bare TiO_2 (Figures 3.3B and 3.8C).

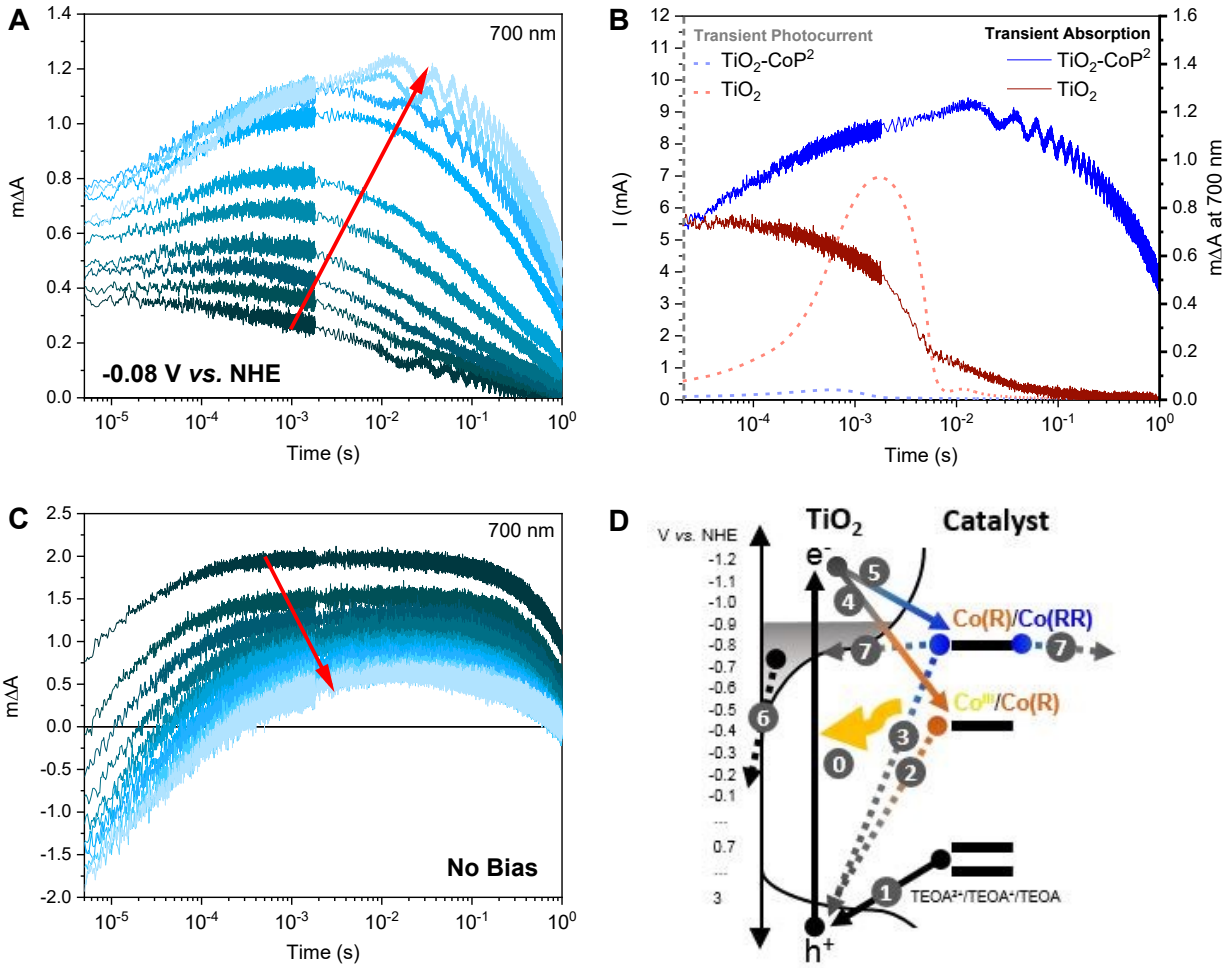

Figure 3.5. Kinetics at 700 nm of TiO_2-**CoP^2** with **(A)** applied potential (−0.08 V *vs.* NHE) in ACN 0.1 M $TBAPF_6$ and 0.1 M TEOA. Consecutive measurements with ~1.4 mJ/cm^2 355-nm excitation, 16 excitation shots averaged per measurement and ~0.9 Hz laser repetition rate are shown. The darkest signal corresponds to the fresh sample, while the lightest corresponds to the final stable signal chosen for the rest of figures. **(B)** Overlap between the stabilised transient absorbance (TA) and transient photocurrent (TPC) signals of TiO_2 and TiO_2-**CoP^2** under -0.08 V *vs.* NHE in ACN 0.1 M $TBAPF_6$ and 0.1 M TEOA with ~1.4 mJ/cm^2 355-nm excitation. **(C)** Kinetics at 700 nm of TiO_2-**CoP^2** without applied potential (−0.08 V *vs.* NHE) in the same conditions. **(D)** Scheme of the different electron transfer processes identified, where (0) corresponds to excitation of TiO_2 with light, (1) corresponds to the scavenging of holes (h^+) by TEOA , (2) and (3) are recombination processes between the reduced catalyst and TiO_2 holes, (4) and (5) are charge transfers from TiO_2 to reduce the catalyst, (6) is the removal of electrons from the conduction band of TiO_2 under bias, and (7) is the back electron transfer from the reduced catalyst to either the valence band of TiO_2 or the electrolyte. *Co(R)* and *Co(RR)* stand for mono- and multi- reduced catalyst species respectively.

To further investigate the identity of these optical signals, the electrons extracted from the photoelectrode were monitored as a transient photocurrent (TPC) signal (Figure 3.5B), which consists of a positive current peaking in ~1 ms after excitation, with this TPC signal being largest for the bare TiO_2. These data together indicate that the initial signal (darkest blue) in Figure 3.5A corresponds to the photoinduced absorbance of electrons in the conduction band of TiO_2, with the decay of this signal on the ms timescale resulting primarily from electron extraction to the external circuit (Figure 3.5D, step 6). Taking into account that the initial state of the catalyst anchored to TiO_2 is Co^{III}, the reduction in amplitude of this signal relative to bare TiO_2 can be assigned to the reduction of Co^{III} to Co(R), which has been reported to be faster than microseconds (Figure 3.5D, step 4).[38] The reduction of this catalyst from Co^{III} to Co(R) is not expected to give a significant signal at 700 nm (Figures 3.1-2), consistent with the initial 700 nm signal being smaller in the presence of catalyst than for bare TiO_2. It is also apparent from Figure 3.5A that the Co(RR) signal (in lightest blue colour) decays within seconds, which is probably related to the reoxidation of Co(RR) to Co(R) (Figure 3.5D, step 7) by injecting electrons from the catalyst into either the conduction band of TiO_2 (observed experimentally as a TPC) or the electrolyte (*e.g.* products from the oxidation of TEOA or trace water). These data therefore indicate that, under this pulsed laser excitation, Co(R) progressively accumulates on TiO_2, resulting in the increasing observation of subsequent transient photoreduction of Co(R) to Co(RR), in agreement with Figure 3.4 above and the assignment in the preceding sub-section.

Moving forward from studying the accumulation of Co(R) at a fixed bias (−0.08 V *vs.* NHE), the accumulation of reduced species without any applied bias (*i.e.*, under open circuit conditions) was investigated, still retaining TEOA as hole scavenger. Applying a bias is an effective way to control the photoelectrode potential (as shown in Figures 3.4 and 3.5A) but is not typically employed in most analogous photocatalytic systems in the literature. In the experiments above, applying a bias at −0.08 V *vs*. NHE between the valence and the conduction band of TiO_2 has been used to minimise the electron density in the conduction band TiO_2, but does not significantly oxidise Co(R) due to the low conductivity of the TiO_2 at this near-midgap potential.[60, 61] Upon prolonged light excitation under open circuit conditions, the potential of the TiO_2-**CoP²** photoelectrode was observed to decrease from ca. −0.08 V to −0.88 V *vs.* NHE, indicative of increased electron accumulation in the electrode. Figure 3.5C shows time-resolved absorbance data at 700 nm as a function of pulsed irradiation time analogous to that in Figure 3.5A discussed above, but now under these open circuit conditions. It is apparent that these TA kinetics are very distinct from those observed under −0.08 V *vs.* NHE bias. The initial signal without applied bias (darkest blue, Figure 3.5C) is most comparable to the stabilised signal observed under applied bias (lightest blue, Figure 3.5A), and therefore assigned, as above, primarily to the reduction of Co(R) to Co(RR) (Figure 3.5D). This is indicative of a much quicker accumulation of Co(R) on the surface of TiO_2 under open circuit conditions, most likely resulting from the lack of electron extraction to the external circuit induced under bias. Under these open circuit conditions, the amplitude of the positive, long-lived TA signal at 700 nm decreases over consecutive

measurements and becomes increasingly negative at early timescales (~μs) (lightest blue in Figure 3.5C). A similar trend was observed when a set of fresh samples were excited with increasing pulse intensities (Figure 3.6A). Because Co(RR) is the species that absorbs the strongest at 700 nm compared to other catalyst species and TiO_2 electrons, the negative signal at early timescales is most likely due to a bleaching of the absorbance of this Co(RR) species (Figure 3.5D, steps 2-3). These data are thus compatible with the accumulation of Co(RR) at the TiO_2 surface under prolonged irradiation, consistent with the observed shift in open circuit potential to –0.88 V. Under these prolonged irradiation conditions, the negative initial signal can be assigned to rapid (< *μs*) oxidation of Co(RR) to Co(R) by valence band holes (*i.e.*, a charge recombination process), with the subsequent appearance at longer times of a positive signal assigned to overall net reduction of Co(R) to Co(RR) by electrons from the conduction band of TiO_2.

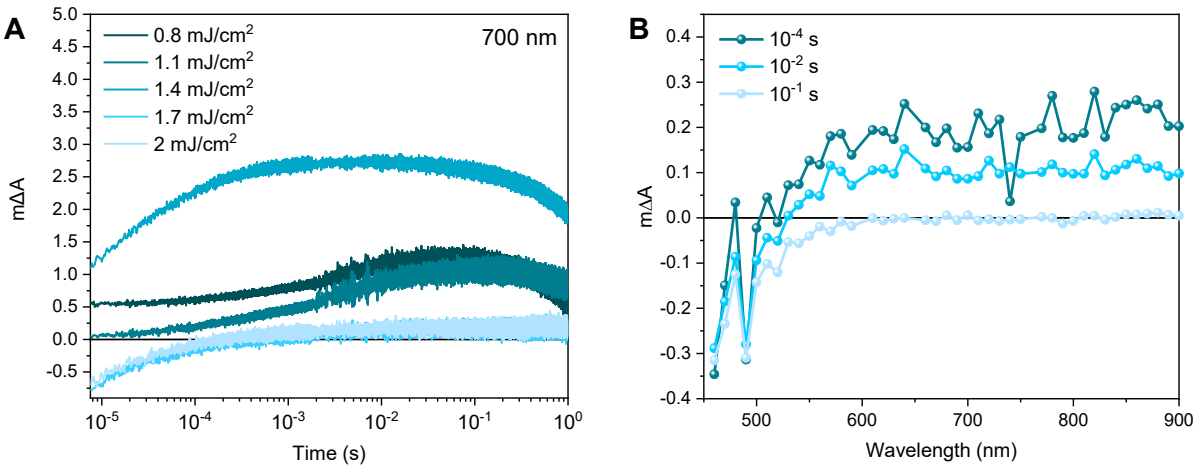

Figure 3.6. **(A)** Kinetics at 700 nm of TiO_2-**CoP²** in ACN 0.1 M $TBAPF_6$ with 0.1 M TEOA at different 355-nm excitation intensities (16 excitation shots averaged per measurement, 1 Hz) after 30 minutes in the dark. This Figure shows the 700-nm kinetics of fresh samples, where the initial oxidation state of the catalyst is Co^{III}. Under 0.8, 1.1 and 1.4 mJ/cm² excitation intensities, a positive signal corresponding to the Co(R)-to-Co(RR) reduction was observed, as assigned in the main text. Taking into account that each signal is the average of 16 laser pulses, this means that the photo-generated electrons reduce Co^{III} to Co(R), which accumulates between pulses, and Co(R) to Co(RR). At higher excitations intensities, however, the 700-nm signal changes radically. At high excitation intensities, Co(R) is likely to be fully reduced to Co(RR) with the first laser pulse. Co(RR) persists in the dark until the next pulse comes and it reacts with photo-generated holes in the valence band. Because Co(RR) is the species in the sample with the highest extinction coefficient at 700 nm, the bleach at 700-nm is therefore due to the recombination of Co(RR) accumulated at the TiO_2 surface with valence band holes. These kinetic changes cannot be due to catalyst degradation because the same amount of photons under −0.08 V *vs.* NHE bias leads to a much more robust signal at 700 nm (Figure 3.4A). **(B)** Transient absorption spectra of TiO_2-**CoP²** in ACN 0.1 M $TBAPF_6$ without TEOA after ~1.4 mJ/cm² 355-nm excitation, 0.8 Hz, at an applied potential of −0.08 V *vs.* NHE. In contrast to Figure 3.5C, with TEOA but without applied bias, the absence of TEOA under -0.02 V leads to a bleach peaking below 500 nm. As shown in Figures 3.2-3, Co(R) accumulates under −0.08 V *vs.* NHE and absorbs the strongest at ~470 nm in the 450-900 nm. Therefore, the bleach at 450-500 nm is most likely due to the reaction of accumulated Co(R) with photo-generated holes.

In contrast, a bleach at 450-500 nm is observed at μs under −0.08 V *vs.* NHE bias without TEOA (Figure 3.6B). Considering that at −0.08 V *vs.* NHE bias Co(R) accumulates (Figure 3.4) and that Co(R) has an absorbance peak at ~470 nm, the bleach at 450-700 nm can be assigned to the recombination of Co(R) with photo-generated holes when a bias is applied but no hole scavenger is added. Therefore, this proves that TEOA is necessary to scavenge holes, independently of the intra-bandgap applied bias, most likely because of the poor hole conductivity of the valence band of TiO_2. Furthermore, the data (summarised in Figure 3.7) indicate that both Co(R) and Co(RR) can recombine with photogenerated holes on < μs timescales, with the relative dominance of these two recombination pathways depending on which species accumulates under the conditions studied (*i.e.*, Co(R) at −0.08 V *vs.* NHE applied bias, and Co(RR) at open circuit potential).

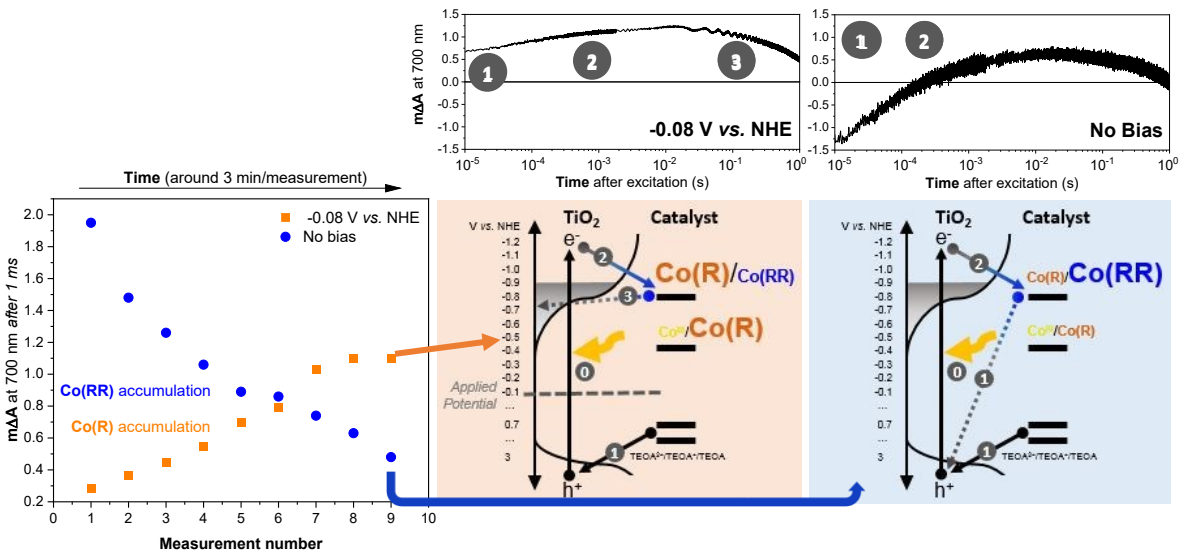

Figure 3.7. Illustration of the main accumulation and recombination processes observed in the data in Figure 3.5, where the kinetic traces shown here correspond to the *lightest-blue* kinetic signals with and without bias in Figure 3.5.

3.3.2.3. Kinetics at 700 nm

With the purpose to further analyse the impact of modulating the initial oxidation state of the catalyst on the observed transient kinetics, two different strategies were adopted: (i) the starting population of the catalyst was modulated by varying the applied potential while keeping the same excitation intensity, and (ii) the concentration of photogenerated electrons in the conduction band relative to the catalyst concentration was regulated by varying the excitation intensity while keeping a constant potential below the conduction band of TiO_2. Starting in the same conditions as in Figure 3.4 (*i.e.*, ~1.4 mJ/cm^2 under −0.08 V *vs.* NHE), with the catalyst in the Co(R) state as concluded above, first, the light excitation intensity was decreased and, second, a more reducing potential was applied. Figure 3.8A-B shows the effect of these changes on the transient absorption spectra and kinetics at 700 nm, compared to TiO_2 (Figure 3.8C), with full TA spectra in Figures 3.3B, 3.4A and 3.9.

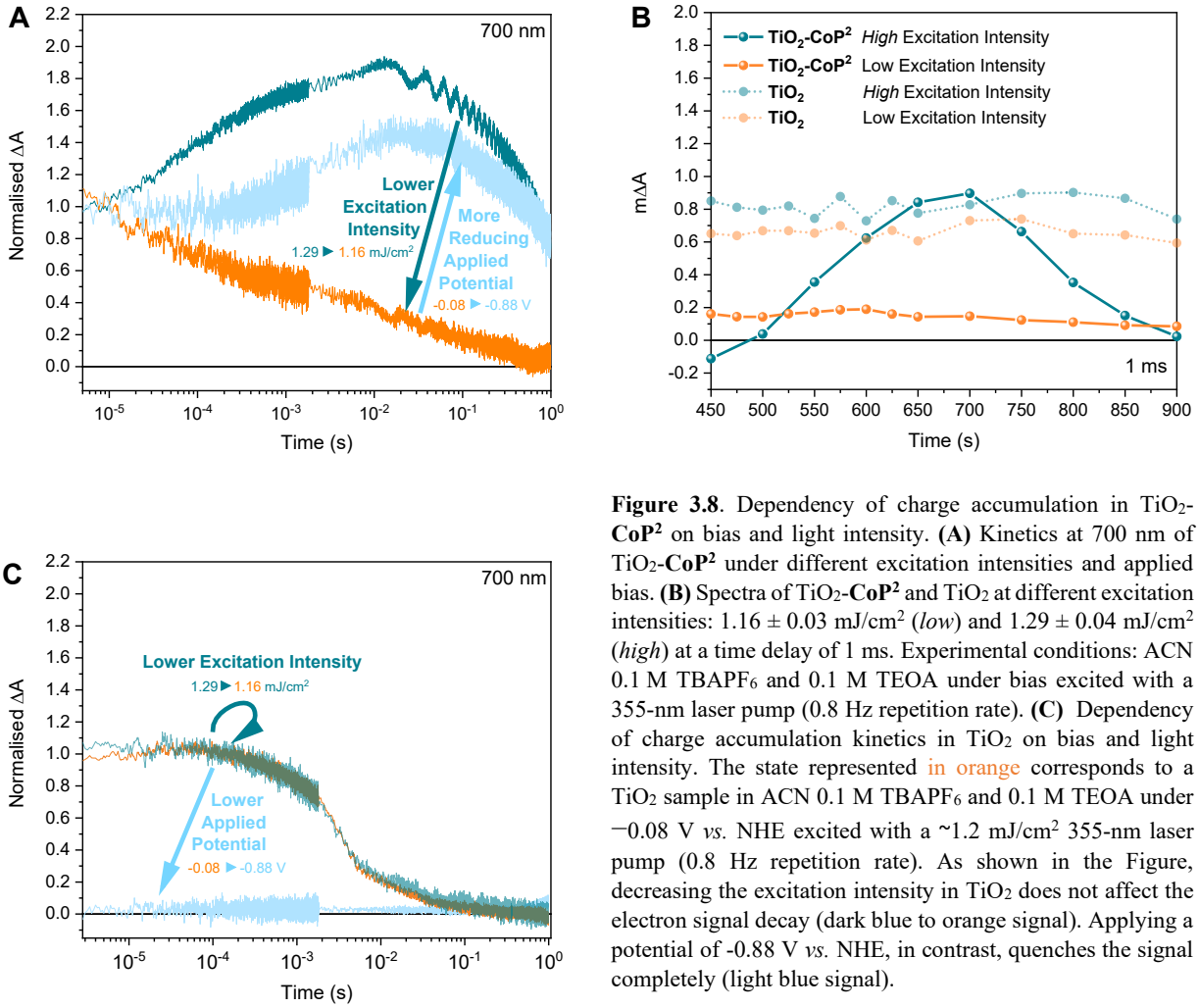

Figure 3.8. Dependency of charge accumulation in TiO_2-**CoP²** on bias and light intensity. **(A)** Kinetics at 700 nm of TiO_2-**CoP²** under different excitation intensities and applied bias. **(B)** Spectra of TiO_2-**CoP²** and TiO_2 at different excitation intensities: 1.16 ± 0.03 mJ/cm^2 (*low*) and 1.29 ± 0.04 mJ/cm^2 (*high*) at a time delay of 1 ms. Experimental conditions: ACN 0.1 M $TBAPF_6$ and 0.1 M TEOA under bias excited with a 355-nm laser pump (0.8 Hz repetition rate). **(C)** Dependency of charge accumulation kinetics in TiO_2 on bias and light intensity. The state represented in orange corresponds to a TiO_2 sample in ACN 0.1 M $TBAPF_6$ and 0.1 M TEOA under −0.08 V *vs.* NHE excited with a ~1.2 mJ/cm^2 355-nm laser pump (0.8 Hz repetition rate). As shown in the Figure, decreasing the excitation intensity in TiO_2 does not affect the electron signal decay (dark blue to orange signal). Applying a potential of -0.88 V *vs.* NHE, in contrast, quenches the signal completely (light blue signal).

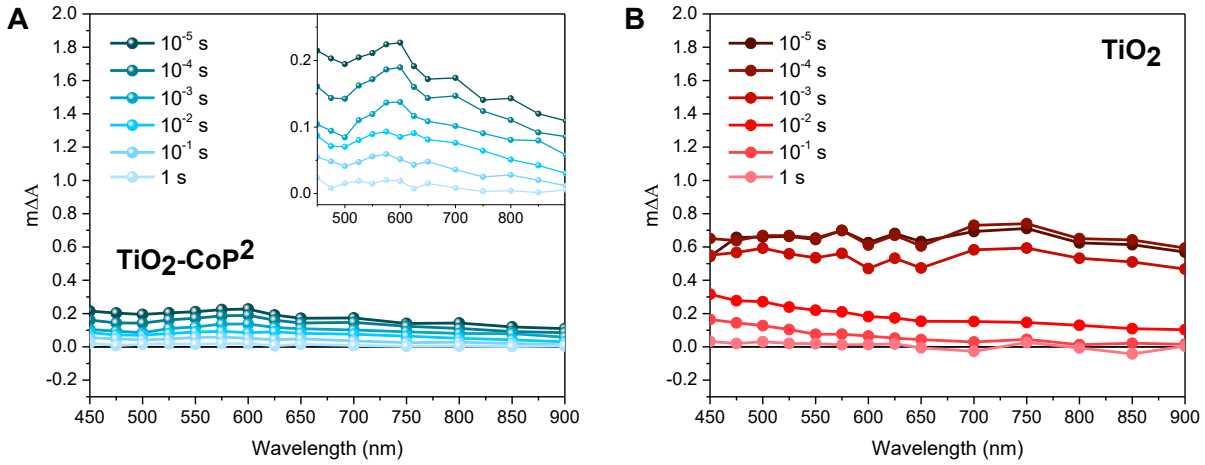

Figure 3.9. Transient absorption spectra of TiO_2-**CoP^2 (A)** and TiO_2 **(B)** in ACN 0.1 M TEOA 0.1 M $TBAPF_6$ at low 355-nm excitation intensities (1.16±0.03 J/cm^2, 0.8 Hz) under −0.08 V *vs.* NHE.

As is apparent in Figure 3.10A, as the laser intensity is reduced, there is a sharp change in kinetics around 1.2 mJ/cm^2, with Figure 3.8A showing data above and below this threshold ('high' and 'low' intensity excitation respectively). Above this threshold (high excitation), the transient absorbance signal of Co(R) to multi-reduced species Co(RR) is observed, apparent both in the kinetics at 700 nm (Figure 3.8A) and the spectrum at 1 ms peaking at 700 nm (Figure 3.8B). Below this threshold (low excitation), the amplitude of the 700 nm signal is much less intense and decays faster, comparable to the initial non-stabilised kinetics in Figure 3.5A assigned to TiO_2 electrons. This weaker, faster decaying signal is also assigned to electron signals of the TiO_2, as confirmed by the low excitation 1-ms spectrum in Figure 3.8B, where the absorbance feature at 700 nm assigned to Co(RR) is now absent, and instead a broad, featureless photoinduced absorbance is observed, similar to that of bare TiO_2 films. It is apparent that electrons which are photogenerated under these low-intensity conditions are thus not capable of reducing Co(R) to Co(RR), attributed to a lack of electron accumulation in TiO_2 under these conditions. Because TiO_2 has a distribution of tail states below the conduction band, these states that are likely to trap photo-generated electrons and limit charge transfer to the catalyst at low light intensities, as is discussed in more detail below.[62] This switch in transient kinetics from high to low excitation, turning off Co(R) reduction to Co(RR), was reversed by applying a more negative applied potential in order to fill up the trap states in the conduction band electrochemically (Figure 3.8A and 3.10B), with the kinetics at 700 nm under –0.88 V *vs.* NHE and low excitation conditions again being indicative of Co(R) reduction to Co(RR). These data illustrate that the accumulation of reduced catalyst species in this samples can be readily modulated by both the excitation intensity and applied bias, with resultant large changes in the observed electron transfer kinetics.

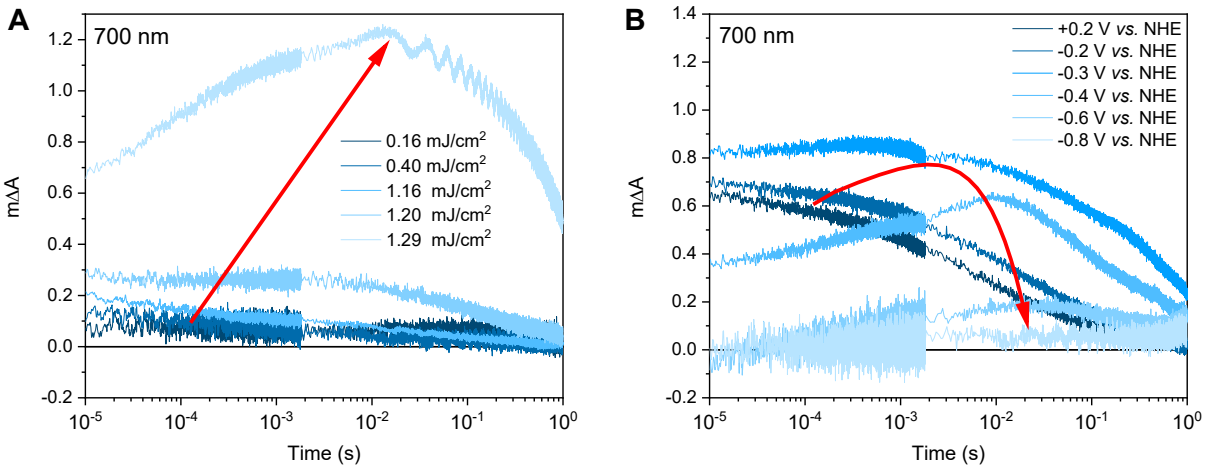

Figure 3.10. Dependency of the 700-nm kinetics in 2 different TiO_2-**CoP²** samples on **(A)** the excitation intensity (under −0.08 V vs NHE) and **(B)** the applied potential (with 1.16 mJ/cm² excitation). Repetition rate: 0.8 Hz.

3.3.2.4. Quantum Yield

Employing the transient data in Figure 3.8, the quantum efficiency for electron transfer from TiO_2 to Co(R) was calculated. Given that the time-resolved signal at 700 nm has been assigned to the one-electron reduction of Co(R) to Co(RR), the quantum yield of electron transfer from TiO_2 to the mono-reduced catalyst can be estimated from the maximum absorbance change at 700 nm (at ~10 ms from excitation), the incident laser pulse energy and the absorbance extinction coefficients at 700 nm deduced from the spectroelectrochemistry in the dark. In TiO_2-**CoP²**, assuming that the 700-nm TAS signal is only due to Co(RR) formed from Co(R) and electrons in the conduction band of TiO_2, the quantum yield of accumulative electron transfer to the catalyst at the point of maximum absorbance change is:

Equation 3.1

$$\frac{moles\ of\ Co(RR)\ formed}{moles\ of\ incident\ photons} = \frac{\frac{\Delta A_{700nm} - \Delta A_{700nm,-0.08\,V,1.16\,mJ/cm^2.}}{\varepsilon_{Co(RR)} - \varepsilon_{Co(R)}}}{(\frac{E_{pulse}}{h\frac{c}{\lambda}})/N}$$

Where $\Delta A_{700nm,max.}$ is the absorbance change at 700 nm 10 ms after excitation; $\Delta A_{700nm,-0.08V,\ 1.16mJ/cm2}$ is the absorbance change baseline due to electrons at 700 nm 10 ms after excitation with a 1.16 mJ/cm² pulse under −0.08 V *vs.* NHE; $\varepsilon_{Co(I)}$ and $\varepsilon_{Co(II)}$ are the absorbance coefficients of Co^{I} and Co^{II} respectively; E_{pulse} is the energy per laser pulse; h is the Planck constant; c is the speed of light; λ is the excitation wavelength; and N is the Avogadro number. The TA signal of bare TiO_2 at 1.16 mJ/cm² under −0.08 V *vs.* NHE, which corresponds to the absorbance of electrons in the conduction band of TiO_2, as discussed previously, was taken as baseline.

Table 3.1 shows the calculated apparent quantum yields as a function of reducing excitation intensities and bias, corresponding to the results in Figure 3.8. It is apparent that the quantum yield for Co(R) reduction under high excitation conditions and −0.08 V *vs.* NHE is remarkably high (44 %), indicative of high efficiency of this reaction. At low excitation conditions and −0.08 V *vs.* NHE, the efficiency of this reaction reduced to near zero. This efficiency is partially recovered at –0.88 V vs. NHE (22%). At this reducing potential, the quantum yield does not improve with increasing light intensity, being 0.06 ± 0.01 at 1.44 ± 0.03 mJ/cm^2, which is lower than under −0.08 V *vs.* NHE and indicates the saturation effects and / or the degradation of the reduced catalyst species under these reducing conditions.[30, 63] It was not possible to record time-resolved spectra at such reducing potentials due to the degradation of reduced species (within ~1 h), where the degradation of the catalyst is assumed when the catalyst signal at 700 nm is not observed any longer. These data emphasise the remarkable large dependence of efficiency of Co(R) reduction to measurement conditions.

Table 3.1. Apparent quantum yields of charge accumulation in **CoP^2** attached to TiO_2 after 355-nm excitation.

Conditions	Quantum Yield (*Co(R)→Co(RR)*) at $\Delta A_{700\ nm,max.}$
1.29 mJ/cm^2 *−0.08 V vs. NHE*	**44 ± 6 %**
1.16 mJ/cm^2 *−0.08 V vs. NHE*	**1 ± 6 %**
1.16 mJ/cm^2 *−0.88 V vs. NHE*	**22 ± 2 %**

3.3.3. Comparison with CO_2-reduction catalyst CotpyP

From all the results above, it was inferred that charge accumulation is highly dependent on the relative energy of photo-excited electrons in TiO_2 with respect to the potentials of **CoP²**'s redox transitions. In order to further investigate the effect of the redox potential position on charge accumulation, the multi-redox molecular catalyst **CotpyP**[40, 41], which is one of the state-of-the-art CO_2 catalysts[64] and has more negative reductive potentials than **CoP²**, was also studied on TiO_2 in the same aprotic and hole scavenging conditions as **CoP²** (*i.e.*, ACN and 0.1 M TEOA) (Figure 3.11A). The catalyst **CotpyP** was loaded on TiO_2 in a similar way as **CoP²** (see Section 3.2.3 above), and its redox potentials in acetonitrile were roughly estimated from cyclic voltammetries on ITO and TiO_2 (Figure 3.11C): $E_{1/2,\,Co(III/II)} \approx -0.78$ V *vs.* NHE and $E_{1/2,\,Co(II/I)} \approx -1.2$ V *vs.* NHE. The spectra of the different oxidation state species was studied by spectroelectrochemistry analogously to the CoP^2: the steady-state absorbance of TiO_2-**CotpyP** was measured at different applied potentials and two characteristic absorption spectra were identified at the two redox potentials, which were consequently assigned to the formation of Co^{II} and Co^{I} from Co^{III} (Figures 3.11C-D). As with **CoP²**, singly- and multi-reduced species of **CotpyP** were labelled as Co(R) and Co(RR) respectively, assuming Co^{III} as the starting oxidation state of the metal centre.

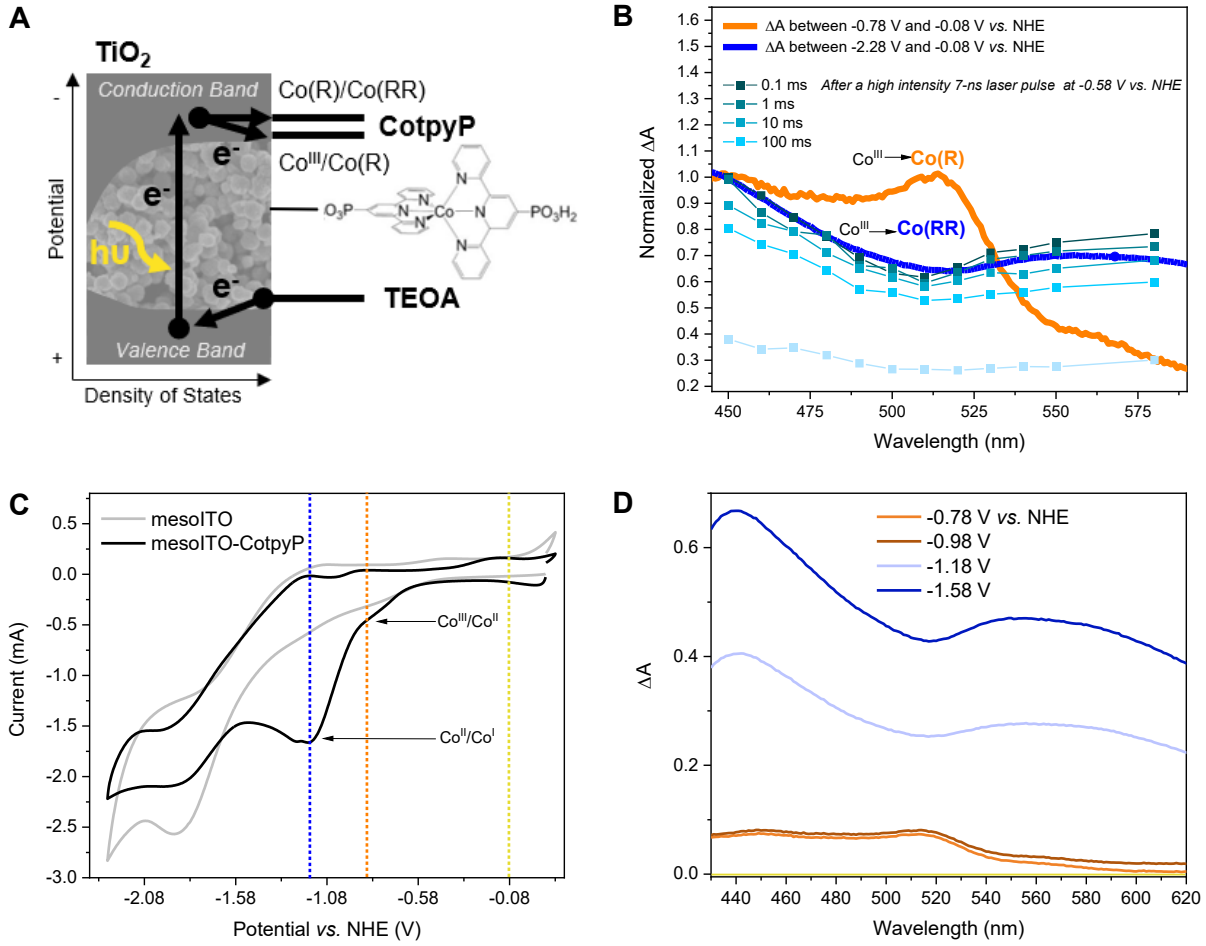

Figure 3.11. Transient and steady-state spectroelectrochemical characterization of the CO_2-reducing catalyst **CotpyP** on TiO_2. **(A)** Scheme of the photocatalytic system, where the arrows indicate the direction of electron transfers. **(B)** Comparison between photo-induced transient spectra (after ~1.4 mJ/cm^2 355-nm excitation with 0.8 Hz laser repetition rate under −0.58 V *vs.* NHE) and electrochemically induced steady-state spectra of TiO_2-**CotpyP**. **(C)** Cyclic voltammetry of **CotpyP** on mesoITO with a scan rate of 100 mV/s. **(D)** Steady-state absorbance difference of TiO_2-**CotpyP** under different applied potentials with respect to –0.08 V *vs*. NHE. All the experiments were done in in ACN 0.1 M $TBAPF_6$ and 0.1 M TEOA.

Photoinduced transient absorption was measured under similar conditions to those where the accumulation of Co(R) and the formation of Co(RR) are photo-induced in TiO_2-**CoP^2**, with ~1.4 mJ/cm^2 355 nm excitation both without bias and under –0.58 V *vs.* NHE, where the catalyst could not be electrochemically reduced. In contrast to TiO_2-**CoP^2**, the transient kinetics in photoexcited TiO_2-**CotpyP** were observed to be very similar both with and without bias (Figure 3.12). The transient spectrum was then matched with the electrochemically induced spectra, obtained in the dark following the same procedure detailed previously for **CoP^2**. The photoinduced transient absorbance overlaps with the electrochemically induced absorbance difference between −0.08 and −2.28 V *vs.* NHE in the dark, which

corresponds to the transition Co^{III} → Co(RR) (Figure 3.11B). Thus, upon light excitation under −0.58 V *vs.* NHE, the observed signal is indicative of two consecutive electron transfers which take place before ~15 microseconds from TiO_2 to the **CotpyP**, reducing Co^{III} to Co(RR). Following the same procedure as with **CoP^2** (see Section 3.3.2.4), the apparent quantum yield for the formation of multi-reduced specie from Co^{III} is 20±10%. In TiO_2-**CotpyP**, the optical signals and the absorbance coefficients considered in the calculation of the quantum efficiency (Equation 3.1) correspond to $\lambda = 550\ nm$ and $t = 12\ \mu s$. In this case, because the signal is assigned to a double reduction ($Co^{III} \rightarrow Co(RR)$), the quantum efficiency is multiplied by 2 (two moles of photons is needed per each mole of Co(RR)).

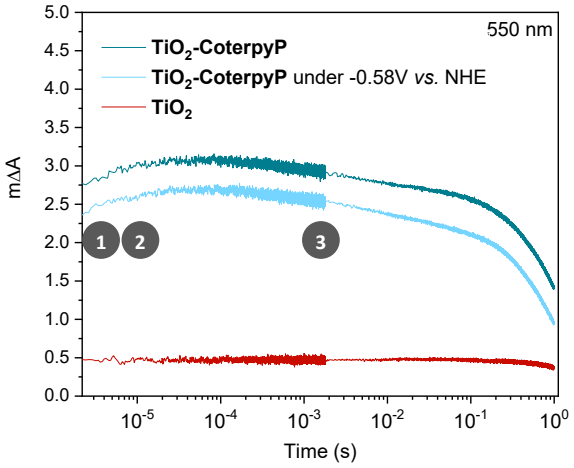

Figure 3.12. Absorbance kinetics at 550 nm of TiO_2-**CotpyP** and TiO_2 in ACN 0.1 M $TBAPF_6$ 0.1 M TEOA after ~1.4 mJ/cm^2 355-nm excitation with 0.8 Hz laser repetition rate. The different processes taking place at different times are (1) the scavenging of holes by TEOA, (2) the transfer of electrons from the TiO_2 conduction band to the catalyst, and (3) the back electron transfer from the catalyst to the TiO_2, as illustrated in Figure 3.17.

This contrasts with TiO_2-**CoP^2** under bias and light excitation, where Co(R) is observed to accumulate during the TA measurements. This difference in charge accumulation can be attributed to the relative positions of the redox states of these catalysts with respect to the conduction band of TiO_2. The observation of two electron transfers to **CotpyP** is particularly striking given its negative reduction potentials, as is discussed further below. In any case, it is apparent that the more negative reduction potentials for **CotpyP** relative to **CoP^2** prevent the steady-state accumulation of reduced catalyst states, consistent with the analyses of **CoP^2** above.

3.4. Discussion

In photodriven catalysis, multi-redox catalysis is particularly challenging due to the need to drive multiple, and typically increasingly energetically challenging, reduction/oxidation steps. In such studies, the accumulation of intermediate oxidation states of the catalyst is often needed, but can result in recombination losses from subsequent photoexcitations. In this study of catalyst functionalised on TiO_2 films, a hole scavenger is used to remove photogenerated holes and an aprotic solvent to minimise the presence of water and focus on the accumulation of different reduced species in the absence of significant proton reduction catalysis. It is shown that varying the applied potential and / or the light intensity are both effective approaches to control the electron density in TiO_2 necessary to induce electron transfer to the catalyst. This thereby regulates both the oxidation state of the catalyst accumulated under prolonged irradiation, and the observed electron transfer kinetics. By using this approach, the results suggest that it is possible to observe selectively electron transfer to reduced states of two different multi-redox molecular catalysts to aid the design of efficient electrode or photocatalytic systems employing TiO_2 as photoabsorber.

Molecular catalysts exhibit well defined energy states and redox potentials.[65] In contrast, TiO_2 exhibits not only a conduction and valence band separated by a bandgap but also a significant density of tail states extending from the band edges into its bandgap,[56, 57] as presented schematically in Figure 3.13. This is observed in the control spectroelectrochemical data for TiO_2 in Figure 3.2C and illustrated in Figure 3.3A. Consideration of charge trapping into, and accumulation in these tail states has been shown to be critical to understanding the function of dye sensitised solar cells, DSSCs,[46, 62, 66-72] and is also likely to be critical to understanding photocatalytic systems employing TiO_2. For example, trap filling resulting from increased electron accumulation in the conduction band tail states has been shown to have multiple impacts, including increasing effective electron mobility by orders of magnitude, and also increasing the energy, and therefore reactivity, of accumulated electrons.[39, 46, 66-68, 72, 73] In addition, the energy of the conduction band states and, thus, that of accumulated electrons varies with pH and the presence of cations;[70, 74-76] in particular, the flat-band potentials of TiO_2 in water compared to acetonitrile differ by around 1.2 V *vs.* NHE, leading to a more pronounced charge trapping and energy loss in water.[76, 77] Therefore, following the initial generation of relatively energetic electrons by UV excitation, the subsequent relaxing / trapping of electrons on ps-ns timescales will result in a progressive loss of electron energy, which will also result in time dependence of electron reactivity following photoexcitation.

For the proton reduction catalyst **CoP²**, the time-resolved absorption studies indicate that, upon excitation, different reduced states of the catalyst can accumulate on the surface of TiO_2, which depends on whether an external bias is applied or not (Figure 3.5). Most of the experiments in this study were carried out under intra-bandgap applied bias, which is distinct from the open circuit conditions present in

most photocatalytic systems employing hole / electron scavengers. However, as shown herein, this allows a better control of the oxidation state of the system for functional characterisation. Under −0.08 V *vs.* NHE (an intra-bandgap potential), the mono-reduced species Co(R) was seen to accumulate under irradiation. This is consistent with the energetic alignment of the Co^{III}/Co(R) redox couple with respect to the distribution of tail states in TiO_2's conduction band, as illustrated in Figure 3.13. Because Co(R) accumulates at −0.08 V *vs.* NHE, subsequent light excitation leads to the reduction of Co(R) to Co(RR), which corresponds to the signal observed with TA (Figure 3.4). The kinetic signal assigned to the formation of Co(RR) peaks at around 1 ms and decays from milliseconds to seconds, the latter being compatible with the back electron transfer from the catalyst to TiO_2 and its equilibration with the applied potential. Under this bias condition, Co(R) accumulation and subsequent reduction to Co(RR) is only observed after relatively high-intensity photoexcitation, whilst Co^{III} reduction to Co(R) is observed under low-intensity irradiation (Figure 3.8), as illustrated in Figure 3.13. This behaviour is assigned to photoinduced electron accumulation both on the catalyst (as Co(R) states) and in TiO_2 conduction band tail states.[56, 57] Long lived Co(RR) species are only obtained upon irradiation in the presence of such electron accumulation. This was further confirmed by applying a more negative potential (−0.88 V *vs.* NHE). At this reducing potential, all the catalyst molecules on the electrode surface are electrochemically forced into the mono-reduced state Co(R) and the tail states in TiO_2 are filled up, facilitating further reduction to Co(RR) upon excitation, independent of irradiation intensity. The formation of multi-reduced species above the conduction band, necessary for catalysis, is therefore highly sensitive on the accumulation of electrons, which depends on the excitation light intensity and the electrochemical potential and highlights the key importance of these two parameters in photocatalysis.

For the proton reduction catalyst **CoP^2**, the time-resolved absorption studies indicate that, upon excitation, different reduced states of the catalyst can accumulate on the surface of TiO_2, depending upon whether an external bias is applied or not (Figure 3.5). Most of the experiments in this study were carried out under intra-bandgap applied bias, which is distinct from the open circuit conditions present in most photocatalytic systems employing hole / electron scavengers. As shown herein, this allows a better control of the oxidation state of the system for functional characterisation. Under −0.08 V *vs.* NHE (an intra-bandgap potential), the mono-reduced species Co(R) was seen to accumulate under irradiation. This is consistent with the energetic alignment of the Co^{III}/Co(R) redox couple with respect to the valence band of TiO_2 and the distribution of tail states in the TiO_2's conduction band, as illustrated in Figure 3.13. The low conductivity of TiO_2 at this near midgap potential and the bulkiness of the catalyst probably prevents Co(R) from being electrochemically oxidised to Co^{III} by either the TiO_2 or charge transfer between neighbouring catalyst molecules. Because Co(R) accumulates at −0.08 V *vs.* NHE, subsequent light excitation leads to the reduction of Co(R) to Co(RR), which corresponds to the signal observed with TA (Figure 3.4). The kinetic signal assigned to the formation of Co(RR) peaks at around 1 ms and decays from milliseconds to seconds, the latter being compatible with the back electron transfer from the catalyst

to TiO_2 and its equilibration with the applied potential. Under this bias condition, Co(R) accumulation and subsequent reduction to Co(RR) is only observed after relatively high-intensity photoexcitation, whilst Co^{III} reduction to Co(R) is observed under low-intensity irradiation (Figure 3.8), as shown in Figure 3.13. This behaviour is assigned to photoinduced electron accumulation both on the catalyst (as Co(R) states) and in TiO_2 conduction band tail states.[56, 57] Long lived Co(RR) species are only obtained upon irradiation in the presence of such electron accumulation. This was further confirmed by applying a more negative potential (−0.88 V *vs.* NHE). At this reducing potentials, all the catalyst molecules on the electrode surface are electrochemically forced in the dark into the mono-reduced state Co(R) and the tail states in TiO_2 are filled up, facilitating further reduction to Co(RR) upon excitation, independent of irradiation intensity. The formation of multi-reduced species, necessary for catalysis, is therefore enhanced at high light intensity suggesting that such systems may be particularly effective under concentrated sunlight.

In contrast to applying a bias, under open circuit conditions with light irradiation, multi-reduced species Co(RR) were observed to accumulate, and the degree of accumulation depended on the presence of the hole scavenger. These conditions are more relevant for comparison to analogous photocatalytic systems reported for water oxidation[67, 78-81], water reduction[82-86] or CO_2 reduction[25, 87, 88], mostly investigated without any bias being applied electrochemically. In many cases, the catalytic activity of molecular catalysts assembled on photosensitised electrodes has been reported to be better than when the components are separately dissolved in solution.[30, 67, 78, 79, 81, 82, 85, 86, 89, 90] From the above results, the improved performance of assembled systems can be attributed, at least in part, to the ability of TiO_2 to accumulate long lived electrons, which is an advantage that most semiconductor oxides may have when used as photosensitisers compared to molecular dyes. Furthermore, this evidence is in accordance with that reported on dye-sensitised solar cells and electrodes. For these, the recombination kinetics between injected electrons in the conduction band of TiO_2 and a photo-oxidised dye at the surface crucially depends on the electron density in TiO_2, which in turn is related to light excitation energy and the tail-state distribution in the material.[46, 62, 67-69, 71, 72] The trap state distribution limits electron transfer to the semiconductor surface, which is an undesired process in dye-sensitised solar cells, but it is an essential step in photocatalysis.

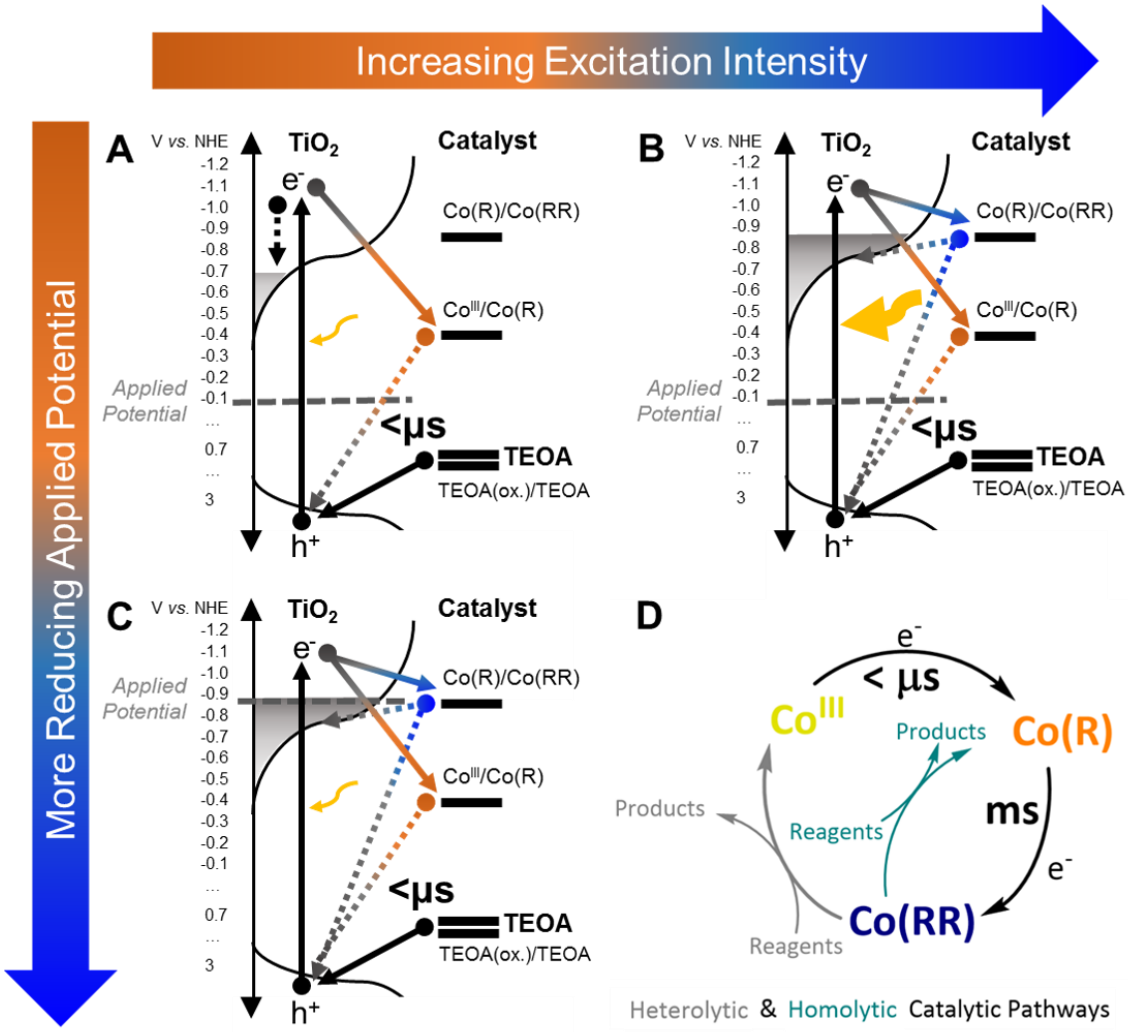

Figure 3.13. Scheme illustrating the processes occurring in TiO_2-**CoP²** at different excitation intensities and applied potentials. Representation of TiO_2-**CoP²** in ACN 0.1 M $TBAPF_6$ and 0.1 M TEOA **(A)** under −0.08 V *vs.* NHE excited with a ~1.2 mJ/cm² 355-nm laser pump (0.8 Hz repetition rate), **(B)** after increasing the excitation intensity by ~200 mJ/cm², and **(C)** after decreasing the potential to −0.88 V *vs.* NHE. **(D)** Simplified scheme of the catalytic mechanism and its timescales, where Co^{III} is the initial catalyst state (with an oxidation number of 3), *Co(R)* stands for mono-reduced catalyst intermediates, and *Co(RR)* corresponds to multi-reduced catalyst species. The arrows in A-C indicate the direction of electron transfers.

Compared to the catalyst **CoP²**, singly-reduced species of the CO_2-reduction catalyst **CotpyP** on TiO_2 do not build up at the surface under intra-bandgap bias even upon high-intensity excitation. In contrast, a double electron transfer is observed to take place from the semiconductor to the molecular catalyst within microseconds under light excitation (Figure 3.12 and scheme in Figure 3.14). The double reduction is most likely due to the initially photoexcited electrons in TiO_2 having relatively high energy (due to the 355 nm excitation employed), with enough driving force to

drive these reductions. This rapid double reduction of **CotpyP**, which was not observed for **CoP²**, could be attributed to direct bonding of the phosphonate binding group to the conjugated terpyridine ligand in **CotpyP**; in contrast for **CoP²**, the phosphonate group is spatially separated from the redox active centre, significantly reducing the electronic coupling for electron transfer from the TiO_2 surface.[39] This is also in accordance with the observations above on TiO_2-**CoP²** under the same high excitation intensity (Figure 3.8), where it is observed that TiO_2 has the ability to transfer electrons to catalyst states above the conduction band when sub-bandgap trap states are filled up. In contrast to **CoP²**, no reduced **CotpyP** species were observed to accumulate on TiO_2-**CotpyP** films after excitation, attributed to **CotpyP** having more reducing potentials than **CoP²**. Once doubly reduced by photoexcitation, **CotpyP**(RR) is reoxidised to **CotpyP** within 1 s, either by reduction of the electrolyte or by back electron transfer to the TiO_2 CB. The CO_2 reduction efficiency of catalyst-semiconductor assemblies is usually related to the high overpotential of the catalyst, which reduces the driving force for electron transfer from the semiconductor to the catalyst, and relates well to the low electron transfer quantum efficiency calculated for the double photoreduction of **CotpyP**.[40, 41, 87, 88] Consequently, the above results for **CotpyP** on TiO_2 indicate that CO_2 reduction activity may be limited by the efficiency of the initial photoreduction, and also by the lack of accumulation of reduced species, caused by back electron transfer from the catalyst to the semiconductor as the catalyst and semiconductor Fermi levels equilibrate.

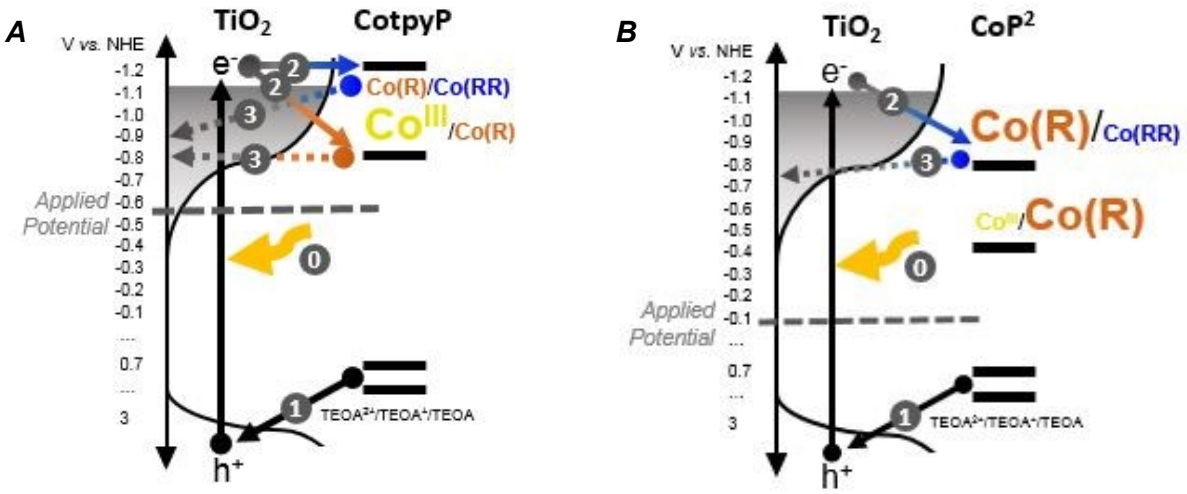

Figure 3.14. Illustration of the main electron transfer processes taking place in **(A)** TiO_2-**CotpyP** and **(B)** TiO^2-**CoP²** under intra-bandgap bias after exciting TiO_2 with high light intensities. The timescale of steps 1-3 is shown in Figures 3.12 and 3.7 respectively.

A further implication of the negative potential of reduced catalyst species is their reactivity. Reduced catalyst species can undergo irreversible degradation, which was detected in the study herein for both catalysts under highly reducing applied biases following the disappearance of the well-defined Co(RR) signal. This is in agreement with previous experimental and theoretical studies,[39, 62] where it was observed that, when the **CoP²** catalyst is in its Co^{I} state (included herein within the label Co(RR)), it is more likely to degrade. Secondly, the data indicate that doubly-reduced species Co(RR) can recombine with photo-generated holes in the valence band of TiO_2 faster than microseconds and can inject electrons back to the conduction band in milliseconds. Similar biphasic recombination kinetics have also been reported by Reynal *et al.* for TiO_2-**CoP²** in an aqueous solution.[38, 39] These Co(RR) species recombine with photogenerated holes faster than microseconds (detected as a strong bleach signal at 700 nm formed on sub-microsecond timescales in Figures 3.5C and 3.7A). On slower timescales, Co(RR) can also transfer electrons back to the conduction band of the semiconductor or the electrolyte shortly after being formed. On the other hand, Co(R) species also recombine with valence band holes, as observed from the lower amplitude at 700 nm of fresh TiO_2-**CoP²** samples (Figure 3.5A) with respect to the corresponding signal in TiO_2 under bias (Figure 3.3B), and from the bleach at 450-500 nm when no TEOA is used under −0.08 V *vs.* NHE (Figure 3.7B). This evidence is in agreement with the recombination of photogenerated charges in previous literature on inorganic-organic photochemical systems or molecular donor-acceptor dyads.[24, 73, 81, 90, 91] In the photo(electro)catalytic systems studied herein, formed by molecular catalysts attached on mesoporous TiO_2 films working as photoabsorber material, recombination of reduced catalyst species with valence band holes is at least three orders of magnitude faster than electron transfer to the catalyst and it is therefore expected to be one of the main causes of solar-to-hydrogen efficiency loss. The efficiency loss due to recombination despite the presence of a sacrificial electron donor might be related to a low accessibility of the sacrificial donor to the TiO_2 surface, which has been measured to have a high catalyst surface coverage.

The slow formation of multi-reduced species Co(RR) in TiO_2-**CoP²** (Figure 3.8A) occurs in hundreds of microseconds to milliseconds, a similar timescale as proton diffusion and hydrogen evolution.[8, 30, 77] This difference in the kinetics of multi-reduced species to the formation of singly-reduced species could be explained by the smaller driving force of the 2nd electron transfer and a larger reorganisation energy. The timescale where the Co(RR) formation signal reaches its maximum (~10 ms) is comparable to that of the slowest step of water oxidation in the Photosystem II (PSII) in natural photosynthesis systems. The charge accumulation kinetics of molecular catalysts is interpreted by taking the oxygen evolution cluster (OEC) in PSII as a blue print, where the enzymatic scaffold plays a crucial role protecting the metal active site from unwanted reactions and substrates and stabilising charges through proton-coupled reactions, hydrogen bonds and van-der-Waals interactions. In the case of the OEC in PSII, the first step is known to be the fastest step (<μs), the second and third occur in microseconds, while the last one is the slowest with lifetimes of milliseconds.[13-16 10-12] Taking into account the similarities with PSII, it

could be hypothesized that the slow kinetics of consecutive electron transfers compared to the first electron transfer in both **CoP^2** and **CotpyP** might minimise the time the highly reactive and unstable intermediates (*i.e.*, Co(RR) species) are exposed to the solution, hence decreasing the probability of catalyst degradation. In artificial catalysts as in PSII, an optimal synchronisation between charge transfer and substrate diffusion may therefore minimise the exposure of reactive species and improve the overall catalytic performance.

3.5. Conclusions

Transient absorption spectroscopy and steady-state spectroelectrochemical techniques were employed to study the kinetics of photogenerated electrons in molecular catalyst/TiO_2 photo(electro)catalytic systems for proton and CO_2 reduction. Consecutive electron transfers from the TiO_2 are observed to induce charge accumulation in the catalyst in the form of multi-reduced species. The oxidation state of the catalyst under steady-state irradiation conditions can be controlled by regulating the applied bias and the light intensity. In aprotic solvents and under illumination, in the proton reduction system TiO_2-**CoP^2**, different singly- or multi-reduced species accumulate on TiO_2 over time either with or without applied bias, depending on the Fermi level of the semiconductor. In contrast, long-term charge accumulation in acetonitrile was not observed in the CO_2-reduction catalyst **CotpyP** on TiO_2, which has more reducing potentials, attributed to back electron transfer to the conduction band of TiO_2. Charge transfer to the catalyst **CoP^2** was shown to depend on the electron density of TiO_2 and tail states filling, while multi-reduced catalyst species are observed to be formed on slower timescales than mono-reduced species. Because multi-redox charge transfer can be slow, both the ease of TiO_2 to accumulate electrons and the accumulation of singly-reduced species are fundamental to form multi-reduced species. However, recombination of such reduced species with both conduction band and valence band states directly competes with charge accumulation and it is likely to severely limit multi-redox catalysis in such systems, as it was shown for both **CoP^2** and the CO_2-reduction catalyst **CotpyP**. Thus, because of the contrast between the ability to retain electrons in the conduction band of TiO_2 and limitations in hole scavenging and recombination, when systems based on molecular catalysts attached to TiO_2 are used as photoelectrodes, interfaces need to be rectifying to block valence band hole recombination in order to allow charge accumulation at the catalyst.

3.6. References

1. N. M. Muresan, J. Willkomm, D. Mersch, Y. Vaynzof and E. Reisner, *Angew. Chem. Int.*, 2012, **51**, 12749-12753.
2. J. L. Dempsey, B. S. Brunschwig, J. R. Winkler and H. B. Gray, *Acc. Chem. Res.*, 2005, **42**, 1995-2004.
3. M. R. Scherer, N. M. Muresan, U. Steiner and E. Reisner, *Chem. Commun.*, 2013, **49**, 10453-10455.
4. K. E. Dalle, J. Warnan, J. J. Leung, B. Reuillard, I. S. Karmel and E. Reisner, *Chem. Rev.*, 2019, **119**, 2752-2875.
5. S. Wang, A. Aster, M. Mirmohades, R. Lomoth and L. Hammarström, *Inorg. Chem.*, 2018, **57**, 768-776.
6. M. Mirmohades, S. Pullen, M. Stein, S. Maji, S. Ott, L. Hammarström and R. Lomoth, *J. Am. Chem. Soc.*, 2014, **136**, 17366-17369.
7. C. Costentin and J.-M. Savéant, *ChemElectroChem*, 2014, **1**, 1226-1236.
8. V. Artero and J. M. Savéant, *Energy Environ. Sci.*, 2014, **7**, 3808-3814.
9. L. Duan, F. Bozoglian, S. Mandal, B. Stewart, T. Privalov, A. Llobet and L. Sun, *Nat. Chem.*, 2012, **4**, 418-423.
10. J. Barber, *Chem. Soc. Rev.* , 2009, **38**, 185–196.
11. F. A. Armstrong, *Philos. Trans. R. Soc. Lond. B Biol. Sci.*, 2008, **363**, 1263-1270; discussion 1270.
12. F. A. Armstrong and J. Hirst, *Proc. Natl. Acad. Sci. U. S. A.*, 2011, **108**, 14049-14054.
13. N. Cox and J. Messinger, *Biochim. Biophys. Acta*, 2013, **1827**, 1020-1030.
14. M. Karge, K.-D. Irrgang and G. Renger, *Biochemistry*, 1997, **36**, 8904-8913.
15. G. Renger, *Photosynth. Res.*, 2007, **92**, 407-425.
16. G. Renger, *J. Photochem. Photobiol. B*, 2011, **104**, 35-43.
17. H. Y. Chen and S. Ardo, *Nat Chem*, 2018, **10**, 17-23.
18. S. Ardo, D. Achey, A. J. Morris, M. Abrahamsson and G. J. Meyer, *J. Am. Chem. Soc.*, 2011, **133**, 16572-16580.
19. V. Saavedra Becerril, E. Sundin and M. Abrahamsson, *J. Phys. Chem. C*, 2018, **122**, 25822-25828.
20. W. Song, A. Ito, R. A. Binstead, K. Hanson, H. Luo, M. K. Brennaman, J. J. Concepcion and T. J. Meyer, *J. Am. Chem. Soc.*, 2013, **135**, 11587-11594.
21. S. Karlsson, J. Boixel, Y. Pellegrin, E. Blart, H.-C. Becker, F. Odobel and L. Hammarström, *J. Am. Chem. Soc.*, 2010, **132**, 17977–17979.
22. K. J. Elliott, A. Harriman, L. Le Pleux, Y. Pellegrin, E. Blart, C. R. Mayer and F. Odobel, *Phys. Chem. Chem. Phys.*, 2009, **11**, 8767-8773.
23. L. Hammarström, *Acc. Chem. Res.*, 2015, **48**, 840-850.
24. M. P. O'Neil, M. P. Niemczyk, W. A. Svec, D. Gosztola, G. L. Gaines III and M. R. Wasielewski, *Science*, 1992, **257**, 63-65.
25. T. E. Rosser and E. Reisner, *ACS Catal.*, 2017, **7**, 3131-3141.
26. F. Lakadamyali, A. Reynal, M. Kato, J. R. Durrant and E. Reisner, *Chem. Eur. J.*, 2012, **18**, 15464-15475.
27. F. Lakadamyali and E. Reisner, *Chem. Commun.*, 2011, **47**, 1695-1697.
28. Y. Pellegrin and F. Odobel, *C. R. Chim.*, 2017, **20**, 283-295.
29. M. Razavet, V. Artero and M. Fontecave, *Inorg. Chem.*, 2005, **44**, 4786-4795.
30. V. Artero, M. Chavarot-Kerlidou and M. Fontecave, *Angew. Chem. Int.*, 2011, **50**, 7238-7266.
31. J. Willkomm, N. M. Muresan and E. Reisner, *Chem. Sci.*, 2015, **6**, 2727-2736.
32. P. A. Jacques, V. Artero, J. Pecaut and M. Fontecave, *Proc. Natl. Acad. Sci. U. S. A.*, 2009, **106**, 20627-20632.
33. N. Kaeffer, M. Chavarot-Kerlidou and V. Artero, *Acc. Chem. Res.*, 2015, **48**, 1286-1295.
34. A. Bhattacharjee, M. Chavarot-Kerlidou, J. L. Dempsey, H. B. Gray, E. Fujita, J. T. Muckerman, M. Fontecave, V. Artero, G. M. Arantes and M. J. Field, *ChemPhysChem*, 2014, **15**, 2951-2958.
35. X. Hu, B. S. Brunschwig and J. C. Peters, *J. Am. Chem. Soc.*, 2007, **129**, 8988-8998.

36. T. Lazarides, T. McCormick, P. Du, G. Luo, B. Lindley and R. Eisenberg, *J. Am. Chem. Soc.*, 2009, **131**, 9192-9194.
37. P. Du, J. Schneider, G. Luo, W. W. Brennessel and R. Eisenberg, *Inorg. Chem.*, 2009, **48**, 4952-4962.
38. A. Reynal, F. Lakadamyali, M. A. Gross, E. Reisner and J. R. Durrant, *Energy Environ. Sci.*, 2013, **6**, 3291.
39. A. Reynal, J. Willkomm, N. M. Muresan, F. Lakadamyali, M. Planells, E. Reisner and J. R. Durrant, *Chem. Commun.*, 2014, **50**, 12768-12771.
40. J. J. Leung, J. Warnan, K. H. Ly, N. Heidary, D. H. Nam, M. F. Kuehnel and E. Reisner, *Nat. Catal.*, 2019, **2**, 354-365.
41. J. J. Leung, J. A. Vigil, J. Warnan, E. Edwardes Moore and E. Reisner, *Angew. Chem. Int.*, 2019, **58**, 7697-7701.
42. N. Elgrishi, M. B. Chambers, V. Artero and M. Fontecave, *Phys. Chem. Chem. Phys.*, 2014, **16**, 13635-13644.
43. X. Li, *Imperial College London*, 2012.
44. S. Ito, T. N. Murakami, P. Comte, P. Liska, C. Grätzel, M. K. Nazeeruddin and M. Grätzel, *Thin Solid Films*, 2008, **516**, 4613-4619.
45. C. J. Barbé, F. Arendse, P. Comte, M. Jirousek, F. Lenzmann, V. Shklover and M. Grätzel, *J. Am. Ceram. Soc.*, 1997, **80**, 3157–3171.
46. J. N. Clifford, E. Palomares, M. K. Nazeeruddin, R. Thampi, M. Grätzel and J. R. Durrant, *J. Am. Chem. Soc.*, 2004, **126**, 5670-5671.
47. J. J. Leung, J. Warnan, D. H. Nam, J. Z. Zhang, J. Willkomm and E. Reisner, *Chem. Sci.*, 2017, **8**, 5172-5180.
48. M. Schreier, J. Luo, P. Gao, T. Moehl, M. T. Mayer and M. Grätzel, *J. Am. Chem. Soc.*, 2016, **138**, 1938-1946.
49. M. Yamamoto, L. Wang, F. Li, T. Fukushima, K. Tanaka, L. Sun and H. Imahori, *Chem. Sci.*, 2016, **7**, 1430-1439.
50. P. G. Hoertz, Z. Chen, C. A. Kent and T. J. Meyer, *Inorg. Chem.*, 2010, **49**, 8179-8181.
51. Z. Chen, J. J. Concepcion, J. F. Hull, P. G. Hoertz and T. J. Meyer, *Dalton Trans.*, 2010, **39**, 6950-6952.
52. A. Bhattacharjee, M. Chavarot-Kerlidou, E. S. Andreiadis, M. Fontecave, M. J. Field and V. Artero, *Inorg. Chem.*, 2012, **51**, 7087-7093.
53. K. P. Jensen, *Inorg. Chem.*, 2008, **47**, 10357-10365.
54. S. Kossmann, B. Kirchner and F. Neese, *Mol. Phys.*, 2010, **105**, 2049-2071.
55. W. Q. Liu, T. Lei, S. Zhou, X. L. Yang, J. Li, B. Chen, J. Sivaguru, C. H. Tung and L. Z. Wu, *J. Am. Chem. Soc.*, 2019, **141**, 13941-13947.
56. R. L. Willis, C. Olson, B. O'Regan, T. Lutz, J. Nelson and J. R. Durrant, *J. Phys. Chem. B*, 2002, **106**, 7605-7613.
57. J. Nelson, *Phys. Rev. B*, 1999, **59**, 15374.
58. J. Tang, J. R. Durrant and D. R. Klug, *J. Am. Chem. Soc.*, 2008, **130**, 13885–13891.
59. Y. Tamaki, A. Furube, M. Murai, K. Hara, R. Katoh and M. Tachiya, *Phys. Chem. Chem. Phys.*, 2007, **9**, 1453-1460.
60. K. Yim, Y. Youn, M. Lee, D. Yoo, J. Lee, S. H. Cho and S. Han, *Npj Comput. Mater.*, 2018, **4**, 1-7.
61. S. Lany, *J. Phys.: Condens. Matter* 2015, **27**, 1-36.
62. J. R. Durrant, S. A. Haque and E. Palomares, *Coord. Chem. Rev.*, 2004, **248**, 1247-1257.
63. N. Kaeffer, A. Morozan, J. Fize, E. Martinez, L. Guetaz and V. Artero, *ACS Catal.*, 2016, **6**, 3727-3737.
64. E. Boutin, L. Merakeb, B. Ma, B. Boudy, M. Wang, J. Bonin, E. Anxolabéhère-Mallart and M. Robert, *Chem. Soc. Rev.*, 2020, **49**, 5772-5809.
65. Atkins' Physical Chemistry, P. Atkins and J. de Paula, *Oxford University Press*, 2014, 10th edition.
66. J. N. Clifford, E. Palomares, M. K. Nazeeruddin, M. Grätzel, J. Nelson, X. Li, N. J. Long and J. R. Durrant, *J. Am. Chem. Soc.*, 2004, **126**, 5225-5233.
67. G. J. Meyer, *Inorg Chem*, 2005, **44**, 6852-6864.

68. T. J. Meyer, G. J. Meyer, B. W. Pfennig, J. R. Schoonover, C. J. Timpson, J. F. Wall, C. Kobusch, X. Chen, B. M. Peek, C. G. Wall, W. Ou, B. W. Erickson and C. A. Bignozzi, *Inorg. Chem.*, 2002, **33**, 3952-3964.
69. S. A. Haque, S. Handa, K. Peter, E. Palomares, M. Thelakkat and J. R. Durrant, *Angew. Chem. Int.*, 2005, **44**, 5740-5744.
70. E. Palomares, J. N. Clifford, S. A. Haque, T. Lutz and J. R. Durrant, *J. Am. Chem. Soc.*, 2003, **125**, 475-482.
71. S. E. Koops, B. C. O'Regan, P. R. F. Barnes and J. R. Durrant, *J. Am. Chem. Soc.*, 2009, **131**.
72. D. F. Watson and G. J. Meyer, *Annu. Rev. Phys. Chem.*, 2005, **56**, 119-156.
73. S. A. Haque, Y. Tachibana, D. R. Klug and J. R. Durrant, *J. Phys. Chem. B* 1998, **102**, 1745-1749.
74. B. Enright, G. Redmond and D. Fitzmaurice, *J. Phys. Chem. B*, 1994, **98**, 6195-6200.
75. C. R. a. D. Fitzmaurice, *J. Phys. Chem.*, 1993, **97**, 1426-1430.
76. G. Redmond, D. Fitzmaurice and M. Grätzel, *J. Phys. Chem.*, 1993, **97**, 6951-6954.
77. CRC Handook of Chemistry and Physics, J. R. Rumble, 2019, 100th edition.
78. K. J. Young, L. A. Martini, R. L. Milot, R. C. Snoeberger, III, V. S. Batista, C. A. Schmuttenmaer, R. H. Crabtree and G. W. Brudvig, *Coord. Chem. Rev.*, 2012, **256**, 2503-2520.
79. X. Ding, Y. Gao, L. Zhang, Z. Yu, J. Liu and L. Sun, *Electrochim. Acta*, 2014, **149**, 337-340.
80. Z. Chen, J. J. Concepcion, J. W. Jurss and T. J. Meyer, *J. Am. Chem. Soc.*, 2009, **131**, 15580–15581.
81. Y. Pellegrin and F. Odobel, *Coord. Chem. Rev.*, 2011, **255**, 2578-2593.
82. J. Willkomm, K. L. Orchard, A. Reynal, E. Pastor, J. R. Durrant and E. Reisner, *Chem. Soc. Rev.*, 2016, **45**, 9-23.
83. T. E. Rosser, M. A. Gross, Y.-H. Lai and E. Reisner, *Chem. Sci.*, 2016, **7**, 4024-4035.
84. D. L. DuBois, *Inorg. Chem.*, 2014, **53**, 3935-3960.
85. R. M. Bullock, A. K. Das and A. M. Appel, *Chem. Eur. J.*, 2017, **23**, 7626-7641.
86. N. Kaeffer, C. D. Windle, R. Brisse, C. Gablin, D. Leonard, B. Jousselme, M. Chavarot-Kerlidou and V. Artero, *Chem. Sci.*, 2018, **9**, 6721-6738.
87. T. E. Rosser, C. D. Windle and E. Reisner, *Angew. Chem. Int.*, 2016, **55**, 7388-7392.
88. B. Reuillard, K. H. Ly, T. E. Rosser, M. F. Kuehnel, I. Zebger and E. Reisner, *J. Am. Chem. Soc.*, 2017, **139**, 14425-14435.
89. S. Bold, L. Zedler, Y. Zhang, J. Massin, V. Artero, M. Chavarot-Kerlidou and B. Dietzek, *Chem. Commun.*, 2018, **54**, 10594-10597.
90. M. R. Wasielewski, *Acc. Chem. Res.*, 2009, **42**, 1911-1921.
91. B. Albinsson, M. P. Eng, K. Pettersson and M. U. Winters, *Phys. Chem. Chem. Phys.*, 2007, **9**, 5847-5864.
92. C. Lee, W. Yang and R. G. Parr, *Phys. Rev. B Condens. Matter*, 1988, **37**, 785-789.
93. A. D. Becke, *Phys. Rev. A*, 1988, **38**, 3098-3100.
94. A. D. Becke, *J. Chem. Phys.*, 1993, **98**, 5648-5652.
95. P. A. M. Dirac, *Proc. Royal Soc. A*, 1929, **123**, 714-733.
96. J. C. Slater, *Phys. Rev.*, 1951, **81**, 385-390.
97. J. P. Perdew and Y. Wang, *Phys. Rev. B Condens. Matter*, 1992, **45**, 13244-13249.
98. J. Tao, J. P. Perdew, V. N. Staroverov and G. E. Scuseria, *Phys. Rev. Lett.*, 2003, **91**, 146401.
99. V. N. Staroverov, G. E. Scuseria, J. Tao and J. P. Perdew, *J. Chem. Phys.*, 2003, **119**, 12129.
100. F. Weigend and R. Ahlrichs, *Phys. Chem. Chem. Phys.*, 2005, **7**, 3297-3305.
101. F. Weigend, *Phys. Chem. Chem. Phys.*, 2006, **8**, 1057-1065.
102. W. J. Hehre, R. Ditchfield and J. A. Pople, *J. Chem. Phys.*, 1972, **56**, 2257-2261.
103. M. M. Francl, W. J. Pietro, W. J. Hehre, J. S. Binkley, M. S. Gordon, D. J. DeFrees and J. A. Pople, *J. Chem. Phys.*, 1982, **77**, 3654.
104. V. A. Rassolov, J. A. Pople, M. A. Ratner and T. L. Windus, *J. Chem. Phys.*, 1998, **109**, 1223-1229.
105. F. Neese, *WIREs Comput. Mol. Sci.*, 2012, **2**, 73-78.
106. S. Sinnecker, A. Rajendran, A. Klamt, M. Diedenhofen and F. Neese, *J. Phys. Chem. A*, 2006, **110**, 2235-2245.
107. S. Grimme, J. Antony, S. Ehrlich and H. Krieg, *J. Chem. Phys.*, 2010, **132**, 154104.
108. S. Grimme, S. Ehrlich and L. Goerigk, *J. Comput. Chem.*, 2011, **32**, 1456-1465.

109. M. D. Hanwell, D. E. Curtis, D. C. Lonie, T. Vandermeersch, E. Zurek and G. R. Hutchison, *J. Cheminformatics*, 2012, **4**.

3.7. Annex

3.7.1. TD-DFT calculations

TD-DFT calculations were done by Dr. Annika Eisenschmidt. Fully optimised molecular structures were obtained through geometry optimisations employing the *B3LYP*[92-94] or *TPSSh*[95-99] functional in conjunction with the *def2-TZVP*[100, 101] or the *6-31G(d,p)*[102-104] basis set. In such computations, that were conducted on Br-containing molecules with *6-31G(d,p)* as the basis set, Br was described by *def2-tzvp*. All calculations were conducted with *ORCA 4.0.1.2*.[105] The solvation was approximated by the conductor-like screening model *COSMO*[106] with the permittivity set to ACN. Long range Coulomb and Hartree-Fock exchange interactions were included using the rijcosx approximation. Dispersion correction was conducted using the Grimme atom-pairwise correction with Becke-Johnson damping scheme.[107, 108] Single point energy and frequency calculations were carried out on the optimised structures. All plots of computed structures were produced with *Avogadro 1.1.0*.[109] TD-DFT calculations were carried out with *ORCA 4.0.1.2* on geometry optimised structures using the same basis set as for the respective geometry optimisation. The structure and absorption spectra of all the intermediates considered are provided in Table 3.3 and 3.2, respectively.

Table 3.2. UV-Vis Absorbance maxima (UV-Vis transitions between 280-1000 nm) predicted by TD-DFT with *B3LYP-def2tzvp*, *B3LYP-6-31G(d,p)*, *TPSSh-def2tzvp*, and *TPSSh-6-31G(d,p)* of the respective CoP^2 species (low-spin only, *i.e.*, Multiplicity(Co^{II})=2, Multiplicity (Co^{III})=1). All transitions are given in nm.

	B3LYP-def2tzvp	*B3LYP-6-31G(d,p)*	*TPSSh-def2tzvp*	*TPSSh-6-31G(d,p)*
$[Co^{I}P^2]$	595	623	560	589
$[(Co^{II}P^2)(ACN)_2]^+$	339, 351	354, 364	374	386, 388
$[(Co^{III}P^2)(ACN)_2]^{2+}$	306, 319	297, 315	292, 327	298, 321
$[(Co^{III}P^2)\ H]^-$	472	512	460	512
$[(Co^{II}P^2)\ H]^-$	631, 674	613, 656	595, 604	605, 621

Table 3.3. Comparison of the Cobalt(III) coordination environment in the crystal structure of $[(Co^{III}P^2)(Br)_2]$[1] with the respective computed structures $[(Co^{III}P^2)(Br)_2]$ and $[(Co^{III}P^2)(MeCN)_2]^{2+}$ (low- and high-spin, *i.e.*, **Multiplicity(Co^{III})=1** and **Multiplicity(Co^{III})=3**).

Parameter	*Experimental* **$[(Co^{III}P^2)(Br)_2]$**	*B3LYP-def2tzvp* **$[(Co^{III}P^2)(Br)_2]$**	*B3LYP-def2tzvp* **$[(Co^{III}P^2)(ACN)_2]^{2+}$**	*B3LYP-6-31G(d,p)* **$[(Co^{III}P^2)(Br)_2]$**	*B3LYP-6-31G(d,p)* **$[(Co^{III}P^2)(ACN)_2]^{2+}$**	*TPSSh-def2tzvp* **$[(Co^{III}P^2)(ACN)_2]^{2+}$**	*TPSSh-6-31G(d,p)* **$[(Co^{III}P^2)(Br)_2]$**	*TPSSh-6-31G(d,p)* **$[(Co^{III}P^2)(ACN)_2]^{2+}$**
Distances								
Co-N	1.91 1.91 1.90 1.90	1.95 1.91 1.91 1.92 1.92 1.94 1.92 1.95	1.96 1.94 1.93 1.93 1.92 1.94 1.96 1.96	1.94 1.91 1.91 1.90 1.92 1.92 1.94 1.93	1.95 1.93 1.92 1.93 1.95 1.95 1.93 1.92	1.95 1.93 1.92 1.92 1.94 1.95 1.90 1.92	1.93 1.90 1.91 1.89 1.93 1.92 1.90 1.90	1.91 1.94 1.91 1.91 1.93 1.91 1.93 1.90
Co-Br/ Co-N (ACN)	2.75 2.99	2.43 2.45 2.68 2.64	1.89 1.89 2.19 2.17	2.40 2.39 2.62 2.61	1.88 1.88 2.14 2.15	1.87 1.87 2.14 2.14	2.37 2.36 2.58 2.58	1.85 1.85 2.10 2.12
C-C (equidistant)	1.51 1.48	1.48 1.46 1.47 1.45	1.46 1.48 1.45 1.48	1.48 1.46 1.47 1.45	1.48 1.46 1.48 1.46	1.47 1.46 1.47 1.44	1.47 1.45 1.46 1.44	1.46 1.47 1.47 1.45
Angle								
N-Co-N	82.8 80.5	82.1 80.8 82.0 80.6	82.1 80.8 82.2 80.5	82.1 80.9 82.1 80.7	82.4 81.1 82.3 80.8	82.3 81.0 80.7 82.3	82.19 81.13 82.07 80.88	81.4 82.4 82.3 81.1

Chapter 4

Insights into the water-reduction mechanism and kinetics of cobalt molecular catalysts

Dr. Annika Eisenschmidt did the TD-DFT calculations, Dr. Daniel Antón-García prepared the ITO films and synthesised the molecular catalysts ***CoP^1*** *and* ***CoP^2****, Dr. Ravi B. Shankar carried out the H_2 production measurements, Dr. Camilo A. Mesa, Dr. Laia Francàs, Prof. Erwin Reisner and Prof. James R. Durrant contributed to the discussion of the results.*

Molecular catalysts based on organometallic catalyst have well-defined active sites that make it easier to characterise catalytic intermediates and mechanisms. This Chapter compares the cobalt-based H_2-production molecular catalysts **CoP^1** and **CoP^2**, which have different structures and activities (Section 4.1). These catalysts are immobilised on TiO_2 (Section 4.2) and evolve hydrogen (Section 4.3.1) upon the excitation of TiO_2 and the subsequent transfer of photogenerated charges to the catalysts. Spectroelectrochemical measurements (Sections 4.3.2 and 4.3.5) and TD-DFT simulations (Section 4.3.3 and 4.3.6) of these catalysts in the presence of water where used to identify the absorption spectra of different possible multi-redox and protonated states. The role of these states in the reduction of water was then studied by transient absorption spectroscopy (Sections 4.3.4 and 4.3.7). With this catalyst arrangement and these techniques, the intrinsic water-reduction kinetics of the catalysts could be distinguished from electrons in TiO_2. A difference of ~0.3 eV in the splitting of the *d* metal orbitals is proposed to account for a difference of at least two orders of magnitude in the catalytic reaction kinetics (Section 4.4). Finally, the kinetics of mono- and bi-molecular pathways suggest that bi-molecular pathways compete with mono-molecular ones at high surface catalyst coverages affecting the catalytic productivity (Section 4.3.8).

4.0. Contents

4.1. Introduction

Molecular catalysts are based on small organometallic complexes consisting of a few metal atoms. Because of their well-defined active site, they can serve as a simplified system to understand the effect of the intrinsic properties of the catalysts (such as the electronic configuration of the metal centre or its coordination sphere) on their reaction mechanisms. In Chapter 3, a H_2-production cobalt diimine-dioxime molecular catalyst (**CoP²**) was investigated on TiO_2 in acetonitrile. With time-resolved absorption spectroscopy and electrochemistry, the charge transfer kinetics from the semiconductor to the catalyst were measured upon the photoexcitation of TiO_2, and the formation of multi-redox / charge accumulated states was identified. In this Chapter, with the purpose of understanding the reactivity of the different catalyst redox states with water to evolve hydrogen, the molecular catalyst **CoP²** has been studied in the same conditions with 10% water. A second H_2-production cobalt-based molecular catalyst, the highly active cobaltoxime **CoP¹** (Scheme 4.1A-B), has also been investigated in ACN:H_2O to better rationalize the relationship between the photo(electro)chemical activity, the chemical structure, and the reaction kinetics.

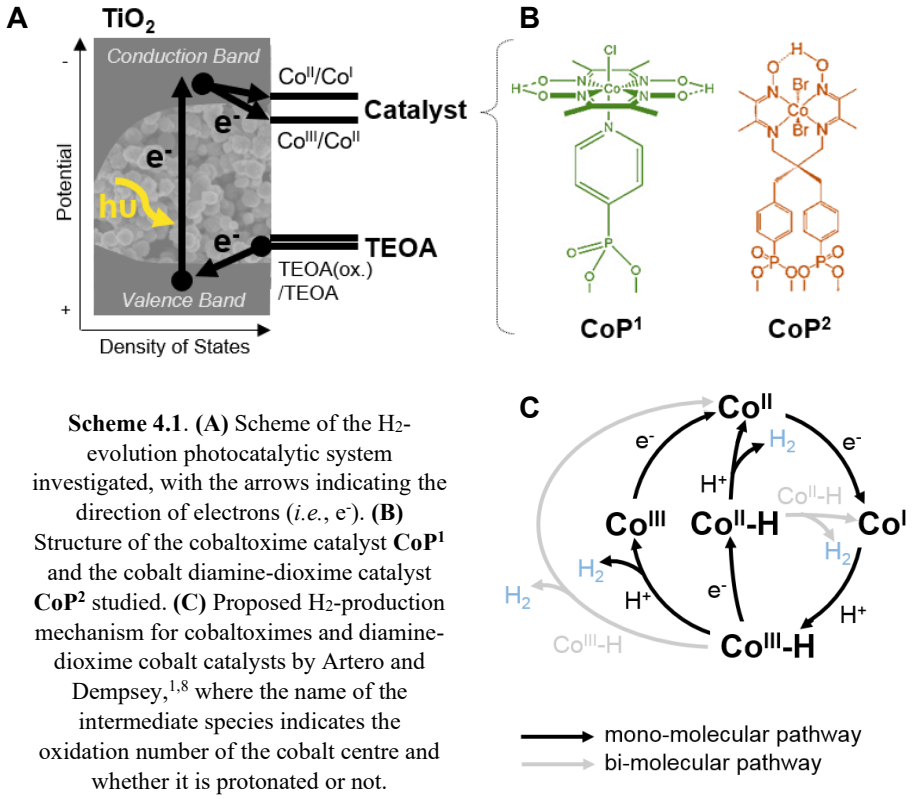

Scheme 4.1. **(A)** Scheme of the H_2-evolution photocatalytic system investigated, with the arrows indicating the direction of electrons (*i.e.*, e^-). **(B)** Structure of the cobaltoxime catalyst **CoP¹** and the cobalt diamine-dioxime catalyst **CoP²** studied. **(C)** Proposed H_2-production mechanism for cobaltoximes and diamine-dioxime cobalt catalysts by Artero and Dempsey,[1,8] where the name of the intermediate species indicates the oxidation number of the cobalt centre and whether it is protonated or not.

The cobaltoxime catalyst **CoP[1]** is among the best molecular catalysts for water reduction, with a turnover frequency of 10^4 s^{-1} at an overpotential of 0.4 V.[1, 2] To optimise the charge transfer efficiency to the catalyst, a phosphonate group was added to the pyridine axial ligand by Reisner et *al.*, facilitating its attachment to oxide electrodes and photosensitisers.[3, 4] However, the catalyst **CoP[1]** degrades within ~1h due to the loss of both the axial and equatorial ligands, which also leads to the catalysts detachment from the (photo)electrode surface.[1, 5] In this context, **CoP[2]** was designed to have a better stability and a more robust anchoring by modifying the equatorial ligands.[5-7] However, whilst showing enhanced stability, under 1h irradiation, the **CoP[2]** has 20 times less activity when immobilised on TiO_2, which means that its robustness and better stability do not compensate for the higher catalytic activity of **CoP[1]**.[5] The optimal catalytic activity most likely depends on finding a balance between the reduction potential (*i.e.*, the capacity to attract electrons), and the nucleophilicity of the metal centre (*i.e.*, the capacity to give these electrons to protons).[1, 8] Following extensive evidence, the H_2-production catalytic mechanism both in cobaltoxime and diamine-dioxime catalysts has been proposed to require the reduction of the starting oxidation state Co^{III} to Co^{I}. Once Co^{I} is formed, multiple pathways are possible, involving either one or two catalyst molecules per hydrogen molecule released (*i.e.*, mono- and bi-molecular pathways respectively). According to Density Functional Theory (DFT) calculations, the formation of Co^{III}-H and Co^{III}-H are most likely the most energetic steps, limiting the reaction rate.[9-11] Scheme 4.1C illustrates all the catalyst intermediates that have been proposed for H_2-production cobaltoximes and diamine-dioximes. However, none of the highly reactive protonated intermediates has been experimentally detected under *operando* conditions.

The two molecular catalysts **CoP[1]** and **CoP[2]** were separately immobilised on TiO_2 and their reaction kinetics were investigated by photoexciting TiO_2 at 355 nm in ACN:H_2O 9:1 in the presence of triethanolamine (TEOA). The TEOA worked as a sacrificial donor scavenging photogenerated holes in the valence band of TiO_2, preventing their recombination with electrons in the conduction band and facilitating the transfer of these electrons to the catalyst immobilised at the surface (Scheme 4.1A). Steady-state spectroelectrochemistry and Time-Dependent Density Functional Theory (TD-DFT) calculations were used in combination to identify the absorption spectra of different possible catalyst intermediates, based on the literature. The reaction kinetics were finally deduced from deconvolving the time-resolved absorption of the TiO_2-catalyst photoelectrode.

4.2. Materials and Methods

4.2.1. TiO_2 Film Preparation

The same mesoporous TiO_2 films were prepared and used in the same way as in Chapter 3. A paste containing a sol-gel colloidal suspension of 12.5 wt% 15-nm anatase TiO_2 nanoparticles TiO_2 particles and 6.2 wt% Carbowax 20000 was doctor-bladed on clean FTO on glass. The paste was left to dry on FTO for ~20 min. and sintered at 450 ˚C degrees for 30 min. The glass-FTO substrate was previously cleaned by washing with soap, distilled water and isopropanol and heating at 450 ˚C degrees for 30 min. The resulting films had a thickness of ~4 μm, 10-50 nm diameter pores, a porosity over 50, a Brunauer-Emmett-Teller (BET) surface area per gram (S_g) of 100 m^2/g, and a roughness factor (surface area divided by projected area) around 450.[12-14]

4.2.2. Film loading with catalyst

The molecular catalysts CoP^1 (ref. [3, 15]) ([$Co^{III}Cl$(dimethylglyoximato)$_2$ (pyridyl-4-hydrophosphonate)]) and CoP^2 (ref. [1, 6-8]) ([Co^{III} Br_2 (N^2,$N^{2'}$-2,2-($CH_2(C_6H_4)PO_3H$) propanediyl-bis (2,3-butanedione-2-imine-3-oxime))]) were synthesized and characterized as reported previously. The catalysts were loaded on the ~1-cm^2 mesoporous TiO_2 films on 1x2 cm^2 FTO-glass in the same way as in Chapter 3. CoP^1 and CoP^2 were loaded by soaking the TiO_2 films in 5 mL MeOH:H_2O 1:1 with ~0.1 mM of catalyst for 12 h. Three films were soaked in each solution. The films never absorbed all the catalyst in the solutions. The TiO_2 films were prepared just before the soaking or heated to 450 ˚C for 30 min. prior to soaking. Once loaded, all the films were rinsed first with methanol and then with ACN or ACN:H_2O 9:1 electrolyte.

4.2.3. Spectroelectrochemistry and transient absorption measurements

Fresh electrolyte containing 0.1 M TEOA and 0.1 $TBAPF_6$ was prepared before each measurement. To prevent oxygen from quenching reduced species, the samples were purged throughout the experiments with electrolyte-saturated argon. Transient absorption measurements were done with an excitation power of ~1.4 mJ/cm^2 and a pulse frequency of 0.8 Hz.

4.3. Results

4.3.1. H_2 production

To confirm that the molecular catalysts **CoP¹** and **CoP²** can produce hydrogen when 10% of water is added to acetonitrile, photochemical measurements were carried out. Previously, the catalysts **CoP¹** and **CoP²** have been reported to evolve H_2 in slightly acidic water when co-attached with a Ru(II)-based dye on TiO_2 and exciting the ruthenium dye at 450 nm.[31] Here, the 4 µm-thick TiO_2 films loaded with **CoP¹** and **CoP²**, separately, were shown to produce H_2 when soaked in ACN:H_2O 9:1 0.1 M TEOA 0.1 M $TBAPF_6$ under constant UV-Vis light irradiation. The photochemically produced H_2 is shown in Figure 4.1, and was detected with a gas chromatograph following the procedure described in the Annex (Section 4.7.1). The catalytic activity of **CoP¹** and **CoP²** in acetonitrile with 10% water was observed to remain proportionally the same as reported in pure water, and the catalysts are therefore considered to operate in a similar ay both in H_2O and in the conditions tested here ACN:H_2O 9:1.

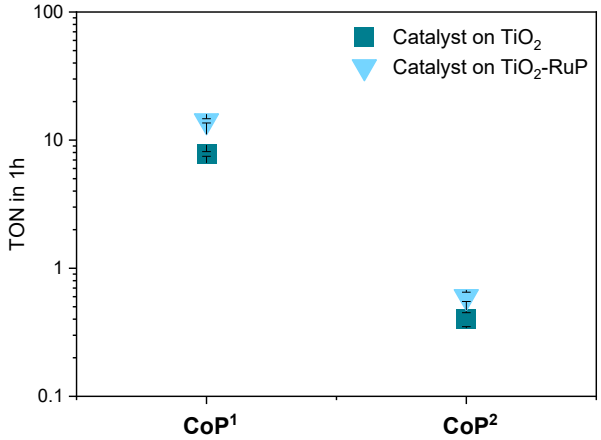

Figure 4.1. Hydrogen production of **CoP²** both on TiO_2 and TiO_2-RuP. To assess the catalytic activity of **CoP²** on TiO_2, another catalyst was immobilised on mesoporous TiO_2 films for comparison (*i.e.*, **CoP¹**). The widely used cobaltoxime **CoP¹** was taken as an indicator of the catalytic functionality of **CoP²** in conditions similar to the conditions reported in this work. The H_2 production of TiO_2-**CoP¹** and TiO_2-**CoP²** was measured in the same conditions used in the rest of experiments reported here with 10% of water (ACN:H_2O 9:1, 0.1 M TEOA, 0.1 M $TBAPF_6$). The H_2 production of RuP-TiO_2-**CoP¹** and RuP-TiO_2-**CoP²** was taken from ref [31] (H_2O 0.1 M TEOA under AM 1.5G 100 mW/cm^2 irradiation, $\lambda > 422$ nm). The ratio of H_2 of the two catalysts in a given condition was calculated and compared in the two conditions (~20:1 **CoP¹**:**CoP²**).

4.3.2. Spectroelectrochemistry of TiO_2-CoP^2

To identify multi-redox catalytic species in TiO_2-**CoP^2**, its absorbance changes at different potentials were measured in ACN:H_2O 9:1 with 0.1 M TEOA and 0.1 M $TBAPF_6$, the same spectroelectrochemistry conditions used in Chapter 3 but with 10% water. Increasingly reducing potentials were applied to TiO_2-**CoP^2**, starting below the conduction band of TiO_2 at -0.08 V *vs.* NHE, and reaching negative enough potentials to inject electrons into the conduction band. Both in ACN and ACN:H_2O 9:1, bare TiO_2 under applied potential showed the characteristic absorbance of electrons in the conduction band, flat throughout the visible range and with an intensity lower than 0.02 (Section 4.7.2. Annex, Figure 4.9). In contrast, TiO_2-**CoP^2** showed much larger differential absorbance signals in both conditions, with maxima at 490 nm down until -0.68 V, and at 600-700 nm below -0.70 V *vs.* NHE (Figures 4.2A, 3.2). In Section 3.3.1, the first signal was assigned to a singly-reduced CoP^2 species, and the second one was assigned to multi-reduced species, either protonated or not. These species, however, could not be unequivocally assigned to any of the intermediates illustrated in Scheme 4.1, with the singly-reduced species most likely being Co^{II} and the multi-reduced species being compatible with Co^{I} and Co^{II}-H in acetonitrile. Compared to ACN, in ACN:H_2O the absorbance of TiO_2-**CoP^2** at 600-700, assigned to multi-reduced species, is much larger below -0.70 V. The larger amplitude of multi-reduced species in the presence of water compared to acetonitrile must therefore be related to a larger concentration of multi-reduced species that are protonated and / or to changes in the band bending at the surface of TiO_2.[16, 17] In any case, because of the similarity in the absorbance maxima and reduction potentials, **CoP^2** can be said to generate the same singly- and multi-reduced species in both ACN and ACN:H_2O 9:1, which is used below to interpret transient absorption kinetics in the two conditions.

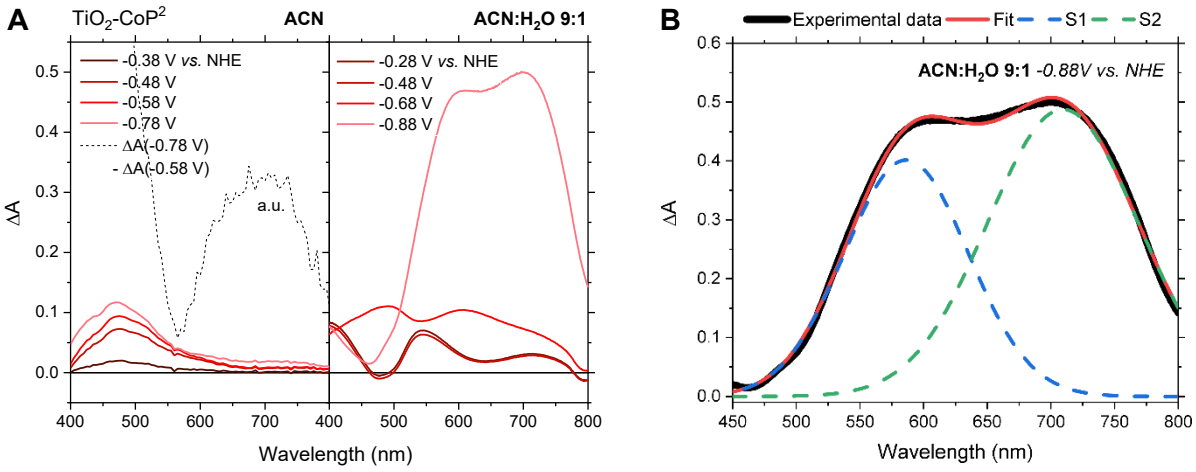

Figure 4.2. Spectroelectrochemistry of TiO_2-**CoP^2**. **(A)** Absorbance changes at different potentials of TiO_2-**CoP^2** in ACN (*left*) and ACN:H_2O 9:1 (*right*) with respect to the absorbance at -0.08 V *vs.* NHE in the presence of 0.1 M TEOA and 0.1 M $TBAPF_6$. **(B)** Fitting of the absorbance changes at -0.88 V *vs.* NHE in ACN:H_2O 9:1 with a linear combination of two Gaussian curves.

4.3.3. Assignment of TiO_2-CoP^2 species

The assignment of the absorption spectra detected above at different potentials was further investigated by mathematically deconvolving the experimental spectra, and by carrying out time-dependent density functional theory calculations (TD-DFT). First, the experimental spectra of TiO_2-**CoP^2** in ACN:H_2O 9:1 was fit with a linear combination of Gaussian functions using the optimisation method described in Section 2.7. At less reductive potentials (-0.68 V *vs.* NHE), one single Gaussian curve fits the optical signal at 490 nm, while, at more negative potentials (-0.88 V *vs.* NHE), a minimum of two Gaussians were necessary to fit the differential absorbance spectrum of TiO_2-**CoP^2** (Figure 4.2B). Second, following the literature, TD-DFT calculations of plausible **CoP^2** species (Scheme 4.1) were ran considering the presence of water, the loss of axial ligands, and a simplified anchoring group, as detailed in Section 4.7.3. Assuming that the starting oxidation state of the cobalt centre before applying any potential is Co^{III},[6, 7] the absorbance at 490 nm is compatible with a one-electron reduced species (*i.e.*, Co^{II}) that has had its axial ligands replaced by either ACN or water (Figures 4.3A, 4.13). This implies that **CoP^2** loses its axial ligands upon the first one-electron reduction. In parallel, the absorbance at 600-700 nm at more reducing potentials fits with a two-electron reduced species (*i.e.*, Co^{I}) and a protonated three-electron reduced species (*i.e.*, Co^{II}-H) without any axial ligand except for H^- (Figures 4.3B, 4.13). The maxima at 700 nm would mostly be due to Co^{II}-H, while the absorbance maxima at 600 nm would be related to both Co^{II}-H and Co^{I}. These results coincide with the assignment of **CoP^2** reduced species in ACN done in Chapter 3, Sections 3.3.1.2-3. Therefore, in ACN:H_2O 9:1 under more negative potentials, the cobalt centre of CoP^2 on TiO_2 is reduced from Co^{III} to Co^{II} and Co^{I}, in parallel to the loss and replacement of the axial ligands by either ACN or H_2O, and to the protonation and further reduction of the doubly reduced state Co^{I} into Co^{II}-H.

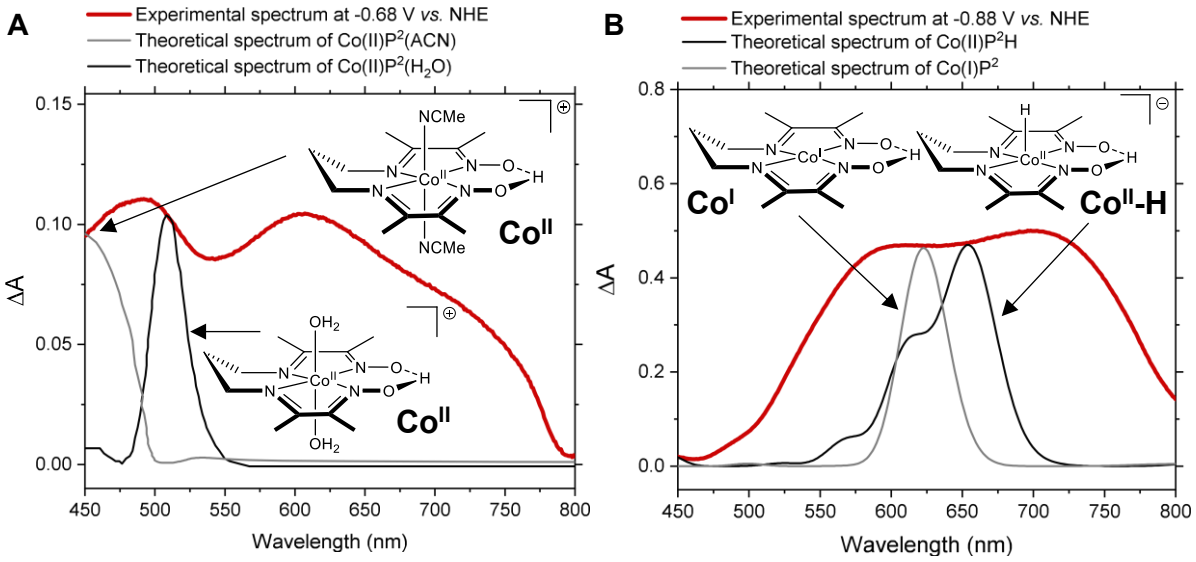

Figure 4.3. TD-DFT spectra and structure of **CoP^2** species (*grey & black*) overlapped with the absorbance change under an applied potential of -0.68 V **(A)** and -0.88 V **(B)** relative to -0.08 V *vs.* NHE from Figure 4.1 (*red*), in ACN:H_2O 9:1 0.1 M TEOA and 0.1 M $TBAPF_6$. The TD-DFT did not include the anchoring group for simplicity.

4.3.4. Transient absorption of TiO_2-CoP^2

Photoinduced charge transfer from TiO_2 to **CoP^2** and the subsequent water-reduction catalysis by **CoP^2** was studied by monitoring the optical signal of the molecular catalyst. Its transient absorption was measured in microseconds to seconds after the 355-nm excitation of the TiO_2. These measurements were done in ACN and ACN:H_2O 9:1 with and without an applied intra-bandgap potential of -0.08 V *vs.* NHE. In Chapter 3, the intra-bandgap potential was shown to prevent the recombination of catalyst multi-reduced species and holes in the valence band of TiO_2 under microseconds. In parallel, this applied potential also prevented the accumulation of charges in the conduction band of TiO_2, and enhanced back electron transfer from the reduced catalyst to the conduction band in a timescale of seconds.

Under photoexcitation, similar transient differential absorbance signals were observed at 600-700 nm in TiO_2-**CoP^2** in the four conditions (Figures 4.4A), comparable to the differential absorbance signal of TiO_2-**CoP^2** under reductive applied potentials in the dark (Figures 4.2 and 4.3B), and significantly different than the signal of trapped electrons in the conduction band of TiO_2 (Figure 4.4B). Considering the TD-DFT simulations above, the observed transient signal at 600-700 nm and the bleach below 500 nm would mostly due to the formation of Co^{I} and Co^{II}-H from Co^{II}. These results imply the reduction of the initial state Co^{III} in fresh samples to Co^{II} and the accumulation of Co^{II} in the dark. The formation and accumulation of Co^{II} is deduced from the changes in the transient absorbance of a fresh samples over consecutive measurements both in ACN and ACN:H_2O 9:1 (Section 4.7.2, Figures 4.10), and it is in agreement with the assignment in Chapter 3. The formation of protonated species detected in ACN (*i.e.*, Co^{II}-H) would be most likely due to the presence of trace amounts of water in the purging flow or the electrolyte. Furthermore, the transient absorbance maxima have different relative intensities at 700 and 600 nm, being particularly larger at 700 nm compared to 600 nm in ACN:H_2O 9:1 without any applied potential. The larger 700-nm absorbance in ACN:H_2O 9:1 without bias is most likely caused by a higher concentration of Co^{II}-H due to the presence of water and the slow back electron transfer from the catalyst to the TiO_2 in the absence of an applied potential. Therefore, Co^{II}-H and Co^{I} are possible catalyst species that could be formed in both ACN:H_2O 9:1 and ACN upon photoexcitation of TiO_2, having different formation and reaction kinetics.

Under −0.08 V *vs.* NHE, the TA signal corresponding to the reduction of Co(R) to Co(RR) in acetonitrile (Figures 3.4 and 3.8) was also detected in ACN:H_2O 9:1 (see Figure 4.4C), showing that Co(R) and Co(RR) species are still formed in catalytic conditions. In ACN:H_2O 9:1, the kinetics at 700 nm decayed faster than in pure ACN, which indicates that Co(RR) species are less long-lived in water, consistent with this intermediates driving proton reduction in this electrolyte. This evidence therefore shows that the absorbance features of **CoP^2** in ACN remain similar when water is added, and that both Co(R) and Co(RR) species can be catalytic intermediates in the H_2-production activity of CoP^2.

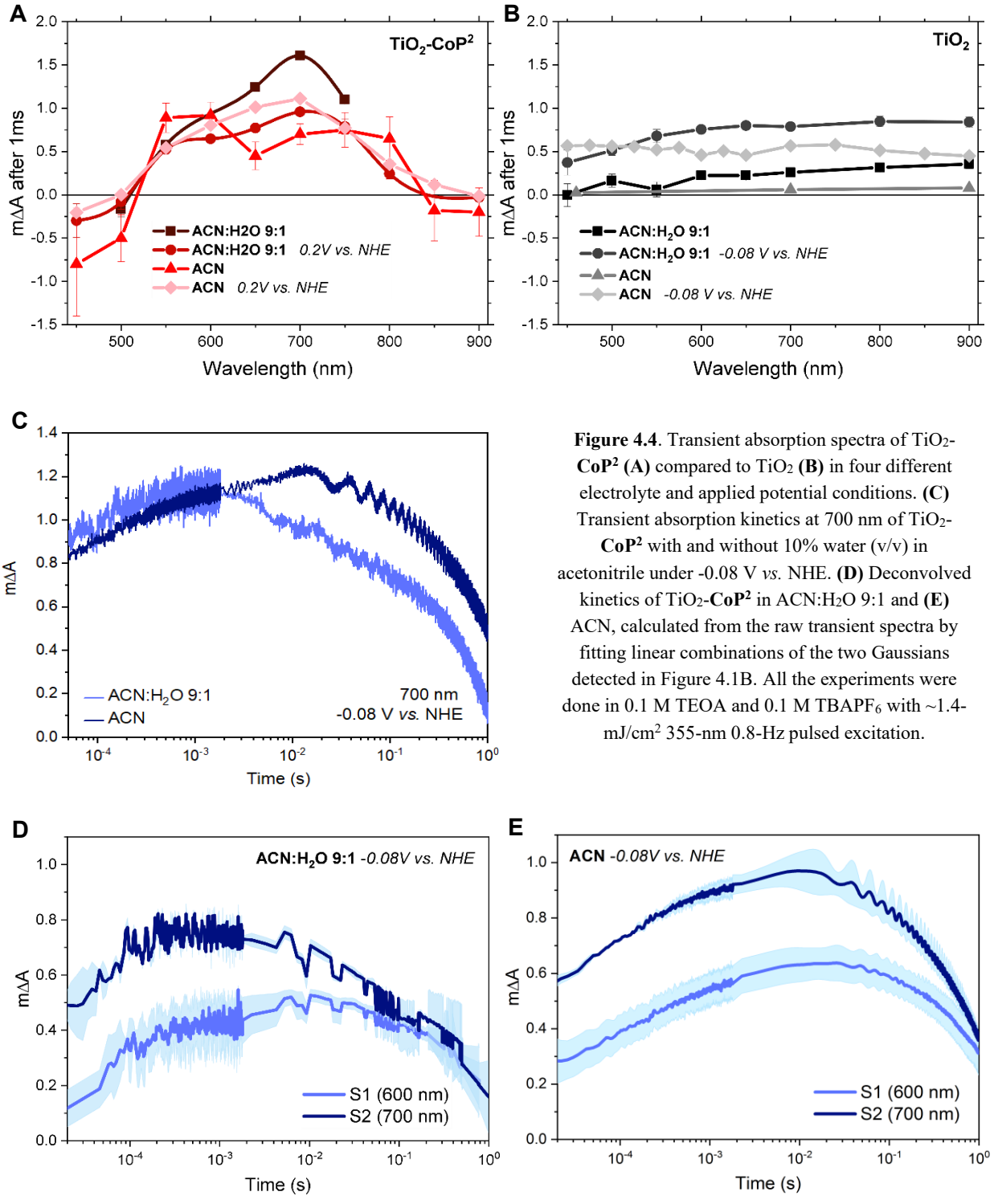

Figure 4.4. Transient absorption spectra of TiO_2-**CoP^2 (A)** compared to TiO_2 **(B)** in four different electrolyte and applied potential conditions. **(C)** Transient absorption kinetics at 700 nm of TiO_2-**CoP^2** with and without 10% water (v/v) in acetonitrile under -0.08 V *vs.* NHE. **(D)** Deconvolved kinetics of TiO_2-**CoP^2** in ACN:H_2O 9:1 and **(E)** ACN, calculated from the raw transient spectra by fitting linear combinations of the two Gaussians detected in Figure 4.1B. All the experiments were done in 0.1 M TEOA and 0.1 M $TBAPF_6$ with ~1.4-mJ/cm^2 355-nm 0.8-Hz pulsed excitation.

To separately investigate the reactivity of the species formed upon photoexcitation of TiO_2-**CoP²** in the presence of water, the kinetics of the 600- and 700-nm absorbance signal in Figure 4.4A were mathematically deconvolved. The deconvolution was done by finding the optimal combination of the two Gaussian curves with maxima at ~570 nm and ~720 nm derived from the spectro-electrochemistry of **CoP²** under reductive potentials (S1 and S2 respectively in Figure 4.1B) at every time frame. The maximum absorbance over time of each deconvolved signal in ACN:H_2O 9:1 and ACN are plotted in Figures 4.4D and 4.4E respectively. It is apparent from Figure 4.4A that the two signals at 600 and 700 nm increase in parallel in the first ~100 μs after photoexcitation, which is compatible with the formation of one single species that, considering the TD-DFT calculations, would most likely be Co^{II}-H. After 1 ms, the 700-nm signal starts decaying while the 600-nm signal increases slightly and decays in tens of milliseconds. Taking into account that both Co^{II}-H and Co^{I} absorb at around 600 nm (Figure 4.2B), the latter would imply the formation of Co^{I} and the simultaneous depletion of Co^{II}-H. In ACN, similar trends are observed but at later timescales, compatible with the smaller concentration of water and a diffusion-limited protonation reaction to form Co^{II}-H from Co^{II}. The optical signals at 700 and 600 nm and their transient kinetics therefore suggest that the photoinduced charges in TiO_2 form Co^{II}-H under 100 μs through electron transfers to Co^{II} and a protonation step. Then, Co^{II}-H would react forming Co^{I} or Co^{II},. The observed kinetics are compatible with H_2-production bi- and mono-molecular mechanisms proposed for **CoP²** (Reactions 4.1 and 4.2 respectively), and further support the assignment of the optical signals at 600-700 nm to Co^{II}-H and Co^{I}.

Reaction 4.1 $2Co^{II}H \rightarrow 2Co^{I} + H_2$

Reaction 4.2 $Co^{II}H + H^{+} \rightarrow Co^{II} + H_2$

4.3.5. Spectroelectrochemistry of TiO_2-CoP^1

To contextualize the findings in TiO_2-**CoP^2**, the more active but less stable cobaltoxime catalyst **CoP^1** was investigated on TiO_2. Its reduced states were studied by doing spectroelectrochemistry in both ACN and ACN:H_2O 9:1 (Figure 4.5A left and right respectively), with 0.1 M TEOA as sacrificial electron donor and 0.1 M $TBAPF_6$. Starting below the conduction band of TiO_2 as in TiO_2-**CoP^2**, more reducing potentials applied to TiO_2-**CoP^1** lead to the appearance of a growing band at ~450 nm below -0.48 V, and a second band at 600 nm above -0.88 V in both electrolytes. The later band is smaller in ACN than in ACN:H_2O 9:1, indicating that this differential absorbance signal is most likely related to the formation of a protonated multi-reduced species of **CoP^1**. The differential spectra at -1.08 V both in ACN and ACN:H_2O 9:1 was fit with a linear combination of at least three Gaussian curves with maxima at ~450, ~600 and ~670 nm (Figure 4.5B in ACN:H_2O 9:1) following the procedure in Section 2.7. These results hint that the absorbance at ~450 nm may be related to one single one-electron reduced species, while the absorbance above 450 nm is maybe associated to at least two different doubly reduced species.

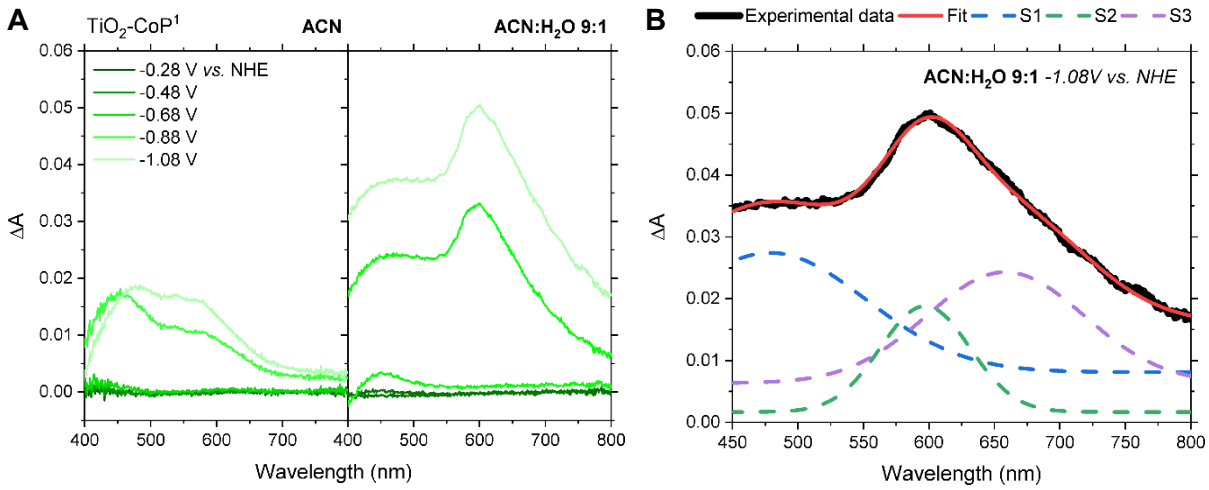

Figure 4.5. Spectroelectrochemistry of TiO_2-**CoP^1**. **(A)** Absorbance changes at different potentials of TiO_2-**CoP^1** in ACN (*left*) and ACN:H_2O 9:1 (*right*) with respect to the absorbance at -0.08 V *vs.* NHE in the presence of 0.1 M TEOA and 0.1 M $TBAPF_6$. **(B)** Fitting of the absorbance changes at -0.88 V *vs.* NHE in ACN (*left*) and ACN:H_2O 9:1 (*right*) with a linear combination of Gaussian curves.

4.3.6. Assignment of TiO_2-CoP^1 species

The absorbance spectra of TiO_2-**CoP^1** under applied potentials in ACN:H_2O 9:1 was compared to theoretical spectra of possible intermediates simulated by TD-DFT (Figures 4.14-15). Based on the literature, the theoretical spectra were calculated for the optimised structures of the intermediates in Scheme 4.1 with and without the pyridine axial, assuming that the other axial is lost and omitting the phosphonate group. Similar as in **CoP^2**, the differential absorbance at low reducing potentials with respect to -0.08 V *vs.* NHE has a distinctive band at 450 nm that fits very well the theoretical spectra of the catalyst with a cobalt oxidation number of 2+ (*i.e.*, Co^{II}), with all or some of the axial ligands replaced by water electrolyte molecular (Figure 4.6A). At more reductive potentials, the band stretching above 450 nm overlaps with the theoretical spectra of a two-electron reduced species with a cobalt oxidation number of 1+ (*i.e.*, Co^{I}) a two-electron reduced protonated species with a cobalt oxidation number of 3+ (*i.e.*, Co^{III}-H) and a three-electron reduced protonated species with a cobalt oxidation number of 2+ (*i.e.*, Co^{II}-H), as shown in Figure 4.6B. It is assumed that the chloride axial ligands are lost, but not the axial pyridine that immobilise the catalyst to the TiO_2, as that would lead to the catalyst detachment and to the absence of any catalyst optical signal. From the TD-DFT calculations, the singly-reduced species Co^{II} and the doubly reduced species Co^{I}, formed from Co^{III}, absorb at ~450 and ~500 nm respectively, with Co^{I} having an additional smaller band at ~600 nm. In contrast, the protonated species absorb in the 500-700 nm range: Co^{III}-H absorbs at around 700 nm and below 450 nm, while Co^{II}-H absorbs at around 700 and 550 nm. Assuming a ~30-50 nm error in the theoretical spectra, the absorbance maxima at 600 nm in the experimental spectrum is most likely related to Co^{II}-H with some contribution from Co^{I}. Therefore, all the reduced species absorb below 450 nm, and the protonated and multi-reduced species have characteristic absorbance maxima at 500 nm (Co^{I}), 650 nm (Co^{II}-H) and 700 nm (Co^{III}-H). The absorbance of different multi-reduced states in **CoP^1** compared to **CoP^2** illustrates differences in the arrangement of the metal *d* orbitals which are likely to affect catalysis.

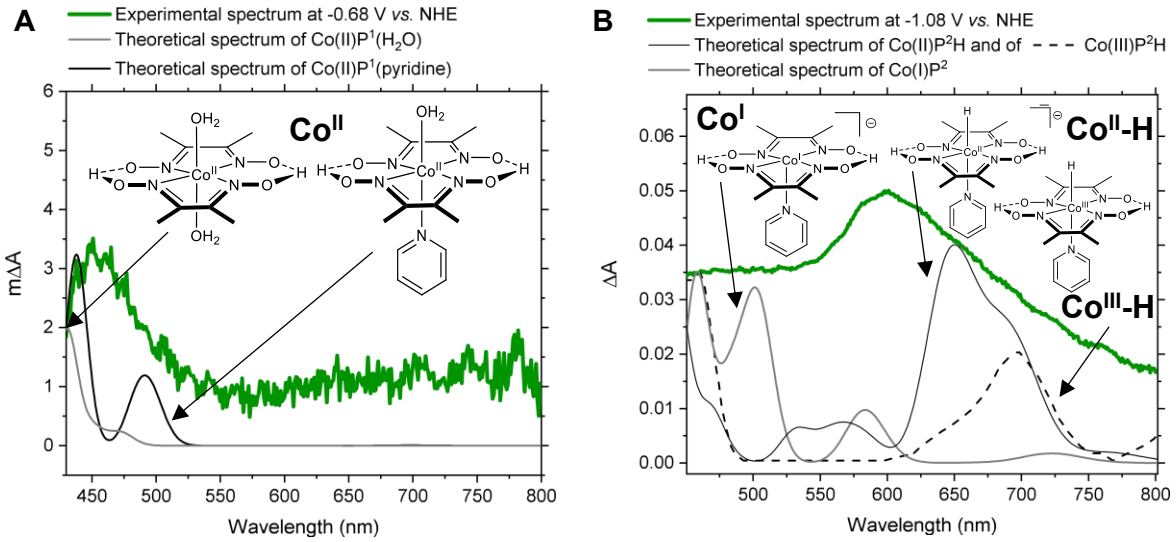

Figure 4.6. TD-DFT spectra (*grey* & *black*) calculated for the structures of **CoP^1** species shown in the graph, overlapped with the absorbance change under an applied potential of -0.68 V **(A)** and -1.08 V **(B)** relative to -0.08 V *vs.* NHE from Figure 4.5 (*red*), in ACN:H_2O 9:1 0.1 M TEOA and 0.1 M $TBAPF_6$. The TD-DFT did not include the phosphonate group for simplicity.

4.3.7. Transient absorption of TiO_2-CoP^1

TiO_2-**CoP^1** was photoexcitated at 355 nm and the photoreduced species were monitored by transient absorption spectroscopy in the same way as with TiO_2-**CoP^2**. Figures 4.7A and B show the transient spectra after 1 ms photoexcitation of TiO_2-**CoP^1** and TiO_2 respectively in the same four conditions tested with TiO_2-**CoP^2**. In the absence of an applied potential, the spectra in TiO_2-**CoP^1** and TiO_2 are very similar, with a broad absorbance signal at large wavelengths which correspond to trapped electrons in the conduction band. Under an intra-bandgap potential, upon excitation, the transient absorbance in both ACN and ACN:H_2O has a broad band at 500-700 nm, which is compatible with the formation of Co^{II}, Co^{I}, Co^{III}-H or Co^{II}-H from Co^{III}. In parallel, the kinetics in the microseconds to seconds are the same at all wavelengths and the same as in bare TiO_2 (insets Figure 4.7C-D). This suggests that the reaction kinetics of catalyst species present at this timescale is limited by the diffusion of trapped conduction-band electrons to **CoP^1**. In contrast, in the absence of an intra-bandgap applied bias, when there is an excess of accumulated charges in the conduction band, no characteristic catalyst signal is detected (Figure 4.7A), probably because catalysts species can be completely reduced under microseconds, reacting with water and returning to the starting state. Therefore, the observed transient spectra under bias are probably due to intermediates that need to be reduced further to evolve hydrogen.

To further investigate the kinetics of the catalyst intermediate species detected upon photoexcitation, the transient spectra in Figure 4.7A were fit at every timeframe with the three Gaussians curves in Figure 4.5B to deconvolve the kinetics at 450, 600 and 700 nm. The kinetics of each one of these deconvolved curves does not

necessarily correspond to an individual catalytic species because different species absorb in the same region (Figure 4.6), but this deconvolution helps to separately analyse the kinetics in different spectral ranges. The major difference in the transient spectra in ACN:H_2O 9:1 compared to ACN is the lower intensity of the signal at 600 nm (Figures 4.7C-D). The absorbance at around 600 nm has been assigned above to Co^{II}-H and Co^{I}, and the lower amplitude implies the reaction of these species with water to either evolve H_2 or generate a protonated species (Reaction 4.2-3). In parallel, in both electrolyte conditions, the amplitude and kinetics of the signal at 450 nm remains the same (Figures 4.7C-D). The catalytic species that is more plausible to accumulate under these conditions is Co^{II}, which is a product of at least two hydrogen evolution pathways (Reaction 4.2 and 4.4), but does not necessarily accumulate in the dark because of the competing H_2-evolving mechanism generating Co^{III} (Reaction 4.5). In any case, upon the photoexcitation of TiO_2, **CoP^1** species probably engage in reaction kinetics with water faster than microsecond, faster than **CoP^2**.

Reaction 4.3 $Co^{II} + e \rightarrow Co^{I} + H^{+} \rightarrow Co^{III}H$

Reaction 4.4 $2Co^{III}H \rightarrow Co^{II} + H_2$

Reaction 4.5 $Co^{III}H + H^{+} \rightarrow Co^{III} + H_2$

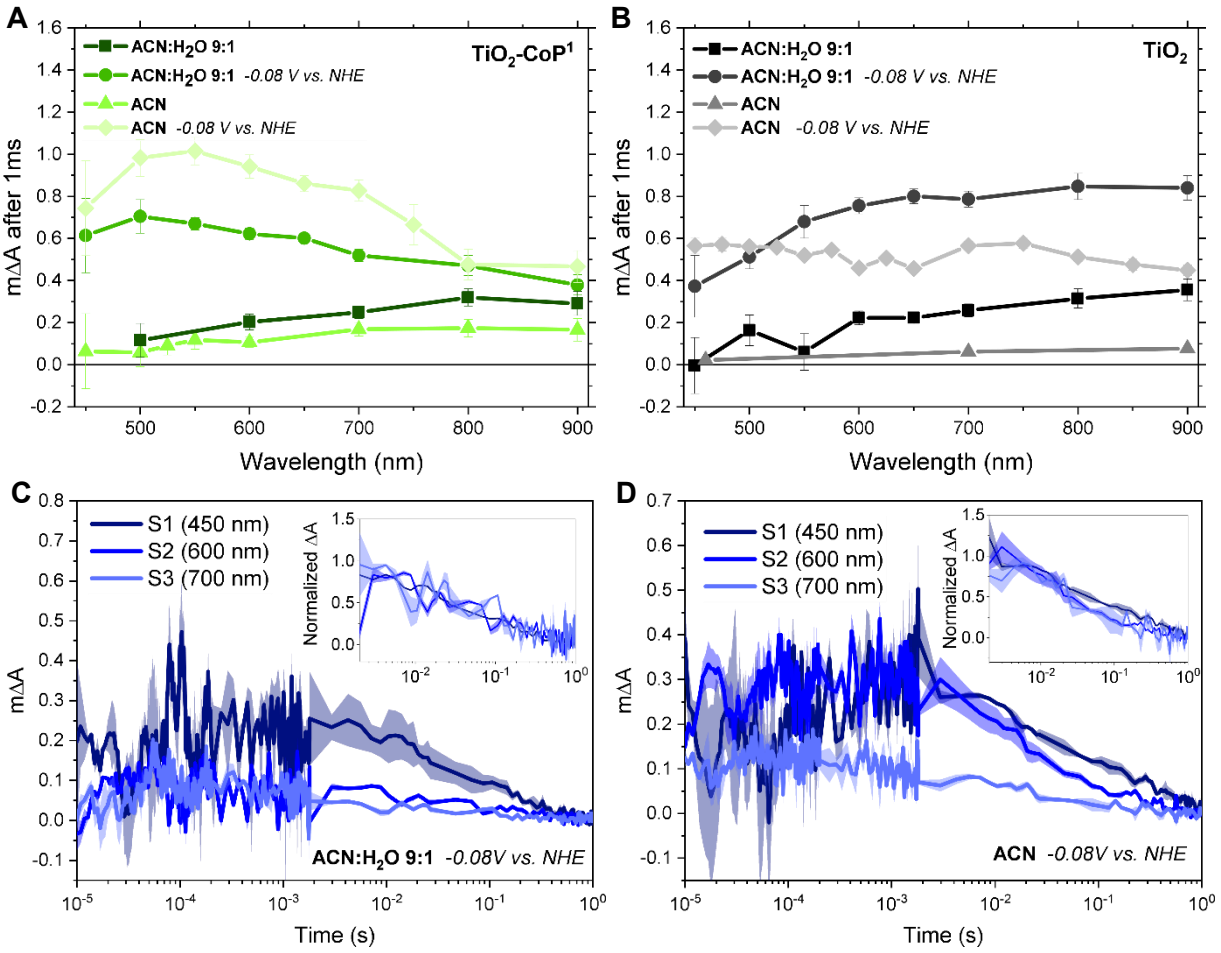

Figure 4.7. Transient absorption spectra of TiO_2-**CoP^1 (A)** compared to TiO_2 **(B)** in four different electrolyte and applied potential conditions. Transient absorption kinetics of TiO_2-**CoP^1** in ACN:H_2O 9:1 **(C)** and ACN **(D)** under -0.08 V *vs.* NHE in 0.1 M TEOA and 0.1 M $TBAPF_6$, deconvolved from the raw transient spectra by fitting linear combinations of the Gaussians detected in Figure 4.5B.

4.3.8. Power and surface coverage dependence

The redox and protonated intermediate species detected above in TiO_2-**CoP²** form and react in the microsecond to second timescale, in contrast to those in TiO_2-**CoP¹**, which kinetics could not be directly measured and would therefore react much faster. To further prove the interpretation of the transient absorbance kinetics in TiO_2-**CoP²**, these kinetics were fit with a mathematical model based on Reactions 4.1-5. The deconvolved kinetics at 700 and 600 nm of TiO_2-**CoP²** (Figure 4.4D) could be successfully fit with three different catalyst species absorbing at 600 nm (Co^{I}), 600 and 700 nm (Co^{II}-H), and not absorbing at those wavelengths (Co^{II}) (Annex Figure 4.12). These procedure was applied to the results in ACN:H_2O 9:1 both with and without an applied bias of -0.08 V *vs.* NHE (Annex Figure 4.11). The model was then used to calculate the H_2 TOF of CoP^2 under different electron concentrations and catalyst surface coverage, as shown in Figure 4.8. The results are in agreement with those measured experimentally in some of these conditions (Figure 4.1). Under applied bias, lower TOFs are obtained, which is compatible with the smaller amount of charge accumulation in the conduction band of TiO_2 observed in Section 4.3.1. On the other hand, in ACN:H_2O 9:1 both with and without applied bias, the TOF increases with lower surface coverage and increasing electron concentrations. While these are approximate calculations, the results may indicate that the bi-molecular pathways operating at higher surface coverages slow down the production of hydrogen.

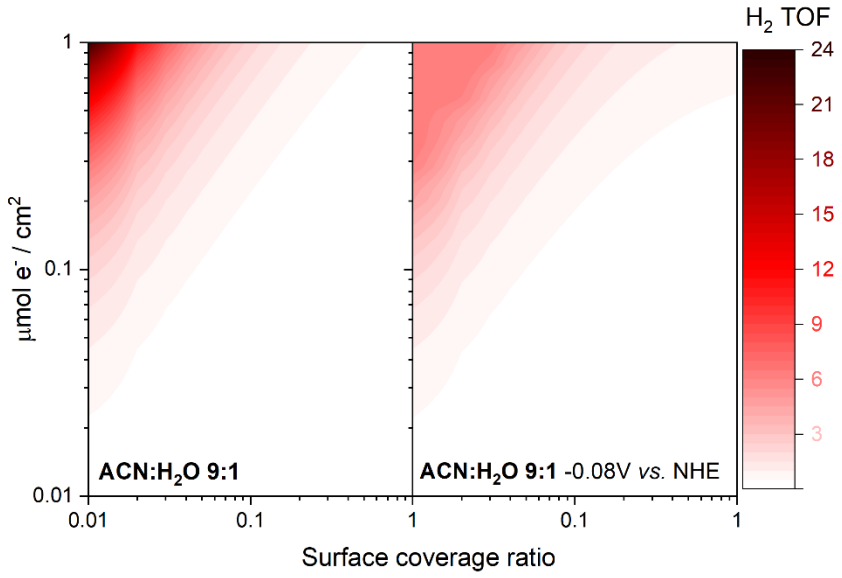

Figure 4.8. Simulation of the H_2 turnover frequency (TOF) in TiO_2-**CoP²** as a function of the light excitation power and the surface catalyst coverage in ACN:H_2O 9:1 without (*left*) and with (*right*) a -0.08-V applied bias. The reaction rate constants were derived by fitting the reactions 4.1-5 to the transient optical signal (Figure 4.11).

4.4. Discussion

Identifying catalytic intermediates and measuring their kinetics is a challenging task because of their fast reactivity, the coexistence of different reaction pathways and the presence of different species under photocatalytic conditions. By combining spectroelectrochemistry and TD-DFT, and based on established literature, it has been possible to detect and assign under catalytic conditions the characteristic optical signals of different protonated and multi-reduced catalytic intermediates of the H_2-production molecular catalysts **CoP²** and **CoP¹**. The unprecedented detection of their formation and reactivity under photocatalytic conditions has been possible with transient absorption spectroscopy using high excitation powers, which have generated high enough concentrations of intermediate species.

Similar catalytic species in both **CoP¹** and **CoP²** have been proposed to be part of the H_2-production mechanism. With TD-DFT, the spectra of these possible species was calculated in ACN:H_2O 9:1 conditions, considering the replacement of the axial ligands by either water or acetonitrile solvent molecules. In the case of **CoP²**, only species without the initial bromide ligands were considered because of their more favourable energetics. In the case of **CoP¹**, the loss of the pyridine ligand would lead to the detachment of the species and, as a consequence, no optical signal would be detected at the surface of the electrode. Therefore, the most likely species of **CoP¹** detected optically are those with the pyridine ligand, although some detached catalyst molecules could remain trapped in the TiO_2 pores. The degradation of either **CoP¹** or **CoP²** would lead to the loss of the optical signal and, because the optical signal does not change by more than 10% within the scope of the measurements presented herein, it is discarded as a possible explanation of the observed behaviour. Disagreements of ~50 nm in the experimental and theoretical absorption spectra are most likely due to the various possible combinations of axial coordinated solvent molecules and the structural simplifications. From spectroelectrochemistry and TD-DFT, the absorbance below 450 nm under an applied potential close to the TiO_2 conduction band limit was assigned to Co^{II} in both catalysts. At more reductive applied potentials, **CoP²** absorbs at 600 and 700 nm, which was assigned to the presence Co^{I} and Co^{II}-H (Figures 4.1-2), while **CoP¹** has major signals around 500, 650 and 700 nm, assigned to Co^{I}, Co^{II} and Co^{III}-H respectively (Figures 4.5-6). The Co^{II}H in **CoP²** has an absorbance maxima at ~100 nm larger wavelengths (~0.3 eV) than Co^{II}-H in **CoP¹**, indicating a smaller splitting in the metal *d* orbitals t_{2g} and e_g, and more stable e_g orbitals in **CoP²** relative to **CoP¹**.[18-20]

With transient absorption spectroscopy, the formation of intermediate catalyst species could be visualised after the photoexcitation of TiO_2 and the transfer of charges to the catalyst (Scheme 4.2). The absorption kinetics of TiO_2-**CoP¹** were the same as the kinetics of bare TiO_2, while the transient spectra had a maximum at ~500 nm and the signal stretched until 700 nm (Figure 4.7). These results are compatible with a turnover frequency over 10^6, where **CoP¹** would quickly react with

photogenerated electrons before microseconds. As a result, after microseconds, only trapped electrons in TiO_2 and unreactive catalyst species would be left. The most likely catalyst species accounting for the 500-nm transient band and which could be a product from H_2 production is Co^{II} and, less certainly, Co^{III}-H (Scheme 4.2). The latter species has been proposed to be able react with protons or with Co^{III}-H to evolve H_2,[9, 10] but the transient absorption of **CoP¹** includes the accumulation of Co^{III}-H. Instead the lower intensity of the transient absorbance at 600 nm in ACN:H_2O compared to ACN (Figure 4.7C-D) indicates that Co^{II}-H is more reactive in water than Co^{III}-H. In contrast to **CoP¹**, the formation and depletion of catalyst intermediates of **CoP²** is clearly identified in the microsecond to second timescale. The species Co^{II}-H forms in hundreds of microseconds and then reacts in hundreds of milliseconds, most likely to evolve hydrogen through either a mono- or a bi-molecular pathway. Therefore, Co^{II}-H is involved in the catalytic cycle of both **CoP¹** and **CoP²**, but its formation is at least two orders of magnitude smaller in **CoP²** than in **CoP¹**. Better activities and faster kinetics in these cobalt octahedral complexes would be achieved by decreasing the stability of the metal *d* orbitals, as illustrated in Scheme 4.2B-C.

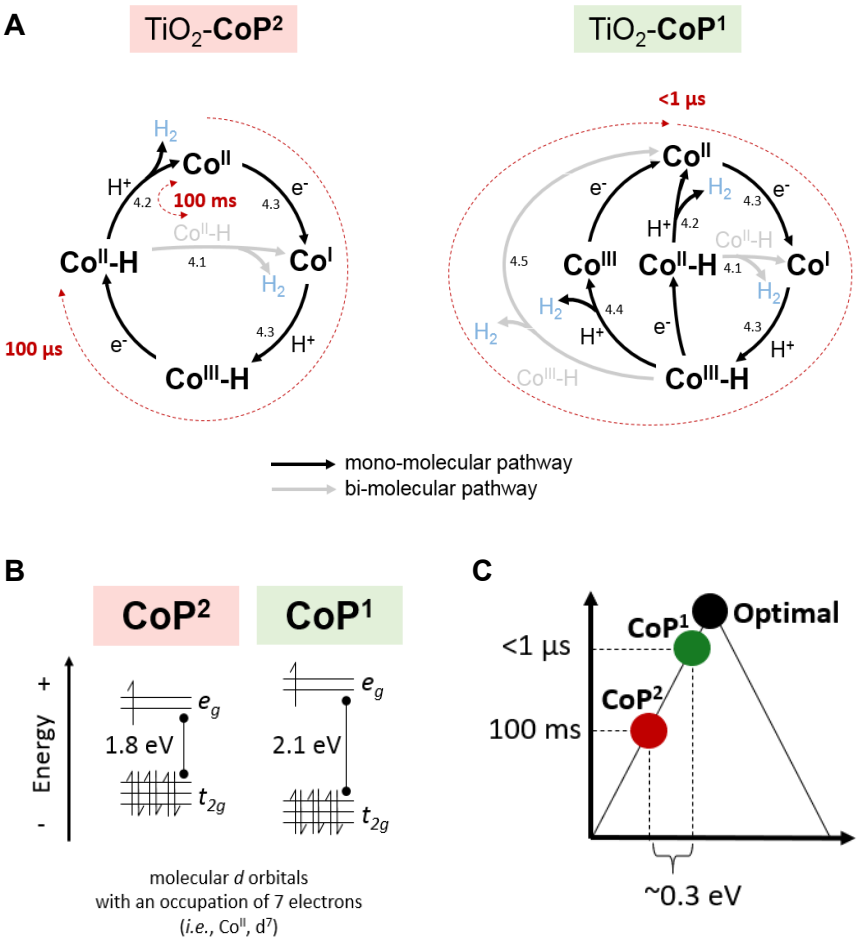

Scheme 4.2. **(A)** H_2-production mechanism of TiO_2-**CoP²** (*left*) and TiO_2-**CoP¹** (*right*) and its kinetics, as deduced from transient absorption, spectroelectrochemistry and TD-DFT. **(B)** Energy diagram and electronic occupancy of the molecular *d* orbitals of the Co^{II} state in the two catalysts. **(C)** Relationship between the kinetics and the orbital relative energy represented as a volcano plot.

Measuring the amount of H_2 produced over time per molecule of catalyst is an alternative way to estimate the time one catalyst molecule takes to undergo a complete catalytic cycle. The H_2-production catalytic rates were measured following this procedure in Sections 4.3.1 and 4.7.1 and they coincide with the TOF in TiO_2-**CoP²** estimated from the transient absorption kinetics assuming Reaction 4.1-5 (Figure 4.8). In contrast, the TOF of **CoP¹** estimated from either photo- or electrochemical experiments, is orders of magnitude slower than the deduced from its transient absorption kinetics. The smaller activity in these experiments may be a consequence of its fast degradation, while time-resolved spectroscopy would only detect active catalyst. Because of the fast reactivity, the kinetics of different catalytic steps in **CoP¹** could not be measured. However, the similarities in the nature of the catalytic species and the catalytic mechanism in the two catalyst make the findings on **CoP²** easier to extrapolate to **CoP¹**. The **CoP¹** has probably the same reaction pathways as **CoP²** and, potentially, due to linear scaling relationships, the kinetics of the different steps in **CoP¹** are proportional to those in **CoP²** but at faster timescales. Compared to other photo(electro)chemical systems such as dye-sensitized solar cells, molecular catalysts on semiconductor surfaces can engage in a larger variety of reactions, other than recombination with photogenerated charges and energy transfer across the surface.[21, 22] In particular, the coexistence of bi- and mono-molecular pathways adds complexity to the mechanism kinetics and H_2-production efficiency. The deconvolution of the kinetics of the transient absorption of the TiO_2-**CoP²**, suggests that the bi-molecular reaction pathways compete with mono-molecular pathways at higher surface coverage, decreasing the catalyst efficiency.

4.5. Conclusions

The optical signal of different singly- and multi-reduced intermediates of the H_2-production molecular catalysts **CoP^1** and **CoP^2** immobilised on TiO_2 have been assigned by comparing the experimental absorbance spectra with TD-DFT simulated spectra in the presence of water. Errors of around 50 nm between the theoretical and experimental spectra are most likely related to different combinations of coordinated solvent molecules and structural simplifications. Both in TiO_2-**CoP^1** and TiO_2-**CoP^2**, Co^{II} is detected at less reducing applied potentials above the conduction band of TiO_2 in the dark, while Co^{II}-H and Co^{I} are probably formed at more reducing potentials. In addition, the presence of Co^{III}-H is detected in TiO_2-**CoP^1**. In microseconds to seconds, the transient spectra of TiO_2-**CoP^1** is most likely related to accumulated Co^{II}, which cannot react with water. In parallel, the transient absorption kinetics of TiO_2-**CoP^1** species are limited by electron trapped in the TiO_2, potentially implying a catalytic cycle faster than microseconds. In TiO_2-**CoP^1**, the formation of Co^{II}-H from Co^{II} is detected in hundreds of microseconds, while its depletion into Co^{I} or Co^{II}, associated to bi- and mono- H_2-evolution respectively, takes place in hundreds of milliseconds. This would directly prove that Co^{II}-H is a key catalytic intermediate in both **CoP^1** and **CoP^2** catalysts, and its reaction with protons or hydrates is most likely the rate-determining step in **CoP^2**. The higher activity of **CoP^1** would be related to ~0.3-eV less stable molecular *d* orbitals compared to **CoP^2**.

4.6. References

1. V. Artero, M. Chavarot-Kerlidou and M. Fontecave, *Angew. Chem. Int.*, 2011, **50**, 7238-7266.
2. V. Artero and J. M. Savéant, *Energy Environ. Sci.*, 2014, **7**, 3808-3814.
3. F. Lakadamyali and E. Reisner, *Chem. Commun.*, 2011, **47**, 1695-1697.
4. J. Willkomm, K. L. Orchard, A. Reynal, E. Pastor, J. R. Durrant and E. Reisner, *Chem. Soc. Rev.*, 2016, **45**, 9-23.
5. J. Willkomm, N. M. Muresan and E. Reisner, *Chem. Sci.*, 2015, **6**, 2727-2736.
6. N. M. Muresan, J. Willkomm, D. Mersch, Y. Vaynzof and E. Reisner, *Angew. Chem. Int.*, 2012, **51**, 12749-12753.
7. M. R. Scherer, N. M. Muresan, U. Steiner and E. Reisner, *Chem. Commun.*, 2013, **49**, 10453-10455.
8. J. L. Dempsey, B. S. Brunschwig, J. R. Winkler and H. B. Gray, *Acc. Chem. Res.*, 2005, **42**, 1995-2004.
9. B. H. Solis and S. Hammes-Schiffer, *Inorg. Chem.*, 2011, **50**, 11252-11262.
10. B. H. Solis and S. Hammes-Schiffer, *J. Am. Chem. Soc.*, 2011, **133**, 19036-19039.
11. A. Bhattacharjee, M. Chavarot-Kerlidou, J. L. Dempsey, H. B. Gray, E. Fujita, J. T. Muckerman, M. Fontecave, V. Artero, G. M. Arantes and M. J. Field, *ChemPhysChem*, 2014, **15**, 2951-2958.
12. C. J. Barbé, F. Arendse, P. Comte, M. Jirousek, F. Lenzmann, V. Shklover and M. Grätzel, *J. Am. Ceram. Soc.*, 1997, **80**, 3157–3171.
13. J. N. Clifford, E. Palomares, M. K. Nazeeruddin, R. Thampi, M. Grätzel and J. R. Durrant, *J. Am. Chem. Soc.*, 2004, **126**, 5670-5671.
14. S. Ito, T. N. Murakami, P. Comte, P. Liska, C. Grätzel, M. K. Nazeeruddin and M. Grätzel, *Thin Solid Films*, 2008, **516**, 4613-4619.
15. F. Lakadamyali, A. Reynal, M. Kato, J. R. Durrant and E. Reisner, *Chem. Eur. J.*, 2012, **18**, 15464-15475.
16. G. Redmond, D. Fitzmaurice and M. Grätzel, *J. Phys. Chem.*, 1993, **97**, 6951-6954.
17. B. Enright, G. Redmond and D. Fitzmaurice, *J. Phys. Chem. B*, 1994, **98**, 6195-6200.
18. Photochemistry and Photophysics of Coordination Compounds I, V. Balzani, S. Campagna, A. de Meijere, K. N. Houk, H. Kessler, J.-M. Lehn, S. V. Ley, S. L. Schreiber, J. Thiem, B. M. Trost, F. Vögtle and H. Yamamoto, *Springer, Topics in Current Chemistry*, 2007.
19. Photochemistry and Photophysics of Coordination Compounds II, V. Balzani, S. Campagna, A. Barbieri, F. Barigelletti, E. C.-C. Cheng, L. Flamigni, T. Gunnlaugsson, R. A. Kirgan, D. Kumaresan, J. P. Leonard, C. B. Nolan, D. P. Rillema, C. Sabatini, R. H. Schmehl, K. Shankar, F. Stomeo, B. P. Sullivan, S. Vaidya, B. Ventura, J. A. G. Williams and V. W.-W. Yam, *Springer, Topics in Current Chemistry*, 2007.
20. Photochemistry and photophysics: concepts, research, applications, V. Balzani, P. Ceroni and A. Juris, *Wiley-VCH*, 2014.
21. D. Moia, V. Vaissier, I. López-Duarte, T. Torres, M. K. Nazeeruddin, B. C. O'Regan, J. Nelson and P. R. F. Barnes, *Chem. Sci.*, 2014, **5**, 281-290.
22. S. A. Trammell and T. J. Meyer, *J. Phys. Chem. B*, 1999, **103**, 104-107.
23. C. Lee, W. Yang and R. G. Parr, *Phys. Rev. B Condens. Matter*, 1988, **37**, 785-789.
24. A. D. Becke, *Phys. Rev. A*, 1988, **38**, 3098-3100.
25. A. D. Becke, *J. Chem. Phys.*, 1993, **98**, 5648-5652.
26. F. Weigend, *Phys. Chem. Chem. Phys.*, 2006, **8**, 1057-1065.
27. F. Weigend and R. Ahlrichs, *Phys. Chem. Chem. Phys.*, 2005, **7**, 3297-3305.
28. M. M. Francl, W. J. Pietro, W. J. Hehre, J. S. Binkley, M. S. Gordon, D. J. DeFrees and J. A. Pople, *J. Chem. Phys.*, 1982, **77**, 3654.
29. W. J. Hehre, R. Ditchfield and J. A. Pople, *J. Chem. Phys.*, 1972, **56**, 2257-2261.
30. V. A. Rassolov, J. A. Pople, M. A. Ratner and T. L. Windus, *J. Chem. Phys.*, 1998, **109**, 1223-1229.
31. F. Neese, *WIREs Comput. Mol. Sci.*, 2012, **2**, 73-78.
32. S. Sinnecker, A. Rajendran, A. Klamt, M. Diedenhofen and F. Neese, *J. Phys. Chem. A*, 2006, **110**, 2235-2245.

33. L. G. Gagliardi, C. B. Castells, C. Ràfols, M. Rosés and E. Bosch, *J. Chem. Eng. Data*, 2007, **52**, 1103-1107.
34. S. Grimme, J. Antony, S. Ehrlich and H. Krieg, *J. Chem. Phys.*, 2010, **132**, 154104.
35. S. Grimme, S. Ehrlich and L. Goerigk, *J. Comput. Chem.*, 2011, **32**, 1456-1465.
36. M. D. Hanwell, D. E. Curtis, D. C. Lonie, T. Vandermeersch, E. Zurek and G. R. Hutchison, *J. Cheminformatics*, 2012, **4**.

4.7. Annex

4.7.1. H_2 production experiments

The H_2 production experiments in Figure 4.1 were carried out by Dr. Ravi Shankar in a purpose-built liquid/solid Teflon-lined reactor setup. A solid Teflon filler was inserted into the Teflon vessel to occupy 50 % of the vessel volume. The TiO_2-CoP^2 films on FTO glass were fixed horizontally on the top surface of the Teflon filler, with the TiO_2-CoP^2 films on the top. The vessel was filled with 22 mL of the electrolyte mixture containing ACN:H_2O in 9:1 v/v ratio, 0.1 M $TBAPF_6$, and 0.1 M TEOA aqueous solution. The vessel was inserted in a closed stainless steel reactor. Zero grade (99.998%) N_2 gas was bubbled through a solution of acetonitrile at controlled rates using mass flow controllers (*Omega Engineering*, 0 to 100 mL min^{-1}). The system was purged with N_2 gas bubbled through ACN for 30 min to ensure that purge gas flux was saturated with acetonitrile to prevent evaporation of the electrolyte. The photoreactor was vacuumed and replenished with N_2 five times. A Xe arc lamp (300 W, $\lambda > 325$ nm, *LOT Quantum Design*), equipped with a water filter was used as the irradiation source, irradiating the samples through the TiO_2 surface where the catalyst was loaded. The total lamp intensity at the sample was 1750 W/m^2 between 315 and 900 nm (455 W/m^2 at 314-500 nm). Under semibatch operation, the reactor was pressurised up to 1.28 bar, with the evolved gases sampled after 5 hours of irradiation. The evolved gases were detected using a gas chromatograph (*Agilent Technologies*, 7890B), which was equipped with *Hayesep* (*Agilent J&W*, 6 foot, 1/8 inch, 2 mm, *HayeSep Q Column* 80/100 *SST*) and molecular sieve (*Agilent J&W*, 6 foot, 1/8 inch, 2 mm, *MolSieve* 5A, 60/80, preconditioned) packed columns in series.

4.7.2. Spectroelectrochemistry and Transient Absorption Spectroscopy

The spectroelectrochemistry data of TiO_2 is shown in Figure 4.9 and the complete transient absorption spectroscopy datasets of samples TiO_2, TiO_2-**CoP^1** and TiO_2-**CoP^2** are shown in Figures 4.10-11, using the procedures and setups described in Sections 2.3-4.

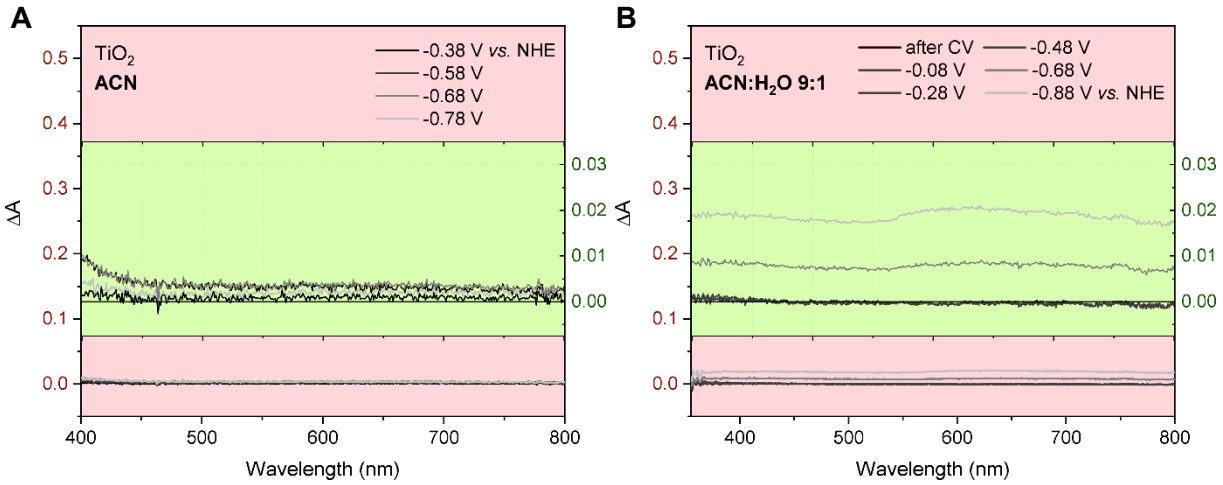

Figure 4.9. Differential absorption spectra of TiO_2 under different applied potentials in ACN **(A)** and ACN:H_2O 9:1 **(B)** with 0.1 M TEOA and 0.1 M $TBAPF_6$, relative to the spectrum under -0.08 V *vs.* NHE.

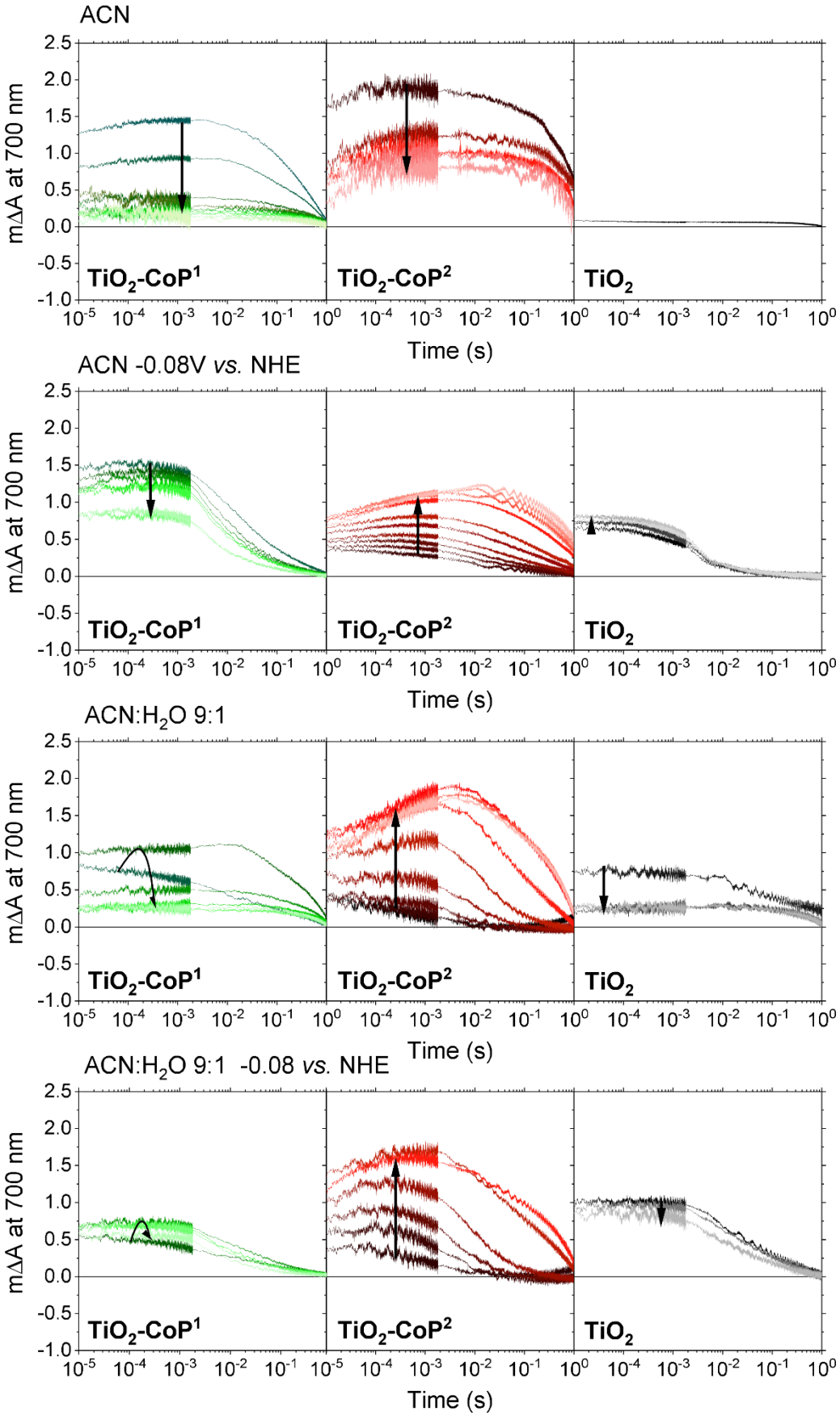

Figure 4.10. Consecutive measurements of fresh samples until the stabilisation of the signal. Transient absorption at 700 nm of TiO_2-**CoP^1** (*left*), TiO_2-**CoP^2** (*middle*) and TiO_2 (*right*) in four different electrolyte and potential conditions.

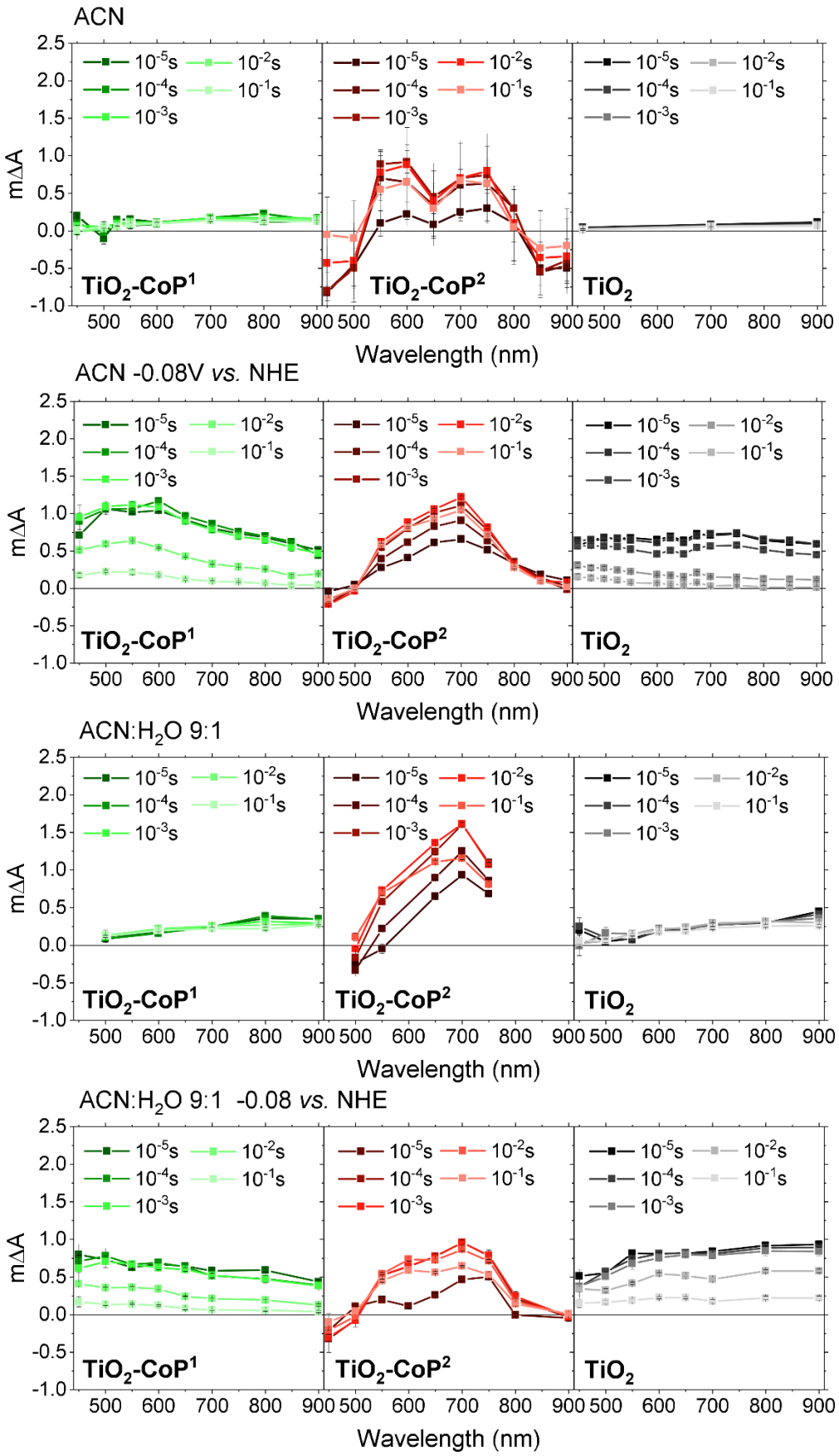

Figure 4.11. Transient spectra of TiO_2-**CoP^1** (*left*), TiO_2-**CoP^2** (*middle*) and TiO_2 (*right*) in four different electrolyte and potential conditions.

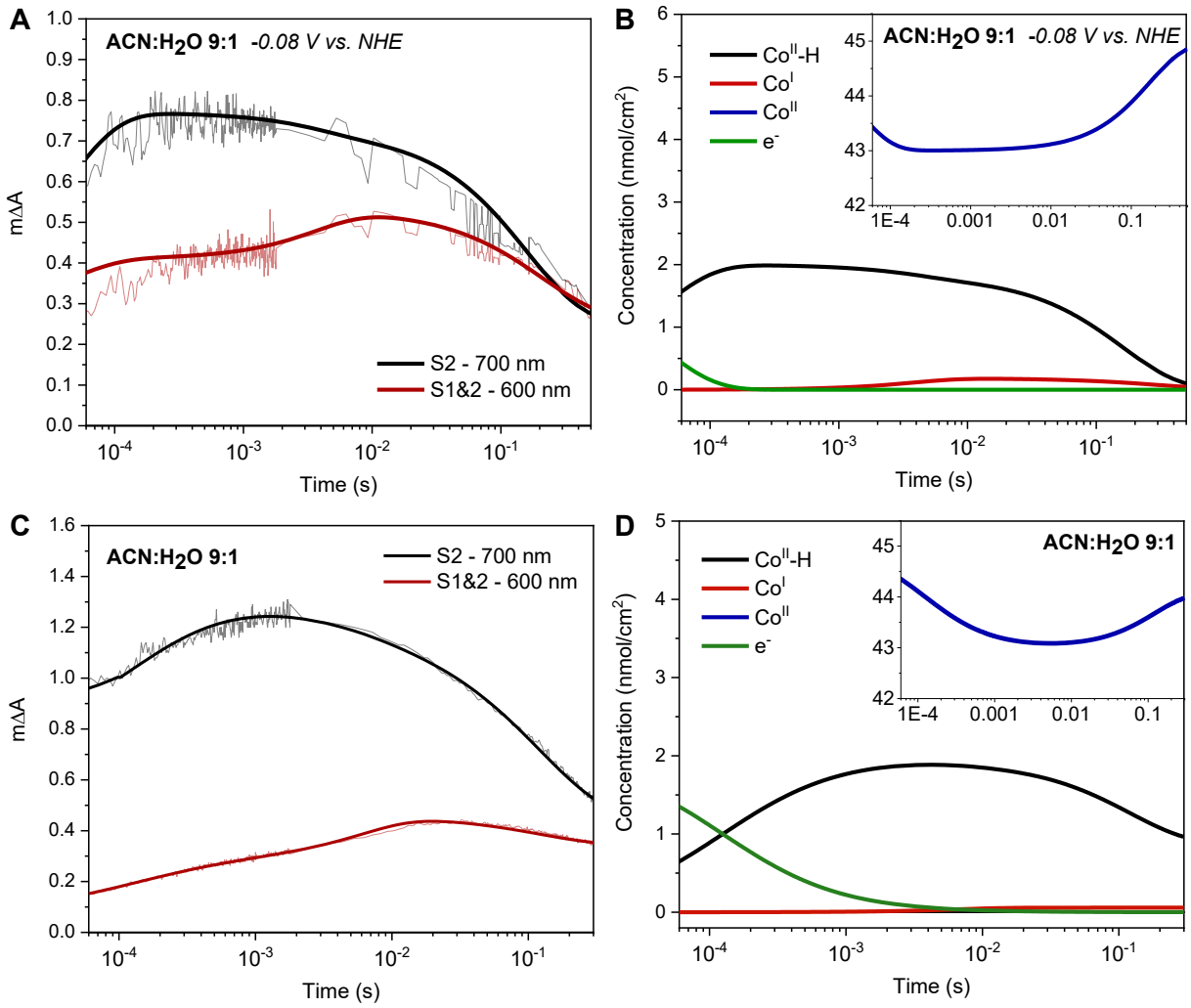

Figure 4.12. Transient absorption of TiO_2-**CoP²** fit with first and second order (Reactions 4.1-5), and the resulting concentration dynamics in ACN:H_2O 9:1 with (**A-B**) and without (**C-D**) a -0.08-V applied bias.

4.7.3. Time-dependent Density Functional Theory Calculations

Time-dependent Density Functional Theory Calculations (TD-DFT) were carried out by Dr. Annila Eisenschmidt. Fully optimised molecular structures were obtained through geometry optimisations employing the *B3LYP*[23-25] functional in conjunction with the *def2-TZVP*[26, 27] or the *6-31G(d,p)*[28-30] basis set. All calculations were conducted with *ORCA 4.0.1.2*.[31] Solvation was approximated by the conductor-like screening model *COSMO*[32] with the relative permittivity (dielectric constant) set to either 90% ACN and 10% water, *i.e.*, 40.39 or 100% water, *i.e.*, 80.14.[33] Long range Coulomb and Hartree Fock exchange interactions were included using the rijcosx approximation. Dispersion correction was conducted using the Grimme atom-pairwise correction with Becke-Johnson damping scheme.[34, 35]

Single point energy and frequency calculations were carried out on the optimised structures. All plots of computed structures were produced with *Avogadro 1.1.0*.[36] TD-DFT calculations were carried out with *ORCA 4.0.1.2* on geometry optimised structures using the same basis set as for the respective geometry optimisation. The structure and absorption spectra of all the intermediates considered here are provided below.

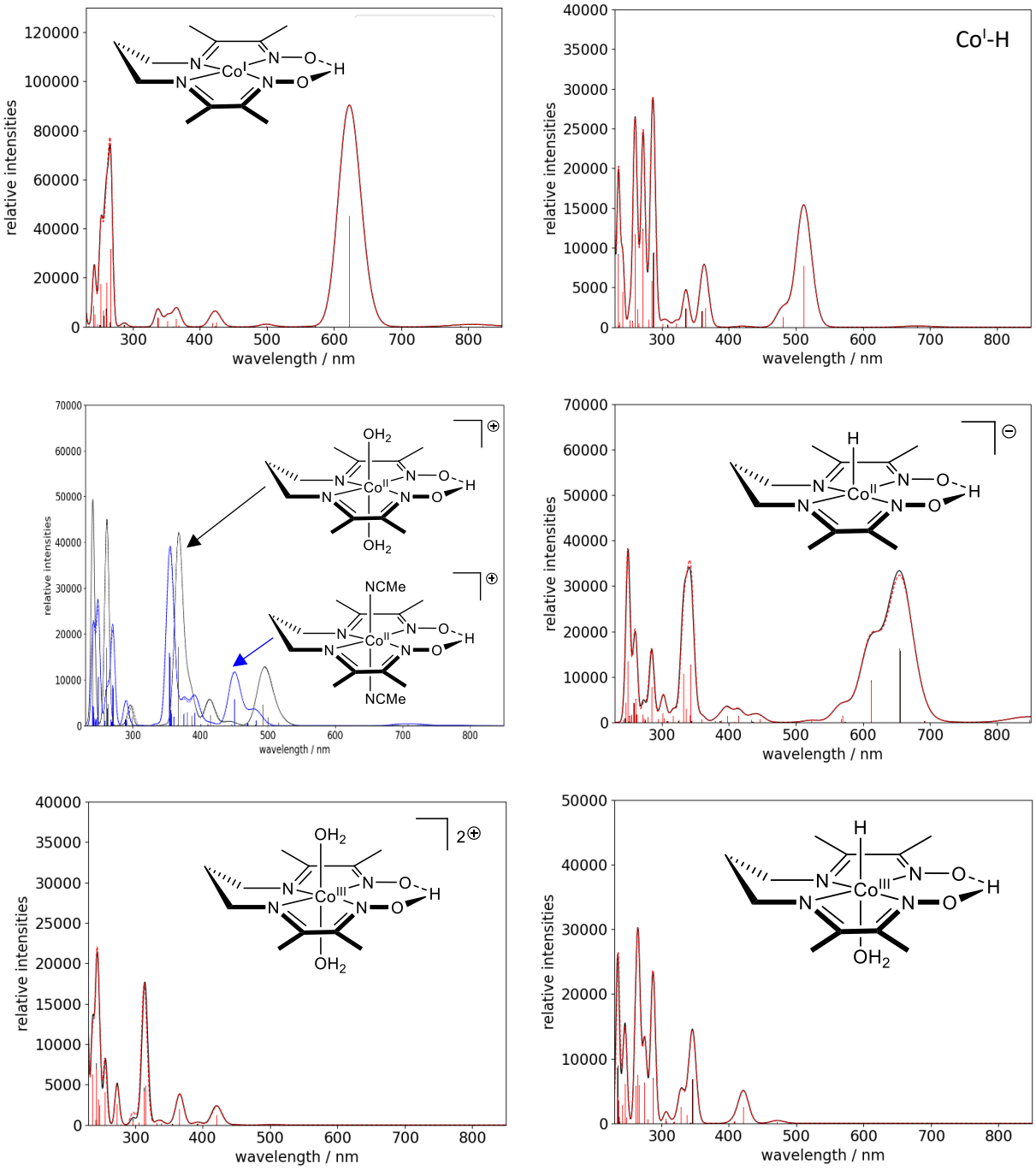

Figure 4.13. Theoretical spectra of different species of **CoP^2** in aqueous solution, calculated with *B3LYP-6-31G(d,p)* TD-DFT, and their corresponding optimised structures. These species include different oxidation states of the cobalt centre (Co^{III}, Co^{II} and Co^{I}) and different coordinated axial ligands (H^+, H_2O and acetonitrile=MeCN).

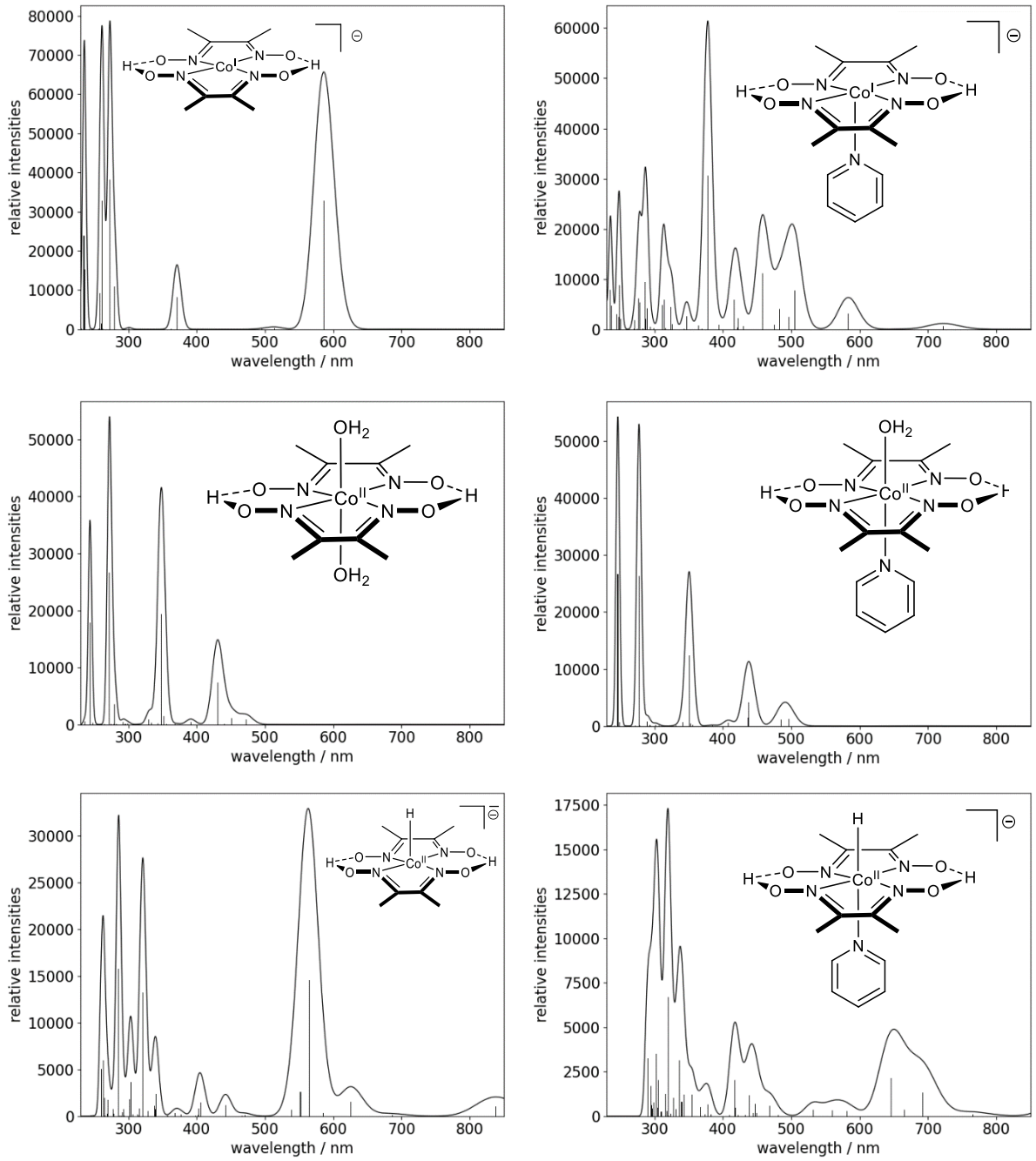

Figure 4.14. Theoretical spectra of different species of **CoP^{I}** with oxidation states Co^{I} and Co^{II} in aqueous solution, calculated with *B3LYP-6-31G(d,p)* TD-DFT, and their corresponding optimised structures. These species include different favourable coordinated axial ligands (H^{+} and H_2O), replacing the original pyridine and chloride ligands.

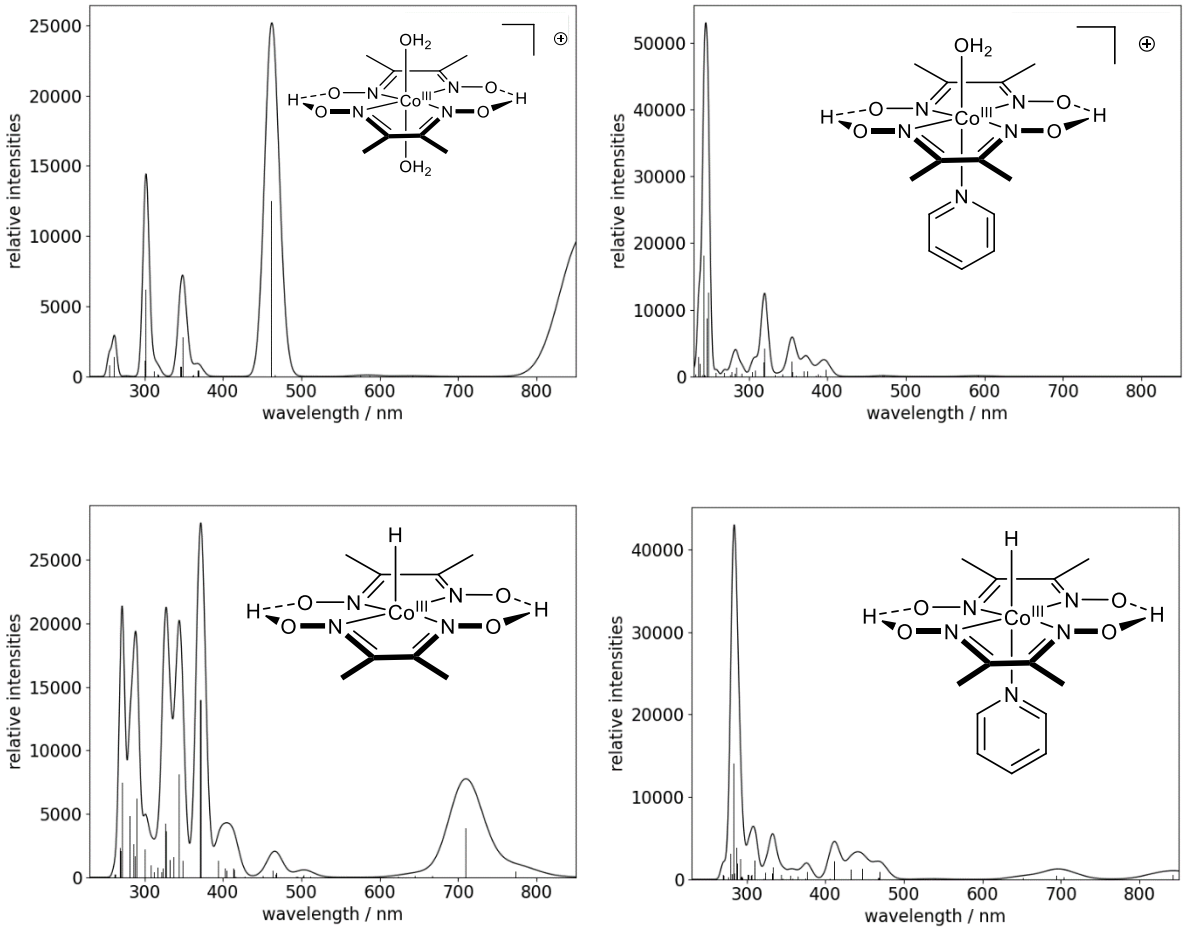

Figure 4.15. Theoretical spectra of different species of **CoP[1]** with an oxidation state Co^{III} in aqueous solution, calculated with *B3LYP-6-31G(d,p)* TD-DFT, and their corresponding optimised structures. These species include different favourable coordinated axial ligands (H^+ and H_2O), replacing the original pyridine and chloride ligands.

Chapter 5

Operando spectroelectrochemical analysis of active state kinetics in water-oxidation IrO_x electrocatalysts

Dr. Reshma R. Rao, Dr. Camilo A. Mesa, Prof. Ifan Stephens and Prof. James R. Durrant contributed to the discussion of the results. Xinyi Liu and Sam Hillman did the spectroelectrochemistry meausurements of some IrO_x samples.

Hydrous iridium oxide (IrO_x) is one of the best oxygen evolution electrocatalysts available but iridium is a scarce element, which limits the scalability of renewable energy conversion technologies based on this material. To maximize the catalytic activity of IrO_x per iridium atom, new strategies to understand its catalytic performance and mechanism at the atomic scale are needed. In this Chapter, a unique insight into the redox surface chemistry of electrodeposited IrO_x (Section 5.2.1) is provided, combining optical and electrochemical steady-state and time-resolved measurements. From spectroelectrochemistry experiments and its mathematical deconvolution (Section 5.2.2-4), three different redox surface states containing Ir^{3+}, Ir^{4+} and $Ir^{4.x+}$ have been identified, and their concentration has been quantified. By looking at the optical signal decay after applying different oxidising potentials (Section 5.2.5), the redox state containing mostly $Ir^{4.x+}$ has been determined to be the oxygen evolution reaction (OER) potential-limiting step, yielding lower-oxidised redox states consisting of Ir^{4+} and Ir^{3+}. The redox catalytic activity of the latter species has been further confirmed in the presence of H_2O_2 (Section 5.2.6). Finally, the derived lifetimes of the active redox state (Section 5.2.7) are observed to plateau and become independent of potential, something that would indicate a first order rate for the OER reaction.

5.0. Contents

5.1. Introduction

Iridium oxides are some of the best electrocatalyst materials for the oxygen evolution reaction (OER), one of the steps that limits the efficiency of emerging technologies converting renewable electricity into chemicals or fuels.[1-5] A particular advantage of iridium oxides is their high OER activities in the acidic conditions of state-of-the-art proton-exchange electrolysers.[5, 6] To overcome the scalability issues related to the scarcity of iridium,[7-9] researchers have focused on improving the OER activity of these materials per iridium atom, developing more porous and amorphous materials such as hydrous iridium oxides (IrO_x).[10-12] These IrO_x materials reach higher OER activities per mass of iridium than crystalline IrO_2, but have lower stabilities.[13-20] The activity of IrO_x, however, is difficult to understand because of their highly disordered structure and their complex redox chemistry. In this context, *in operando* techniques are a unique way to probe the redox states accumulated under catalytic conditions. Herein, we use time-resolved spectroelectrochemical methods to identify the active sites of IrO_x involved in OER and their reactivity.

The OER reaction at the catalyst-electrolyte interface can be framed as a localised molecular problem, providing a way to understand the intrinsic catalytic performance per iridium atom and / or intermediate state.[21-25] Experimentally, techniques such as X-ray[26-31] and Ultraviolet-Visible (UV-Vis) absorption,[32-35] and Raman[36, 37] spectroscopies have facilitated the identification of IrO_x surface species at different applied potentials under steady-state conditions. In these reports, it has become widely accepted that the redox state Ir^{3+} is oxidised to Ir^{4+} at potentials over the open circuit potential (OCP).[28, 31, 33, 38-40] There is less consensus on the exact nature of the oxygen and hydroxide bonded OER intermediates and, over the onset potential, the role of higher-oxidised redox states like Ir^{5+} and Ir^{6+} is still debated.[29, 41-43] In these steady-state spectroscopic measurements, it is not possible to quantify the concentration of species present and to determine if they are really part of the catalytic cycle. Given the uncertainty in the nature and concentration of active species, to evaluate the intrinsic catalytic activities, turnover frequencies (TOF) are commonly based either on the mass of catalyst, or on the assumption of a packed crystalline catalyst surface where all the surface iridium atoms are active sites.[44-47] However, this is not accurate in highly disordered materials like IrO_x because of the difficulty to measure the real surface area, the presence of undercoordinated iridium atoms, and the potential participation of bulk iridium. In contrast, the activity of IrO_x is directly related to the kinetics of its redox states and on their distribution *in operando*, which is most likely dependant on the applied potential.

By combining time-resolved spectroscopy and electrochemistry, we can identify several redox transitions in IrO_x as a function of potential and quantify the concentration of the resulting redox states. These techniques have been successfully applied to investigate water oxidation on Ni-based electrocatalysts in alkaline solution and hematite photoelectrodes,[25, 48, 49] but it is particularly challenging to use them on IrO_x because of its multiple redox states. In this work, we investigate electrodeposited IrO_x in 0.1 M $HClO_4$ aqueous solution at pH 1.2. A

spectroelectrochemical approach complemented with signal deconvolution methods is applied, followed by measurements of the optical signal lifetime after turning the applied potential off. The lifetimes and turnover frequency derived using this technique do not rely on assumptions about the density of active sites and are therefore more representative of the intrinsic kinetics of IrO_x species, providing a unique insight into the kinetics of electrochemical water oxidation in hydrous iridium oxides electrocatalysts.

5.2. Materials and Methods

5.2.1. Electrodeposition of IrO_x

Hydrous iridium oxide films (IrO_x) were prepared by electrodeposition following a well-established procedure.[50, 51] A solution of iridium salt was prepared by dissolving 0.2 mmol of $Ir^{3+}Cl_3$ hydrate (*Fluorochem*) and 2 mmol of oxalic acid dehydrate (*Sigma Aldrich*) in 30 mL of water. The pH was adjusted to 10 with ~5 mmol of Na_2CO_3 (*Sigma Aldrich, ReagentPlus® ≥ 99.0%*), making the solution turn from yellow to green. The volume of the solution was increased to 50 mL by adding more water. The solution was left to rest for 4 days at 35 ºC (the changes in its UV-Vis absorbance are shown in Figure 5.1) and was then stored in the freezer at 4 ºC. The electrodeposition of IrO_x from this iridium solution was done by soaking a clean FTO on a glass substrate (~1·2·0.2 cm^3) and applying a current of 35 µA for ~1000 s. Polyimide tape was attached on the FTO surface to limit the surface of the IrO_x to ~1·1 cm^2. This preparation procedure is similar to that in the literature.[50, 51]

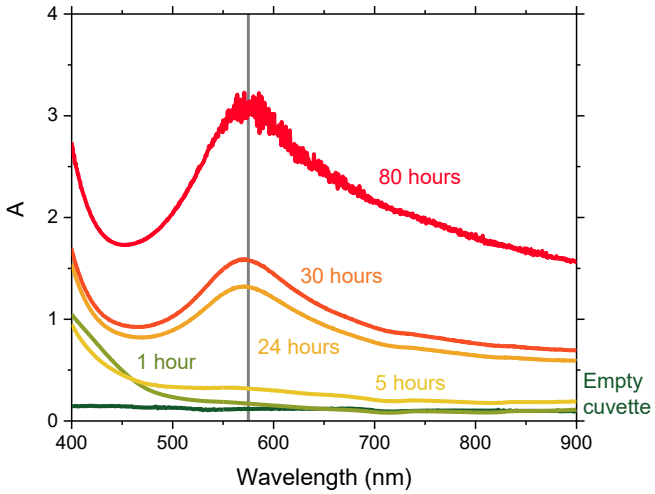

Figure 5.1. Absorbance over time of the aqueous solution with 4 mM $IrCl_3$ and 2 mM oxalic acid at pH 10. Measured by Dr. Reshma R. Rao.

5.3. Results

5.3.1. Electrochemistry of IrO_x

The cyclic voltammetry (CV) of the resulting films, shown in Figure 5.2A, features three different redox transitions, which are considered to lead to at least three different redox states. Two distinct capacitive bands are observed at ~0.95 V and ~1.25 V *vs.* RHE (iR_u corrected). At an onset potential of ~1.45 V, the current increases exponentially, similar to other porous IrO_x electrocatalysts (Figure 5.2B) and is related to the OER electrocatalysis. Because of the high current densities of the material, all the potentials were corrected by subtracting $i \cdot R_u$, where i is the current measured at the corresponding potential and R_u is the uncompensated resistance The resistance R_u (~35Ω) was calculated by fitting electrochemical impedance data in the 0.1-1Hz range with the Randles circuit model. Overall, these multiple redox transitions and their overlap illustrates the complexity of the redox chemistry on IrO_x surfaces. Notably, the OER activity is comparable to previous reports on amorphous films.[14, 18, 20]

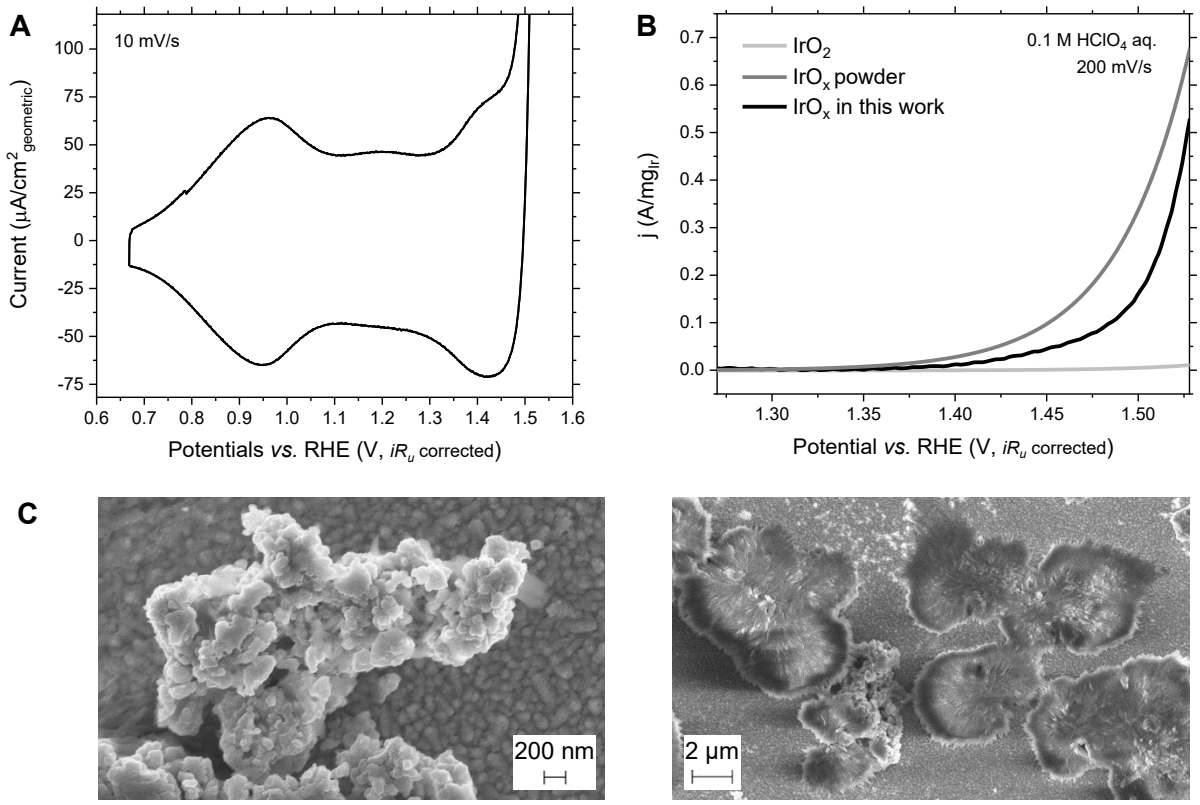

Figure 5.2. **(A)** Cyclic voltammetry of an IrO_x film electrodeposited on FTO and soaked in 0.1 M $HClO_4$ aqueous solution at pH 1.2, with a scanning speed of 100 mV/s and starting at ~0.8 V *vs.* RHE (iR_u corrected). **(B)** Current density normalised by mass of iridium of the IrO_x samples investigated in this work and IrO_x and IrO_2 reported in the literature,[18] measured in 0.1 M $HClO_4$ aqueous solution with a scan rate: of 200 mV/s. **(C)** Scanning electron microscopy (SEM) pictures of IrO_x on FTO measured by Dr. Reshma Rao.

5.3.2. Spectroelectrochemistry

To better identify the redox states of IrO_x in the cyclic voltammetry above, the absorbance of IrO_x films was measured at different applied potentials in 0.1 M $HClO_4$ aqueous solution at pH 1.2 (see Section 2.3 for the technical details). The absorbance was first measured at a potential around the open circuit potential (~0.8 V *vs.* RHE) and was subsequently monitored at increasingly oxidising applied potentials until 1.52 V *vs.* RHE, above the catalytic onset potential. In this potential range, broad absorbance changes were observed across the visible range (Figure 5.3A): a band at 600 nm dominated the differential spectrum at low oxidation potentials, and two new features at 800 nm and 480 nm appeared above 1.11 V and 1.36 V *vs.* RHE respectively (Figure 5.3B). These optical changes roughly coincide with the redox transitions detected between the open circuit potential and the onset potential in the cyclic voltammetry (Figure 5.2A). These results therefore show that the three redox transitions above the open circuit potential have characteristic absorbance signals, similar to the electrochromism of other IrO_x films reported in the same potential range.[32, 33, 40, 50, 52, 53] Below, we go one step further deconvolving these absorbance trends to quantitatively analyse the reactivity of the different redox states involved, a useful approach to circumvent the overlap between redox and catalytic processes.

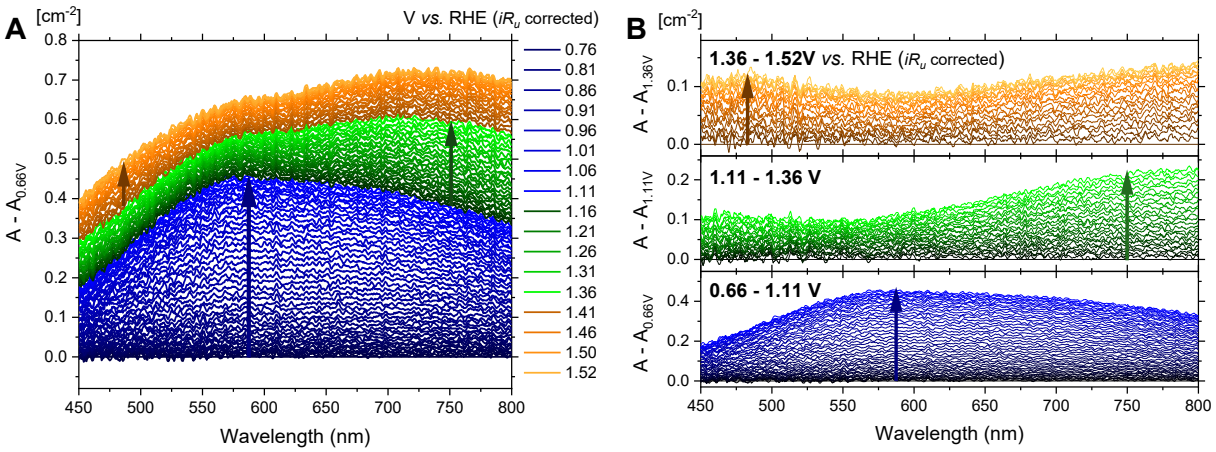

Figure 5.3. Absorbance changes of IrO_x upon applying an oxidative potential in 0.1 M $HClO_4$ aqueous solution at pH 1.2. Absorbance changes calculated with respect to **(A)** 0.66 V, and **(B)** 0.66 V (*bottom*), 1.11 V (*middle*), and 1.36 V (*top*) *vs.* RHE, (iR_u corrected).

5.3.2.1. Deconvolution of spectroelectrochemical data

To investigate individually the redox states of IrO_x, the absorption changes detected in Figure 5.3 were deconvoluted as a function of the redox transition and the corresponding redox state. Model data $\Delta A_{fit}(E,\lambda)$ was built by making four approximations, where ΔA is the absorbance difference as a function of the potential E and the wavelength λ. First, taking into account the data above, we assumed three different contributions $A_i(E,\lambda)$ to the absorbance (Equation 5.1), where i is the redox transition number. Second, following the Lambert-Beer law, the absorbance changes were considered linearly proportional to the concentration of the redox state formed at each transition (Equation 5.2), $C_i(E)$. Third, the concentration of the redox state formed at each potential was approximated as a Gaussian distribution over potential (Equation 5.3), which is expected to be a good representation of capacitive redox transitions but a less accurate approximation for the onset of catalytic and Faradaic processes. Fourth, the absorption coefficients $\varepsilon_i(\lambda)$ were calculated from the experimental absorbance at three different potentials following Equations 5.1-2 (Equations 5.4-6). The model data was fit to the experimental data by adjusting the center (μ), width (σ) and amplitude (A) of the Gaussian distributions ($A \cdot Gaussian(\mu,\sigma)$), corresponding to the concentration changes over potential of each redox state. The process of fitting sought to minimise the difference between the experimental and the model data ($|\Delta A_{real}(E,\lambda) - \Delta A_{fit}(E,\lambda)|$) across all the wavelengths and potentials (see Section 2.7 for more details on the optimisation method). As a result, this procedure allowed separating the contributions to the absorbance of the three different redox transitions with a minimal error (Figure 5.4).

Equation 5.1 $$\Delta A_{fit}(E,\lambda) = A_1(E,\lambda) + A_2(E,\lambda) + A_3(E,\lambda)$$

Equation 5.2 $$A_i(E,\lambda) = C_i(E) \cdot \varepsilon_i(\lambda)$$

Equation 5.3 $$C_i(E) = \int_{0.55}^{E} \left(\frac{\mathrm{d}C}{\mathrm{d}E}\right) \mathrm{d}E = \int_{0.55}^{E} A \cdot Gaussian(\mu,\sigma)\, \mathrm{d}E$$

Equation 5.4 $$\varepsilon_1(\lambda) = \frac{\Delta A_{real}(0.8V,\lambda)}{C_1(0.8V)}$$

Equation 5.5 $$\varepsilon_2(\lambda) = \frac{\Delta A_{real}(1V,\lambda) - C_1(1V) \cdot \varepsilon_1(\lambda)}{C_2(1V)}$$

Equation 5.6 $$\varepsilon_3(\lambda) = \frac{\Delta A_{real}(1.5V,\lambda) - C_1(01.5V) \cdot \varepsilon_1(\lambda) - C_2(1.5V) \cdot \varepsilon_2(\lambda)}{C_3(1.5V)}$$

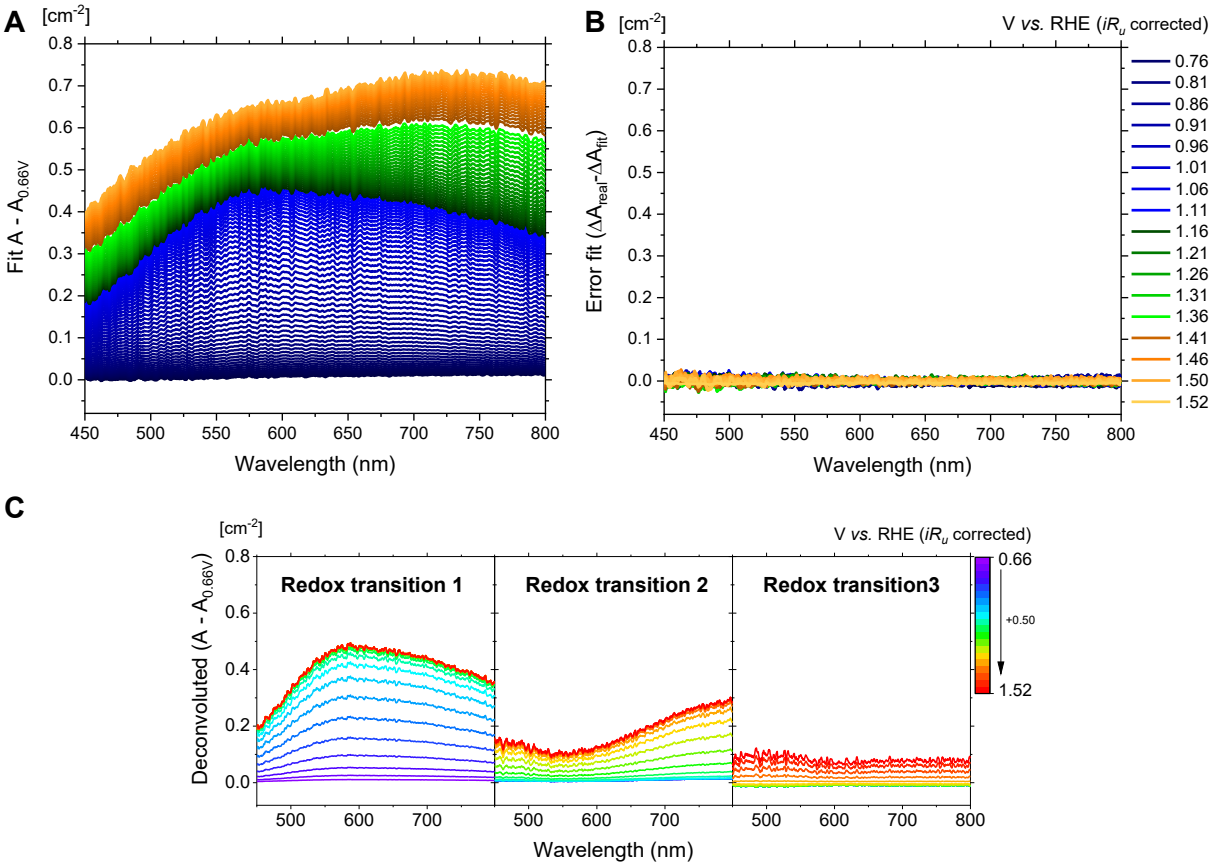

Figure 5.4. **(A)** Best fit of the spectroelectrochemical data in Figure 5.3 generated with Equations 5.1-6. **(B)** Difference between the experimental data in Figure 5.3 and the model data in Figure 5.4A. **(C)** Absorbance changes over potential associated to each redox transition, as derived from the model data in Figure 5.4A with Equations 5.1-6.

5.3.2.2. Assignment of spectroelectrochemical data

As a result of the deconvolution described above, differential absorption coefficients and concentration distributions of redox states were obtained for each redox transition. Figure 5.5 shows these parameters after being adjusted against the experimental values of $\varepsilon_1(600\ nm)$, $\varepsilon_2(800\ nm)$ and $\varepsilon_3(460\ nm)$, a calculation that is described in the following sub-section. From these results, it becomes clear that the three redox redox states resulting from the three different redox transitions are formed at ~0.9 V, ~1.3 V and ~1.5 V *vs.* RHE (iR_u corrected), and have characteristic differential absorbances at 600, 800 and 460 nm respectively. This evidence is in agreement with the dark-blue coloration reported for IrO_x at 0.8-1.3 V *vs.* RHE, which is independent of pH and has little hysteresis. These optical transitions have traditionally been assigned to an intervalence charge transfer within the iridium *d* orbitals derived from the oxidation of Ir^{3+} to Ir^{4+}.[32, 33, 39, 40, 52, 54, 55] Recent evidence suggests that the redox transitions 1 and 2 (detected in the CV in Figure 5.2 and represented more precisely in Figure 5.5A) are due to the oxidation of Ir^{3+} to Ir^{4+} in different steps, and that the existence of stable states including both Ir^{3+} and Ir^{4+} is possible and has characteristic absorbance features in the visible range.[34, 37, 56] The latter is compatible with our observation of two initial redox transitions with different absorption spectra. With respect to the redox transition 3, it is assigned to the oxidation of Ir^{4+}.[28-30, 38] Therefore, the starting state of the material is called **Ir(3+)**, the redox state resulting from the redox transition 1 is called **Ir(3.x+)**, the redox state from the redox transition 2 is called **Ir(4+)**, and the redox state from redox transition 3 is **Ir(4.x+)**. This terminology aims at representing the iridium oxidation numbers present at each redox state, but not their exact stoichiometry; it is used from here onwards to refer to the four redox states.

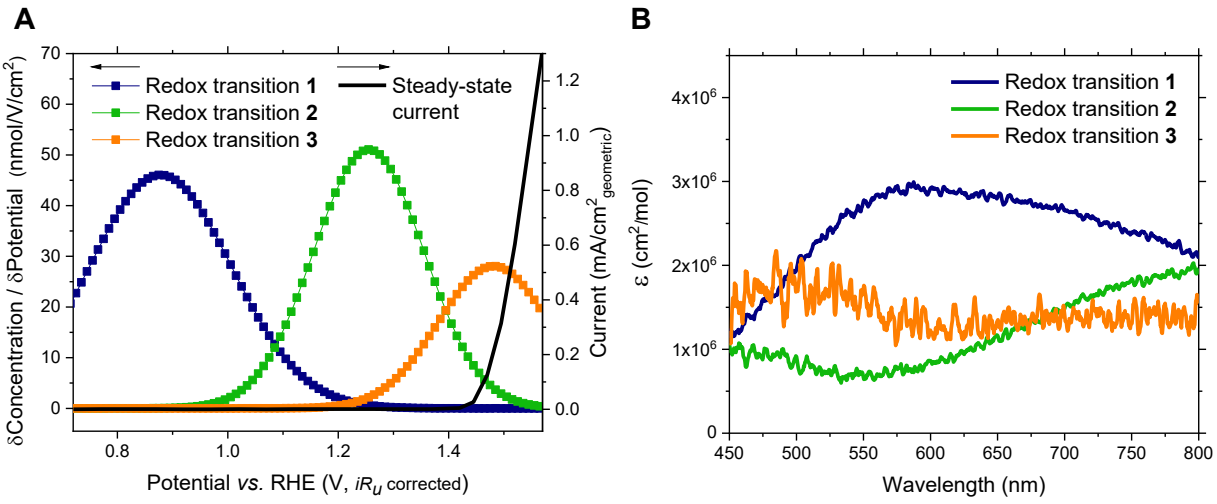

Figure 5.5. **(A)** Change in the concentration of redox states over potential in contrast with the steady-state current under constant applied potential, and **(B)** differential absorption coefficients corresponding to the deconvolution and calibration of the three redox transitions fit to the spectroelectrochemical data in Figure 5.3.

5.3.3. Calculation of absorption coefficients

Because the concentrations and differential absorption coefficients derived from the previous deconvolution have arbitrary units, these parameters were calibrated with the experimental values of $\varepsilon_1(600\ nm)$, $\varepsilon_2(800\ nm)$ and $\varepsilon_3(460\ nm)$, as mentioned before. These differential absorption coefficients were estimated from the concentration of states and absorbance changes at potentials were only one redox transition takes place. To quantify the concentration of states, the transient current density was measured during potential cycles where two potentials with a difference of 50 mV were applied in consecutive steps of 5 s and 8 s (as illustrated in Scheme 5.1). This technique is called Step Potential Spectroelectrochemistry (SP-SEC) and is described in more detail in Section 2.6. When changing the applied potential, the current peaks and, after ~1 s, stabilises (Figure 5.6A). This current spike is assumed to be mostly due to the oxidation and reduction of states in IrO_x, in contrast to the OER that drives the steady-state current after 1 s. Therefore, in order to estimate the moles of redox state formed at each potential interval, the current spike was integrated over time after subtracting the steady-state current. For each redox transition, the extracted charges were measured at potential intervals around 0.9 V, 1.2 V and 1.5 V where only redox transition 1, 2 and 3 are expected to occur respectively, as deduced from Figure 5.5A.

To calculate the differential absorption coefficients of the redox state formed at each redox transition, the deconvoluted absorbance changes at the maximum absorbance wavelength (600, 800 and 460 nm for the redox transitions 1, 2 and 3 respectively) were plotted against the moles of extracted charges removed from the film for each redox transition (Figures 5.6B-D). The slope of the linear regression was taken as the differential absorption coefficient ($\varepsilon_i(\lambda_{max.})$ in Equation 5.2), corresponding to the relative absorbance change per one-electron-oxidised redox state during each redox transition. Having calculated $\varepsilon_1(600\ nm)$, $\varepsilon_2(800\ nm)$ and $\varepsilon_3(460\ nm)$, the differential absorption coefficients and the concentration changes over potential were adjusted accordingly in Figure 5.5A-B following Equation 5.2. It is apparent from Figure 3A that the area below the concentration distributions, resulting from one-electron oxidations, is similar in redox transitions 1 and 2, and larger than in redox transition 3. This indicates that the 3rd redox transition involves a smaller amount of charges than the previous ones, which is probably related to a relatively smaller concentration of the resulting redox state compared to lower-oxidised redox states.

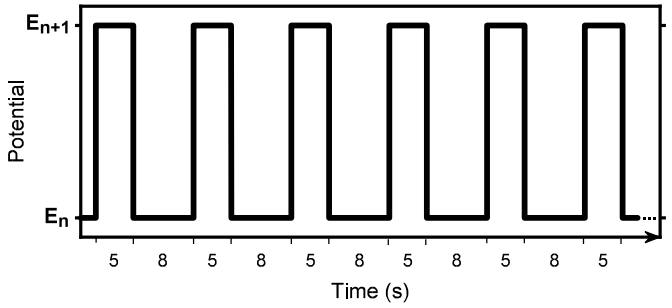

Scheme 5.1. Potential steps in a step potential spectroelectrochemistry measurement (SP-SEC). Consecutively and in cycles, the potential E_n is applied during 8 s, and the potential E_{n+1} is applied during 5 s. Simultaneously, the absorbance difference ΔA of the sample is monitored ($\Delta A = A(E_{n+1}) - A(E_n)$).

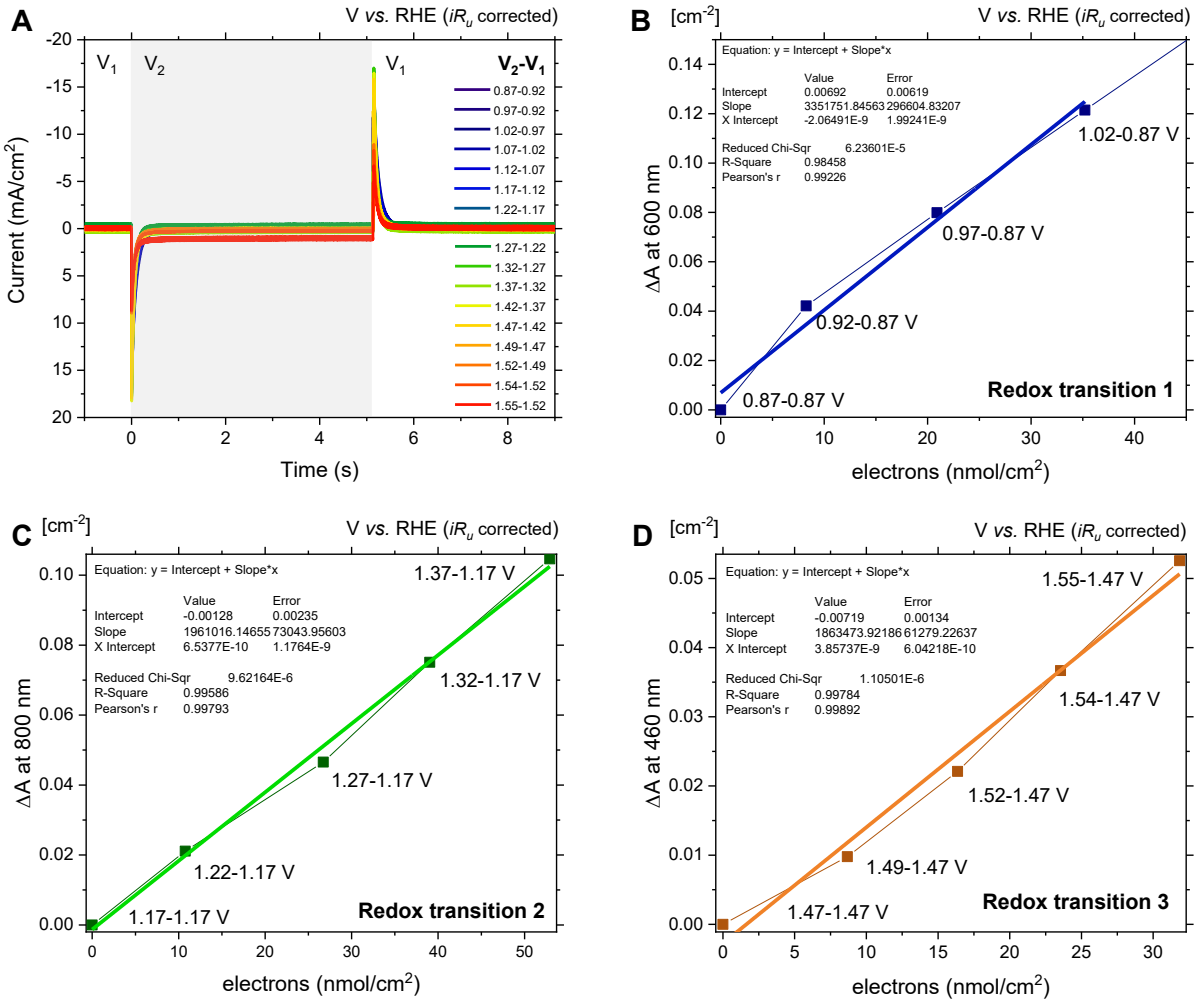

Figure 5.6. **(A)** Transient currents measured during potential steps between two different applied potentials, as illustrated in Scheme 5.1. **(B-D)** Dependency of the deconvoluted absorbance on the extracted charge for the three redox transitions. The charges are calculated by integrating the reductive peak in Figure 5.6A. The slope of the linear regression is the differential absorption coefficient of the new redox state formed at the corresponding redox transition. The label next to each data point indicates the potential interval where the absorbance changes and the charges were measured.

5.3.4. Kinetics of the redox states

Once the potential and absorption of the different redox states was identified and the species were assigned, their reaction kinetics was investigated. With this goal, the decay of the optical signal was measured after turning the applied potential off in the same 0.1 M $HClO_4$ aqueous solution at pH 1.2. As described above (SP-SEC), these measurements consisted of regular two-step cycles illustrated in Scheme 5.2, where the potential was applied for 5 s and was turned off for 8 s. This technique is described in detail in Section 2.6 and it only differs from the SP-SEC described above (Scheme 5.1) in that no potential is applied during one of the steps in each cycle.

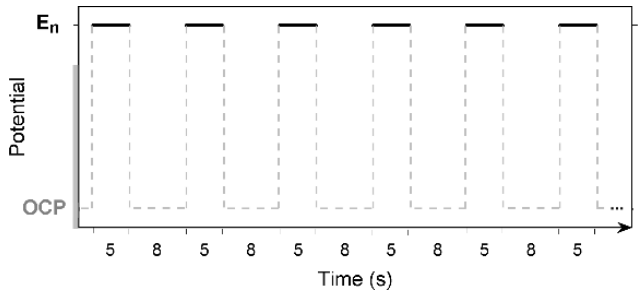

Scheme 5.2. Potential intervals in a step potential spectroelectrochemistry measurement (SP-SEC), where a potential E_n is cyclically turned on (for 5 s) and off (for 8 s), while the absorbance difference ΔA is monitored ($\Delta A = A(E_n) - A(OCP)$). The OCP potential depends on the applied potential E_n and is therefore represented with dashed lines.

The maximum absorbance after applying a potential E_n for 4 s at different wavelengths and potentials is shown in Figure 5.7A. A significant absorbance change between E_n and OCP was only detected at $E_n > \sim 1$ V *vs.* RHE (iR_u corrected) and, under a constant applied potential, it stabilised within 1-2 s. In contrast, the bare FTO substrate did not show any optical change in the same potential range (Figure 5.8). Under these applied potentials, the differential spectrum of IrO_x overlaps with a combination of the absorbance changes associated to the redox transitions 2 and 3 (Figure 5A in green and orange) and, therefore, it must be related to the oxidation of **Ir(3.x+)** (present before the redox transition 2) to **Ir(4.x+)** (resulting from redox transition 3). In parallel, the OCP after turning the potential off was around 1 V *vs.* RHE, consistent with the absence of the characteristic absorbance features of the redox transition 1. When turning the potential off, the optical signals decay as shown in Figure 5B. The decay is increasingly fast after ~1 V, plateauing at around 1.5 V *vs.* RHE (Figure 5B). This decay can be attributed to the depletion of **Ir(4.x+)**, the redox state formed before turning the potential off, and its faster decay at higher potentials implies a greater reactivity of this state. Furthermore, the coincidence between the onset potential and the formation of **Ir(4.x+)** (Figure 3A) directly relates this state with the OER catalysis. Combined, these results indicate that the redox state **Ir(4.x+)** is the most reactive IrO_x state in water, probably yielding O_2 and **Ir(3.x+)**.

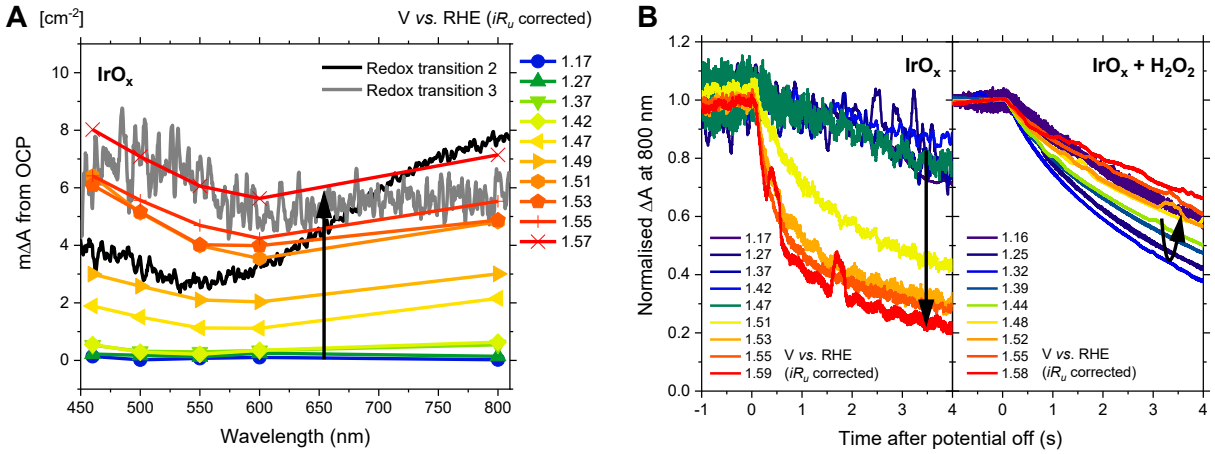

Figure 5.7. **(A)** Maximum absorbance of IrO_x after applying a potential for 4 s compared to the deconvoluted differential absorbance of redox transitions 1 and 2. **(B)** Normalised absorbance decay after turning the potential off in 0.1 M $HClO_4$ aqueous solution at pH 1.2 (*gray*) and with additional 20 mM of H_2O_2 (*red*).

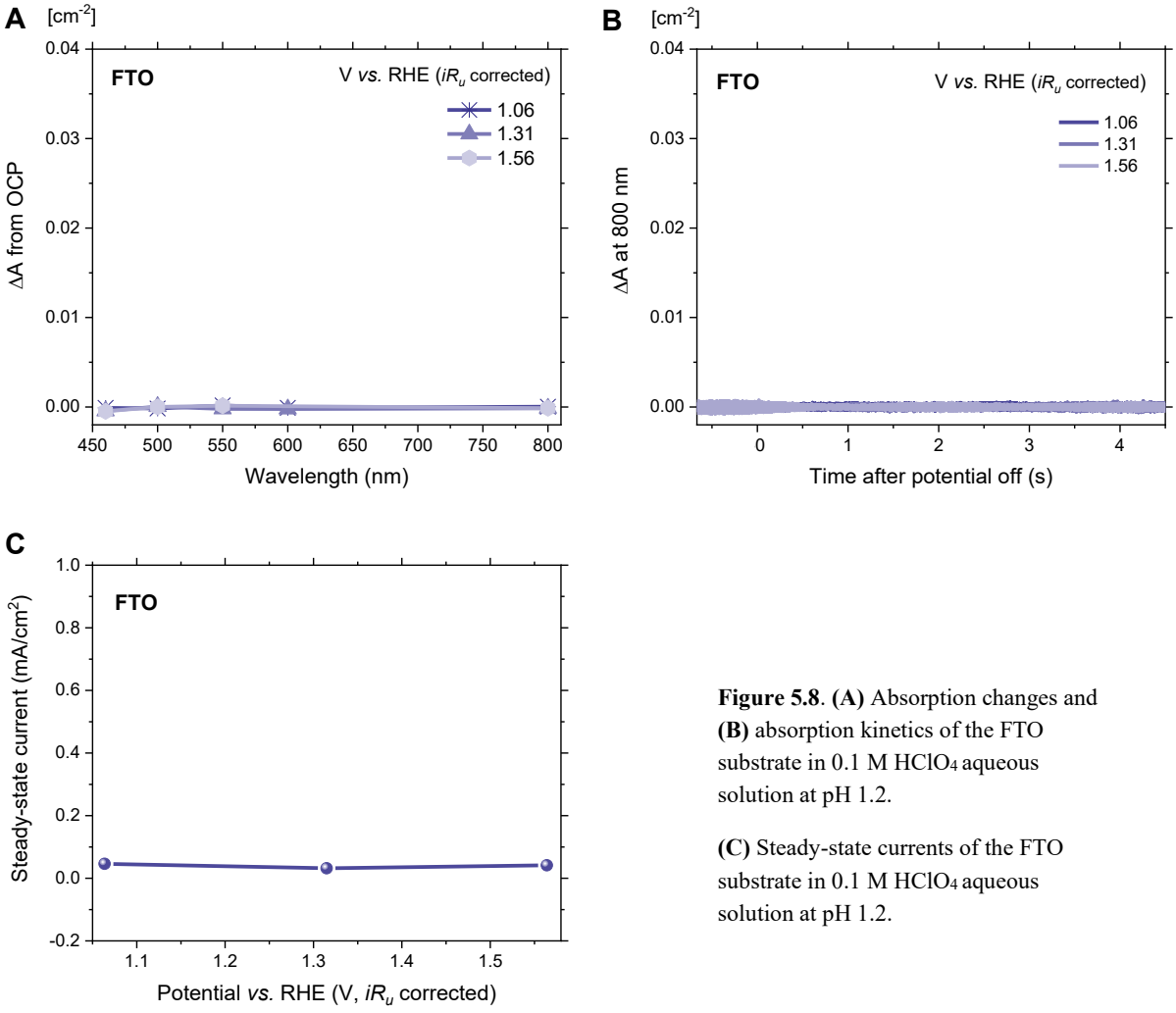

Figure 5.8. **(A)** Absorption changes and **(B)** absorption kinetics of the FTO substrate in 0.1 M $HClO_4$ aqueous solution at pH 1.2.

(C) Steady-state currents of the FTO substrate in 0.1 M $HClO_4$ aqueous solution at pH 1.2.

5.3.5. Reactivity of the redox states with H_2O_2

For a more in-depth analysis of the reactivity of the redox states detected, hydrogen peroxide was added to the electrolyte to investigate how its less-demanding two-electron oxidation into O_2 affects the stead-state concentration and kinetics of the IrO_x redox states. The absorbance of the same IrO_x sample was measured at different potentials in 0.1 M $HClO_4$ at pH 1.2 with 20 mM H_2O_2, observing broadly the same trends as in IrO_x without H_2O_2 (Figure 5.9A-B). Following the same deconvolution procedure as before (Equations 5.1-6 and Section 2.7), the spectroelectrochemical data was best fit with two different absorbance contributions or redox transitions (Equation 5.1, Figure 5.9C-D). Very similar results were obtained from fitting three absorbance contributions, with the 3rd one being negligible.

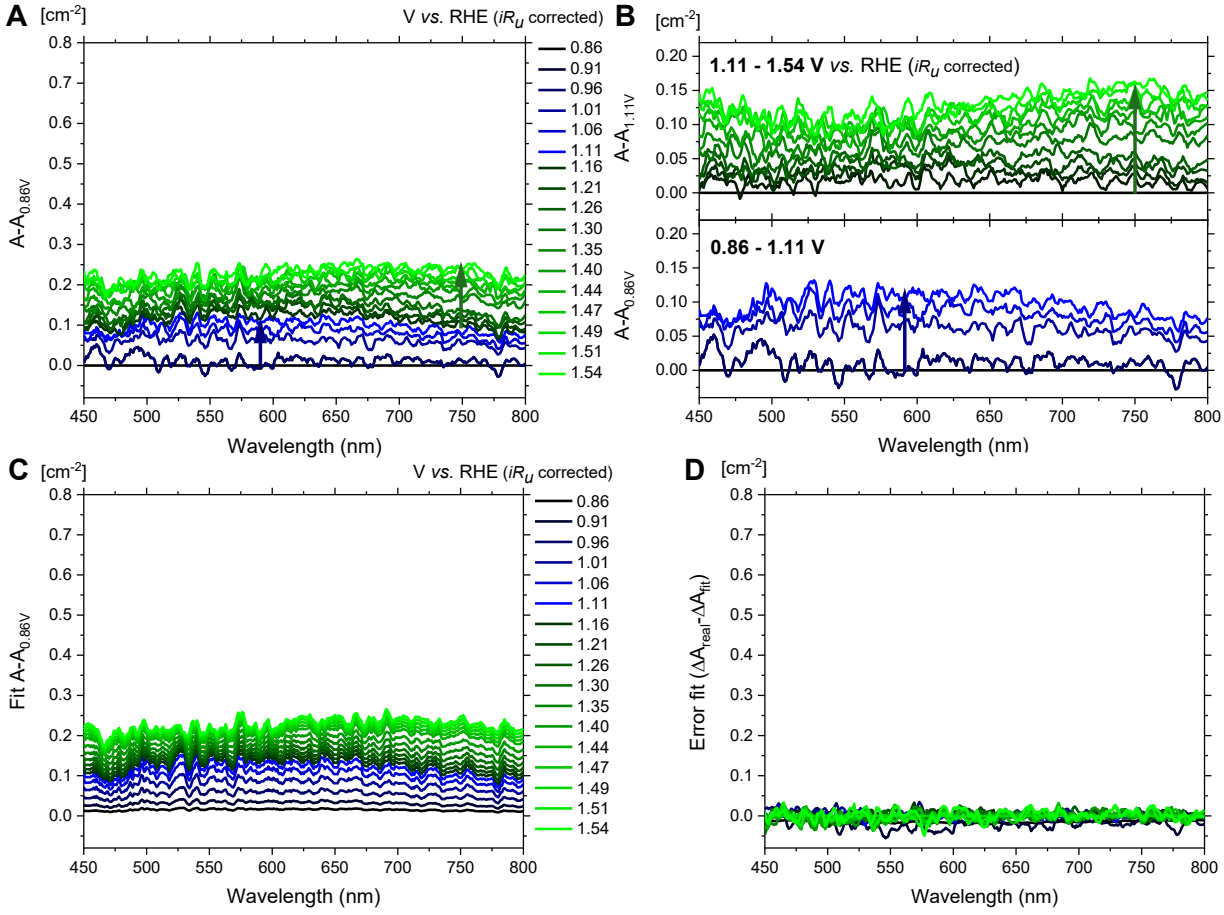

Figure 5.9. Absorbance changes of IrO_x upon applying an oxidative potential in 20 mM H_2O_2 0.1 M $HClO_4$ aqueous solution at pH 1.2. Absorbance changes calculated with respect to **(A)** 0.86 V, and **(B)** 0.86 V (*bottom*) and 1.11 V (*top*) *vs.* RHE, (iR_u corrected). **(C)** Best fit of the spectroelectrochemical data in Figure 5.9A generated with Equations 5.1-6. **(B)** Difference between the experimental data in Figure 5.9A and the model data in Figure 5.9C.

Figure 5.10A shows the deconvoluted concentration changes over potential and the absorbance changes related to the two redox transitions detected in H_2O_2, compared to the two first redox transitions without H_2O_2. It is apparent that redox transitions 1 and 2 are very similar in both conditions, with maximum absorbance changes at 600 and 800 nm taking place around 0.9 and 1.3 V *vs.* RHE (iR_u corrected) respectively. This indicates that the nature of the redox states are most likely the same in these conditions and that **Ir(3+)** is oxidised into **Ir(3.x+)** and **Ir(4+)**, while **Ir(4.x+)** probably does not accumulate enough to be detected. In parallel, the steady-state current of IrO_x with H_2O_2 was measured, as shown in Figure 5.10B. In the presence of H_2O_2, the potential onset is lower and is in the range of the redox transition 2, where **Ir(3.x+)** is oxidised to **Ir(4+)**. Furthermore, the current above the OER onset potential at ~1.5 V *vs*. RHE is larger with H_2O_2 than without, which could be due to the coexistence of H_2O_2 and H_2O oxidation, the extra current deriving from the oxidation of the additional H_2O_2. This would indicate that the redox state **Ir(4+)** can oxidise H_2O_2, while **Ir(4.x+)** can oxidise both water and H_2O_2.

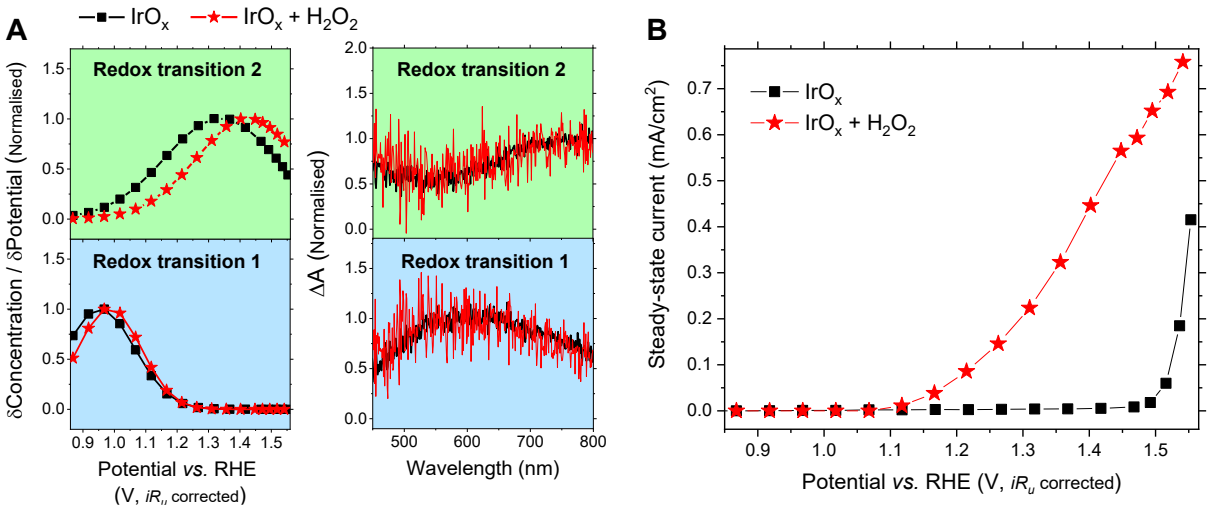

Figure 5.10. **(A)** Deconvoluted differential absorbance and concentration changes and **(B)** steady-state current of IrO_x with and without 20 mM H_2O_2 in $HClO_4$ aqueous solution at pH 1.2.

Once the redox states of IrO_x in the presence of H_2O_2 were identified, their kinetics in these conditions were measured. The same SP-SEC measurement done with IrO_x in acid media was repeated after adding 20 mM H_2O_2 (Scheme 5.2). Under increasingly oxidising potentials, the differential absorption spectra *versus* OCP has larger absorbance changes at 800 nm with H_2O_2 than without H_2O_2 (see Figures 5.11 and 5.7A, with and without H_2O_2 respectively). This is the characteristic feature of the redox transition 2 and the formation of **Ir(4+)**, which means that this redox state

is being depleted to a larger extent in the presence of H_2O_2. Furthermore, after turning the potential off, the decays of the optical signals behave differently over potential with H_2O_2, becoming faster between 1.1 and 1.4 V, but slowing down after 1.4 V *vs.* RHE (iR_u corrected) (Figure 5.7B).

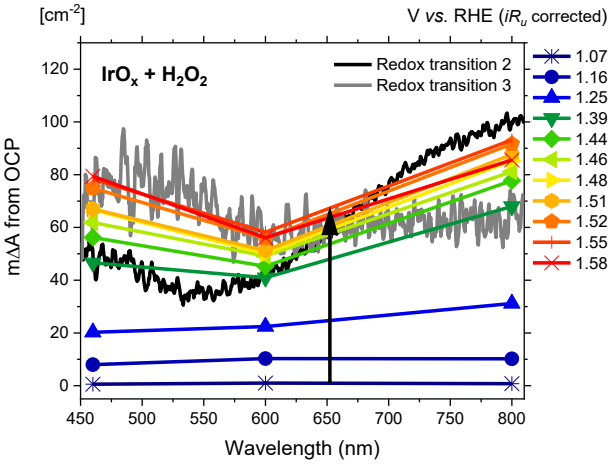

Figure 5.11. Absorbance changes of IrO_x upon applying a potential from OCP in 20 mM H_2O_2 0.1 M $HClO_4$ aqueous solution at pH 1.2. Overlapped in green and orange, the deconvoluted absorbance changes associated with redox transitions 2 and 3 respectively.

5.3.6. Calculation of lifetimes

To better compare the signal lifetimes with and without H_2O_2, the normalised decays were fit with a linear regression between ΔA 1 and 0.75, when the decay in the potential is not significant. The lifetimes were then calculated as the inverse of the slope extracted from the linear regression. Once the optical signal decays were normalised and fit, the lifetime τ was derived as follows:

Equation 5.7 $\Delta A = k \cdot t + c$

Equation 5.8 $\tau = 1/k$

Where ΔA is the experimental differential absorbance, t is time, and k and c are fit constants.

Figure 5.12A shows the lifetimes of the optical signals at 460, 600 and 800 nm for IrO_x both with and without H_2O_2. In the presence of H_2O_2, the decay of the optical signal is the fastest at around the redox transition 2 (~1.1 V *vs.* RHE, iR_u corrected), and is faster than without H_2O_2 at the same potential. This further proves the conclusions above that the redox state **Ir(4+)**, formed at this potential range, triggers the two-electron oxidation of H_2O_2, thus being reduced back to the OCP redox state in its presence. At potentials over 1.5 V, the lifetimes without H_2O_2 are shorter that with H_2O_2 in the whole potential range investigated (1-1.6 V *vs.* RHE, iR_u corrected). The low concentration of H_2O_2 and the mass transport limitations are probably the cause of this difference in the minimum lifetimes reached under these conditions. At >1.5 V with H_2O_2, the decay of the optical signal becomes progressively slower while the steady-state current keeps increasing and remains larger than in water without H_2O_2 (Figure 5.12A and 5.10B respectively). This could indicate that the redox state present at these potentials, **Ir(4.x+)**, is less efficient than **Ir(4+)** at oxidising H_2O_2. On the other hand, **Ir(4.x+)** may need to reach a critical concentration to oxidise water and it cannot reach it in 20 mM H_2O_2, as evidenced from the lag between the onset potential and the formation of **Ir(4.x+)** (Figure 5.5A), and the higher A(800 nm):A(460 nm) ratio and **Ir(4+)**:**Ir(4.x+)** ratio in H_2O_2 (Figure 5.11 compared to 5.7A). The calculation of the redox state lifetimes in IrO_x with and without H_2O_2 from the optical signal decay, confirms the trends observed in the spectroelectrochemical measurements, and provide an assumption-free method to calculate real oxidation kinetics.

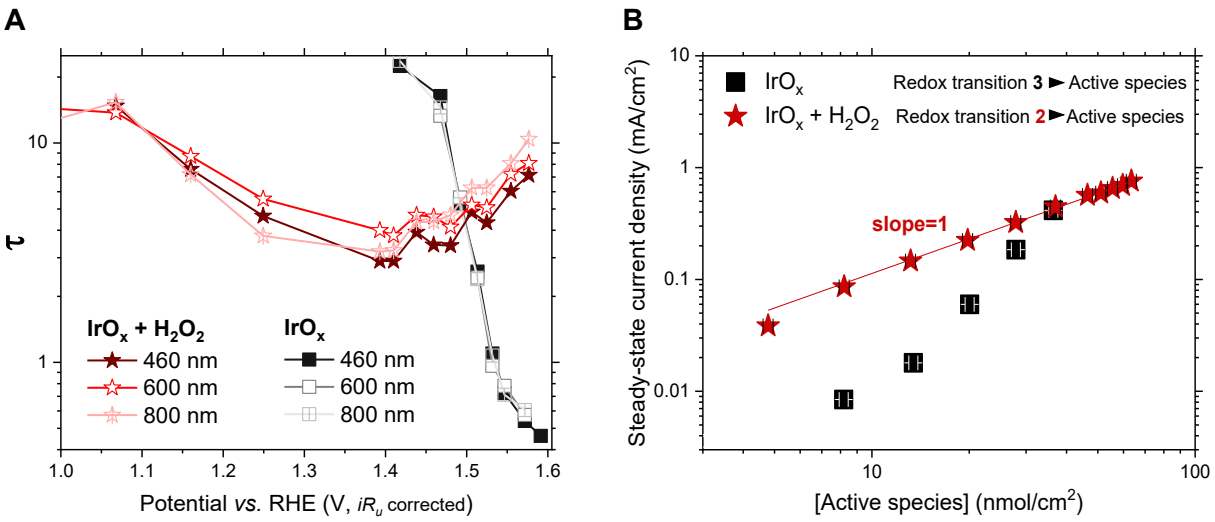

Figure 5.12. **(A)** Lifetimes derived from the decay of the optical signal over potential of IrO_x with and without 20 mM H_2O_2. **(B)**. Steady-state current plotted against the concentration of active species derived from the deconvoluted optical signal. The active species of IrO_x is considered to be **Ir(4.x+)** in acid solution and **Ir(3.x+)** in the presence of H_2O_2. All the measurements were done in 0.1 M $HClO_4$ aqueous solution at pH 1.2.

An alternative method to study the OER mechanism and kinetics, is to plot the steady-state current *versus* the concentration of active species (Figure 5.12B). In Figure 5.12B, the active species concentration was measured from the deconvoluted spectroelectrochemical absorbance of the corresponding redox transition (2 with H_2O_2 and 3 without, in Figures 5.4 and 5.9 respectively). Two other ways to measure the optical signal of the concentration of active states were based on potential steps applied cyclically, between a potential E_n and OCP (SP-SEC, Scheme 5.2) or between E_n and the potential of formation of the active species (Scheme 5.1). In IrO_x without H_2O_2, the relationship between the steady-state and the concentration is not consistent throughout the different measurements. This inconsistency can be attributed to the coexistence of multiple redox states at high potential such as **Ir(4+)** and **Ir(4.x+)** and to the resulting complexity of the optical signal. In contrast, the samples of IrO_x in 20 mM H_2O_2 have always a dependency between the steady-state current and the concentration of active species **Ir(4+)** with a slope equal to one. This slope is the order of the reaction, meaning that each pair of active species generates a pair of extracted electrons, and one molecule of O_2 from H_2O_2.

5.4. Discussion

Determining the oxygen evolution reaction mechanism and kinetics of heterogeneous catalysts is specially challenging because a diversity of mechanisms are possible and occur simultaneously, leading to a complex mixture of intermediate states under catalytic steady-state conditions. Another complication is to determine which atoms or states are catalytically active and if they are localised at the surface. Herein, a useful insight into the redox chemistry of IrO_x is given combining optical and electrochemical time-resolved measurements. From the spectroelectrochemical data, it has been possible to identify different redox states and quantify their concentration. Furthermore, by monitoring the optical signal under catalytic conditions and its decay after turning the potential off, a unique perspective is provided on the steady-state concentration and its intrinsic kinetics, not available from bulk current densities alone.

From optical and electrochemical data of IrO_x under applied potential, three redox transitions and three redox states have been identified beyond the starting redox state at the initial open circuit potential (Figures 5.2A and 5.3). With a model based on the Lambert-Beer law and Gaussian distributions of concentration over potential, the real experimental data can be reproduced accurately, and it has been used to deconvolve the spectroelectrochemical data and derive the concentrations of each redox state at the different potentials (Figure 5.5). From the experimental data and the fit model, the higher-oxidised redox states incorporate the optical transitions of lower-oxidised redox states unaltered. The latter would mean that the energy level of the electronic states in the material is minimally affected by the applied potential in the investigated potential range, which therefore only alters their electronic occupancy.[57-59] Following the literature,[15, 16, 18, 20, 28-30, 32, 33, 38] it is assumed that the starting state under the initial OCP includes Ir^{3+} oxidation numbers only, and it is called herein **Ir(3+)**. Before the onset potential, two redox states are detected whose optical transitions are assigned to the formation of a mixed valence state at ~0.9 V including Ir^{3+} and Ir^{4+}, **Ir(3.x+)**, followed by a redox state with a larger content of Ir^{4+} at ~1.3 V *vs.* RHE, **Ir(4+)**. Finally, the species oxidised at the onset potential is referred to as **Ir(4.x+)**. Compared to the colourless **Ir(3+)**, the redox states in IrO_x over OCP absorb in the UV-Vis as a result of deprotonation of adsorbed –OH to form –O , which leads to the degeneracy in the *d* orbitals of iridium and to an intervalence d-d transition upon light excitation.[39, 40, 54, 60, 61] On the other hand, the total concentration (the integral of the Gaussians in Figure 3A) is 97%, 88% and 42% of the total amount of iridium atoms in redox transitions 1, 2 and 3 respectively, assuming that each charge extracted from the film is related to one-electron oxidation process in a different Ir centre. Therefore, all the iridium atoms in the film are likely to be involved in redox transitions 1 and 2 and, consequently, the three redox transitions must correspond to sequential redox steps. The three redox transitions, assigned to the partial oxidation of Ir centres, must involve the adsorption or desorption of aqueous species in close proximity with the electrolyte.

The reactivity and kinetics of the oxidised states in IrO_x have been analysed right after turning the applied potential off in 0.1 M $HClO_4$ aqueous solution with and without H_2O_2 at pH 1.2. At potentials up to ~1.2 V *vs.* RHE (iR_u corrected), any optical signal *versus* OCP is detected upon applying increasingly oxidising potentials on and off for 5 s and 8 s respectively, which means that the species formed at these potentials do not react with anything and accumulate under OCP (Figure 5.7). Over 1.2 V, the differential spectrum versus OCP resembles a combination of the optical changes during redox transitions 2 and 3 (Figure 5.5B). This means that **Ir(4.x+)** triggers the oxidation of water and that, consequently, it is reduced back to **Ir(3.x+)**. In other words, the redox states **Ir(4.x+)**, **Ir(4+)** and **Ir(3.x+)** are part of the OER catalytic cycle, but the potential-determining step is the formation of **Ir(4.x+)**, which is compatible with some of the mechanism proposed in the literature (Scheme 5.3).[24, 62] The catalytic potential of **Ir(4+)** is further confirmed by its two-electron oxidation of H_2O_2 to O_2 and **Ir(3.x+)**, as confirmed by the differential absorbance (Figure 5.11), steady-state current (Figure 5.10B) and optical signal decays (Figure 5.7B) at ~1.3 V *vs.* RHE (iR_u corrected) in the presence of H_2O_2.

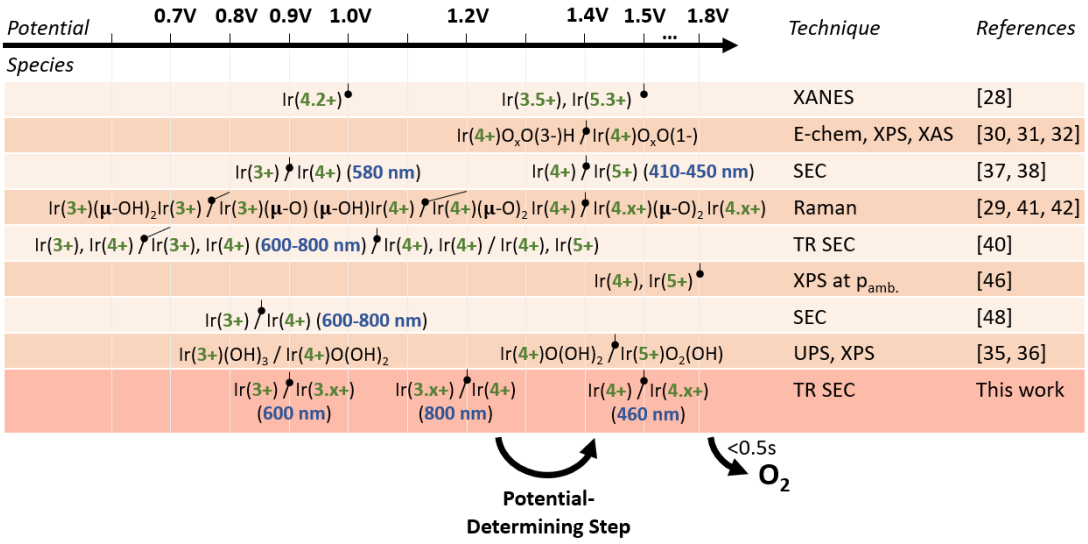

Scheme 5.3. Role and kinetics of the IrO_x redox states in the OER mechanism, as detected in this work.

The optical signal lifetime over potential (Figure 5.12A) can be directly related to the intrinsic OER activity of the IrO_x catalyst because it is directly related to the concentration of redox states in the material. In the aqueous acid conditions used in this work, the lifetimes seem to plateau at >1.5 V *vs.* RHE (iR_u corrected). In addition to the relationship between the steady-state current and the concentration of active species (Figure 5.12B), the independence of the lifetime *versus* potential suggests a first order reaction rate, where each active state is involved in the

generation of one molecule of oxygen. Although more experiments are needed at these potentials to further prove the latter, this data shows that a kinetic and mechanistic analysis of IrO_x reactivity based on localised states and concentrations is suitable. In contrast to the classic Butler-Volmer model, where these parameters are described as a function of the increasing energy of free charges in a continuum distribution of states,[63] this kinetic spectroelectrochemical investigation may open the door to a more accurate calculation of iridium surface atoms and their OER performance, following some recent evidence in this direction.[25, 49]

5.5. Conclusions

The redox states of IrO_x have been identified by steady-state spectroelectrochemistry methods, while their reactivity has been investigated in H_2O_2 and by measuring the optical signal decay after turning the applied potential off. Monitoring the optical signal under catalytic conditions has provided a unique perspective on the steady-state concentration of IrO_x states. The absorbance of IrO_x in the UV-Vis has been assigned to surface redox states. It has allowed the identification of three different ones with the presence of Ir^{3+}, Ir^{4+} and $Ir^{4.x+}$ at potentials over the open circuit potential. Given the absorbance changes from and to the OCP, the states containing both Ir^{4+} and $Ir^{4.x+}$ have been determined to be part of the OER catalytic cycle, but the state containing mostly $Ir^{4.x+}$ needs to be electrochemically oxidised first, meaning that it is the potential-limiting step. Finally, the active state lifetimes have been measured to plateau at >1.5 V *vs.* RHE, suggesting the independence of its chemical activity with respect to potential and a first order reaction rate. This insight into the intrinsic kinetics of single redox states offers a promising alternative to the Butler-Volmer approach to quantify the real intrinsic activity of disordered electrocatalysts.

5.6. References

1. Z. W. Seh, J. Kibsgaard, C. F. Dickens, I. Chorkendorff, J. K. Nørskov and T. F. Jaramillo, *Science*, 2017, **355**.
2. R. Frydendal, E. A. Paoli, B. P. Knudsen, B. Wickman, P. Malacrida, I. E. L. Stephens and I. Chorkendorff, *ChemElectroChem*, 2014, **1**, 2075-2081.
3. C. Wei, R. R. Rao, J. Peng, B. Huang, I. E. L. Stephens, M. Risch, Z. J. Xu and Y. Shao-Horn, *Adv. Mater.*, 2019, **31**, e1806296.
4. S. Haussener, C. Xiang, J. M. Spurgeon, S. Ardo, N. S. Lewis and A. Z. Weber, *Energy Environ. Sci.*, 2012, **5**, 9922.
5. A. Marshall, B. Børresen, G. Hagen, M. Tsypkin and R. Tunold, *Energy*, 2007, **32**, 431-436.
6. M. Carmo, D. L. Fritz, J. Mergel and D. Stolten, *Int. J. Hydrog. Energy*, 2013, **38**, 4901-4934.
7. Study on the review of the list of Critical Raw Materials. Non-critical Raw Materials Factsheets, *European Comission*, 2017.
8. Study on the review of the list of Critical Raw Materials. Criticality Assessments, *European Comission*, 2017.
9. Research needs towards sustainable production of fuels and chemicals, J. K. Nørskov, A. Latimer and C. F. Dickens, 2019.
10. D. Chandra, T. Sato, Y. Tanahashi, R. Takeuchi and M. Yagi, *Energy*, 2019, **173**, 278-289.
11. H. Jang and J. Lee, *J. Energy Chem.*, 2020, **46**, 152-172.
12. K. Yamanaka, *Jpn. J. Appl. Phys.*, 1989, **28**, 632-637.
13. A. R. Zeradjanin, A. A. Topalov, Q. Van Overmeere, S. Cherevko, X. Chen, E. Ventosa, W. Schuhmann and K. J. J. Mayrhofer, *RSC Adv.* 2014, **4**.
14. M. Ledendecker, S. Geiger, K. Hengge, J. Lim, S. Cherevko, A. M. Mingers, D. Göhl, G. V. Fortunato, D. Jalalpoor, F. Schüth, C. Scheu and K. J. J. Mayrhofer, *Nano Res.*, 2019, **12**, 2275-2280.
15. O. Kasian, J. P. Grote, S. Geiger, S. Cherevko and K. J. J. Mayrhofer, *Angew. Chem. Int.*, 2018, **57**, 2488-2491.
16. O. Kasian, S. Geiger, T. Li, J.-P. Grote, K. Schweinar, S. Zhang, C. Scheu, D. Raabe, S. Cherevko, B. Gault and K. J. J. Mayrhofer, *Energy Environ. Sci.*, 2019, **12**, 3548-3555.
17. S. Geiger, O. Kasian, B. R. Shrestha, A. M. Mingers, K. J. J. Mayrhofer and S. Cherevko, *J. Electrochem. Soc.* 2016, **163**, F3132-F3138.
18. S. Geiger, O. Kasian, M. Ledendecker, E. Pizzutilo, A. M. Mingers, W. T. Fu, O. Diaz-Morales, Z. Li, T. Oellers, L. Fruchter, A. Ludwig, K. J. J. Mayrhofer, M. T. M. Koper and S. Cherevko, *Nat. Catal.*, 2018, **1**, 508-515.
19. S. Cherevko, S. Geiger, O. Kasian, A. Mingers and K. J. J. Mayrhofer, *J. Electroanal. Chem.*, 2016, **773**, 69-78.
20. S. Cherevko, S. Geiger, O. Kasian, A. Mingers and K. J. J. Mayrhofer, *J. Electroanal. Chem.*, 2016, **774**, 102-110.
21. I. C. Man, H. Y. Su, F. Calle-Vallejo, H. A. Hansen, J. I. Martínez, N. G. Inoglu, J. Kitchin, T. F. Jaramillo, J. K. Nørskov and J. Rossmeisl, *ChemCatChem*, 2011, **3**, 1159-1165.
22. H. A. Hansen, V. Viswanathan and J. K. Nørskov, *J. Phys. Chem. C*, 2014, **118**, 6706-6718.
23. C. F. Dickens, C. Kirk and J. K. Nørskov, *J. Phys. Chem. C*, 2019, **123**, 18960-18977.
24. T. Naito, T. Shinagawa, T. Nishimoto and K. Takanabe, *Inorg. Chem. Front.*, 2021, DOI: 10.1039/d0qi01465f.
25. C. A. Mesa, L. Francas, K. R. Yang, P. Garrido-Barros, E. Pastor, Y. Ma, A. Kafizas, T. E. Rosser, M. T. Mayer, E. Reisner, M. Grätzel, V. S. Batista and J. R. Durrant, *Nat. Chem.*, 2020, **12**, 82-89.
26. A. Minguzzi, C. Locatelli, O. Lugaresi, E. Achilli, G. Cappelletti, M. Scavini, M. Coduri, P. Masala, B. Sacchi, A. Vertova, P. Ghigna and S. Rondinini, *ACS Catal.*, 2015, **5**, 5104-5115.
27. V. A. Saveleva, L. Wang, D. Teschner, T. Jones, A. S. Gago, K. A. Friedrich, S. Zafeiratos, R. Schlögl and E. R. Savinova, *J. Phys. Chem. Lett.*, 2018, **9**, 3154-3160.
28. V. Pfeifer, T. E. Jones, J. J. Velasco Velez, C. Massue, M. T. Greiner, R. Arrigo, D. Teschner, F. Girgsdies, M. Scherzer, J. Allan, M. Hashagen, G. Weinberg, S. Piccinin, M. Havecker, A. Knop-Gericke and R. Schlögl, *Phys. Chem. Chem. Phys.*, 2016, **18**, 2292-2296.

29. V. Pfeifer, T. E. Jones, J. J. Velasco Velez, R. Arrigo, S. Piccinin, M. Havecker, A. Knop-Gericke and R. Schlögl, *Chem. Sci.*, 2017, **8**, 2143-2149.
30. V. Pfeifer, T. E. Jones, S. Wrabetz, C. Massue, J. J. Velasco Velez, R. Arrigo, M. Scherzer, S. Piccinin, M. Havecker, A. Knop-Gericke and R. Schlögl, *Chem. Sci.*, 2016, **7**, 6791-6795.
31. A. F. Pedersen, M. Escudero-Escribano, B. Sebok, A. Bodin, E. Paoli, R. Frydendal, D. Friebel, I. E. L. Stephens, J. Rossmeisl, I. Chorkendorff and A. Nilsson, *J. Phys. Chem. B*, 2018, **122**, 878-887.
32. H. Ooka, T. Takashima, A. Yamaguchi, T. Hayashi and R. Nakamura, *Chem. Commun.*, 2017, **53**, 7149-7161.
33. H. Ooka, Y. Wang, A. Yamaguchi, M. Hatakeyama, S. Nakamura, K. Hashimoto and R. Nakamura, *Phys. Chem. Chem. Phys.*, 2016, **18**, 15199-15204.
34. S. B. Sinha, D. Y. Shopov, L. S. Sharninghausen, C. J. Stein, B. Q. Mercado, D. Balcells, T. B. Pedersen, M. Reiher, G. W. Brudvig and R. H. Crabtree, *J. Am. Chem. Soc.*, 2017, **139**, 9672-9683.
35. G. S. Nahor, P. Hapiot, P. Neta and A. Harriman, *J. Phys. Chem.*, 1991, **95**, 616-621.
36. Z. Pavlovic, C. Ranjan, M. van Gastel and R. Schlögl, *Chem. Commun.*, 2017, **53**, 12414-12417.
37. Z. Pavlovic, C. Ranjan, Q. Gao, M. van Gastel and R. Schlögl, *ACS Catal.*, 2016, **6**, 8098-8105.
38. H. G. Sanchez Casalongue, M. L. Ng, S. Kaya, D. Friebel, H. Ogasawara and A. Nilsson, *Angew. Chem. Int.*, 2014, **53**, 7169-7172.
39. Electrochromism and Electrochromic Devices, P. M. S. Monk, R. J. Mortimer and D. R. Rosseinsky, *Cambridge University Press*, 2008.
40. S. Gottesfeld, J. D. E. McIntyre, G. Beni and J. L. Shay, *Appl. Phys. Lett.*, 1978, **33**, 208-210.
41. J. A. Gauthier, C. F. Dickens, L. D. Chen, A. D. Doyle and J. K. Nørskov, *J. Phys. Chem. C*, 2017, **121**, 11455-11463.
42. Y. Ping, R. J. Nielsen and W. A. Goddard III, *J. Am. Chem. Soc.*, 2017, **139**, 149-155.
43. J. Rossmeisl, Z. W. Qu, H. Zhu, G. J. Kroes and J. K. Nørskov, *J. Electroanal. Chem.*, 2007, **607**, 83-89.
44. M. S. Burke, L. J. Enman, A. S. Batchellor, S. Zou and S. W. Boettcher, *Chem. Mater.*, 2015, **27**, 7549-7558.
45. T. R. Eaton, M. P. Campos, K. A. Gray and J. M. Notestein, *J. Catal.*, 2014, **309**, 156-165.
46. K. A. Stoerzinger, L. Qiao, M. D. Biegalski and Y. Shao-Horn, *J. Phys. Chem. Lett.*, 2014, **5**, 1636-1641.
47. D. Y. Kuo, J. K. Kawasaki, J. N. Nelson, J. Kloppenburg, G. Hautier, K. M. Shen, D. G. Schlom and J. Suntivich, *J. Am. Chem. Soc.*, 2017, **139**, 3473-3479.
48. L. Francas, S. Corby, S. Selim, D. Lee, C. A. Mesa, R. Godin, E. Pastor, I. E. L. Stephens, K. S. Choi and J. R. Durrant, *Nat. Commun.*, 2019, **10**, 5208.
49. H. N. Nong, L. J. Falling, A. Bergmann, M. Klingenhof, H. P. Tran, C. Spori, R. Mom, J. Timoshenko, G. Zichittella, A. Knop-Gericke, S. Piccinin, J. Perez-Ramirez, B. R. Cuenya, R. Schlögl, P. Strasser, D. Teschner and T. E. Jones, *Nature*, 2020, **587**, 408-413.
50. M. A. Petit and V. Plichon, *Phys. Chem. Chem. Phys.*, 1998, **444**, 247.
51. Y. Zhang, M. Cao, H. Lv, J. Wei, Y. Gu, D. Liu, W. Zhang, M. P. Ryan and X. Wu, *Electrochim. Acta*, 2018, **265**, 507-513.
52. S. Gottesfeld and J. D. E. McIntyre, *J. Electrochem. Soc.*, 1979, 742-750.
53. S. Gottesfeld and S. Srinivasan, *J. Electroanal. Chem.*, 1978, **86**, 89-104.
54. Electrochromism: Fundamental and Applications, P. M. S. Monk, R. J. Mortimer and D. R. Rosseinsky, *VCH*, 1995.
55. M. B. Robin and P. Day, 1968, **10**, 247-422.
56. K. H. Saeed, M. Forster, J. F. Li, L. J. Hardwick and A. J. Cowan, *Chem. Commun.*, 2020, **56**, 1129-1132.
57. D. Maric and J. P. Burrows, *J. Phys. Chem.*, 1996, **100**, 8645-8659.
58. Computational spectroscopy : methods, experiments and applications, J. Grunenberg, *Weinheim: Wiley-VCH*, 2010.
59. D. Loco and L. Cupellini, *Int. J. Quantum Chem.*, 2019, **119**.
60. G. Beni, C. E. Rice and J. L. Shay, *J. Electrochem. Soc.*, 1980, **127**, 1342-1348.

61. W. C. Dautremont-Smith, G. Beni, L. M. Schiavone and J. L. Shay, *Appl. Phys. Lett.*, 1979, **35**, 565-567.
62. M. T. M. Koper, *J. Solid State Electrochem.*, 2012, **17**, 339-344.
63. Electrochemical Methods. Fundamentals and Applications, A. J. Bard and L. R. Faulkner, *John Wiley & Sons, Inc.*, 2001, 2nd edition.

Chapter 6

Comparative study of active states in a molecular iridium dimer and IrO_x water-oxidation electrocatalysts

Dr. Reshma R. Rao, Dr. Camilo A. Mesa, Prof. James R. Durrant, Prof. Erwin Reisner, Prof. Gary Brudvig and Prof. Dunwei Wang contributed to the discussion of the results. Dr. Daniel Antón-García prepared the mesoporous indium tin oxide samples, Dr. Gongfang Hu prepared the molecular iridium precursor, and Dr. Yuanxing Wang and Dr. Yanyan Zhao prepared the molecular iridium catalyst.

The oxygen evolution reaction (OER) in iridium electrocatalysts is mostly localised on iridium atoms, and the activity of these catalysts is most likely related to the exposure of active iridium sites and their chemical environment (Section 6.1). To investigate the chemical effects of the coordination sphere of iridium, the dimeric iridium catalyst $[Ir(pyalc)(H_2O)_2\text{-}(\mu\text{-}O)]_2^{2+}$ (**$Ir_{Molecular}$**) (pyalc = 2-(2'pyridyl)-2-propanolate) was immobilised on mesoporous ITO (Section 6.2.1), and its activity was compared to that of amorphous hydrous iridium (**IrO_x**) investigated in Chapter 5 (Sections 6.2.2-5). Spectroelectrochemical kinetic experiments and mathematical deconvolution were applied to identify the absorbance and potential of its redox states (Section 6.2.3.1-2) and their reactivity in aqueous acid solution (6.2.3.3). To investigate the effect of iridium exposure, **$Ir_{Molecular}$** was compared to samples of **IrO_x** with different iridium content. The redox states of **IrO_x** remained similar independently of the amount of iridium (Section 6.2.4) and thus its OER activity was expected to only depend on the exposure of iridium centres to the electrolyte (Section 6.2.5-6). These results suggest that the stabilisation of the iridium *d* orbitals would lead to a higher first-order OER activity at low potentials, while it confirms that a greater porosity of iridium oxides leads to a greater iridium utilisation (Section 6.2.6).

6.0. Contents

6.1. Introduction

Iridium-based electro-catalysts are some of the most active and most stable catalysts towards the oxygen evolution reaction (OER).[1-6] However, iridium is a scarce noble metal and OER catalysis is a key limiting factor in the efficiency and cost competitiveness of emerging clean energy conversion technologies based on water splitting.[3, 7-14] With the goal of improving the utilisation of iridium and its activity per atom, it is necessary to better understand how the electro-catalytic performance of iridium catalysts relates to their morphology and chemical composition.[15-17] In this context, spectroelectrochemistry techniques operating under catalytic conditions are essential to identify the catalyst states accumulated and depleted during the reaction and their kinetics. Herein, we use *operando* time-resolved spectroelectrochemistry to investigate two different iridium-based catalysts. The dimeric iridium complex $[Ir(pyalc)(H_2O)_2\text{-}(\mu\text{-}O)]_2^{2+}$ (**$Ir_{Molecular}$**) (pyalc = 2-(2'pyridyl)-2-propanolate) and electrodeposited hydrous iridium oxides (**IrO_x**) are compared to explain their OER activity as a function of their redox states concentration and reactivity.

The OER catalysis in iridium electrocatalysts is mostly localised on iridium atoms. Therefore, the activity of these catalysts is probably related to the exposure of active iridium sites and their chemical environment.[18-23] Compared to crystalline IrO_2 analogues, the amorphous **IrO_x** and bi-metallic **$Ir_{Molecular}$** have larger current densities per mass of iridium at lower overpotentials, but have lower stabilities.[24-27] When immobilised on mesoporous indium tin oxide (mesoITO), the molecular catalyst **$Ir_{Molecular}$**, with its well-defined bi-metallic active site, can reach turnover frequencies around 7 s^{-1} with ~50 mV less overpotential than IrO_2, and do not degrade under ~1.40 V *vs*. NHE at pH 2.6 (1.55 *vs.* RHE) for at least 11h.[24] In parallel, electrodeposited hydrous iridium oxides **IrO_x**, with larger porosities than crystalline IrO_2, have current densities per mass of iridium three orders of magnitude larger than IrO_2 under the same potential, but degrade at least 10 times faster on a timescale of months.[27-34] To further understand the electrochemical activity as a function of the active site rather than potential, it is necessary to first identify the active sites and their redox states. However, the identification of active sites in these catalysts is difficult because of their complex redox chemistry and, in the case of **IrO_x**, because of its highly disordered structure and the difficulty to measure the real surface area of the material.

Time-resolved spectroscopy and electrochemistry have been useful to investigate water oxidation in **IrO_x**, Ni-based electrocatalysts and hematite photoelectrodes.[22, 35, 36] In Chapter 5, spectroelectrochemistry techniques were applied in **IrO_x** to identify several redox transitions and to quantify the concentration of the resulting redox states at each potential. Time-resolved studies were then used to determine the active redox state of the catalyst and its OER kinetics. In this Chapter, to investigate the effects of the chemical environment and the degree of iridium exposure on the catalytic activity, we combine spectroelectrochemistry with signal deconvolution methods and kinetic measurements to characterise iridium-

based catalysts with different coordination spheres around the iridium atoms and different content of iridium. In particular, $\mathbf{IrO_x}$ electrodeposited during different times and the dimeric complex $\mathbf{Ir_{Molecular}}$ are investigated in 0.1 M $HClO_4$ aqueous solution at pH 1.2. By comparing the redox states and their intrinsic kinetics, this work aims at providing a rationale to explain the activity towards electrochemical water oxidation in the iridium electrocatalysts.

6.2. Materials and Methods

6.2.1. Preparation of mesoporous indium tin oxide films

Mesoporous indium tin oxide (ITO) films (mesoITO) with a geometrical area of ~1 cm^2 were prepared by spin-coating a dispersion of ITO nanoparticles onto FTO-glass. To clean the FTO-glass substrate, an aqueous solution with 50:17:33 v/v of HCl (37%), NH_4OH (30% NH_3) and H_2O_2 was first prepared. The FTO-glass was soaked in the solution at 80ºC for 15 minutes, rinsed with water, consecutively sonicated in ethanol and acetone for 15 minutes each, and finally dried at 70ºC in air. The dispersion of ITO nanoparticles (20% weight) was prepared in 5 M acetic acid ethanol and sonicated for 30 minutes in an ice-cooled sonication bath. The dispersion was then spin-coated onto the clean FTO-glass and sintered at 450ºC for 30 minutes. The mesoITO films were prepared by Dr. Daniel Antón-García.

6.2.2. $Ir_{Molecular}$ preparation and immobilisation on mesoITO

Following a previously reported procedure,[1-3] a solution of 1.25 mM $[Ir(pyalc)(H_2O)_2\text{-}(\mu\text{-}O)]_2^{2+}$ (**$Ir_{Molecular}$**) (pyalc = 2-(2'pyridyl)-2-propanolate) was prepared by mixing 2.5 mM aqueous [Cp*Ir(pyalc)OH] (Cp = pentamethyl-cyclopentadienyl) and $NaIO_4$ with an approximate molar ratio of 1:100. The pH of the solution was then adjusted to ~3 with nitric acid. The organometallic precursor [Cp*Ir(pyalc)OH] was synthesised by following the same method reported by Hintermair *et al.*[4, 5] To immobilise **$Ir_{Molecular}$** on mesoITO, the mesoITO films were soaked in the previsous **$Ir_{Molecular}$** solution for 16 h and rinsed with water. The molecular catalyst was prepared and immobilised by Dr. Gongfang Hu, Dr. Yuanxing Wang and Dr. Yanyan Zhao.

6.2.3. Electrodeposition of IrO_x

Following the same procedure as in Chapter 5 (Section 5.2.1), the **IrO_x** films were all prepared from a solution of iridium salt consisting of 0.2 mmol of $Ir^{3+}Cl_3$ hydrate (*Fluorochem*) and 2 mmol of oxalic acid dehydrate in 30 mL of water. The pH of the iridium salt solution was adjusted to 10 by adding ~5 mmol of Na_2CO_3 (*ReagentPlus® ≥ 99.0%*), turning the colour of the solution from yellow to green. The volume of the solution was increased to 50 mL by adding more water. The solution was left to rest for 4 days at 35ºC and then stored in the freezer at 4ºC. The electrodeposition of **IrO_x** from this iridium solution was done by soaking a clean FTO on a glass substrate (~1·2·0.2 cm^3) and applying a current of 35 µA. To prepare **IrO_x** samples with different thicknesses, the current was applied for 1000 s, 700 s, 500 s, 120 s and 60 s. Polyimide tape was attached on the FTO surface to limit the surface of the IrO_x to ~1 cm^2. This preparation procedure is similar to that in the literature.[6, 7]

6.3. Results

6.3.1. Electrochemistry of $Ir_{Molecular}$

The molecular iridium catalyst $[Ir(pyalc)(H_2O)_2\text{-}(\mu\text{-}O)]_2^{2+}$ (**$Ir_{Molecular}$**) (pyalc = 2-(2'pyridyl)-2-propanolate) was immobilised on mesoporous ITO (mesoITO) following a previously reported procedure.[24, 37, 38] As detailed in the previous Section, the **$Ir_{Molecular}$** catalyst was prepared by oxidising an organometallic precursor with $NaIO_4$ in water, and was anchored to mesoITO by soaking ~1 cm^2 mesoITO-FTO-glass films in the catalyst solution for 12 h. The **$Ir_{Molecular}$** catalyst was first characterised electrochemically and compared to hydrous iridium oxide (**IrO_x**) which was electrodeposited for 1000 s on FTO-glass from an iridium salt solution. The cyclic voltammetry of the resulting **$Ir_{Molecular}$** films (*dotted blue* in Figure 6.1A) shows several oxidation features above the open circuit potential (OCP) at ~0.7 V *vs.* RHE (iR_u corrected). A clear redox peak is observed at ~1.15 V *vs.* RHE and, at an onset potential of ~1.35 V, the current increases exponentially. These features do not coincide entirely with the three signals detected in **IrO_x** electrocatalysts under the same conditions (Figure 5.2A), with oxidation maxima at ~0.95, ~1.25 and ~1.45 V *vs.* RHE. On the other hand, the exponential current of **$Ir_{Molecular}$** above 1.35 V is also observed under constant applied potential (*i.e.*, steady-state current, Figure 6.1A right y-axis) and is therefore related to the OER electrocatalysis, as in **IrO_x** above 1.45 V. The steady-state current of **$Ir_{Molecular}$**, normalised by gram of iridium, is higher than that of **IrO_x** under 1.45 V, in accordance with the higher activities per mass of iridium at lower overpotentials reported in **$Ir_{Molecular}$** compared to its inorganic analogue.[24] As their current-voltage curves illustrate, the iridium-based electrocatalysts **$Ir_{Molecular}$** and **IrO_x** have slightly different electrochemical behaviour, which is likely to be related to their complex redox chemistry.

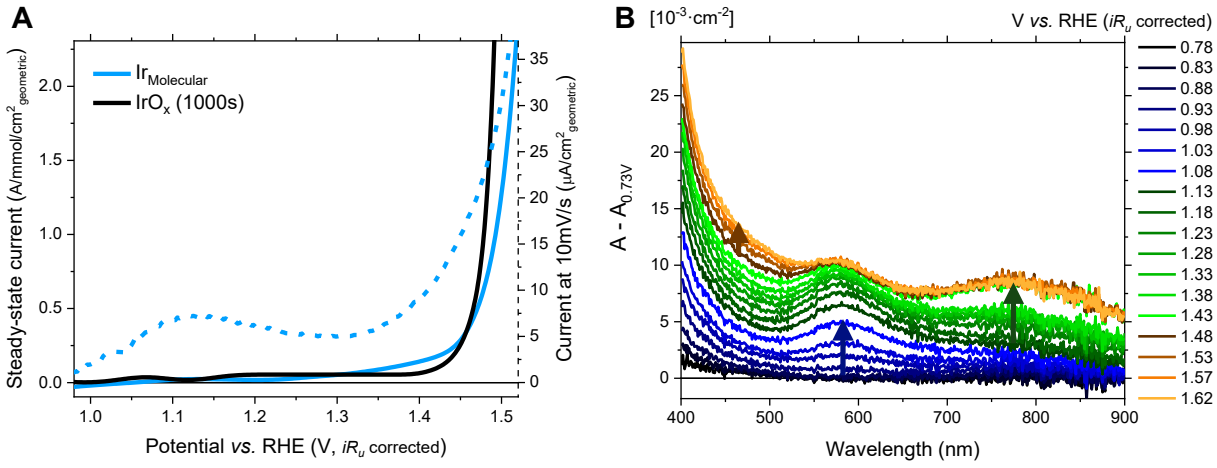

Figure 6.1. **(A)** Linear sweep voltammetry (with a scan rate of 10 mV/s) and steady-state current of **$Ir_{Molecular}$**, compared to the steady-state current of electrodeposited **IrO_x**. **(B)** Absorbance changes at different potentials of **$Ir_{Molecular}$** on mesoporous ITO. Measurements done in aqueous $HClO_4$ 0.1 M at pH 1.2.

6.3.2. Spectroelectrochemistry of $Ir_{Molecular}$ *vs.* IrO_x

To compare $Ir_{Molecular}$ to IrO_x, its spectroelectrochemistry was measured and deconvoluted to derive the concentration changes over potential and the differential absorption coefficients of its different redox states (Section 6.3.2.1). These results were then normalised and compared in Section 6.3.2.2 to those of IrO_x. Finally, the kinetics of the identified active site of $Ir_{Molecular}$ was measured and compared to IrO_x in Section 6.3.2.3.

6.3.2.1. Spectroelectrochemical characterisation of $Ir_{Molecular}$

To better characterise the redox transitions and states of $Ir_{Molecular}$, its absorbance in the UV-Vis was measured at different potentials in 0.1 M $HClO_4$ water at pH 1.2. Increasingly oxidising potentials were applied in ~0.05 V intervals starting at 0.73 V *vs.* RHE (iR_u corrected). Three different absorbance changes were observed at different potentials in $Ir_{Molecular}$ on mesoITO (Figure 6.1B), in contrast to the absence of any significant optical signal in bare mesoITO on FTO glass. At 0.78-1.08 V *vs.* RHE, an absorbance band at 590 nm dominated the spectrum, a new feature appeared at 800 nm at 1.13-1.43 V and, above 1.43 V, absorbance changes were only detected below 500 nm. To investigate individually the three redox transitions detected, the spectra was fit with a model based on three additive contributions to the absorbance, each linearly proportional to a concentration of redox states following the Lambert-Beer law:

Equation 6.1 $$\Delta A\ (E) = \sum_{i=1}^{3} \varepsilon_i \cdot C_i(E)$$

Where ΔA is the absorbance changes with respect to the starting applied potential (0.73 V *vs.* RHE in Figure 6.1B), E is the applied potential, i is the number identifying the redox transition and the resulting redox state, ε is the differential absorption coefficient of the redox transition (relative to the starting applied potential), and C is the total concentration of the redox state formed. To generate the model data using Equation 6.1, the differential absorption coefficients corresponding to each redox transition were derived from experimental spectra, and the concentration of redox states formed at each potential was assumed to follow a Gaussian distribution over potential, as described in more detail in Chapter 5 (Section 5.3.2.1, Equations 5.1-6). The model data was fit to the experimental data by adjusting the concentration distributions of each redox state. This deconvolution procedure allowed separating the three contributions to the absorbance of the different redox transitions with a minimal error (Figures 6.2-3).

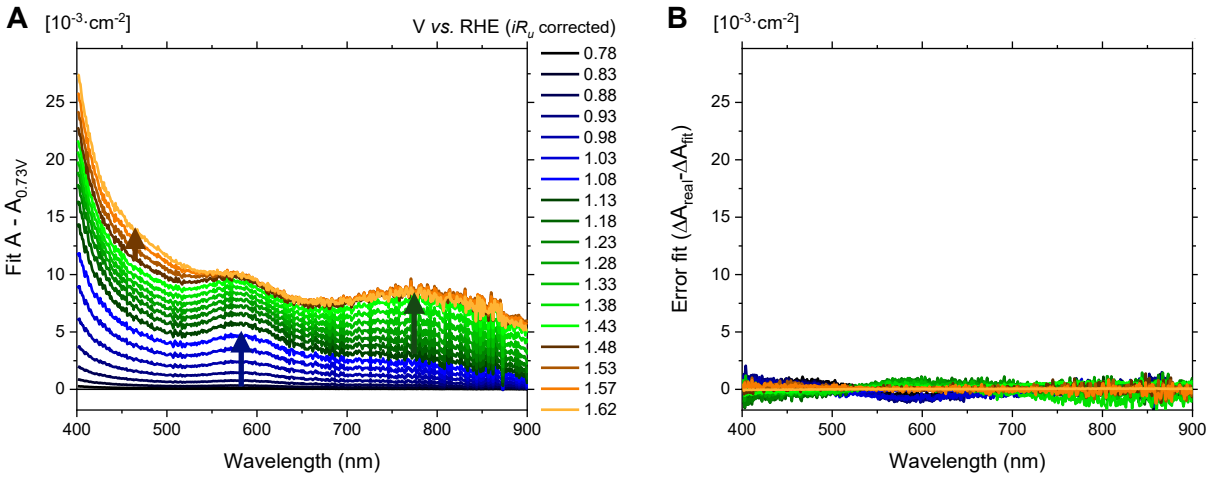

Figure 6.2. **(A)** Best fit of the spectroelectrochemical data of $\mathbf{Ir_{Molecular}}$ in Figure 1A generated with Equations 5.1-6. **(B)** Difference between the experimental data in Figure 6.1A and the model data in Figure 6.2A.

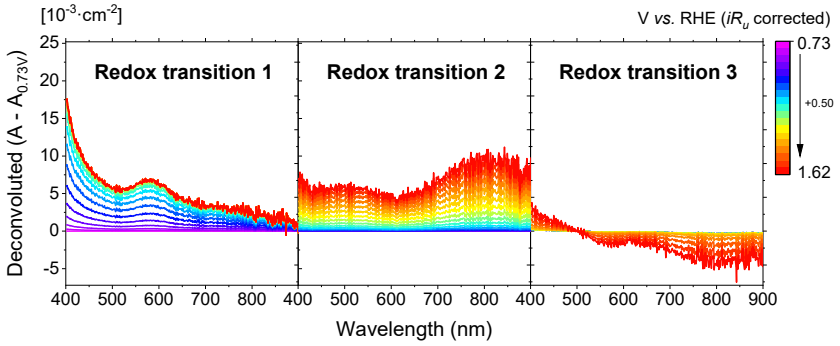

Figure 6.3. Absorbance changes over potential associated to each redox transition of $\mathbf{Ir_{Molecular}}$ on mesoITO. This data was generated with Equations 5.1-6 and the sum of the three components at each potential yields the model data in Figure 6.2A.

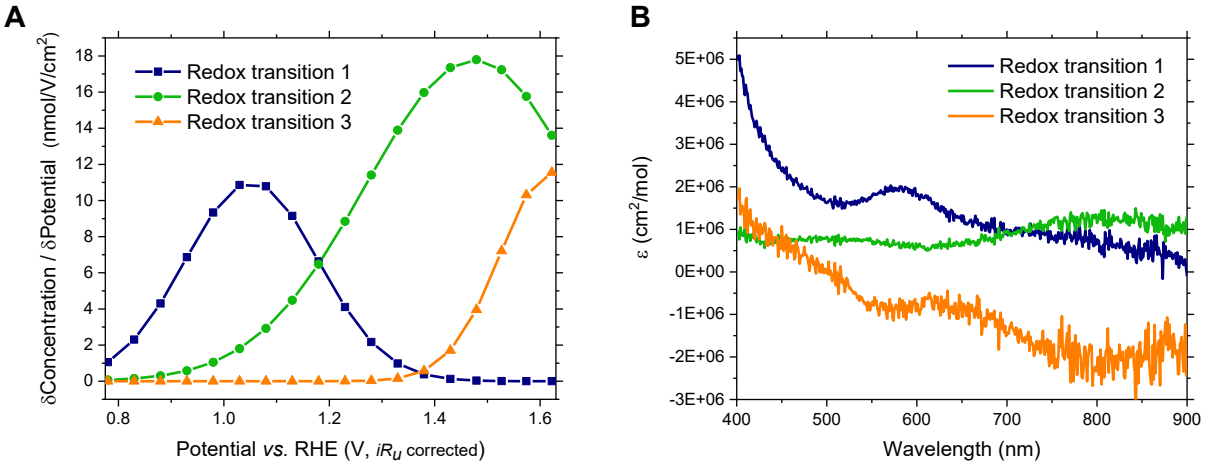

Figure 6.4. Deconvolution results of the spectroelectrochemical data of $\mathbf{Ir_{Molecular}}$. **(A)** Change in the concentration of the three redox states formed at increasing potentials and **(B)** differential absorption coefficients of the corresponding redox transitions. These results are derived from the spectroelectrochemical experimental data in Figure 6.1B and the fit data in Figure 6.2A.

The concentration changes and differential absorption coefficients of the redox states that best fit the spectroelectrochemical data are shown in Figure 6.4. These parameters were adjusted with the experimental values of ε_1*(600 nm)*, ε_2*(800 nm)* and ε_3*(460 nm)*, the differential absorption coefficients at the absorbance maxima during the 1st, 2nd and 3rd redox transitions respectively. To calculate these differential absorption coefficients, the current and absorbance changes were simultaneously measured during step potential spectroelectrochemistry measurements (SP-SEC), where two potentials with a difference of 50 mV were cyclically applied in consecutive steps of 5 s and 8 s (as described in Section 2.6 and illustrated in Scheme 5.1). When changing the applied potential, the current peaked and stabilised after <1 s, in parallel to a change in the absorbance (Figure 6.5). The current spike is assumed to be mostly due to the oxidation and reduction of states in **Ir$_{Molecular}$**, and the absorbance change is assigned to the differential absorbance of the newly formed redox state relative to the starting state in the less oxidising potential. In order to estimate the moles of redox state formed at each potential interval, we integrated the current spike over time, having subtracted the background current. For the redox transitions 1 and 2, the maximum absorbances changes at 600 nm and 800 nm were plotted against the extracted charges at potential intervals around 0.8 V and 1.3 V *vs.* RHE respectively, where the corresponding redox transition is the dominant process (Figure 6.6). For the redox transition 3, the same methodology was applied using the absorbance changes at 460 nm and the charges extracted above 1.2 V but, because it overlaps significantly with the redox transition 2, the charges and absorbance corresponding to the latter redox transition were previously subtracted. The slope of the linear regression was taken as the differential absorption coefficient corresponding to a one-electron oxidation per redox transition. The differential coefficients obtained this way were compatible with those reported in the literature for **Ir$_{Molecular}$** derived with other methods.[24, 38]

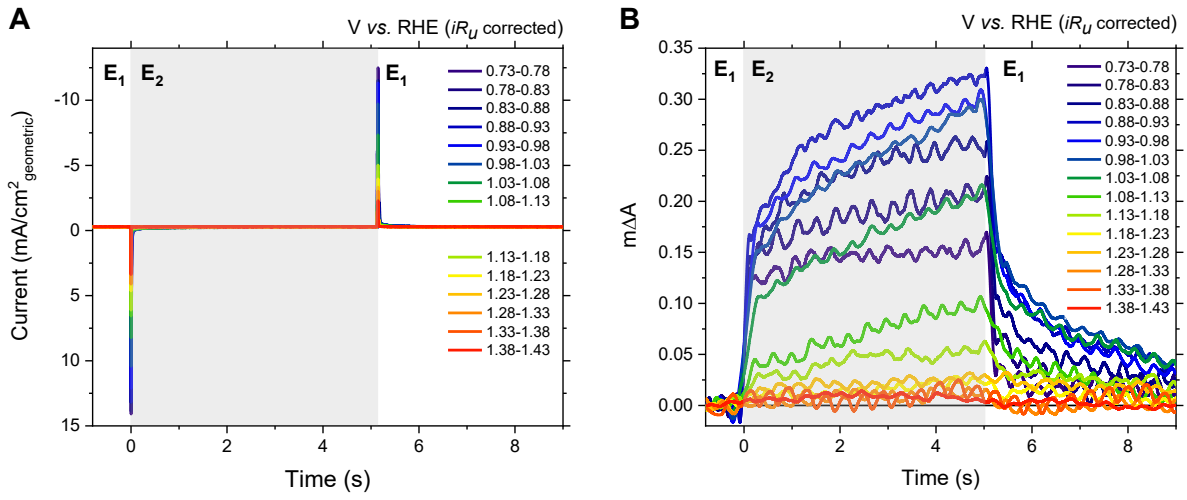

Figure 6.5. **(A)** Transient currents and **(B)** transient absorbance changes measured in **Ir$_{Molecular}$** during potential steps between two different applied potentials in 0.1 M $HClO_4$ water at pH 1.2, as illustrated in Scheme 5.1.

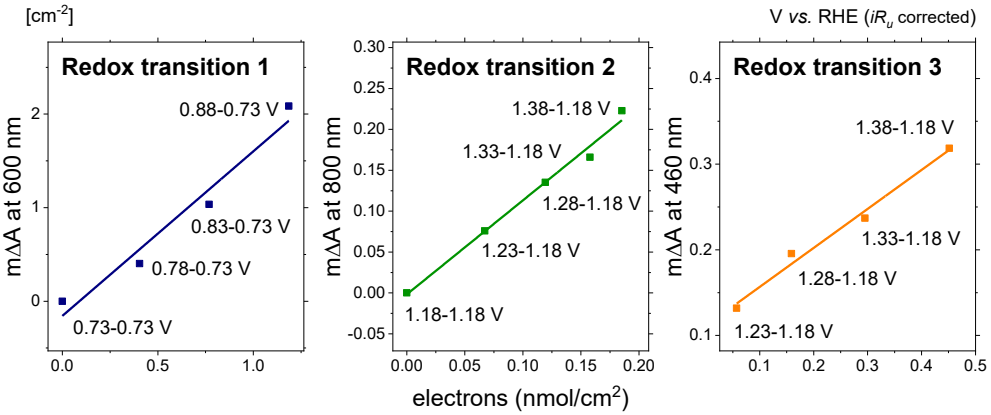

Figure 6.6. Dependency of the deconvoluted absorbance changes on the extracted charge for each redox transition. The charges are calculated by integrating the reductive peak in Figure 6.5A and the deconvoluted absorbance is derived from the Figure 6.3. The slope of the linear regression is the differential absorption coefficient of the new redox state formed at the corresponding redox transition. The label next to each data point indicates the potential interval where the absorbance changes and the charges were measured.

Comparing the electrochemical and spectroelectrochemical data in Figures 6.1A and 6.4 respectively, it is apparent that the electrochemical peak detected at 1.15 V *vs.* RHE (Figure 6.1A, iR_u corrected) corresponds to the 1st redox transition with an absorbance maximum at 600 nm (Figure 6.4 in *blue*). In parallel, the electrocatalytic current above 1.35 V masks the 2nd and 3rd redox transitions detected spectroelectrochemically (Figure 6.4 in *green* and *orange*). Furthermore, assuming one-electron oxidations per each redox transition, the total concentration of the corresponding redox state was calculated by integrating the area below the concentration distribution in Figure 6.4A. Similar concentrations of one-electron-oxidated redox state were derived from redox transitions 1 and 3, which was half the total concentration generated from redox transition 2. While there may not be sufficient data points to evaluate redox transition 3, the difference between the redox transition 1 and 2 means that the second redox transition involves more charges than the first.

6.3.2.2. Steady-state spectroelectrochemistry of $\mathbf{Ir_{Molecular}}$ *compared to* $\mathbf{IrO_x}$

Once the optical signals of $\mathbf{Ir_{Molecular}}$ were deconvolved as a function of three redox transitions and resulting redox states, they were compared with those observed in $\mathbf{IrO_x}$. The spectroelectrochemistry of $\mathbf{IrO_x}$ was measured in 0.1 M $HClO_4$ water at pH 1.2, and deconvolved following the same procedure as with $\mathbf{Ir_{Molecular}}$. Three optical transitions at three different potential ranges were observed in $\mathbf{IrO_x}$, comparable to those of $\mathbf{Ir_{Molecular}}$ (Figures 5.2A, 5.4-5). Figure 6.7 shows the

normalised concentration distributions and differential absorbance corresponding to the three redox transitions detected in both catalysts. The optical signals related to the three redox transitions in the two catalysts have similar features, with maxima at around 600, 800 and <500 nm respectively (Figure 6.7A), slightly blue-shifted in $\mathbf{Ir_{Molecular}}$. On the other hand, the concentration distribution in $\mathbf{Ir_{Molecular}}$ is shifted by ~100 mV to more oxidising potentials with respect to $\mathbf{IrO_x}$ in the three redox transitions (Figure 6.7B). In the 0.8-1.4 V range, these optical transitions in $\mathbf{IrO_x}$ have been assigned to an intervalence charge transfer within the iridium *d* orbitals derived from the oxidation of Ir(3+) to Ir(4+) in different steps and deprotonation of hydroxyl groups coordinated to the Ir centre.[39-45] Above 1.4 V, redox states of iridium higher than 4+ are expected to be formed.[29, 30, 34, 46-48] In the case of molecular iridium complexes, Crabtree *et al.* reported an iridium dimer which has a dimeric structure and absorbance similar to $\mathbf{Ir_{Molecular}}$: Ir(3+)-Ir(3+) absorbs below 450 nm, Ir(4+)-Ir(4+) absorbs at 600-750 nm, and Ir(4+)-Ir(5+) absorbs at 500 nm.[49, 50] Taking this iridium dimer as a reference, the three redox transitions in $\mathbf{Ir_{Molecular}}$ would yield Ir(3+)-Ir(4+), Ir(4+)-Ir(4+), and Ir(4+)-Ir(5+) respectively. Considering the relative amount of charges in each redox transition calculated above, and the oxidation numbers of the iridium centres assigned according to the literature, the 2nd redox transition of $\mathbf{Ir_{Molecular}}$ most likely involves the oxidation of non-innocent coordinated ligands in addition to the iridium centres. Therefore, the oxidation processes detected between 0.8 V *vs.* RHE and the onset potential in both iridium $\mathbf{IrO_x}$ and $\mathbf{Ir_{Molecular}}$ are based on the same oxidation numbers of iridium, although the exact ratio of iridium centres with these oxidation numbers in each redox state cannot be demonstrated.

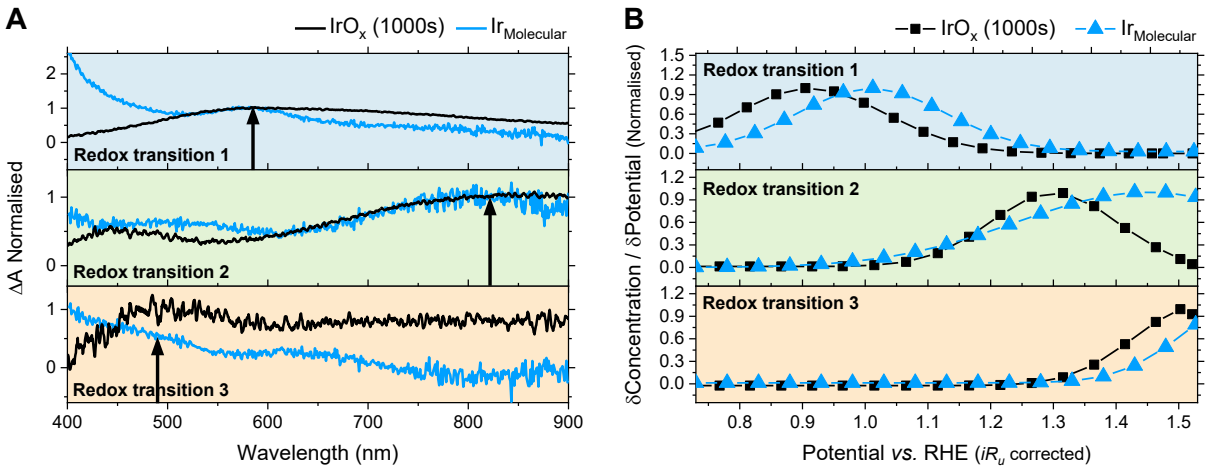

Figure 6.7. **(A)** Deconvoluted differential absorbance and concentration changes and **(B)** steady-state current of $\mathbf{Ir_{Molecular}}$ and $\mathbf{IrO_x}$ in 0.1 M $HClO_4$ aqueous solution at pH 1.2. The absorbance and currents were measured under constant applied potentials every 0.05 V.

6.3.2.3. Active state kinetics in $\mathbf{Ir_{Molecular}}$ *and* $\mathbf{IrO_x}$

To analyse the activity of the redox states in $\mathbf{Ir_{Molecular}}$, the optical signal decay was measured after turning the applied potential off in the same 0.1 M $HClO_4$ aqueous solution at pH 1.2. These measurements were based on SP-SEC consisting of regular two-step cycles, where a potential was applied for 5 s and then was turned off for 8 s. When applying a potential from OCP to $\mathbf{Ir_{Molecular}}$, an absorbance change relative to OCP was detected only at applied potentials above 1.3 V *vs.* RHE (iR_u corrected) (Figure 6.1A). This potential coincides approximatively with the OER onset potential (Figure 6.1A) and the 3rd redox transition (*orange* in Figure 6.4A). In $\mathbf{IrO_x}$, an optical signal relative to OCP was also detected exclusively above 1.3 V, which also corresponds to the onset potential and the formation of the 3rd redox transition in $\mathbf{IrO_x}$ (Figures 5.2A and 5.5A). This means that the redox state resulting from the 3rd redox transition both in $\mathbf{IrO_x}$ and $\mathbf{Ir_{Molecular}}$ reacts in water after turning the potential off, most likely generating O_2. On the other hand, the decay kinetics of the optical signal in $\mathbf{Ir_{Molecular}}$ is similar throughout the 1.3-1.6 V range, while in $\mathbf{IrO_x}$ the optical signal becomes faster at increasing potentials in this range (Figure 6.8A). The latter is illustrated in Figure 6.8B, where the optical signal lifetimes at different potentials were extracted from fitting the signal decays with an initial linear regression (Equations 5.7-8, Section 5.3.6). It is apparent from Figure 6.8B that $\mathbf{Ir_{Molecular}}$ has shorter lifetimes than $\mathbf{IrO_x}$ below 1.45 V *vs.* RHE and longer above, the same trend observed in the steady-state current in Figure 6.1A. This implies that the redox state resulting from the 3rd redox transition can trigger OER both in $\mathbf{IrO_x}$ and $\mathbf{Ir_{Molecular}}$, but has different OER reactivity in $\mathbf{IrO_x}$ depending on the applied potential.

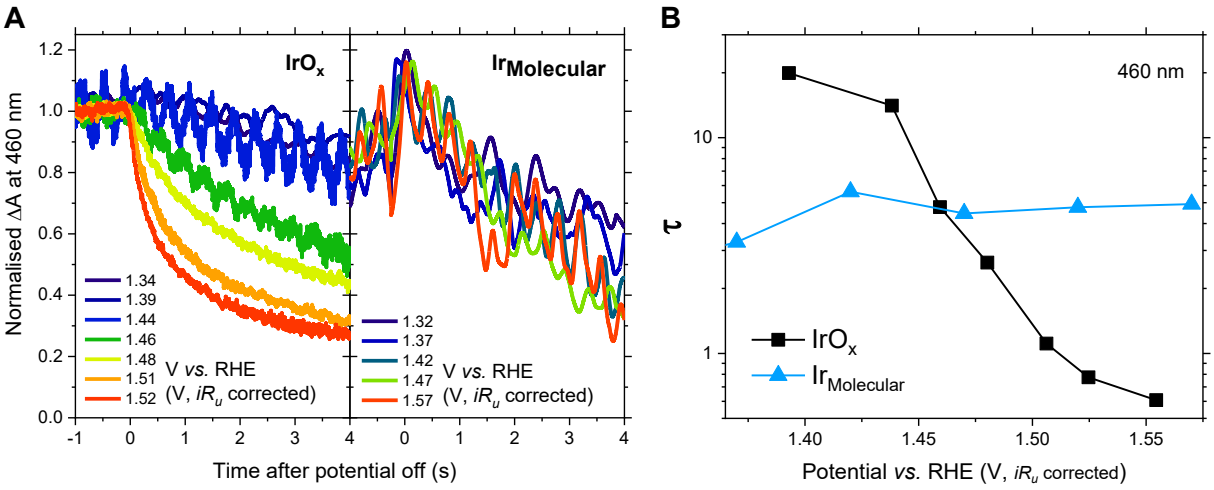

Figure 6.8. **(A)** Absorbance decay after turning the potential off, and **(B)** optical signal lifetimes derived from fitting an initial linear regression in Figure 6.8A in $\mathbf{Ir_{Molecular}}$ and $\mathbf{IrO_x}$ in 0.1 M $HClO_4$ water at pH 1.2.

6.3.3. Spectroelectrochemistry of IrO_x with different iridium content

Samples of **IrO_x** with different amounts of iridium and OER activities were prepared to systematically compare the inorganic and molecular catalysts. The different samples were prepared by controlling the electrodeposition time of an aqueous iridium anion on FTO-glass under ~35 µA (see Section 6.2.3). In addition to the **IrO_x** sample presented above, which was electrodeposited for 1000s, four new samples were prepared with electrodeposition times of 700s, 500s, 120s and 60s. From the currents measured during the electrodeposition of the **IrO_x** samples, the amount of iridium in the different films should be approximately proportional to the electrodeposition times. The steady-state current of the resulting films under different constant applied potentials in 0.1 M HCl_4 water at pH 1.2 is shown in Figure 6.9A. The steady-state current is larger with increasing electrodeposition times. To investigate the redox states of these samples involved in the OER activity and electrocatalytic current, we measured the spectroelectrochemistry of the different **IrO_x** samples and deconvolved the results following the same procedure as with **$Ir_{Molecular}$** and **IrO_x** 1000s above (Figure 6.10). The normalised concentration changes and differential absorption coefficients, resulting from the deconvolution of the spectroelectrochemical data, overlap in all the **IrO_x** samples (Figure 6.9B), which would imply that the chemical nature of the redox states in all the **IrO_x** samples is similar. In the samples **IrO_x** 120s and 60s, broader concentration distributions are observed and, in the case of **IrO_x** 60s, the redox transitions 1 and 2 are detected as one, which is most likely due to the smaller optical signal and signal-to-noise ratio of these samples. The larger activities of the films electrodeposited for longer times is therefore related to a larger content of iridium and concentration of active sites, rather than to a different nature of the redox states in **IrO_x**.

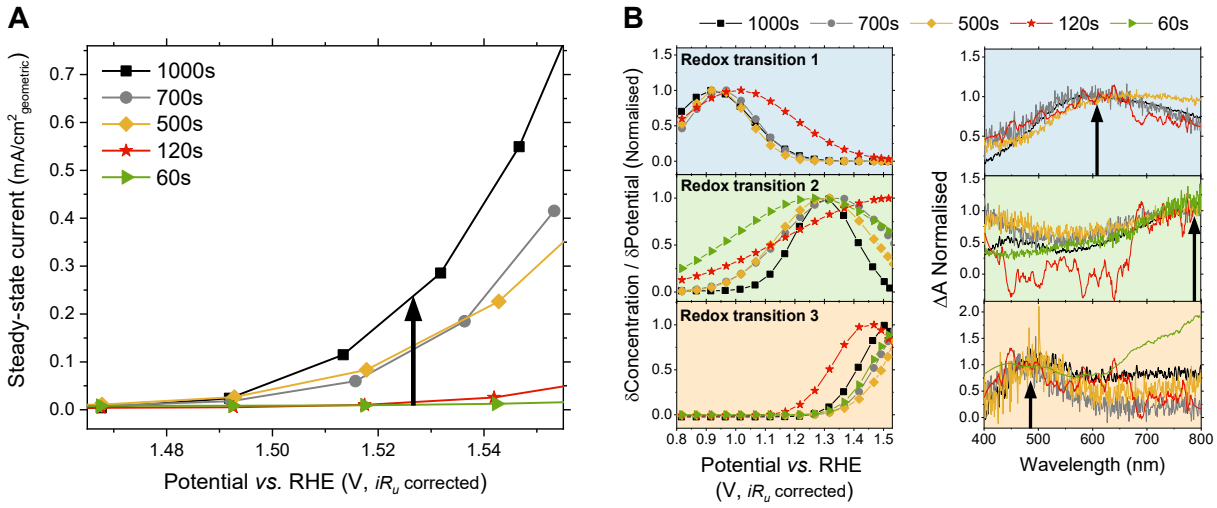

Figure 6.9. **(A)** Steady-state current and **(B)** normalised concentration changes and differential absorption coefficients obtained from spectroelectrochemical data of **IrO_x** samples electrodeposited for 1000s, 700s, 500s, 120s and 60s in 0.1 M $HClO_4$ water at pH 1.2.

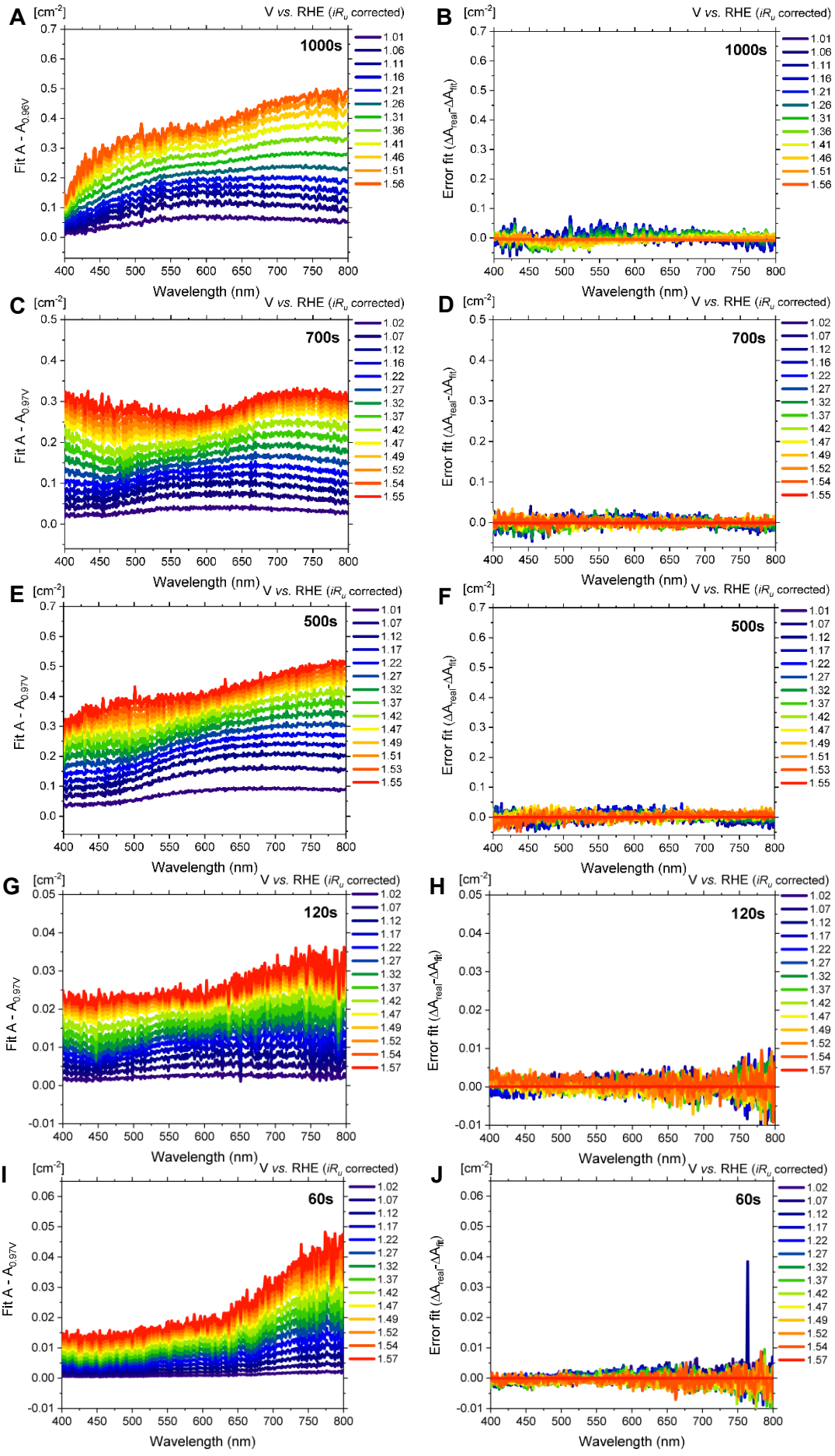

Figure 6.10. Fit spectroelectrochemistry data and calculation error of **IrO_x** electrodeposited for **(A-B)** 1000 s, **(C-D)** 700 s, **(E-F)** 500 s, **(G-H)** 120 s and **(I-J)** 60 s in 0.1 M $HClO_4$ water at pH 1.2. Model data generated with equations 5.1-6.

6.3.4. Activity of iridium electrocatalysts as a function of the active state concentration

To relate the OER activity of both **IrO_x** and **$Ir_{Molecular}$** to the concentration of their active states (defined as the 3rd redox state above) instead of the potential, the steady-state current is plotted against the concentration of active species in Figure 6.11. The active species concentration was derived from the deconvoluted spectroelectrochemical absorbance of the 3rd redox transition, with the corresponding differential absorption coefficient (Figures 6.4A and 6.9B-10 for **$Ir_{Molecular}$** and **IrO_x** respectively). From Figure 6.11, it is apparent that steady-state currents up to ~0.1 mA/cm^2 are reached with lower concentrations of active sites in **$Ir_{Molecular}$**, **IrO_x** 60s and **IrO_x** 120s, which means that the active sites in these samples have a larger activity than in other samples. The latter higher activity is most likely due to a better accessibility of the active iridium centres by the electrolyte. In contrast, the **IrO_x** 1000s, 700s and 500s samples show similar dependences between the steady-state current and the concentration of active species, indicating the same activity per active site. Higher steady-state currents above 0.1 mA/cm^2 are only observed in samples with electrodeposited times longer than 120s, as shown by the increasing concentrations of active species under the same potential in the samples with increasing electrodeposition times, probably because of the larger absolute concentration of active species in the material.

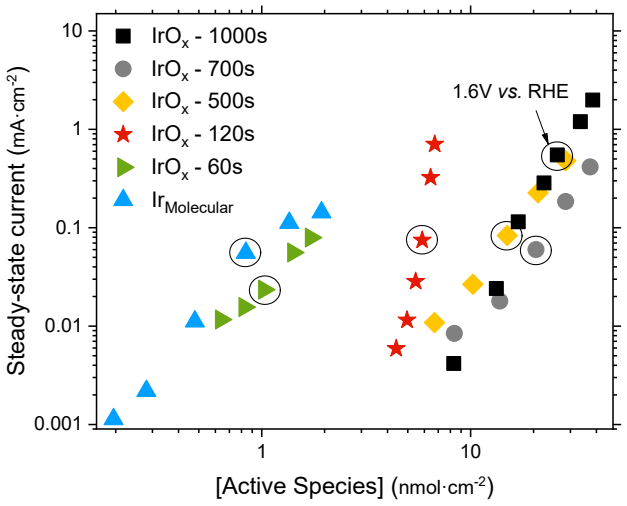

Figure 6.11. Steady-state current plotted against the concentration of active species in **IrO_x** samples with different electrodeposition times (1000s, 700s, 500s, 120s and 60s) and in **$Ir_{Molecular}$**. The concentration of active sites is derived from the deconvoluted and calibrated spectreoelectrochemical data (Figure 6.4 and 6.9B) and the active state is assumed to be the redox state resulting from the 3rd redox transition.

6.4. Discussion

The relatively high OER activity of iridium electrocatalysts, following the *Sabatier principle* and classic thermodynamic principles, stems from the optimal activation energy barriers and formation energies of reaction intermediates based on iridium centres, which maximise the rate and energy efficiency of the reaction.[1] Therefore, the OER activity is also influenced by the accessibility of the iridium centres and their chemical environment, including the ligand or atoms directly coordinated or bonded to the iridium centres and their surrounding. However, to systematically investigate these effects is very challenging because of the difficulty to identify the different possible active sites, distinguish their different individual reactivity, and measure the effect of different parameters experimentally. By measuring the redox states concentration and their reaction kinetics in $\mathbf{Ir_{Molecular}}$ and $\mathbf{IrO_x}$ samples with different electrodeposition times, we have attempted herein to separately investigate (1) the effect of the chemical and electronic configuration and (2) the accessibility of iridium centres on the OER reactivity.

When measuring the absorbance under applied potential, three different characteristic optical signals are observed at different potentials ranges in both $\mathbf{IrO_x}$ and $\mathbf{Ir_{Molecular}}$. These three redox transitions could be deconvolved and individually quantified with minimal error in both electrocatalysts, assuming additive absorbances which are linearly proportional to a Gaussian concentration redox states formed over potential. The redox transitions 1, 2 and 3 are similar in the two materials, having characteristic absorbance peaks at 600, 800 and <500 nm respectively (Figures 6.7 and 6.9B). These transitions are associated with *d-d* transitions resulting from the deprotonation of coordinated hydroxyl and the oxidation of Ir(3+) to Ir(4+) and beyond.[29, 30, 34, 39-50] In the molecular catalyst, the absorbance maxima are slightly shifted towards lower wavelengths, and there is an additional absorbance change below 500 nm at low applied potentials that is compatible with the metal to ligand charge transfers typical of organometallic complexes (Figure 6.7A).[51, 52] Furthermore, the potential of maximum concentration change for each redox transition in $\mathbf{Ir_{Molecular}}$ is shifted by ~100 mV compared to $\mathbf{IrO_x}$ (Figure 6.7B). This could partially be due to the poorer electronic contact between the $\mathbf{Ir_{Molecular}}$ catalyst and the substrate, caused either by the different nature of the substrates (mesoITO-FTO and FTO) or by the bulkiness of the ligand scaffold. A plausible cause for both the increase in redox potential and the blue-shift of the absorbance (based on *d-d* transitions) in $\mathbf{Ir_{Molecular}}$ is the stabilisation of the t_{2g} *d* iridium orbitals by pyridine π orbitals, which have the same symmetry in octahedral organometallic complexes (Scheme 6.1).[51, 52] In the case of the $\mathbf{IrO_x}$ samples (Figure 6.9B), differences in the samples with less amount of iridium are most likely due to the small signal-to-noise ratio. In parallel, the redox state concentration between redox transition 1 and 2 varies across the different samples (Table 6.1), which may originate from the different degrees of hydroxyl coordination in the samples at the start of the spectroelectrochemistry measurements. This leads to the conclusion that iridium centres in $\mathbf{Ir_{Molecular}}$ compared to $\mathbf{IrO_x}$ are based on iridium atoms with the

same oxidation numbers but different chemical environment, while those in **IrO_x** have most likely a similar chemical environment independently of the electrodeposition time and the iridium content.

Table 6.1. Ratio between the concentration of the redox states 1, 2 and 3 in each **IrO_x** and **$Ir_{Molecular}$** sample. The concentration in moles per cm^2 has been derived from the deconvolution of the spectroelectrochemistry data (Equations 5.1-6). *In **IrO_x** 60s, the first redox transition detected has been considered to be a combination of redox transitions 1 and 2 in the rest of the samples.

Sample	*Molar ratio of redox states 1:2:3 at 1.57 V vs. RHE*
IrO_x 1000s	10 : 9 : 3
IrO_x 700s	6 : 10 : 3
IrO_x 500s	10 : 8 : 3
IrO_x 120s	10 : 10 : 3
IrO_x 60s	10 : 10 : 2 *
$Ir_{Molecular}$	6 : 10 : 1

To investigate the intrinsic reactivity of the redox states of the iridium centres identified above, the kinetics were measured by fitting the optical signal decay after turning the potential off. Based on the overlap in the potentials where both a steady-state current and an optical signal change from OCP were observed (Figure 6.1A and 6.8), the 3rd redox state was identified as the active site in both electrocatalysts. In the case of molecular catalyst, the optical signal lifetime corresponding to the reaction kinetics of the 3rd redox state were observed to remain constant above the onset potential (Figure 6.8B). This implies that the reaction mechanism of the active redox state is constant at all potentials and that the changes in the steady-state current over potential are only due to changes in the concentration of the redox state. In contrast, the onset potential in **IrO_x** is at ~1.45 V *vs.* RHE, ~100 mV more that the formation of the active redox state. The lifetimes of the active state in **IrO_x** change from being longer and less-reactive than in **$Ir_{Molecular}$** before 1.45 V, to shorter and more-reactive above 1.45 V. This would indicate that, in **IrO_x**, the OER mechanism is different than in **$Ir_{Molecular}$** and requires a critical concentration of active site. At low potentials, the reactivity in **IrO_x** and **$Ir_{Molecular}$** could be determined by the chemical environment, as illustrated in Scheme 6.1. At high potentials, the different chemistry in **IrO_x** could be related to the reaction between two active redox states nearby involving more than two iridium centres.

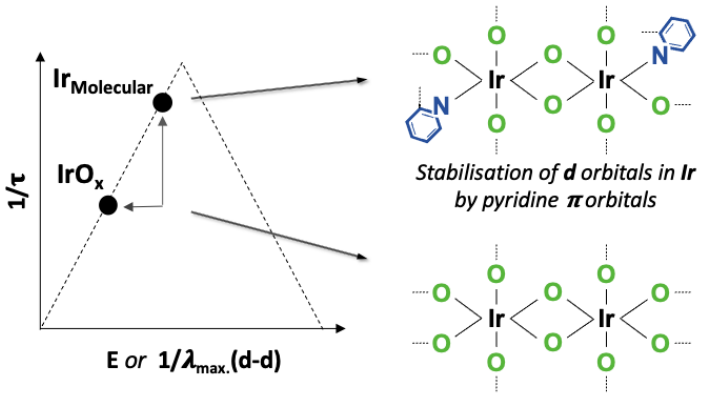

Scheme 6.1. Chemical effects of the atoms coordinated to the iridium active sites on the redox potential (E) and maximum absorbance wavelength of d-d transitions ($\lambda_{max.}(d\text{-}d)$), and lifetimes ($\tau$) in water 0.1 M $HClO_4$ at pH 1.2.

The activity of electrocatalysts is usually compared based on the exponential dependence between the current density and the applied potential, with a steeper dependence (*i.e.*, tafel slope) being an indicator of higher activity. In crystalline metal and semiconductor materials, this behaviour is typically assigned to the changing energy of free charges in the material assuming a continuum distribution of states.[53, 54] However, in non-crystalline disordered materials such as $\mathbf{IrO_x}$ or nickel oxides and localised organometallic molecules such as $\mathbf{Ir_{Molecular}}$,[22, 35] the dependence of the current on potential has been shown to be proportional to the increasing concentration of a discrete redox active state. In particular, smaller concentrations of active sites are needed to yield similar current densities in $\mathbf{Ir_{Molecular}}$ and $\mathbf{IrO_x}$ with less content of iridium compared to $\mathbf{IrO_x}$ with larger content of iridium (Figure 6.11). Rather than the intrinsic chemistry and activity of the iridium centres, as determined from the optical signal kinetics, this trend is most likely due to the exposure of the active sites to the electrolyte. More available active sites producing higher current densities, and $\mathbf{Ir_{Molecular}}$, which consists of a well-characterised monolayer on mesoITO,[24, 38, 55] serves as a reference.

6.5. Conclusions

The redox chemistry of $\mathbf{Ir_{Molecular}}$ was investigated by deconvolving the absorbance at different potentials. Three redox transitions and four redox states were identified between the open circuit and the catalytic onset potential. These redox states had similar absorbance maxima and redox potentials to $\mathbf{IrO_x}$, but shifted to the blue and to larger oxidation potentials respectively in $\mathbf{Ir_{Molecular}}$. The active redox state was determined by comparing the electrocatalytic onset potential to the optical signal changes when turning an applied potential on and off, which is related to the reactivity of the redox states with water. In both $\mathbf{IrO_x}$ and $\mathbf{Ir_{Molecular}}$, the active state was the redox state resulting from the 3rd redox transition. Below 1.45 V *vs.* RHE, this active state had faster kinetics in $\mathbf{Ir_{Molecular}}$ than in $\mathbf{IrO_x}$, but had slower kinetics above 1.45 V. The latter effect is most likely related to the different chemical environment of the iridium centres in the two electrocatalysts, and to different OER mechanisms with different reaction orders, which critically depend on the concentration. Compared to $\mathbf{IrO_x}$ electrodeposited during different times and with different iridium contents, $\mathbf{Ir_{Molecular}}$ could reach similar current densities up to 0.1 mA/cm^2 with a smaller concentration of active sites because of the accessibility of the iridium centres. Therefore, these results show that the exposure of the iridium centres and their chemical environment play key roles in the activity of iridium electrocatalysts.

6.6. References

1. Z. W. Seh, J. Kibsgaard, C. F. Dickens, I. Chorkendorff, J. K. Nørskov and T. F. Jaramillo, *Science*, 2017, **355**.
2. R. Frydendal, E. A. Paoli, B. P. Knudsen, B. Wickman, P. Malacrida, I. E. L. Stephens and I. Chorkendorff, *ChemElectroChem*, 2014, **1**, 2075-2081.
3. C. Wei, R. R. Rao, J. Peng, B. Huang, I. E. L. Stephens, M. Risch, Z. J. Xu and Y. Shao-Horn, *Adv. Mater.*, 2019, **31**, e1806296.
4. S. Haussener, C. Xiang, J. M. Spurgeon, S. Ardo, N. S. Lewis and A. Z. Weber, *Energy Environ. Sci.*, 2012, **5**, 9922.
5. A. Marshall, B. Børresen, G. Hagen, M. Tsypkin and R. Tunold, *Energy*, 2007, **32**, 431-436.
6. M. Carmo, D. L. Fritz, J. Mergel and D. Stolten, *Int. J. Hydrog. Energy*, 2013, **38**, 4901-4934.
7. M. Bernt and H. A. Gasteiger, *J. Electrochem. Soc.*, 2016, **163**, F3179-F3189.
8. M. Bernt, A. Siebel and H. A. Gasteiger, *J. Electrochem. Soc.*, 2018, **165**, F305-F314.
9. Photoelectrochemical Hydrogen Production, R. van de Krol and M. Grätzel, *Springer, Electronic Materials: Science & Technology*, 2012.
10. Study on the review of the list of Critical Raw Materials. Criticality Assessments. *European Comission*, 2017.
11. Study on the review of the list of Critical Raw Materials. Non-critical Raw Materials Factsheets, *European Comission*, 2017.
12. Technological Roadmap, *Sunergy*, 2020.
13. Basic Research Needs: Catalysis for Energy, U.S.A. D.O.E., 2007.
14. Research needs towards sustainable production of fuels and chemicals, J. K. Nørskov, A. Latimer and C. F. Dickens, 2019.
15. D. Chandra, T. Sato, Y. Tanahashi, R. Takeuchi and M. Yagi, *Energy*, 2019, **173**, 278-289.
16. H. Jang and J. Lee, *J. Energy Chem.*, 2020, **46**, 152-172.
17. K. Yamanaka, *Jpn. J. Appl. Phys.*, 1989, **28**, 632-637.
18. I. C. Man, H. Y. Su, F. Calle-Vallejo, H. A. Hansen, J. I. Martínez, N. G. Inoglu, J. Kitchin, T. F. Jaramillo, J. K. Nørskov and J. Rossmeisl, *ChemCatChem*, 2011, **3**, 1159-1165.
19. H. A. Hansen, V. Viswanathan and J. K. Nørskov, *J. Phys. Chem. C*, 2014, **118**, 6706-6718.
20. C. F. Dickens, C. Kirk and J. K. Nørskov, *J. Phys. Chem. C*, 2019, **123**, 18960-18977.
21. T. Naito, T. Shinagawa, T. Nishimoto and K. Takanabe, *Inorg. Chem. Front.*, 2021, DOI: 10.1039/d0qi01465f.
22. C. A. Mesa, L. Francàs, K. R. Yang, P. Garrido-Barros, E. Pastor, Y. Ma, A. Kafizas, T. E. Rosser, M. T. Mayer, E. Reisner, M. Grätzel, V. S. Batista and J. R. Durrant, *Nat. Chem.*, 2020, **12**, 82-89.
23. J. Rossmeisl, Z. W. Qu, H. Zhu, G. J. Kroes and J. K. Nørskov, *J. Electroanal. Chem.*, 2007, **607**, 83-89.
24. S. W. Sheehan, J. M. Thomsen, U. Hintermair, R. H. Crabtree, G. W. Brudvig and C. A. Schmuttenmaer, *Nat. Commun.*, 2015, **6**, 6469.
25. K. J. Young, L. A. Martini, R. L. Milot, R. C. Snoeberger, III, V. S. Batista, C. A. Schmuttenmaer, R. H. Crabtree and G. W. Brudvig, *Coord. Chem. Rev.*, 2012, **256**, 2503-2520.
26. J. M. Thomsen, D. L. Huang, R. H. Crabtree and G. W. Brudvig, *Dalton Trans.*, 2015, **44**, 12452-12472.
27. S. Geiger, O. Kasian, M. Ledendecker, E. Pizzutilo, A. M. Mingers, W. T. Fu, O. Diaz-Morales, Z. Li, T. Oellers, L. Fruchter, A. Ludwig, K. J. J. Mayrhofer, M. T. M. Koper and S. Cherevko, *Nat. Catal.*, 2018, **1**, 508-515.
28. A. R. Zeradjanin, A. A. Topalov, Q. Van Overmeere, S. Cherevko, X. Chen, E. Ventosa, W. Schuhmann and K. J. J. Mayrhofer, *RSC Adv.*, 2014, **4**.
29. M. Ledendecker, S. Geiger, K. Hengge, J. Lim, S. Cherevko, A. M. Mingers, D. Göhl, G. V. Fortunato, D. Jalalpoor, F. Schüth, C. Scheu and K. J. J. Mayrhofer, *Nano Res.*, 2019, **12**, 2275-2280.
30. O. Kasian, J. P. Grote, S. Geiger, S. Cherevko and K. J. J. Mayrhofer, *Angew. Chem. Int.*, 2018, **57**, 2488-2491.

31. O. Kasian, S. Geiger, T. Li, J.-P. Grote, K. Schweinar, S. Zhang, C. Scheu, D. Raabe, S. Cherevko, B. Gault and K. J. J. Mayrhofer, *Energy Environ. Sci.*, 2019, **12**, 3548-3555.
32. S. Geiger, O. Kasian, B. R. Shrestha, A. M. Mingers, K. J. J. Mayrhofer and S. Cherevko, *J. Electrochem. Soc.*, 2016, **163**, F3132-F3138.
33. S. Cherevko, S. Geiger, O. Kasian, A. Mingers and K. J. J. Mayrhofer, *J. Electroanal. Chem.*, 2016, **773**, 69-78.
34. S. Cherevko, S. Geiger, O. Kasian, A. Mingers and K. J. J. Mayrhofer, *J. Electroanal. Chem.*, 2016, **774**, 102-110.
35. L. Francàs, S. Corby, S. Selim, D. Lee, C. A. Mesa, R. Godin, E. Pastor, I. E. L. Stephens, K. S. Choi and J. R. Durrant, *Nat. Commun.*, 2019, **10**, 5208.
36. H. N. Nong, L. J. Falling, A. Bergmann, M. Klingenhof, H. P. Tran, C. Spori, R. Mom, J. Timoshenko, G. Zichittella, A. Knop-Gericke, S. Piccinin, J. Perez-Ramirez, B. R. Cuenya, R. Schlögl, P. Strasser, D. Teschner and T. E. Jones, *Nature*, 2020, **587**, 408-413.
37. W. Li, S. W. Sheehan, D. He, Y. He, X. Yao, R. L. Grimm, G. W. Brudvig and D. Wang, *Angew. Chem. Int.*, 2015, **54**, 11428-11432.
38. W. Li, D. He, S. W. Sheehan, Y. He, J. E. Thorne, X. Yao, G. W. Brudvig and D. Wang, *Energy Environ. Sci.*, 2016, **9**, 1794-1802.
39. Electrochromism: Fundamental and Applications, P. M. S. Monk, R. J. Mortimer and D. R. Rosseinsky, *VCH*, 1995.
40. Electrochromism and Electrochromic Devices, P. M. S. Monk, R. J. Mortimer and D. R. Rosseinsky, *Cambridge University Press*, 2008.
41. Mixed Valence Chemistry-A Survey and Classification, M. B. Robin and P. Day, 1968, **10**, 247-422.
42. S. Gottesfeld, J. D. E. McIntyre, G. Beni and J. L. Shay, *Appl. Phys. Lett.*, 1978, **33**, 208-210.
43. S. Gottesfeld and J. D. E. McIntyre, *J. Electrochem. Soc.*, 1979, 742-750.
44. H. Ooka, T. Takashima, A. Yamaguchi, T. Hayashi and R. Nakamura, *Chem. Commun.*, 2017, **53**, 7149-7161.
45. H. Ooka, Y. Wang, A. Yamaguchi, M. Hatakeyama, S. Nakamura, K. Hashimoto and R. Nakamura, *Phys. Chem. Chem. Phys.*, 2016, **18**, 15199-15204.
46. V. Pfeifer, T. E. Jones, J. J. Velasco Velez, R. Arrigo, S. Piccinin, M. Havecker, A. Knop-Gericke and R. Schlögl, *Chem. Sci.*, 2017, **8**, 2143-2149.
47. V. Pfeifer, T. E. Jones, J. J. Velasco Velez, C. Massue, M. T. Greiner, R. Arrigo, D. Teschner, F. Girgsdies, M. Scherzer, J. Allan, M. Hashagen, G. Weinberg, S. Piccinin, M. Havecker, A. Knop-Gericke and R. Schlögl, *Phys. Chem. Chem. Phys.*, 2016, **18**, 2292-2296.
48. V. Pfeifer, T. E. Jones, S. Wrabetz, C. Massue, J. J. Velasco Velez, R. Arrigo, M. Scherzer, S. Piccinin, M. Havecker, A. Knop-Gericke and R. Schlögl, *Chem. Sci.*, 2016, **7**, 6791-6795.
49. L. S. Sharninghausen, S. Bhushan Sinha, D. Y. Shopov, B. Q. Mercado, D. Balcells, G. W. Brudvig and R. H. Crabtree, *Angew. Chem.*, 2017, **129**, 13227 –13231.
50. S. B. Sinha, D. Y. Shopov, L. S. Sharninghausen, C. J. Stein, B. Q. Mercado, D. Balcells, T. B. Pedersen, M. Reiher, G. W. Brudvig and R. H. Crabtree, *J. Am. Chem. Soc.*, 2017, **139**, 9672-9683.
51. Photochemistry and Photophysics of Coordination Compounds II, V. Balzani, S. Campagna, A. Barbieri, F. Barigelletti, E. C.-C. Cheng, L. Flamigni, T. Gunnlaugsson, R. A. Kirgan, D. Kumaresan, J. P. Leonard, C. B. Nolan, D. P. Rillema, C. Sabatini, R. H. Schmehl, K. Shankar, F. Stomeo, B. P. Sullivan, S. Vaidya, B. Ventura, J. A. G. Williams and V. W.-W. Yam, *Springer, Topics in Current Chemistry*, 2007.
52. Photochemistry and Photophysics of Coordination Compounds I, V. Balzani, S. Campagna, A. de Meijere, K. N. Houk, H. Kessler, J.-M. Lehn, S. V. Ley, S. L. Schreiber, J. Thiem, B. M. Trost, F. Vögtle and H. Yamamoto, *Springer, Topics in Current Chemistry*, 2007.
53. Electrochemical Methods. Fundamentals and Applications, A. J. Bard and L. R. Faulkner, *John Wiley & Sons, Inc.*, 2001, 2nd edition.
54. Scanning Electrochemical Microscopy, A. J. Bard and M. V. Mirkin, *CRC Press, Taylor & Francis group*, 2012, 2nd edition.
55. B. Rudshteyn, K. J. Fisher, H. M. C. Lant, K. R. Yang, B. Q. Mercado, G. W. Brudvig, R. H. Crabtree and V. S. Batista, *ACS Catal.*, 2018, **8**, 7952-7960.

Chapter 7

Excited-state dynamics of a charged homogeneous iridium molecular photocatalyst

*Dr. Noufal Kandoth synthesised the **IrPS** photocatalyst investigated in this Chapter. Dr. Camilo A. Mesa, David Pascual, Prof. Julio Lloret-Fillol and Prof. James R. Durrant contributed to the discussion of the results.*

The photocatlayst Ir^{III}(phenylpyridine)$_2$(2,2'-bipyridine)]PF_6 (**IrPS**) is a popular reductive and oxidative catalyst which has been used in many reactions ranging from water splitting to organic synthesis. Despite its well-known excited state dynamics, the reactivity and photochemistry of the anion formed under steady-state irradiation in the presence of sacrificial electron donors are yet to be fully understood (Section 7.1). In this Chapter, both **IrPS** and its anion are investigated by time-resolved absorption spectroscopy (Section 7.2.2). The excited state of **IrPS** is detected in acetonitrile with and without triethylamine (Section 7.2.2.1), while the excitation of $\mathbf{IrPS}^-$ is only observed in the latter case (Section 7.2.2.2-3).

7.0. Contents

7.1. Introduction

Transition metals with an electronic configuration d^6, such as Ir^{3+} and Ru^{2+}, form octahedral polypyridine complexes that can absorb UV-Vis light, yield long-lived triplet excited states up to microseconds, and have large emission quantum yields.[1-6] Upon light excitation, these compounds become both stronger reductants and stronger oxidants, as illustrated in Scheme 7.1A, and engage easily in one-electron transfers.[1, 2, 7] The latter has been specially relevant in the development of dye-sensitised solar cells[8-10] and redox photocatalysis,[11-20] where the right alignment between the redox potentials of the photosensitisers and the semiconductor contacts or the photocatalysts and reactants, respectively, is essential for the conversion of light into electrochemical energy. One of the most widely studied transition complex photocatalysts is the $Ir^{III}(ppy)_2(bpy)]PF_6$ (**IrPS**), where *ppy* and *bpy* stand for phenylpyridine and 2,2'-bipyridine respectively.[15, 16] Recently, the **IrPS** has been proposed to undergo two consecutive photon excitations in the presence of a sacrificial electron donor, generating an excited state anion with larger reductive powers and an unprecedented redox photochemistry (Scheme 7.1B).[21-26] To clarify this possibility, the excited state dynamics of **IrPS** in acetonitrile solution were investigated by transient absorption spectroscopy in the picosecond to nanosecond timescale.

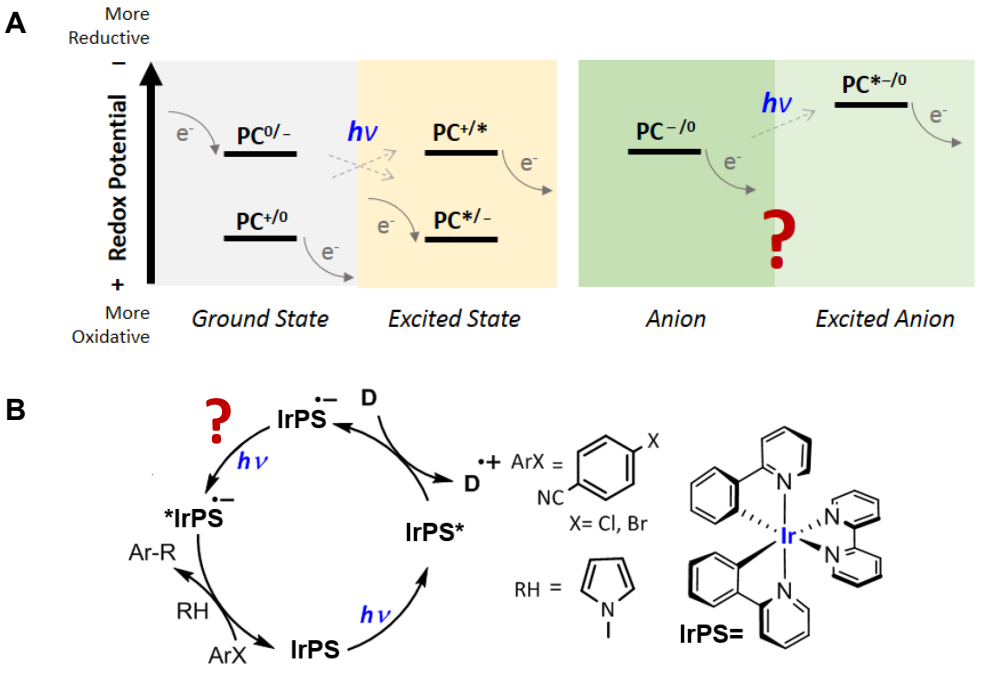

Scheme 7.1. **(A)** Relative redox potentials of a photocatalyst (PC) in its ground state (*grey*) and excited states (*yellow*), of the anion formed by reductively quenching PC (*dark green*) and of the hypothesised excited state anion (*light green*), where *hν* represents the energy of an absorbed photon, ^{0} is the ground state, and * is a photoexcited state. The redox potentials of each PC state depends on its electronic configuration. **(B)** Hypothetical mechanism for the photocatalytic activation of an aryl halide by the photocatalyst **IrPS**, where *D* is a sacrificial electron donor (Figure elaborated by Dr. Noufal Kandoth).

The one-photon excitation of **IrPS** and its excited state dynamics are well known. Previous kinetic studies have investigated **IrPS** under ~400-nm excitation in acetonitrile (ACN). Under such conditions, a nanosecond-lived signal at 500 nm was observed to raise within hundreds of femtoseconds.[27, 28] In similar iridium complexes, long lived (nanoseconds) absorbance signals in the visible range have also been detected within hundreds of femtoseconds after light excitation below 400 nm.[29-32] Supported by further photoluminescence and DFT studies,[29-39] this 500 nm signal in **IrPS** has been commonly assigned to the formation of triplet metal-to-ligand charge transfer (^{3}MLCT) excited states, mostly based on the bipyridine ligand ($^3MLCT_{bpy}$) at room temperature rather than on the pyridine ($^3MLCT_{ppy}$). As summarised in Scheme 7.2, the excitation of the ground state of **IrPS** yields a singlet excited state that, in just a few hundreds of femtoseconds, undergoes an intersystem crossing and an interligand charge transfer forming $^3MLCT_{ppy}$ and, finally, the nanosecond-lived $^3MLCT_{bpy}$.[27, 28] In the presence of an electron donor, the excited ^{3}MLCT state is reductively quenched and, as a result, the anion species **IrPS**$^-$ is formed.

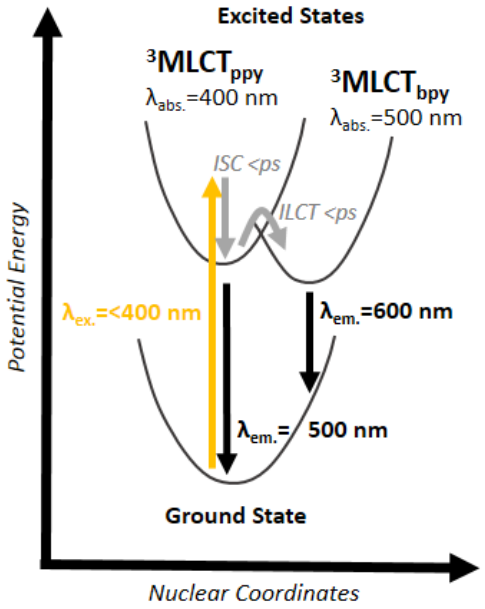

Scheme 7.2. Potential energy level diagram of the photocatalyst **IrPS** ground and excited states, where $^3MLCT_{ppy}$ and $^3MLCT_{bpy}$ stand for Metal-to-Ligand Charge Transfer states based on the pyridine and bipyridine ligands respectively, *ISC* is Intersystem Crossing, *ILCT* is Inter-Ligand Charge Transfer, and $\lambda_{abs.}$, $\lambda_{em.}$, and $\lambda_{ex.}$ correspond to the absorbance, emission and excitation wavelengths respectively.

The anion **IrPS**$^-$ can accumulate under constant irradiation in the presence of a sacrificial electron donor like trimethylamine (Et_3N). Figure 7.1A shows the absorbance over time of a solution of **IrPS** in acetonitrile with 100 mM Et_3N under 447-nm LED irradiation. The new features that appear at 390, 500 and 530 nm after a few minutes correspond to those of the anion **IrPS**$^-$, following the evidence in the literature on **IrPS**$^-$ and anions of similar complexes.[21, 23, 40-44] Furthermore, under LED irradiation, the light emission of the complex shifts from 600 nm to 500 nm (Figure 7.1B), which could be due to the excited anion photochemistry. Because the photoexcitation of this anion species has been hypothesised to generate a highly reductive state different from that of **IrPS** and unexpected optical signal dynamics are observed in the presence of Et_3N, transient absorption measurements in acetonitrile were done both with and without the sacrificial electron donor Et_3N to better understand the dynamics of the excited states of **IrPS** and **IrPS**$^-$ separately.

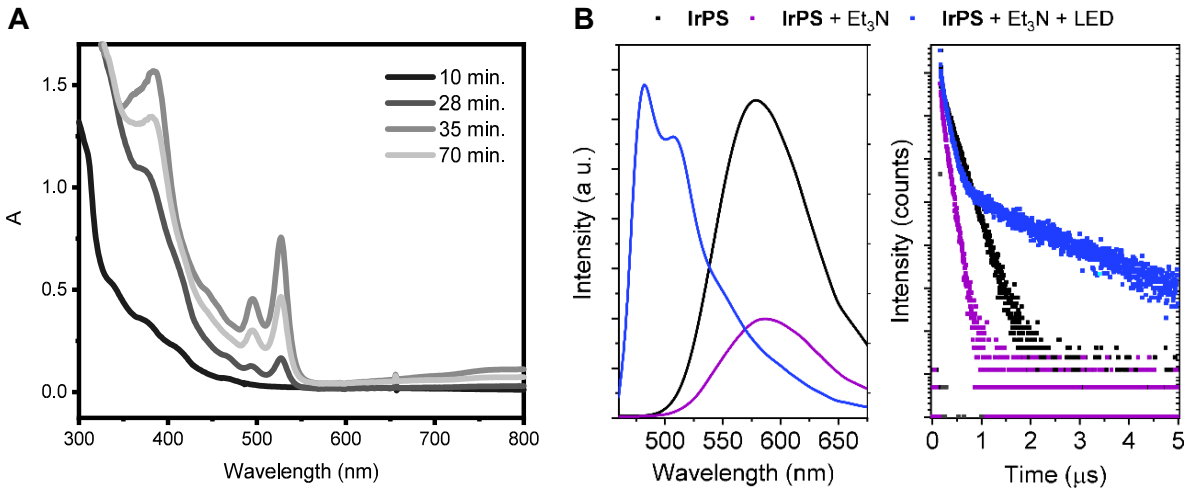

Figure 7.1. **(A)** Absorbance changes at different times under LED irradiation ($\lambda_{ex.}$ = 447±20 nm) of **IrPS** 100 μM with Et_3N 100 mM in CH_3CN at 25 ºC. **(B)** Steady-state luminescence spectra (*left*) and luminescence lifetime decay (*right*) of **IrPS** (50 μM), with and without Et_3N (25 mM) and after 7 s irradiation with at 447-nm LED (275 mW·cm^{-2}) in CH_3CN, λ_{ex} = 355 nm. Data recorded by Noufal Kandoth.

7.2. Materials and Methods

The photocatalyst Ir^{III}(phenylpyridine)$_2$(2,2'-bipyridine)]PF_6 (**IrPS**) was synthesied by Noufal Kandoth. The investigated samples contained 50 μM of **IrPS** in acetonitrile (99.8%, ACN). In some of the measurements,7.5 mM triethylamine anhydrous (≥99%, Et_3N) was added to the solution. The solvent and Et_3N were purchased from *Sigma Aldrich* and were freeze-pump-thawed before preparing the samples. All the samples were prepared under N_2 atmosphere right before each transient absorption spectroscopy measurement.

The transient absorption of **IrPS** in the picosecond to nanosecond timescale was measured with the setup and methodology described in Section 2.4.

7.3. Results

7.3.1. Picosecond to nanosecond transient absorption with and without Et_3N

IrPS was analysed by transient absorption spectroscopy in the picosecond to nanosecond timescale, as described in Section 2.4. The photocatalyst was studied in acetonitrile both in the absence (Section 7.3.1.1) and presence (Section 7.3.1.2) of Et_3N, which worked as electron donor. The **IrPS** anion was detected in the latter conditions, and its photochemistry and kinetics are investigated in Section 7.3.2. A UV-Vis absorption spectrum of **IrPS** was measured before and after each transient absorption experiment (Figure 7.2). The changes in the relative intensities of its characteristic bands indicate the irreversibility of some of the changes induced by light excitation. However, the identification of these irreversible reaction pathways is outside the scope of this work.

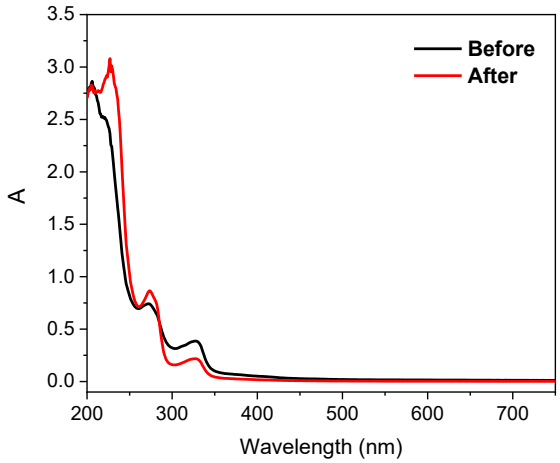

Figure 7.2. Steady-state UV-Vis absorbance of the samples (**IrPS** 50 μM in ACN with Et_3N 7.5 mM) before and after a picosecond-to-second transient absorption measurement

7.3.1.1. Transient absorption in the absence of Et_3N

In the absence of Et_3N, a band at 500 nm dominates the transient absorption spectra after the 355-nm light excitation of **IrPS** in ACN (shown in Figure 7.3A). This band is formed in the pre-picosecond timescale (the time resolution of this experiment), and its decay is almost negligible in the picosecond to nanosecond timescale (Figure 7.3A). The 500-nm signal is very similar to that reported by the studies described above in almost identical conditions and it is, therefore, assigned to the ultrafast formation of ^{3}MLCT excited states from ground state **IrPS**.

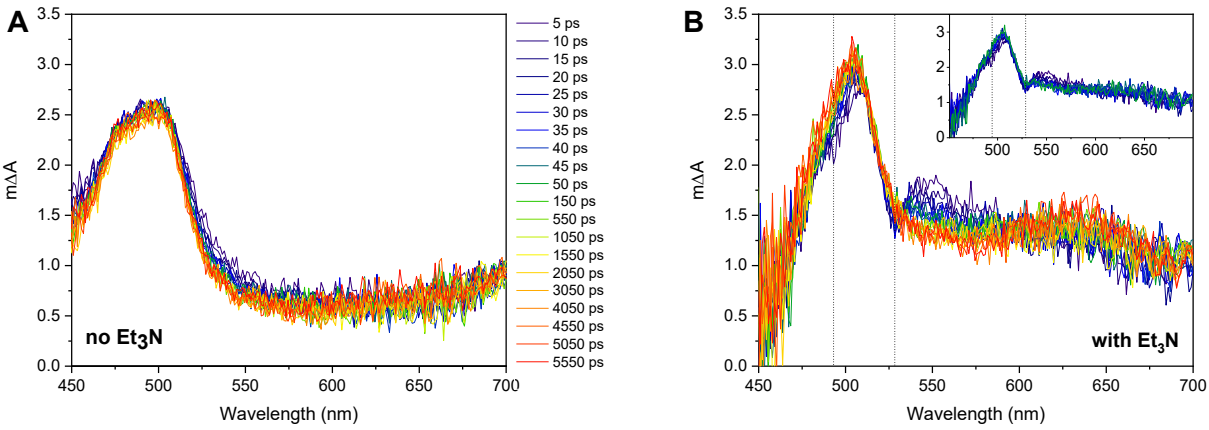

Figure 7.3. Transient absorbance of 50 µM **IrPS** in ACN upon 355 nm excitation **(A)** without and **(B)** with 7.5 mM Et_3N.

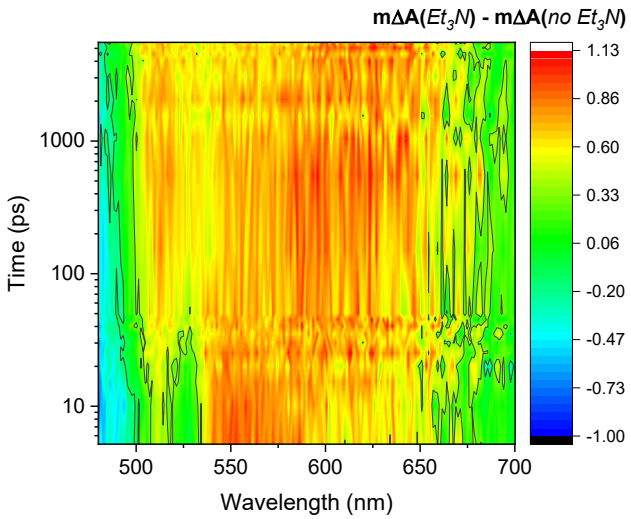

Figure 7.4. Difference in transient absorbance between the two 50 µM **IrPS** samples in Figure 7.3 with and without Et_3N (7.5 mM) in ACN. Excitation pulses: 92 fs, 355 nm, ~2 µJ/cm^2. Repetition rate: 1 kHz.

7.3.1.2. Transient absorption with Et_3N

Subsequently, the same TA measurement was repeated in the presence of Et_3N as sacrificial electron donor. The resulting transient spectra are also dominated by this broad band at around 500 nm up to nanoseconds, assigned above to ^{3}MLCT states. However, the presence of additional features centred at 500 and 530 nm at early timescales (Figure 7.3B and 7.5A) is also detected. To further investigate the characteristic features observed in **IrPS** with Et_3N in ACN, compared to pure ACN, the transient absorption spectra obtained without Et_3N were subtracted to those with Et_3N (Figure 7.4). This procedure was used to isolate the new features of **IrPS** detected in ACN with Et_3N from the typical ^{3}MLCT signal of **IrPS** detected both with and without Et_3N. Figure 7.4B shows in black the subtracted spectrum at 10 ps, which has two negative peaks at 500 and 530 nm. These distinctive peaks were only detected in the presence of Et_3N, also when the **IrPS** + Et_3N solution was pumped at ~1 mL/min. through the cuvette where TA was measured. These TA spectra were overlapped with the absolute steady-state absorbance signal of the photocatalyst in the presence of Et_3N after being excited with LED light, which corresponds to the formation of the anion **IrPS**$^-$ [21, 45] (Figures 7.5B in grey and 7.1A). It is apparent from Figure 7.5B that the subtracted spectrum at 10 ps closely matches the negative anion absorbance bands at 500 and 530 nm, indicating the photobleaching of the anion absorbance, which would be excited by the laser pulses. Consequently, this data is consistent with the existence of anion in the sample of **IrPS** with Et_3N under femtosecond-pulsed excitation. The presence of anion is most likely due to the high frequency of the pump pulses (*i.e.*, 1 kHz, see Section 2.4), which generates a steady-state population of **IrPS**$^-$ *in situ* under these light irradiation conditions. These results therefore show that excitation of the anion **IrPS**$^-$ with 355-nm light is possible in the presence of a sacrificial electron donor.

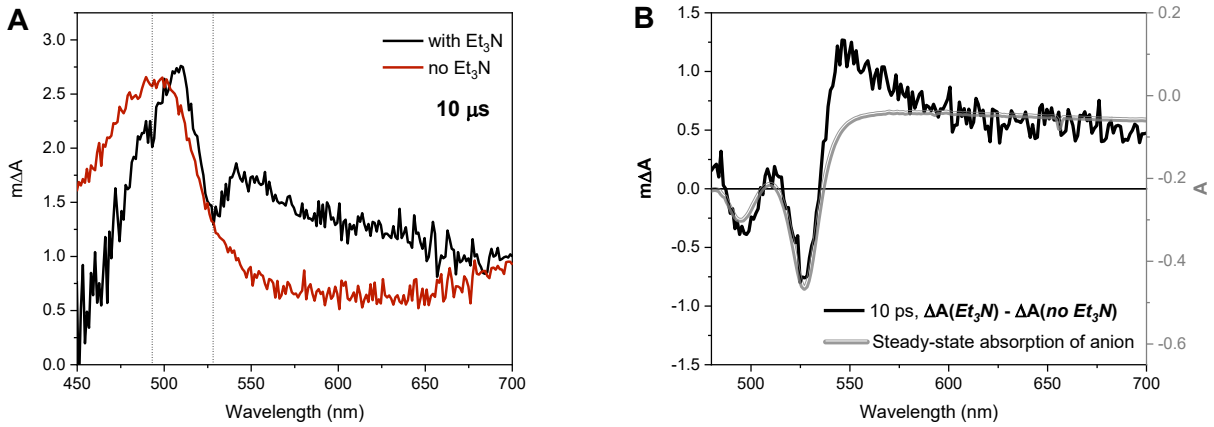

Figure 7.5. **(A)** Transient absorbance of **IrPS** with Et_3N (5-5500 ps). **(B)** Difference between transient absorbance of one single sample with and without Et_3N (black) overlapped with the negative steady-state absorbance of the anion (*grey*, spectrum corresponding to 70s after under constant irradiation in a flow cell, Figure 7.1A). Measurement conditions: **IrPS** 50 µM in ACN with Et_3N 7.5 mM.

7.3.2. Anion kinetics

Once the accumulation of anion species could be identified under the pulsed excitation conditions, and the subsequent photoexcitation of these anions, the kinetics of the anion photoexcited state are examined. The decay of the anion is calculated by subtracting the kinetics of **IrPS** in ACN with Et_3N, where the optical signal of the anion has been detected (as assigned above and in Figure 7.5), to the kinetics of **IrPS** in ACN without Et_3N, where the anion cannot be formed. The difference in kinetics at 530 nm decays within 50 ps, with a half-time of ~ 20 ps (Figure 7.6A and 7.4). A similar timescale was observed for recovery of the anion photobleaching signals in the spectra with Et_3N (Figure 7.3B). It can thus be concluded that the photoexcited anions primarily recover to their anion ground state within 50 ps.

At slower timescales (*i.e.*, nanoseconds), the transient spectra with and without Et_3N differ slightly across the 450-700 nm range, as shown in Figure 7.6B. These differences cannot be assigned to any of the known species, including photoionized aqueous electrons that would have an absorbance maximum at 700 nm.[22, 41, 46-49] Therefore, this evidence implies that, while the photoexcited anion primarily recovers its initial ground state anion in 50 picoseconds, some additional long lived species may also be generated.

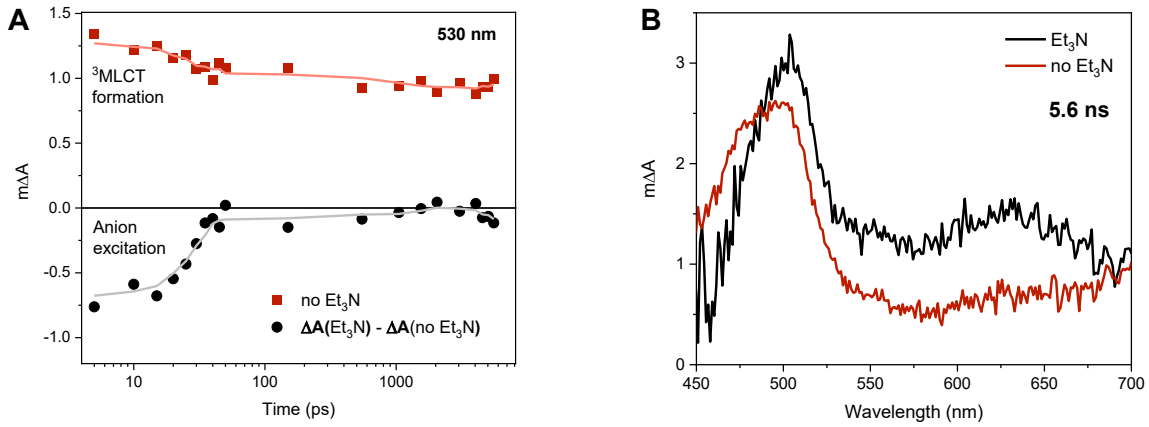

Figure 7.6. **(A)** Kinetics at 530 nm of **IrPS** without Et_3N in ACN (*red* trace) and **IrPS**$^-$ (*black* trace, calculated by subtracting the kinetics of **IrPS** with and without Et_3N in ACN). (B) Transient spectra of **IrPS** after 5.6 ns of photoexcitation in ACN with and without Et_3N.

7.4. Discussion

The **IrPS**$^{-}$ has been accumulated and excited under high frequency pulsed laser and its excited state has been observed to decay with a lifetime τ~ 20 ps (Scheme 7.2). Because of the fast decay of the excited anion, the excited anion cannot explain neither the unexpected photoreductive chemistry observed by König et al.[21] nor the photoluminescence at 500 nm after LED irradiation (Figure 7.1B). However, this does not exclude that the excited anion may have different photochemical properties than the neutral complex **IrPS** or that it may alter the photochemistry of the solution at slower timescales. The latter could also explain the irreversible UV-Vis absorbance changes after the measurements (Figure 7.2).

Photoluminescence of **IrPS** at 500 nm has previously been observed at low temperatures and has been assigned to a higher energy triplet state based on the phenyl-pyridine ligands ($^{3}MLCT_{ppy}$), in contrast to the triplet states formed at room temperature which is based on the bipyridine ligand ($^{3}MLCT_{bpy}$).[30, 36] These two triplet states absorb at 400 nm and 500 nm respectively and emit at 500 nm and 600 nm respectively, as represented in Schemes 7.2-3. The photoluminiscence at 500 nm after LED irradiation reveals a larger presence of $^{3}MLCT_{ppy}$ in these conditions, which absorbs at 400 nm, outside of our detection range. Therefore, in accordance to similar available evidence,[50-54] it is a possibility that the presence of the anion alters the equilibrium between $^{3}MLCT_{ppy}$ and $^{3}MLCT_{bpy}$ in **IrPS**, or that the anion itself has similar but slightly different photochemistry compared to **IrPS**.

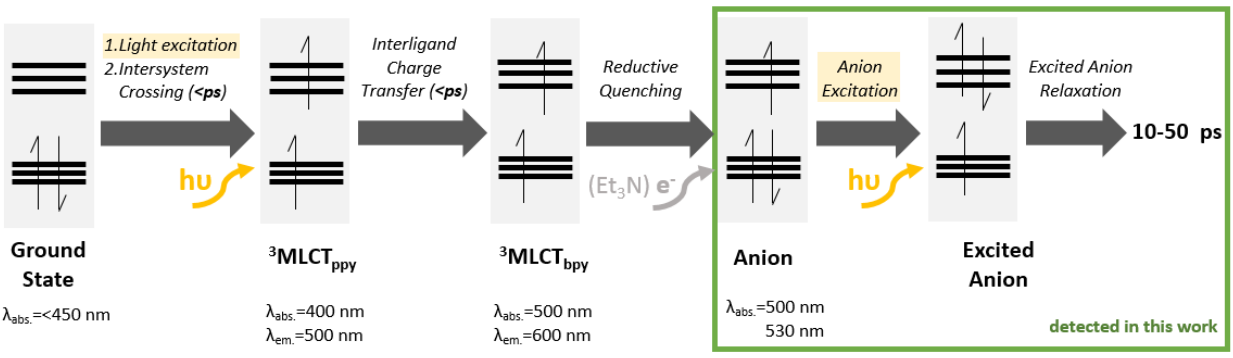

Scheme 7.3. Known photochemistry of **IrPS**,[27, 30, 36] and photochemical processes detected in this work, where $\lambda_{abs.}$ and $\lambda_{em.}$ correspond to the wavelengths of maximum absorption and emission respectively. Each bloc represents an energy state, while the horizontal lines are a representation of the higher occupied and lower unoccupied molecular orbitals. While the relative energy of **IrPS** is determined by the state, its redox potential depends on the electronic configuration of each state.

7.5. Conclusions

Picosecond to nanosecond transient absorption spectroscopy has been used to investigate the excited state dynamics of the photocatalyst **IrPS** and its anion in acetonitrile. At high pulse frequencies and in the presence of Et_3N, a steady-state concentration of anion is formed and excited, which is detected as a bleach of its characteristic absorbance bands at 390, 500 and 530 nm. The half-life of the excited anion derived from the recovery of the anion bleaching signal is around 50 ps. This indicates that the excited anion is not responsible for the photochemistry under steady-state illumination.

7.6. References

1. Photochemistry and Photophysics of Coordination Compounds II, V. Balzani, S. Campagna, A. Barbieri, F. Barigelletti, E. C.-C. Cheng, L. Flamigni, T. Gunnlaugsson, R. A. Kirgan, D. Kumaresan, J. P. Leonard, C. B. Nolan, D. P. Rillema, C. Sabatini, R. H. Schmehl, K. Shankar, F. Stomeo, B. P. Sullivan, S. Vaidya, B. Ventura, J. A. G. Williams and V. W.-W. Yam, *Springer, Topics in Current Chemistry*, 2007.
2. Photochemistry and Photophysics of Coordination Compounds I, V. Balzani, S. Campagna, A. de Meijere, K. N. Houk, H. Kessler, J.-M. Lehn, S. V. Ley, S. L. Schreiber, J. Thiem, B. M. Trost, F. Vögtle and H. Yamamoto, *Springer, Topics in Current Chemistry*.
3. C. Adachi, M. A. Baldo, S. R. Forrest and M. E. Thompson, *Appl. Phys. Lett.*, 2000, **77**, 904-906.
4. C. Adachi, M. A. Baldo, M. E. Thompson and S. R. Forrest, *J. Appl. Phys.*, 2001, **90**, 5048-5051.
5. M. A. Baldo, M. E. Thompson and S. R. Forrest, *Nature*, 2000, **403**, 750-753.
6. I. M. Dixon, J.-P. Collin, J.-P. Sauvage, L. Flamigni, S. Encinas and F. Barigelletti, *Chem. Soc. Rev.*, 2000, **29**, 385-391.
7. Photochemistry and photophysics: concepts, research, applications, V. Balzani, P. Ceroni and A. Juris, *Wiley-VCH*, 2014.
8. S. Aghazada and M. Nazeeruddin, *Inorganics*, 2018, **6**, 52.
9. Y. Qin and Q. Peng, *Int. J. Photoenergy*, 2012, **2012**, 1-21.
10. F. Légalité, D. Escudero, Y. Pellegrin, E. Blart, D. Jacquemin and O. Fabrice, *Dyes Pigm.*, 2019, **171**.
11. K. L. Skubi, T. R. Blum and T. P. Yoon, *Chem. Rev.*, 2016, **116**, 10035-10074.
12. T. P. Yoon, *Acc. Chem. Res.*, 2016, **49**, 2307-2315.
13. C. S. Wang, P. H. Dixneuf and J. F. Soule, *Chem. Rev.*, 2018, **118**, 7532-7585.
14. M. Yan, Y. Kawamata and P. S. Baran, *Chem. Rev.*, 2017, **117**, 13230-13319.
15. C. K. Prier, D. A. Rankic and D. W. MacMillan, *Chem. Rev.*, 2013, **113**, 5322-5363.
16. M. H. Shaw, J. Twilton and D. W. MacMillan, *J. Org. Chem.*, 2016, **81**, 6898-6926.
17. J. M. Narayanam and C. R. Stephenson, *Chem. Soc. Rev.*, 2011, **40**, 102-113.
18. B. König, *Eur. J. Org. Chem.*, 2017, **2017**, 1979-1981.
19. W. T. Eckenhoff and R. Eisenberg, *Dalton Trans.*, 2012, **41**, 13004-13021.
20. J. Willkomm, K. L. Orchard, A. Reynal, E. Pastor, J. R. Durrant and E. Reisner, *Chem. Soc. Rev.*, 2016, **45**, 9-23.
21. M. Giedyk, R. Narobe, S. Weiß, D. Touraud, W. Kunz and B. König, *Nat. Catal.*, 2020, **26**, 10355-10361.
22. C. Kerzig and M. Goez, *Chem. Sci.*, 2016, **7**, 3862-3868.
23. C. Kerzig, X. Guo and O. S. Wenger, *J. Am. Chem. Soc.*, 2019, **141**, 2122-2127.
24. C. Kerzig and O. S. Wenger, *Chem. Sci.*, 2019, DOI: 10.1039/c9sc04584h.
25. I. Ghosh, T. Ghosh, J. I. Bardagi and B. König, *Science*, 2014, **346**, 725-728.
26. I. Ghosh, L. Marzo, A. Das, R. Shaikh and B. Konig, *Acc. Chem. Res.*, 2016, **49**, 1566-1577.
27. S. Tschierlei, A. Neubauer, N. Rockstroh, M. Karnahl, P. Schwarzbach, H. Junge, M. Beller and S. Lochbrunner, *Phys. Chem. Chem. Phys.*, 2016, **18**, 10682-10687.
28. R. Bevernaegie, L. Marcelis, A. Moreno-Betancourt, B. Laramee-Milette, G. S. Hanan, F. Loiseau, M. Sliwa and B. Elias, *Phys. Chem. Chem. Phys.*, 2018, **20**, 27256-27260.
29. E. Erdmann, M. Lutgens, S. Lochbrunner and W. W. Seidel, *Inorg. Chem.*, 2018, **57**, 4849-4863.
30. Y. J. Cho, S. Y. Kim, H. J. Son, D. W. Cho and S. O. Kang, *Phys. Chem. Chem. Phys.*, 2017, **19**, 8778-8786.
31. G. J. Hedley, A. Ruseckas and I. D. W. Samuel, *Chem. Phys. Lett.*, 2008, **450**, 292-296.
32. G. J. Hedley, A. Ruseckas and I. D. W. Samuel, *J. Phys. Chem. Lett. A*, 2009, **113**, 2-4.
33. G. J. Hedley, A. Ruseckas and I. D. W. Samuel, *J. Phys. Chem. A* 2010, **114**, 8961–8968.
34. M. Chergui, *Acc. Chem. Res.*, 2015, **48**, 801-808.
35. F. Messina, E. Pomarico, M. Silatani, E. Baranoff and M. Chergui, *J. Phys. Chem. Lett.*, 2015, **6**, 4475-4480.

36. E. Pomarico, M. Silatani, F. Messina, O. Braem, A. Cannizzo, E. Barranoff, J. H. Klein, C. Lambert and M. Chergui, *J. Phys. Chem. C*, 2016, **120**, 16459-16469.
37. X. Y. Liu, Y. H. Zhang, W. H. Fang and G. Cui, *J. Phys. Chem. A*, 2018, **122**, 5518-5532.
38. R. D. Costa, F. Monti, G. Accorsi, A. Barbieri, H. J. Bolink, E. Orti and N. Armaroli, *Inorg. Chem.*, 2011, **50**, 7229-7238.
39. H. S. Duan, P. T. Chou, C. C. Hsu, J. Y. Hung and Y. Chi, *Inorg. Chem.*, 2009, **48**, 6501-6508.
40. B. C. Noble and R. D. Peacock, *Spectrochim. Acta*, 1990, **46A**, 407-412.
41. M. Brautzsch, C. Kerzig and M. Goez, *Green Chem.*, 2016, **18**, 4761-4771.
42. J. H. Shon and T. S. Teets, *Inorg. Chem.*, 2017, **56**, 15295-15303.
43. H. Y. Cheong, S. Y. Kim, Y. J. Cho, D. W. Cho, C. H. Kim, H. J. Son, C. Pac and S. O. Kang, *Inorg. Chem.*, 2017, **56**, 12042-12053.
44. W. Yang, B. Ashwood, J. Zhao, W. Ji, D. Escudero, D. Jacquemin and C. E. Crespo-Hernández, *J. Phys. Chem. C*, 2017, **121**, 21184-21198.
45. B. C. Noble and R. D. Peacock, *Spectrochim. Acta*, 1990, **46A**, 407-412.
46. G. V. Buxton, C. L. Greenstock, W. P. Helman and A. B. Ross, *J. Phys. Chem. Ref. Data*, 1988, **17**, 513-886.
47. M. Goez, C. Kerzig and R. Naumann, *Angew. Chem. Int.*, 2014, **53**, 9914-9916.
48. R. Naumann, C. Kerzig and M. Goez, *Chem. Sci.*, 2017, **8**, 7510-7520.
49. R. Naumann, F. Lehmann and M. Goez, *Angew. Chem. Int.*, 2018, **57**, 1078-1081.
50. H. Takeda and O. Ishitani, *Coord. Chem. Rev.*, 2010, **254**, 346-354.
51. S. Sato, T. Morikawa, T. Kajino and O. Ishitani, *Angew. Chem. Int.*, 2013, **52**, 988-992.
52. M. S. Lowry and S. Bernhard, *Chem. Eur. J.*, 2006, **12**, 7970-7977.
53. V. Mdluli, S. Diluzio, J. Lewis, J. F. Kowalewski, T. U. Connell, D. Yaron, T. Kowalewski and S. Bernhard, *ACS Catal.*, 2020, **10**, 6977-6987.
54. T. U. Connell, C. L. Fraser, M. L. Czyz, Z. M. Smith, D. J. Hayne, E. H. Doeven, J. Agugiaro, D. J. D. Wilson, J. L. Adcock, A. D. Scully, D. E. Gomez, N. W. Barnett, A. Polyzos and P. S. Francis, *J. Am. Chem. Soc.*, 2019, **141**, 17646-17658.

Chapter 8

Concluding remarks

Time-resolved spectroscopy and electrochemistry have been effectively used to characterise redox states of catalyst materials and their reaction pathways under catalytic conditions. This thesis has attempted to better explain the catalytic activity of various catalyst as a function of their physicochemical properties and chemical structure, aiming at guiding the design of better catalysts in the future.

Efficient charge accumulation has been identified as a key challenge to improve the direct photo(electro)chemical conversion of solar energy. Chapters 3 and 4 focused on multi-redox molecular catalysts in photocatalytic electrodes. These Chapters investigated water- and CO_2- reduction cobalt-based molecular catalysts immobilised on TiO_2 and investigated how photogenerated charges in the TiO_2 were transferred and accumulated onto the catalyst. Charge accumulation was characterised by identifying multi-redox states of the catalyst spectro-electrochemically. The formation of the catalytically necessary multi-redox states was observed to occur in hundreds of microseconds, and was critically affected by the microsecond recombination of these states mostly with photogenerated holes in the valence band. An intra-bandgap applied potential combined with high excitation intensities was shown to be an effective approach to prevent recombination while favouring charge accumulation simultaneously. This would support the use of concentrated solar energy schemes, specially in the case where the redox potentials of the different components are close and the reaction driving force is small. Apart from the widely studied TiO_2 used here as photosensitizer, other semiconductor metal oxides or polymers would most likely have similar photoelectrochemical behaviour, which is determined by the band alignment and the depth and distribution of trapped states in the conduction band. Therefore, a hybrid approach between the photoelectrochemical and the photovoltaic-electrolyser scheme could potentially have better efficiencies than the first and lower complexity than the latter. With the advent of smart grids and the internet of things, it may also be possible to create flexible self-optimising devices which only take the necessary potential and light intensity. This scheme also offers the possibility to control the charge of a semiconductor electrode with light.

Similar catalytic multi-reduced catalytic intermediates were observed in different cobalt-based H_2-production catalysts under catalytic conditions. The mathematically deconvolved reaction kinetics was consistent with the catalytic hydrogen production and could be related to differences in the stability of key molecular orbitals in the different catalysts. The activity of molecular catalyst could therefore be parametrised with volcano plots similar to those used for heterogeneous

inorganic catalysts. This is not completely surprising because, even if volcano plots are mostly calculated for solid-state catalyst operating under a heterogeneous regime, the activity trends are mostly analysed with respect to intermediates based on electrolyte species adsorbed to one or a few metal atoms. Compared to electrochemical studies, spectroscopical measurements probe electronic transitions that are unique to specific intermediates and reveal information about their electronic configuration independently of the reaction conditions. It remained a challenge, however, to establish a closer relationship between the concentration of intermediate species and the production of H_2 *in situ*.

To better establish the relationship between activity and the chemical environment of metal centres, iridium catalysts have been brought into focus in Chapters 5, 6 and 7. Water-oxidation hydrous iridium oxide and a molecular iridium dimer were studied in acid aqueous media. Mathematical deconvolution was used to separately identify the optical and electrochemical signal of different overlapping redox transitions and redox states. The spectroelectrochemical properties of redox states in iridium was very similar in both molecular and inorganic catalysts, with shift in the absorption maxima and redox potentials that were related to the energetics of metal orbitals. It was shown that reaction lifetimes derived from the optical signal decays can be a promising way to detect localised active surface states in highly disordered and molecular multi-redox catalysts. However, the rate law of iridium oxide remains to be measured for a deeper understanding of the reaction mechanism. All this evidence proves that the catalysis is localised on a few iridium atoms and that these can be effectively tuned by the ligands around it. This would also be extensive to catalyst based on earth-abundant metals and would hold promise for their future improvement. Considering the high activities of amorphous IrO_x and molecular catalyst per metal atom and their instability, a better compromise between fine-tuned localised active sites and material stability may be found through the development of highly ordered hybrid materials like metal-organic frameworks. Finally, Chapter 7 investigated the multi-photon excitation of and iridium molecular photocatalysts. The fast decay of its excited anion prevents its application to the homogeneous catalysis of highly energetic reactions, but it higher reducing power could potentially be more effectively exploited in heterogeneous and supramolecular schemes.

In conclusion, this thesis has shown that molecular catalysts can be used as catalysis probes and be applied to understand catalysis at the atomic scale. Second, an approach to experimentally measure the impact of the first coordination sphere to the metal active site has been successfully developed, which could enable the study of surface-modified heterogeneous catalysis. Furthermore, the challenge remains to quantitatively link spectroscopic and electrochemical results to H_2 or O_2 production, which may be improved in the future with multi-modal simultaneous measurements and high-throughput screening and computer-guided experimentation and optimization.